SEISMIC BEHAVIOR OF LIGHTLY REINFORCED CONCRETE SQUAT SHEAR WALLS

THÈSE N^{O} 3512 (2006)

PRÉSENTÉE LE 28 AVRIL 2006

À LA FACULTÉ ENVIRONNEMENT NATUREL, ARCHITECTURAL ET CONSTRUIT
Laboratoire d'informatique et de mécanique appliquées à la construction
SECTION DE GÉNIE CIVIL

ÉCOLE POLYTECHNIQUE FÉDÉRALE DE LAUSANNE

POUR L'OBTENTION DU GRADE DE DOCTEUR ÈS SCIENCES

PAR

Christian GREIFENHAGEN

Dipl.-Ing., Technische Universität Dresden, Allemagne
et de nationalité allemande

acceptée sur proposition du jury:

Prof. M.A. Hirt, président du jury
Dr P. Lestuzzi, Dr. M. Badoux, directeurs de thèse
Prof. P. Bisch, rapporteur
Prof. A. Dazio, rapporteur
Prof. L. Stempniewski, rapporteur

ÉCOLE POLYTECHNIQUE
FÉDÉRALE DE LAUSANNE

Lausanne, EPFL
2006

Acknowledgements

First, I would like to thank my supervisor, Dr. Pierino Lestuzzi, for offering me the opportunity to work at the applied computing and mechanics laboratory (IMAC). I am highly indebted for his continuous support, encouragement, and constant discussion throughout this research.

I would also like to thank Dr. Marc Badoux who is the co-director of this thesis. He initiated the research project and contributed significantly by advice and guidance.

My thanks go to Prof. Ian F. C. Smith, Head of the applied computing and mechanics laboratory, for giving an opportunity to conduct research and providing me with all the necessary support.

I would also like to thank Profs. Philippe Bisch, Alessandro Dazio, and Lothar Stempniewski for their invaluable suggestions which have significantly helped me in advancing the research.

I am gratefully to my colleagues and friends who contributed by both reviewing the text and figures, as well as in discussion. It was a pleasure to work in an amicable and friendly environment with Dr Francine Laferrière, Bernard Adam, Dr Vincent Pellissier, Abhijit Patil, Dr Prakash Kripakaran, Eckart Hars, Dr Michel Thomann, François Barrot, Dr Miguel Ruiz Fernandez, and Rui Vaz Rodrigues.

My thanks also go to Patrice Gallay, Dhimitris Papas, Charles Gilliard, and Jean-Louis Guignard for providing me with necessary equipments, materials, and help in experimental investigations.

I would also like to thank the Swiss National Science Foundation for supporting me with the research grant from period 2002-2006 for conducting the research.

Finally, I am grateful to my parents and my sister for their patience and encouragement throughout the research work.

Abstract

This thesis addresses the seismic evaluation of existing buildings. In particular, it focuses on the seismic behavior of lightly reinforced shear walls that are not designed to withstand earthquake actions. A shear strength envelope for the assessment of deformation capacity of these non-ductile walls is presented. The approach is the result of experimental investigations and analytical modeling. Existing models for plastic hinges in beams are enhanced in order to determine drift capacity of lightly reinforced concrete shear walls.

The static-cyclic behavior of non-ductile, reinforced concrete shear walls is investigated by testing four small-scale specimens of shear span ratio equal to 0.8. The design of the specimens includes reinforcement ratios, and axial force levels in existing shear wall buildings. Although the specimens were expected to fail in brittle shear, low to moderate ductile response is obtained. The deformation capacity, not the shear strength, is found to be restricted by shear failure. It is observed that inherent shear strength of concrete and the concrete compression zone are the principal contributors to the shear capacity of lightly reinforced shear walls. It is also observed that low reinforcement ratios and moderate levels of axial force can efficiently prevent brittle response in shear.

The analytical model consists of a plastic hinge over the entire height of the low-rise shear wall. Proposals are made for the strain distribution inside the plastic hinge. Explicit relationships between drift and base shear are established and it is found that the model accurately predicts the envelope curve of static-cyclic loading.

The shear strength envelope is formulated by using the analytical model. Criteria for the failure modes of diagonal tension, of concrete crushing, and of sliding enclose the shear strength envelope. In addition, inherent shear strength forms the lower bound of this envelope. The contributions of reinforcement and concrete to shear capacity are formulated in terms of initial strength and strength decay. Accurate prediction of both the ductility supply and the drift capacity obtained in static-cyclic tests is observed.

Validation of the shear strength envelope on full-size walls prevalent in existing buildings shows potential for further application. The proposal contributes to more realistic evaluation of shear strength in selected situations where available methods are too conservative. Hence, it allows for both avoiding costly seismic strengthening in such situations and better allocation of resources where they are really needed.

Keywords

Seismic evaluation, existing buildings, reinforced concrete, shear wall, deformation capacity, shear strength, static-cyclic tests

Résumé

Cette thèse s'inscrit dans le contexte de l'évaluation sismique de bâtiments existants. Elle se concentre en particulier sur le comportement sismique des murs faiblement armés qui n'ont pas étés conçus pour résister à l'effet d'un tremblement de terre et qui sont actuellement considérés comme vulnérables. Une enveloppe de cisaillement servant à l'estimation réaliste de la capacité en déformation de ces murs non-ductiles est proposée. L'approche adoptée s'appuie sur une partie expérimentale et sur une partie analytique. Des modèles existants pour les rotules plastiques des poutres sont adaptés en vue de déterminer la capacité de déformation des murs de refend faiblement armés.

Le comportement statique-cyclique des murs de refend non-ductiles en béton armé est analysé en testant à l'échelle 1:3 des spécimens modèles réduits dont la portée de cisaillement est égale à 0.8 par rapport de la longueur des murs. La conception des spécimens prend en compte les taux d'armature, le niveau de la force axiale, et des détails des armatures couramment rencontrés dans les bâtiments existants. Bien que les spécimens auraient dû se rompre en rupture fragile à l'effort tranchant, une réponse plutôt ductile a été obtenue. La capacité de déformation, et non le niveau de cisaillement, apparaît ainsi restreinte par une rupture à l'effort tranchant. Il a été observé que la résistance du béton au cisaillement, ainsi que la zone de compression du béton, sont les principaux facteurs participants à la capacité en cisaillement des murs de refend peu armés. Il a aussi été observé que de faibles taux d'armature, ainsi que des niveaux modérés de la force axiale, permettent d'éviter, de façon efficace, une rupture fragile à l'effort tranchant.

Le modèle analytique est constitué d'une rotule plastique sur toute la hauteur d'un mur de refend et de la distribution des déformations qui y est admise. Des relations explicites entre le déplacement relatif et l'effort tranchant à la base sont établies et il est démontré que le modèle prédit de façon précise la courbe enveloppe d'un chargement statique-cyclique.

L'enveloppe de cisaillement est formulée en utilisant le modèle analytique. Des critères pour les modes de rupture en tension diagonale ainsi qu'en écrasement du béton sont incorporés dans l'enveloppe de cisaillement. De plus, la résistance du béton au cisaillement forme la limite inférieure de cette enveloppe. Les contributions des armatures horizontales et du béton à la capacité de cisaillement sont formulées en termes de résistance initiale et de la dégradation de la résistance due à l'augmentation de déformation. On observe une prédiction précise à la fois de l'offre en ductilité et de la capacité en déplacement relatif obtenue lors des tests statiques-cycliques.

La validation de l'enveloppe de cisaillement sur des murs de taille réelle, dans des bâtiments existants, est prometteuse pour d'autres applications. Ce projet contribue à une évaluation plus réaliste de la résistance au cisaillement dans des situations où les méthodes disponibles sont trop prudentes. Par conséquent, il permettra d'éviter des assainissements sismiques onéreux et injustifiés.

Mots clés

Evaluation sismique, bâtiments existants, béton armé, murs de refend, capacité en déformation, résistance à l'effort tranchant, essai statique-cyclique

Kurzfassung

Die vorliegende Arbeit liefert einen Beitrag zur Erdbebenüberprüfung bestehender Gebäude. Im Mittelpunkt steht dabei das Erdbebenverhalten schwach bewehrter Tragwände aus Stahlbeton die nicht für Einwirkungen infolge Erdbeben bemessen wurden. Für solche Wände wird oft ein ungenügendes Erdbebenverhalten erwartet. Die Arbeit schliesst den Vorschlag eines Bruchkriteriums ein, mit dem die realistische Abschätzung des Verformungsvermögens von nicht-duktilen, gedrungenen Tragwänden möglich ist. Der Vorschlag stützt sich auf experimentelle und analytische Forschung ab. Bereits existierende Modelle für plastische Gelenke in Stahlbetonbalken werden modifiziert, um das Verformungsvermögen schwach bewehrter Tragwände zu bestimmen.

Das statisch-zyklische Verhalten von nicht-duktilen, gedrungenen Tragwänden wird experimentell in Versuchen an vier kleinmasstäblichen Prüfkörpern (Masstab 1:3) mit Schubspannweiten von 80% der Wand-länge analysiert. Die Konzeption der Prüfkörper orientiert sich hinsichtlich Bewehrungsgehalt, bezogener Normalkraft und konstruktiver Durchbildung der Bewehrung an bestehenden Wandscheibenbauten. Entgegen den Erwartungen, dass die Prüfkörper ein sprödes Schubversagen aufweisen, wurde in den Versuchen ein duktiles Verhalten erzielt. Damit wird nicht der maximale Schubwiderstand sondern das Verformungsvermögen durch Schubversagen begrenzt. Es wurde beobachtet, dass die Betonzugfestigkeit und die Betondruckzone massgeblich zum Schubwiderstand von schwach bewehrten Tragwänden beitragen können. Weiterhin wurde beobachtet, dass die Begrenzung von Bewehrungsgehalt und bezogener Normalkraft sprödes Schubversagen wirkungsvoll verhindern kann.

Das Berechnungsmodell besteht aus einem Fliessgelenk über die gesamte Schubspannweite der Tragwand. Für die Dehnungen innerhalb des Fliessgelenks werden Vorschläge gemacht. Explizite Beziehungen zwischen der Rotation im Fliessgelenk und der Querkraft werden aufgestellt. Die berechneten Hüllkurven erlauben eine zutreffende Vorhersage des im statisch-zyklischen Versuch beobachteten Verhaltens.

Das Berechnungsmodell wird anschliessend zur Ableitung eines verformungsbasierten Bruchkriteriums für Schubversagen angewendet. Dieses bildet Versagen infolge Schrägzug und Gleiten sowie Betondruckversagen ab. Das Bruchkriterium schliesst auch eine untere Schubspannungsgrenze ein. Die Beiträge von Beton und Querbewehrung zum Schubwiderstand werden als Initialbeitrag und Abminderungsfaktor infolge Zunahme der Verformungen formuliert. Mit dem vorgeschlagenen Bruchkriterium wird das im statisch-zyklischen Versuch beobachtete Verformungsvermögen zuverlässig abgeschätzt.

Die Anwendung auf Tragwände bestehender Gebäude zeigt das Potential des vorgeschlagenen Bruchkriteriums für die Erdbebenüberprüfung bestehender Gebäude. Die vorliegende Arbeit trägt damit zu einer realistischeren Bewertung des Schubtragvermögens von Tragwänden bei. Dies gilt besonders für Situationen in denen vorhandene Modelle zu konservative Ergebnisse liefern. Damit können unnötig kostpielige Erdbebenertüchtigungen vermieden werden.

Stichworte

Erdbebenüberprüfung, bestehende Gebäude, Stahlbeton, Tragwand, Verformungsvermögen, Schubwiderstand, statisch-zyklischer Versuch

Contents

Chapter 1

Introduction

1.1 Context

The built environment of many countries with moderate seismic exposure, for example Switzerland, often includes numerous multistorey buildings designed for gravity loads featuring lightly reinforced concrete shear walls. These buildings were not designed to current seismic requirements. So, it is often necessary to evaluate their seismic capacity which may to be increased by retrofitting. The research presented in this thesis aims at improving models for predicting actual seismic capacity of such buildings.

Reinforced concrete shear walls represent one of the most widespread bracing system for buildings. Post-earthquake reconnaissance missions report surprisingly good seismic behavior of structural wall buildings (Fintel 1995) while evaluation of existing buildings according to modern standards concludes often at insufficient safety margins. An important number of existing buildings is stabilized by shear walls that are only designed for gravity loads, and not for lateral loads. Low reinforcement ratios, slenderness ratios less than 2.0, and inadequate seismic detailing characterize such walls. According to widely held views, squat reinforced concrete walls with low reinforcement ratios are susceptible to brittle shear failure restricting deformation capacity. Poor seismic performance is thus expected.

In this context, experimental studies not only provide physical insight into seismic behavior for development of models, but also the data to calibrate them, so that realistic and efficient evaluation methods can be achieved. Since deformation based methods promise more realistic results than the force based methods, the former should be applied on existing buildings too (Priestley 1997). Nevertheless, the characteristic details of existing buildings can lead to restricted deformation capacity which is investigated in this research.

1.2 Motivation

The seismic evaluation of existing buildings requires appropriate tools to identify vulnerable structures and to allocate retrofitting resources where there is a need for intervention. In this context, the research focuses on reinforced concrete shear walls that have not been designed for earthquake actions. Since these walls do not meet the required reinforcement ratios and reinforcement configurations, the seismic behavior of lightly reinforced shear walls is not yet well understood. Scientific research has to be carried out in order to investigate the seismic performance of such walls.

During the last two decades, significant progress was made in seismic engineering and this has lead to better knowledge of parameters that influence seismic risk. In this context, a principal task for structural engineers is to quantify and to reduce the vulnerability of building stock. Appropriate evaluation methods can help to improve the management of seismic risk.

The response of reinforced concrete structures to seismic ground motion is generally non-linear and energy dissipation is assured for the most part by plastic deformations. Earthquake actions depend strongly on deformation behavior and effective stiffness of structural members. Since brittle to low ductile behavior generally believed for lightly reinforced shear walls, conservative estimates on capacity in both strength and deformation are included in seismic evaluation. Better knowledge of deformation capacity can allow more economic retrofitting through more realistic prediction of earthquake actions.

1.3 Objective

This research focuses on both the experimental and theoretical investigation of the behavior of lightly reinforced shear walls subjected to cyclic loading. Emphasis is on shear dominated response and deformation based formulations. This response is governed by several parameters such as the aspect ratio, normal force, reinforcement detailing, longitudinal and lateral reinforcement ratios. The seismic performance is characterized by failure modes, the force-deflection relationship, and the available ductility. To quantify this, this research aims to provide progress related to the following questions:

- What is the influence of cyclic reversed shear loading on failure modes?
- When does the structural response change from a brittle to a ductile failure mode?
- What is the ductility supply of walls having a shear dominated behaviour?
- Are there interactions between shear and axial force and between shear force and bending moment that influence the ductility supply?

Research into these questions will improve knowledge for the seismic evaluation of existing buildings.

1.4 Overview

The second chapter provides a review of literature that is related to this thesis. The observed earthquake performance of shear wall buildings is reviewed and a database of shear wall tests is presented. This chapter also introduces concepts and models that are employed within the subsequent chapters.

The third chapter presents a series of static-cyclic tests on small scale specimens representing shear walls that are prevalent in existing buildings. The test series, performed by the author, is briefly described and the obtained data are analyzed to determine failure modes, ductility supply, effective stiffness, and energy dissipation capacity. The chapter also compares the observed performance with experimental investigations of the literature.

The fourth chapter outlines the development of an analytical model predicting deformation capacity of lightly reinforced concrete shear walls. After the consideration of the assumptions used for this model, relationships between drift and base shear are formulated. The model then is used to derive criteria that bound the shear strength envelope of lightly reinforced shear walls.

The fifth chapter reports on validation of the analytical model. The potential of the analytical for the prediction of deformation capacity is shown through comparison with experimental data. This chapter also includes attempts on application of the proposed shear strength envelope on full-size shear walls.

Finally, the conclusions of this research are given in the sixth chapter.

1.5 Limitations

In this thesis, experimental and analytical research is presented that contributes to the seismic evaluation of existing shear wall buildings.

The experimental investigations include small scale specimens that model shear walls of such buildings. However, some characteristics that can arise in the evaluation of existing buildings were precluded. These are the following:

- Reinforcement detailing such as lap splicing near the base of the wall.
- Complicated cross-sections such as Barbell-shaped cross-sections.
- Restraints of rotation at top of walls due to interaction with other structural elements.

Chapter 2

State of the art

2.1 Earthquake performance of shear wall buildings

Many researchers, for example Fintel (1995), reported excellent earthquake performance of shear wall type building structures. Compared to frame-type structures, advantages of shear wall structures were the following:

- Less distortions - less damage on non-structural elements.
- Robustness - even conventionally reinforced walls or masonry infilled frames have the capacity to withstand severe earthquakes.

These claims were substantiated by observations from post-earthquake investigations in

- Chile 1960
  - Efficiency of controlling both structural and non-structural damage,
  - Cracking of walls did not affect the performance of the buildings,
  - Walls continued to function after occurrence of damage,
  - Amounts of steel less than code specifications.
- Skopje 1963
  - Plain concrete walls helped to reduce damage of frame systems (wall-frame interaction).
  - Unreinforced concrete cores behaved well.
  - Interaction of monolithic stairs with cores and frames (stairs = vertical truss).
- Caracas 1967
  - Better performance achieved by shear walls than frames,
  - Low strength brittle partitions in flexible frames caused costly damage,
  - Short columns and beam failed in shear independent of the amount of reinforcement.
- San Fernando 1971
  - Soft storey - invitation for trouble - because of restricted restoring force,

  - Shear wall structures showed superior performance because of limited interstorey drifts.

- Romania 1977
  - Minor damage of precast concrete panel buildings,
  - Period of those buildings was between 0.6 and 0.7s while periods near to 1.5s dominated the earthquake motion.

- Mexico City 1985
  - Non-ductile frame buildings failed in severe earthquakes,
  - Flate-plate structures without stiffened walls were revealed to be not suitable for seismic action.

- Chile 1985 - minor damage due to extensive use of non-ductile shear walls.

  Wyllie, Abrahamson, Bolt, Castro & Durkin (1986) reported following damage of rectangular shear walls:
  - Sliding in construction joints,
  - Spalling and degradation of concrete at the extremities near to the wall base,
  - Buckling of longitudinal rebars near to the boundaries.

  The typical failure of shear walls during the Chilean Earthquake of 1985 is shown in Fig. 2.1. Such walls stabilized four-storey-buildings (Wyllie et al. 1986). The walls were usually of 200 mm thickness and 5 to 6 m in length. The reinforcement consisted of boundary reinforcement (2 rebars of 16 mm diameter) as well as of distributed horizontal and vertical reinforcement. The latter was formed by rebars of 8 mm diameter at 250 mm spacing. Despite the local damage, the walls fulfilled their structural function. In addition, structural failure of some shear wall buildings due to torsional effects was reported.

Fig. 2.1: Failure of shear wall observed after Chilean Earthquake 1985 (Wyllie et al. 1986).

- Armenia 1988 - minor damage on precast panel buildings, while more than 28000 people lost their lives in buildings of other framing systems.

2.2 Failure modes

2.2.1 Low rise shear walls

Failure modes describe the physical reason for the rupture of a structural element. Because of the different material properties of reinforcing steel and concrete, a number of failure modes can occur depending on parameters such as type of cross-section, reinforcement detailing and quantities, properties of reinforcing steel, concrete compressive strength, and boundary conditions.

Paulay, Priestley & Singe (1982) have reported failure modes for squat shear walls that are likely to fail in shear. Accordingly, diagonal tension failure can occur when a diagonal corner to corner crack forms in case of insufficient amount of horizontal reinforcement (Fig. 2.2). Furthermore, monotonically loaded walls with large flexural capacities and adequate horizontal reinforcement may fail in diagonal compression. The concrete crushes in the compression zone near the base of the wall. For cyclic loading, two sets of diagonal cracks appear, and concrete crushing can extend over the entire length of the wall due to degradation that is provoked by the load reversals.

Another reported failure mode by Paulay et al. (1982) is sliding shear (Fig. 2.2). Originated by flexure, a continuous horizontal crack develops along the base of the wall. Due to degradation of aggregate interlock with increase in number of cycles, the crack slip increases, and hence the wall displacements include a significant portion due to sliding, especially at the load reversals. This phenomenon results in pinching of hysteretic loops that reduces energy dissipation.

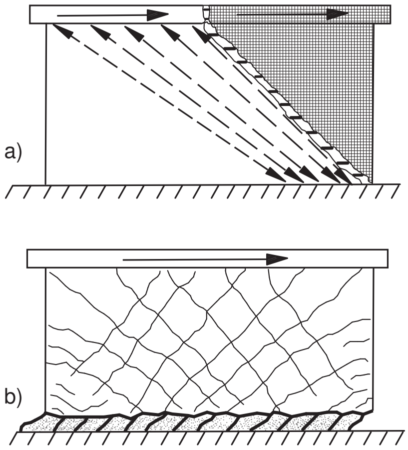

Fig. 2.2: Selected failure modes of low rise shear walls, a) diagonal tension, b) sliding shear according to (Paulay et al. 1982).

A literature review on recommendations for design against the aforementioned failure modes is presented in Sec. 2.6.5.

2.2.2 Columns

A classification of columns was proposed by Ghee, Priestley & Paulay (1989) who experimentally studied the static-cyclic response of 25 circular columns. The specimens had aspect ratios between 1.5 and 2.0. They were tested as cantilevers. Ghee et al. (1989) classified the specimens into four categories:

- Ductile flexural ($\mu_\Delta \geq 6$). The maximum observed base shear was greater than the base shear at nominal flexural strength. The specimens failed in flexure.

- Moderately ductile with shear failure ($4 < \mu_\Delta < 6$). The maximum observed base shear exceeded the base shear at nominal flexural strength but deformation capacity was restricted by shear failure.
- Limited ductile with shear failure ($2 < \mu_\Delta < 4$). The maximum observed base shear attained the base shear at nominal flexural strength and shear failure governed deformation capacity.
- Brittle shear failure ($\mu_\Delta < 2$). The column units failed at base shears below the base shear at nominal flexural strength.

Yoshikawa & Miyagi (2001) suggested classifying columns by the factor α_V which refers to ratio of achieved shear strength and the base shear at nominal flexural strength. This classification included three failure types:

1)	Shear failure:	$\alpha_V < 0.8$
2)	Shear failure after yielding of longitudinal reinforcement:	$0.8 < \alpha_V < 1.5$
3)	Flexural failure:	$1.5 < \alpha_V$

The review on failure modes and failure types showed that shear governed behavior can be identified by applying the following criteria:

- Physical phenomenon (failure mode)
- Ratio of shear strength to the base shear at flexural strength
- Displacement ductility

The static-cyclic behavior of lightly reinforced shear walls has rarely been studied under the aforementioned aspects. The present research intends to contribute to a rationale that allows the identification of wall units that are susceptible to shear failure.

2.3 Laboratory performance of shear walls

This section intends to establish a database of shear wall tests. Characteristics of existing buildings in Switzerland are described in order the examine the relevance of available test data to these buildings. The review of test data is subdivided into two parts:

- Slender walls - shear span ratios greater than or equal to 2.0.
- Squat walls - shear span ratios less than 2.0.

where the shear span ratio denotes the shear span divided by the wall length. It is however found that test data of configurations prevalent in existing buildings are missing.

2.3.1 Characteristics of existing buildings in Switzerland

Configurations of existing buildings in Switzerland are reported by Peter (2000). A typical existing building for which seismic evaluation would be required has between five and eight storeys. These buildings are usually stabilized by shear walls or by a mixed frame-wall system, and in-situ casted slabs of reinforced concrete.

The shear walls are of 4 to 9 m length and 0.18 to 0.25 m in thickness. Prevalent cross-sections are rectangular or composed of rectangular cross-sections. Distributed horizontal and vertical reinforcement with ratios of 0.2 to 0.8 % is characteristic for such walls. In general, the reinforcing steel provides hardening ratios greater than or equal to 1.15 and uniform strains greater than 6 %. Finally, the concrete compressive strength meets values between 20 and 50 MPa. An example for an existing building in Switzerland is shown in Fig. 2.3.

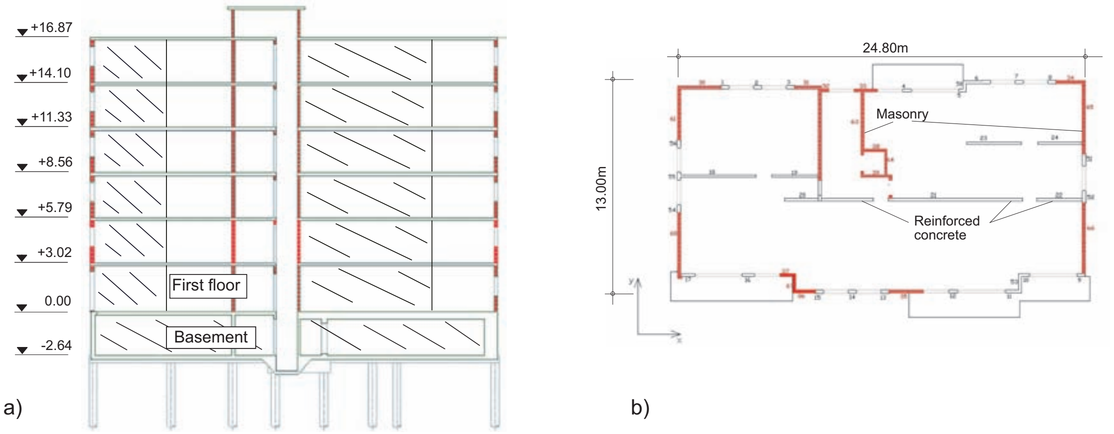

Fig. 2.3: Example for existing shear wall building, a) longitudinal section, b) floor plan.

2.3.2 Slender walls

Research carried out by Dazio, Wenk & Bachmann (1999), Lestuzzi, Wenk & Bachmann (1999) and Thiele, Wenk & Bachmann (2000) focused on the experimental confirmation of capacity design adapted to local conditions in Europe. Shear walls were the object of this research. Static-cyclic, dynamic and pseudo-dynamic tests were carried out on walls of shear span ratios between 2.3 and 3.0. Results showed clearly that ductile shear walls are very suitable for stabilizing buildings in regions exposed to moderate seismicity. Nevertheless, these studies contributed to the design of new structures. Their applicability to existing structures is restricted since special detailing of reinforcement is required for the achieved ductilities. Increase in ductility can only be attained when a flexure-dominated response is ensured by applying capacity design principles. It was shown that applying these principles effectively can prevent shear failure. Investigating shear dominated behavior was not the object of this research.

A very different point of view lead to the research program "CAMUS 2000" that was recently completed in France (Coin, Mazars & Bisch 2002). Contrary to capacity design, that obliges structures to dissipate energy in well defined plastic hinge regions, the French code PS 92 is based on the assumption of distributed dissipation of energy. This leads to a significant reduction of reinforcement.

Two specimens have been tested on shake-tables within CAMUS 2000, both stand as part of a 5-story building in 1:3 scale. Although the specimen had only boundary reinforcement and one horizontal tie at each story, stable hysteretic loops were observed. The specimen showed relatively stable rocking modes, and damage was concentrated at the boundaries of the walls. Analysis of the test data revealed that the lever arm of base shear can be less than two-third of height of the wall. The tests provided evidence for energy dissipation due to geometrically non-linear response. This kind of energy dissipation originated from uplifting of masses. Moreover, significant increase of axial force was observed. Sec. 2.7.2 (p. 47) presents an overview how to consider such behavior in design.

The review of tests of slender walls provide evidence for seismic response dominated by flexure. It is possible to prevent preliminary shear failure if the wall design includes hierarchical order of strength. In this case, the flexural strength determines the level of shear. Such behavior can also be achieved with relatively small ratios of both horizontal and transversal reinforcement.

2.3.3 Static-monotonic tests of squat walls

Maier and Thürlimann (Maier & Thürlimann 1985) studied the behavior of barbell shaped and rectangular shear walls subjected to monotonic and cyclic loading. The specimens were tested as cantilevers that have uniformly distributed vertical reinforcement and horizontal reinforcement ratios of 0 and 1.1 %. Of particular interest for this study are specimens S4 and S9 on which constant axial load and monotonically increasing lateral load were applied. Details of these specimens are shown in Tab. 2.2. Specimen S9 was a replica of specimen S4 but without horizontal reinforcement. It was observed that the horizontal reinforcement had only minor influence on the peak load whereas the failure mode changed and the ultimate drift decreased. Specimen S4 failed in diagonal compression. Diagonal tension failure was reported for specimen S9.

A study of walls with concentrated boundary reinforcement was conducted by Lefas, Kotsovos & Ambraseys (1990). One of the parameters of this study was the amount of horizontal reinforcement (0.37 %, 1.1 %). The vertical web reinforcement ratio was equal to 2.4 %, and the specimens had 3.1 % boundary reinforcement ratio (Tab. 2.2). The test set-up consisted of simple cantilevers with tip load. Although the amount of horizontal reinforcement was almost reduced by a factor of three, this reduction seemed to have minor consequences on failure mode, peak load, and achieved drift. The specimens failed in diagonal compression failure and it was concluded that the concrete compression zone contributes significantly to the overall shear strength of the wall.

2.3.4 Static-cyclic tests of squat walls

Cantilever walls

The static-cyclic behavior of squat walls of rectangular and flanged cross-sections was addressed by Paulay et al. (1982). In the context of this paper, the specimen Wall1 is of particular interest. Its horizontal reinforcement ratio (1.6 %) was double the vertical one (0.8 %). The specimen was designed without strong boundary reinforcement (Tab. 2.2) and it was only subjected to lateral static-cyclic load. Axial force was not applied on this specimen. The response of this specimen was dominated by sliding shear. Significant strength loss of strength occurred at displacement ductilities greater than $\mu_\Delta = 4$. This was due to degradation of aggregate interlock. In addition, stable diagonal cracking was observed and displacements due to sliding movement yielded up to 65 % of the total displacements.

Salonikos, Kappos, Tegos & Penelis (1999) carried out an experimental investigation of the validity of the design provisions of EC8 (EC8 2003) for walls of height to length ratios of 1.0 and 1.5. Parameters of this test series were the web reinforcement ratios, the amount of boundary reinforcement, and the presence of diagonal reinforcement. The specimens were tested as cantilevers. Displacement ductilities up to 5.3 were observed. Furthermore, sliding shear was evident for the specimens LSW1, LSW2, and LSW3 (Tab. 2.2) which had no diagonal reinforcement. Failure occurred due to local damage such as concrete spalling and rebar buckling at the edges of the walls. The reduction of vertical and horizontal reinforcement ratios from 0.57 % to 0.28 % and boundary reinforcement from 1.7 % to 1.3 % neither affected the failure mode nor the observed drift. However, it was concluded that the lack of diagonal reinforcement anchored in the wall foundation leads to pinched hysteretic loops and diminution of energy dissipation.

Both non-ductile behavior and possible degradation are primarily due to the shear span ratio and both are marginally influenced by reinforcement patterns (e.g. LSW2 which shows significant differences in stiffness in positive and negative loading direction).

Double curvature walls

Fouré (1993) reported static cyclic tests of walls with height to length ratios of 0.5 that had full rotational restraint at the top and that were subjected to axial force ratios of almost 0.03. The specimens failed in diagonal tension. Horizontal reinforcement did marginally affect strength and deformation capacity while vertical reinforcement was seen to be necessary for both flexure and shear. In addition, it was concluded that efficiency of horizontal reinforcement reduces as the aspect ratio of walls decreases.

To investigate the unexpected good behavior of Chilean buildings in past earthquakes, Hidalgo, Ledezma & Jordan (2002) studied specimens that were designed to fail in diagonal tension. Important properties of these specimens were strong vertical boundary reinforcements (6 to 11 cm^2), rotational and vertical restraining of the top section, and web reinforcement ratios between 0 and 0.38 %. Hidalgo, Jordan & Ledezma (1998) tested walls with nominal shear stress ratios of 0.54 to 1.8. A selection of these specimens is included in Tab. 2.2. Diagonal tension failure restricted the strength of the walls so that the observed strength was between 36 and 73 % of the base shear at nominal flexural strength. An example for both the observed static-cyclic response and the crack-pattern is shown in Fig. 2.4.

Other selected test results by Hidalgo et al. (1998) are shown in Fig. 2.5. The plot includes only data of specimens without horizontal reinforcement. The observed shear capacity was

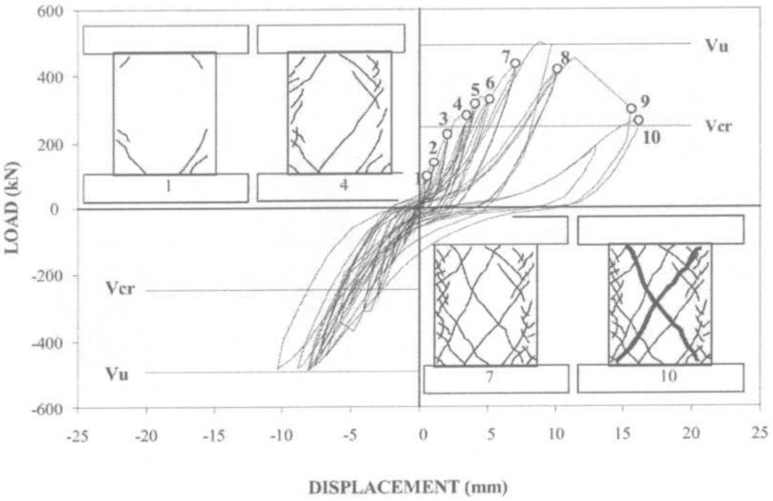

Fig. 2.4: Static-cyclic response and crack patterns of lightly reinforced shear wall with both vertical and rotation restraint at the top (Hidalgo et al. 1998).

normalized to the square root of compressive strength. For all specimens, it is observed that the inherent shear strength is greater than $0.3\sqrt{f_c}$. Moreover, inherent shear strength is observed for aspect ratios less than 0.5.

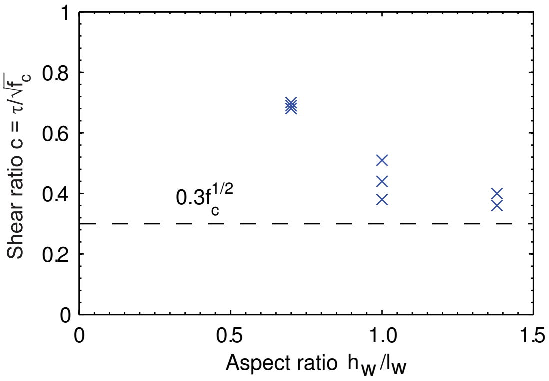

Fig. 2.5: Normalized shear strength of specimens without horizontal reinforcement (Experimental data by Hidalgo et al. (1998)).

2.3.5 Dynamic tests of squat walls

Rothe (1992) investigated experimentally the static-monotonic, static-cyclic, and dynamic behavior of cantilever walls with rectangular and flanged cross-sections. Of particular interest are the specimens T01, T04, T10, and T11 because of their different failure modes. The reinforcement arrangement of all these specimens was the same except for specimen T04, for which the horizontal reinforcement was omitted. The specimen T01 failed because of rupture of vertical rebars while diagonal tension caused failure of the specimen T04. Both specimens were tested on a shaking table. Sliding shear was observed in the static-cyclic test of T10. Specimen T11 was subjected to an axial force ratio of 0.07 and failed in diagonal compression. It was concluded that a sliding shear mode of failure would not occur in dynamic tests because dynamic sliding shear strength was considered to be significantly greater than that of the static case.

Pseudo-dynamic tests on low-rise, barbel shaped walls were reported by Ile (2000). These walls were of 3 m length, 1.2 m height, and 0.2 thickness of both web and flanges. The width of the flanges was equal to 0.8 m. The reinforcement provided yield strength, ultimate strength, and ultimate strain of 580 MPa, 660 MPa, and 23%, respectively. Characteristics of selected specimens are shown in Tab. 2.1. Note that the reinforcement ratios of flanges and web were equal to each other.

Specimen	ρ_h [%]	ρ_v [%]	$f_c\,[MPa]$	$f_t\,[MPa]$
T5	0.8	0.8	32.2	4.73
T6	0.6	0.4	36.9	4.77
T8	0.4	0.4	32.2	4.61

Tab. 2.1: Test series SAFE: characteristics of selected specimens.

The specimens failed due to concrete crushing of the web at drifts between 0.77% and 1.20%. Shear capacities equal to dimensionless shear stresses between $1.14\sqrt{f_c}$ and $1.64\sqrt{f_c}$ were achieved. It is interesting to note that significant decrease of stiffness was observed. The stiffness decreased by approximately 92% during testing.

2.3.6 Summary of database

Available experimental data of shear wall tests were reviewed for relevance to existing buildings. Tab. 2.2 includes tests of rectangular walls of shear span ratios less than or equal to 1.5. Both the shear and drift capacity are shown in Fig. 2.6. The specimens included in the database achieved shear stresses between $0.3\sqrt{f_c}$ and $0.9\sqrt{f_c}$, and maximum drifts of 2.3%. The shear capacity decreases as drift increases.

The review indicates that squat, lightly reinforced walls tend to fail either in diagonal tension or in sliding while for slender walls shear modes can be prevented by limiting the flexural strength. The failure mode depends on the restraint of the top of the wall. In addition, the loading can influence the failure mode. Although sliding shear was not reported in dynamic tests, it is observed under static-cyclic loading.

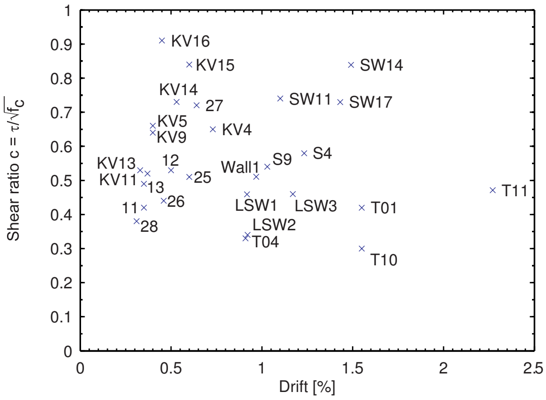

Fig. 2.6: Available experimental data for squat walls of rectangular cross-section.

Ref.	Specim.	Load	h_F [m]	l_w [m]	t [m]	h/l [-]	ρ_h [%]	ρ_v [%]	ρ_e [%]	f_c' [MPa]	f_y [MPa]	a [-]
(Maier & Thürlimann 1985)	S4	mon	1.20	1.18	0.10	1.02	1.03	1.05	1.05	32.90	574	1.12
	S9	mon	1.20	1.18	0.10	1.02	0.00	1.05	1.05	29.20	560	1.12
(Lefas et al. 1990)	SW11	mon	0.75	0.75	0.07	1.00	1.10	2.40	3.10	44.46	470/520	1.10
	SW14	mon	0.75	0.75	0.07	1.00	1.10	2.40	3.10	35.79	470/520	1.10
	SW17	mon	0.75	0.75	0.07	1.00	0.37	2.40	3.10	41.06	470/520	1.10
(Rothe 1992)	T01	dyn	1.10	0.80	0.08	1.38	0.47	0.71	1.42	24.31	420	1.50
	T04	dyn	1.10	0.80	0.08	1.38	0.00	0.71	1.42	28.80	420	1.50
	T05	dyn	1.10	0.80	0.08	1.38	0.47	0.71	2.52	24.20	420	1.50
	T10	st	1.10	0.80	0.08	1.38	0.47	0.71	1.42	33.57	500	1.50
	T11	st	1.10	0.80	0.08	1.38	0.47	0.71	1.42	26.86	500	1.50
(Paulay et al. 1982)	Wall1	st	1.50	3.00	0.10	0.50	1.60	0.81	0.85	27.20	300	0.57
(Salonikos et al. 1999)	LSW1	st	1.20	1.20	0.10	1.00	0.57	0.57	1.70	22.20	585/610	1.09
	LSW2	st	1.20	1.20	0.10	1.00	0.28	0.28	1.30	21.60	585/610	1.09
	LSW3	st	1.20	1.20	0.10	1.00	0.28	0.28	1.30	23.90	585/610	1.09
(Hidalgo et al. 2002)	11	st	1.40	1.40	0.10	1.00	0.13	0.26	(8.0 cm^2)	16.30	362	0.50
	12	st	1.40	1.40	0.10	1.00	0.26	0.13	(8.0 cm^2)	17.00	366	0.50
	13	st	1.40	1.40	0.10	1.00	0.26	0.26	(8.0 cm^2)	18.10	370	0.50
	25	st	1.40	1.40	0.10	1.00	0.00	0.00	(6.0 cm^2)	23.90	431	0.50
	26	st	1.40	1.40	0.10	1.00	0.00	0.00	(6.0 cm^2)	17.70	431	0.50
	27	st	1.40	1.40	0.10	1.00	0.25	0.00	(9.1 cm^2)	23.90	431	0.50
	28	st	1.40	1.40	0.10	1.00	0.00	0.25	(6.0 cm^2)	23.30	431	0.50
(Fouré 1993)	KV11	st	0.75	1.50	0.10	0.50	0.12	0.12	1.07	30.20		0.25
	KV4	st	0.75	1.50	0.10	0.50	0.20	0.20	1.13	32.50		0.25
	KV5	st	0.75	1.50	0.10	0.50	0.28	0.28	1.57	30.20		0.25
	KV13	st	0.75	1.50	0.10	0.50	0.12	0.12	1.07	15.60		0.25
	KV9	st	0.75	1.50	0.10	0.50	0.20	0.20	1.13	16.60		0.25
	KV14	st	0.75	1.50	0.10	0.50	0.28	0.28	1.57	16.10		0.25
	KV15	st	0.75	1.50	0.10	0.50	0.39	0.39	2.01	27.10		0.25
	KV16	st	0.75	1.50	0.10	0.50	0.68	0.68	3.14	28.20		0.25

Tab. 2.2: Tests of shear walls up to shear span ratios equal to 1.5. (Applied loadings: mon - static-monotonic, dyn - dynamic, st - static-cyclic.)

2.4 Behavior of reinforced concrete

In this section, research in both compressive and tensile behavior of concrete, in aggregate interlock action, and in bond is reviewed for possible application in modeling of lightly reinforced walls.

2.4.1 Compressive loading

Monotonic loading

The compressive strength of concrete is closely linked to the level of transversal straining. Increase in transversal straining results in decrease of compressive strength. This decrease is called compression softening and it was studied by Vecchio & Collins (1986) in the context of the modified compression field theory.

The transversal strains can originate from straining of transversal reinforcement. Muttoni, Schwartz & Thürlimann (1996) reported that the damage due to transversal straining is similar to the damage in the post-peak response of uniaxially loaded concrete. Thus, the transversal straining reduces the stiffness. The influence of transversal strains on response of concrete in compression is shown in Fig. 2.7 and the softened response is compared with the uniaxial response.

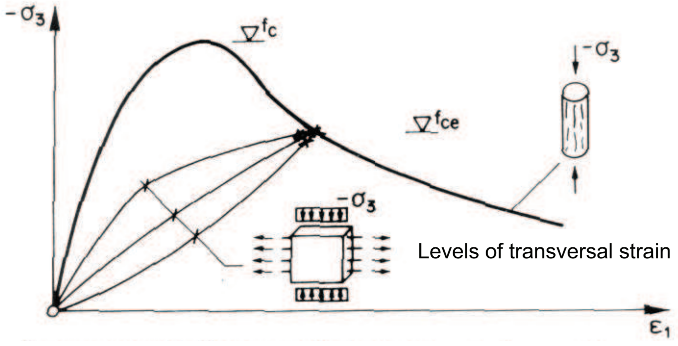

Fig. 2.7: Static-monotonic loading: Reduction of young's modulus due to transverse straining. (Muttoni et al. 1996).

Static-cyclic loading

The behavior of concrete under static-cyclic compressive loading was studied by Karsan & Jirsa (1969). It was found that the monotonic response forms an envelope of the static-cyclic response (Fig. 2.8a). Karsan & Jirsa (1969) proposed to model the envelope by a parabolic curve in the pre-peak and a linear curve in the post-peak branch.

Darwin & Pecknold (1977) suggested equivalent stress-strain relationships for plain concrete (Fig. 2.8b). These relationships were used in the finite element analysis of panels. In this context, equivalent relationship refers to the modeling of the biaxial response by a modified uniaxial relationship. It was supposed that the post-peak branch decreases linearly up to strains of four times the peak strain at uniaxial response. The corresponding stress was equal to $0.2\,f_c$.

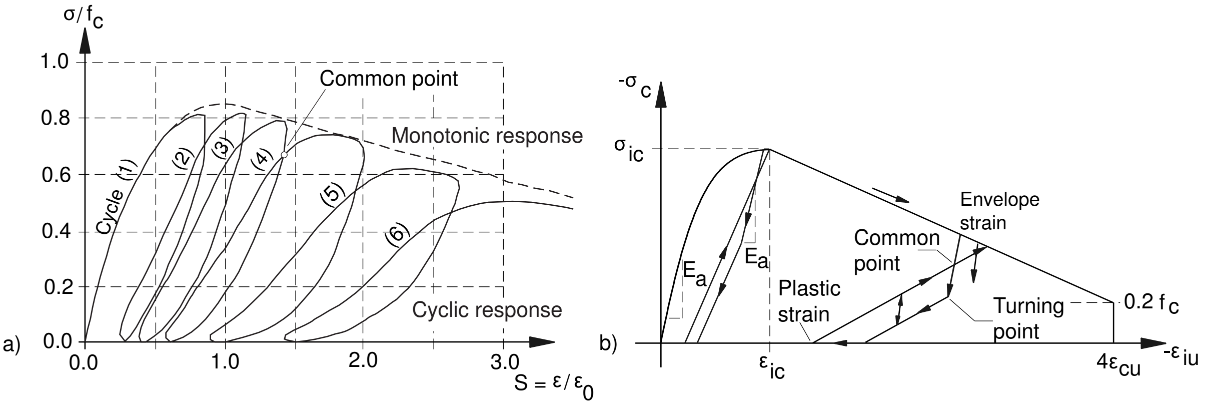

Fig. 2.8: Stress-strain relationships concrete, a) test data (Karsan & Jirsa 1969), b) model for equivalent stresses according to (Darwin & Pecknold 1977).

Review of other available stress-strain relationships for uniaxial and multiaxial loading as well as test results was published by Aoyama & Noguchi (1979). From this literature, it is concluded that strains of three and four times the peak strain correspond to the ultimate strains in case of cyclic and monotonic loading. It is also concluded that suitable ultimate stress is equal to $0.2\,f_c$.

Maekawa, Pimanmas & Okamura (2003) proposed a softening law for cyclic analysis of concrete in order to account for compression softening. The strength reduction in current cycle was modeled as a function of the achieved transversal strain in the previous cycle. The compression coefficient ζ decreases with increase in transversal strain (Fig. 2.9a). The application of this softening law is shown in Fig. 2.9b.

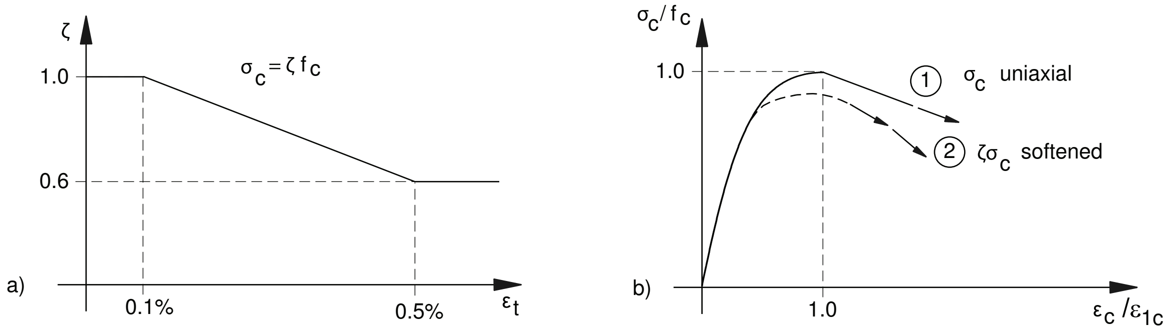

Fig. 2.9: Model for compression softening under cyclic loading according to (Maekawa et al. 2003), a) softening coefficient ζ as a function of past transversal strain ϵ_t, b) application of softening law.

2.4.2 Tensile Strength

The tensile strength of concrete influences crack pattern and deformation capacity. In current design specifications, the tensile strength is considered to calculate crack widths (EC2 2002) and upper bounds of tensile strength are used to ensure serviceability of concrete structures. However, the tensile strength is depends on loading history. As it was shown by Maekawa et al. (2003), the tensile strength in case of cyclic loading can decrease by 60% to 80% of the monotonic tensile strength.

2.4.3 Aggregate Interlock

Aggregate interlock refers to the shear transfer by asperities in cracks. The contact mechanism in rough cracks was studied by Walraven (1994). It is shown in Fig. 2.10. The shear transfer is enabled by both normal and tangential forces on the contact surfaces. The total area of contact surfaces available in the crack depends on both crack width and damage of the crack asperities. Walraven (1994) provided a method for the calculation of the total area of contact surfaces as a function of the crack width. This method is used in Sec. 4.5.5 to model the decay of shear capacity due to increase in deformation.

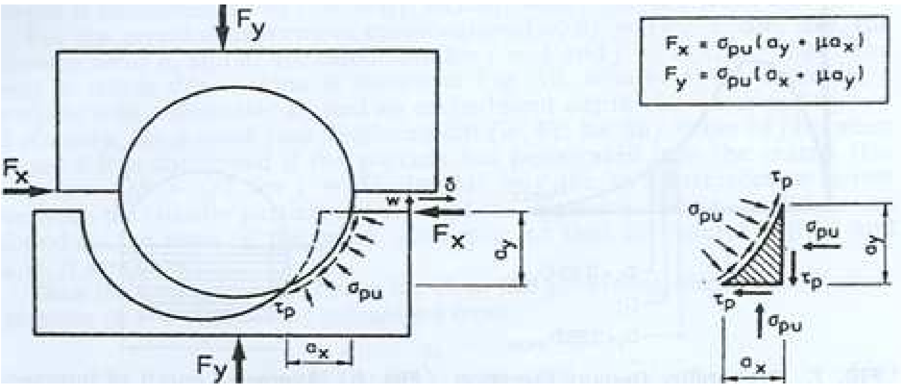

Fig. 2.10: Contact mechanism at shear displacement (Walraven 1994).

Skrikerud & Bachmann (1986) proposed discrete crack modeling for investigations on the dynamic behavior of unreinforced concrete structures. For rough cracks, a relationship for the decay of shear capacity as a function of the dimensionless crack width was proposed (Fig. 2.11). Note that the shear transfer in the crack was modeled by springs of which the stiffness was chosen according to Fig. 2.11.

Application on members without shear reinforcement

Reineck (1991a) studied the static-monotonic behavior of structural members without transversal reinforcement failing in preliminary shear failure. The following characteristics of members without transversal reinforcement were outlined:

- Limit of crack opening to transmit shear forces by aggregate interlock: 0.9 mm.
- Aggregate interlock effect decreases with increasing static height of beams.
- Triangular stress distribution in concrete compression zone.

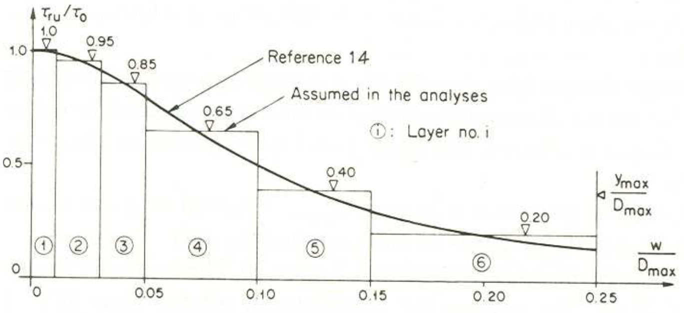

Fig. 2.11: Decay of shear capacity with increase in crack width (Skrikerud & Bachmann 1986) (Reference 14: Bazant & Gambarova (1980)).

- Principal contributor to shear capacity: tensioned part of cross section (>70%).
- Failure mechanism: widening of cracks and subsequent loss of load carrying capacity of crack lips.

To investigate the size effect in shear, Collins & Kutchma (1999) conducted an experimental study on lightly reinforced beams of shear span ratios of 3.0. It was found that the crack spacing governed the performance of such beams in shear. It was also found that increase in height of deep beams result in decrease of shear strength. This size effect in shear was believed to be related to an increase in crack width.

Muttoni (2003) proposed approaches for both shear in beams and punching of slabs. The deformation capacity of members failing in shear was related to a reference crack width. The following proposals were made for beams without transversal reinforcement:

- Definition of reference crack width.
- Critical region: 0.5d from support, 0.6d below compressed fiber, where d is statical height of the beam.
- Strain in the critical region: $\epsilon_{eff} = 0.41\epsilon_s$

where the symbol ϵ_s denotes the steel strain at the outermost tensioned fiber. The shear strength was supposed as a function of strain, aggregate size, and concrete shear strength (Eq. (2.1)).

$$\tau_R = \frac{V_r}{b \cdot d} = \frac{\tau_c}{0.9 + 2.3\epsilon_{eff}\, d\, k_{dg}} \tag{2.1}$$

where:

τ_c : Concrete shear strength, $\tau_c = 0.3\sqrt{f'c}$.
ϵ_{eff} : Mean axial strain in critical region.
k_{dg} : Coefficient aggregate size, $k_{dg} = \frac{48}{d_g+16}$.
d_g : Maximum aggregate size [mm].

Validation of Eq. (2.1) against available experimental data from beam tests showed asymptotic values of $0.2\tau_c/\tau_R$ for $\epsilon_{eff}\, d\, k_{dg} = 2.2$. It is of particular interest that the corresponding shear strength yields $0.06\sqrt{f'_c}$ which is closed to the residual concrete contribution to shear strength proposed by Kowalsky & Priestley (2000) (p. 39).

Nevertheless, validity of Eq. (2.1) limited to the pre-yield domain. Test series to extend this validity were conducted by Rodrigues, Burdet & Muttoni (2005).

2.4.4 Bond behavior

Bond coefficient (Bachmann 1991)

The local increase in rebar strain due to cracking can be simply accounted for by the bond coefficient reported by Bachmann (1967). The localization of rebar tensile strains in the cracks is taken into account by a bond coefficient which equals the follows

$$\kappa = \frac{\epsilon_{sm}}{\epsilon_{smax}} \tag{2.2}$$

where

$\epsilon_{sm} = \frac{1}{s}\int_0^s \epsilon_s(x)\,dx$: mean steel strain.
ϵ_{smax} : maximum steel strain in the crack.
ϵ_s : steel strain.

The following parameters affect κ:

- **Bond quality** including variation and magnitude of bond stress along the rebars.
- **Diameter of rebars**
- **Crack spacing**
- **Steel properties** such as hardening ratio
- **Magnitude of load** limit state

Reported values:

1) No bond action, heavily damaged bond : $\kappa = 1.0$
2) Thick rebars, small crack spacing : $\kappa = 0.8 .. 0.9$
3) Middle rebar diameter, middle crack spacing : $\kappa = 0.5 .. 0.7$
4) small rebar diameter, elevated bond action, greater crack spacing : $\kappa = 0.2 .. 0.4$

In general, case 4) corresponds to low reinforcement ratios.

Two limit states occur for $\sigma_{smax} \geq f_y$:

- Thick rebars, degraded bond → $\kappa = 0.9..1.0$
- Thin rebars, intact bond (yielding is limited to the crack) → $\kappa \leq 0.2$

Purpose:
The mean rebar strain ϵ_{sm} may result from a cross section analysis (curvature analysis). So, the local increase in strain may be evaluated by the help of κ.

Crack widths

Fehling (1990) studied energy dissipation in bond under cyclic loading. The following proposals for crack widths of single cracks were made:

Single cracks

$$max\ w_R = \frac{d_s \cdot \left(\sigma_s^{II}\right)^2}{4 \cdot \tau_0 \cdot E_s} \cdot \frac{1}{1 + n \cdot \rho} \tag{2.3}$$

Single cracks with bond degradation at crack surface:

$$max\ w_R = \frac{d_s \cdot \left(\sigma_s^{II}\right)^2}{4 \cdot \tau_0 \cdot E_s} \cdot \frac{1}{1 + n \cdot \rho} + \frac{\sigma_s^{II}}{E_s} \cdot 2 \cdot s_0 \tag{2.4}$$

where

s_0 : unbonded length near to the crack.
d_s : rebar diameter.
E_s : elastic modulus of steel.
τ_0 : Bond strength.
σ_s^{II} : Steel steel stress.

Formulas for the completed crack pattern are also given, but they are not reported herein.

Bond properties

Equilibrium in longitudinal direction of rebar is written as follows

$$\frac{s}{2}\tau_b \pi d = \sigma_s \frac{\pi}{4} d^2 \tag{2.5}$$

Assuming that between two cracks at onset of cracking the tensile force is entirely transfered to the concrete, Eq. (2.5) is rewritten in order to determine crack spacing:

$$s = \frac{\sigma_c}{\tau_b} d \frac{1 - \rho}{2\rho} \tag{2.6}$$

Popov (1984) studied the degradation of bond due to cyclic loading:

- Effect of cyclic loading: bond strength reduces to 60% of that of monotonic loading,
- Slip at peak (peak cyclic: 9MPa) increases in reloading,
- Plastification of rebar propagates into crack element with increasing strain.

König & Fehling (1988) proposed to consider the degradation of bond strength due to cyclic loading by reduction of the monotonic bond strength to 70% ($\tau_{cycl.} = 0.7\tau_{monot.}$).

Bond models

Marti, Alvarez, Kaufmann & Sigrist (1999) proposed the "tension chord model" that can be used to determine the bond properties of concrete and reinforcement under static-monotonic loading. This model was calibrated on pull out tests from the literature. The model includes a simplified relationship for the bond strength which depends on both the rebar strain and the tensile strength of concrete. Thus, maximum bond stress yields two times the tensile strength of concrete. The bond stress reduces to the tensile strength when rebars undergo hardening. With these proposals Eq. (2.6) modifies to

$$s = \frac{\sigma_c}{\tau_b} d \frac{1-\rho}{2\rho} \rightarrow (\sigma_c = f_{ct}, \tau_b = 2f_{ct}) \rightarrow s = d\frac{1-\rho}{4\rho} \tag{2.7}$$

The crack spacing thus is independent of concrete properties. Application of the bond model by Marti et al. (1999) is shown in Fig. 2.12.

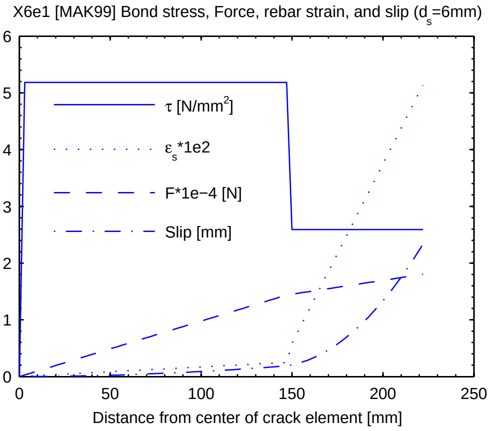

Fig. 2.12: Bond stress, rebar force, strain, and slip according to Marti et al. (1999) for rebar of 6 mm diameter.

Maekawa et al. (2003) reported a bond model for both cyclic and static-monotonic loading. The relationship of bond stress and slip is shown in Eq. (2.8).

$$\tau = 0.73 f_c \frac{(\log(1 + 5\, s\, 1000/d_s))^3}{1 + 10^5 \epsilon} \tag{2.8}$$

where τ, s, d_s, and ϵ refer to bond stress, slip, rebar diameter, and rebar strain. The model can be iteratively or explicitly resolved. The explicite solution refers to solution starting from the crack interface. This is shown in Fig. 2.13a. Maekawa et al. (2003) proposed for this explicit model to account for degradation of bond near to the crack interface. This is also shown in Fig. 2.13a. Degradation of bond at the crack interface results in increase in yield penetration.

Application of the implicit solution of the bond model by Maekawa et al. (2003) is shown in Fig. 2.13b. Comparison of the bond model in this figure and the bond model by Marti et al. (1999) leads to the following conclusions:

- Similar predictions of anchoring length.

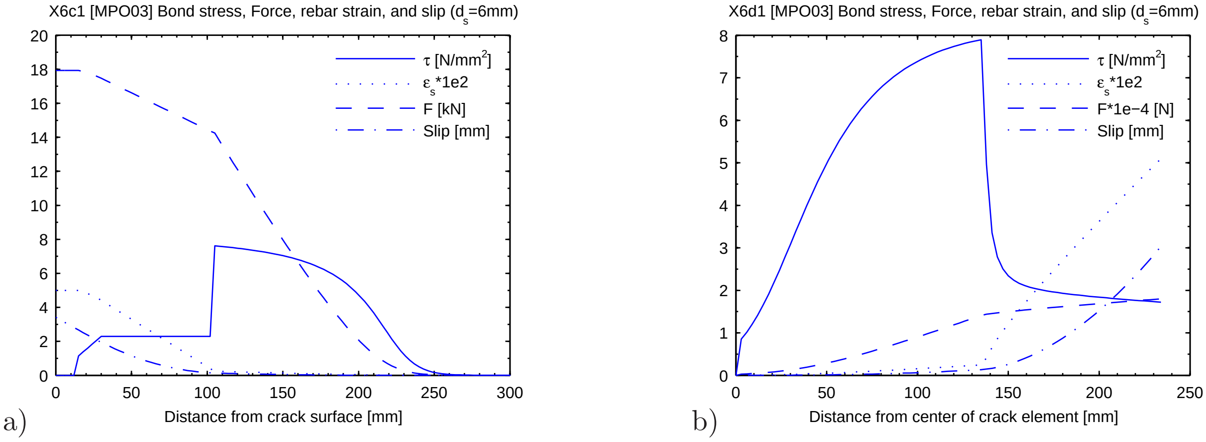

Fig. 2.13: Bond stress, rebar force, strain, and slip according to (Maekawa et al. 2003), results of explicit (a) and implicit solution (b).

- Higher bond stress in the yield range predicted by the model proposed by Marti et al. (1999).
- The model reported by Maekawa et al. (2003) predicts higher slip.

Hence, it is found that the bond model reported by Maekawa et al. (2003) is more suitable for the prediction of behavior of bond under cyclic loading than the tension chord model proposed by Marti et al. (1999).

2.4.5 Rebar buckling

Compressive behavior of rebars is governed by the length to diameter ratio (L/D). Therein, length L refers to the spacing of transversal restraints.
Based on monotonic compressive tests of rebars of 16, 20, and 24 mm diameter, Monti & Nuti (1992) reported stress-strain relationships for L/D ratios of 5, 8, and 11. Rebars of mild steel of $f_y = 440MPa$, $\epsilon_u \approx 10\epsilon_y$, and $f_u/f_y \approx 1.40$ were used for the test series.

- L/D$\leq$5: as tensile response
- $5 <$ L/D < 11: softening started at $\epsilon_{5\%}$ strain is reached. This strain corresponds to 5% decrease in stress.

  $$\epsilon_{5\%} = \gamma_s + \epsilon_y$$

  $$\gamma_s = \frac{11 - L/D}{e^{c(L/D)} - 1} \geq 0$$

- L/D $\geq$ 11: Buckling of rebars at yield strain ϵ_y
- Softening ratio at $\epsilon = 10\epsilon_y$ (not affected by hardening ratio of steel).

  $$b^- = 0.006\,[5 - (L/D)]$$

- softening branches tend to an asymptotic value of

  $$\sigma_\infty = 6\sigma_y/(L/D)$$

2.5 Plastic theory of reinforced concrete

This section intends to give a brief review of the plastic theory and it presents concepts that are used in Chapter 4 and Chapter 5.

2.5.1 Limits of application

Plastic theory for reinforced concrete focuses on the determination of lower and bounds for ultimate loads. It is an efficient method to determine such bounds. However, compatibility of deformations generally is omitted. Muttoni (1990) reported that the application of plastic theory of reinforced concrete

- is possible for structures with brittle elements if ductile mechanisms produce first and the brittleness of these elements is prevented,
- offers limited use for structural elements behaving in brittle shear, and
- requires surface reinforcement or self-stress-states that ensure distributed deformation.

2.5.2 Behavior of plastic hinges

Bachmann (1970) proposed a model for plastic hinges in the support zones of continuous beams (Fig. 2.14).

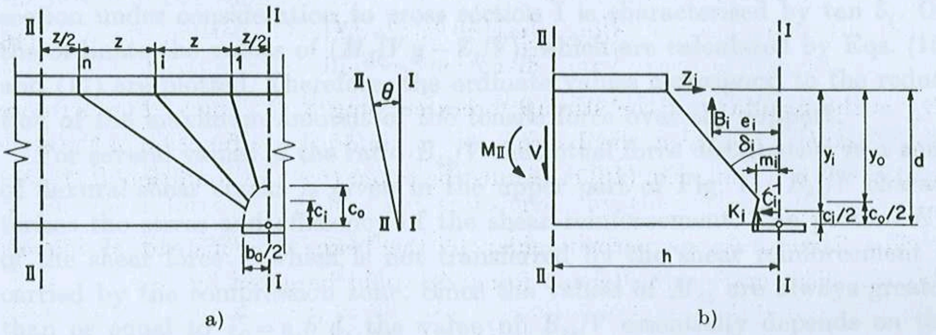

Fig. 10. Model and internal forces of a shear crack hinge.

Fig. 2.14: Shear crack hinge (Bachmann 1970).

The internal forces were reported as follows:
Shear force transmitted in a 45° inclined crack:

$$B_{45} = f_y \rho b_w (h - l_w) \tag{2.9}$$

horizontal component of strut longitudinal force:

$$D_h = \frac{\Delta B_{i,i+1}}{\cos \delta_{i,i+1}} \tag{2.10}$$

Reduction of tensile force due to transmitted shear:

$$\Delta Z_{i,i+1} = -\frac{B_{45}}{\eta} \cdot \frac{(\tan\delta_i - x/(2l_w))^2 - (\tan\delta_{i+1} - x/(2l_w))^2}{2\,(1 - x/2l_w)} \tag{2.11}$$

Decrease in shear force along plastic hinge:

$$\Delta B = B_{45} \left(\frac{\tan\delta_i - \tan\delta_{i+1}}{1 - x/2l_w} \right) \tag{2.12}$$

Sigrist (1995) studied deformation capacity of reinforced concrete beams. An example for the domain of feasibility of rotations is shown in Fig. 2.15.

- Ultimate strains from analysis of tests: $\epsilon_{cu} = 0.005$ (0.0035 is used in (Fig. 2.15))
- Proposal for ultimate plastic rotations:

$$\theta^{(p)}_{su} = \frac{l^{(p)}}{d(1-\omega)} (\epsilon_{smu} - \epsilon_{smy}) \tag{2.13}$$

$$\theta^{(p)}_{cu} = \frac{l^{(p)}}{d} \left(\frac{\epsilon_{cnu}}{\omega} - \frac{\epsilon_{smy}}{1-\omega} \right) \tag{2.14}$$

where:

ϵ_{cnu}	Ultimate concrete strain.
ϵ_{smy}	Average of rebar yield strain.
ϵ_{smu}	Average of rebar ultimate strain.
$l^{(p)}$	Length of plastic hinge.
d	Static height of cross-section.

- Length of plastic hinge: equal to d (based on strut inclination of 45°).
- The numerical evaluation of both Eq. (2.13) and Eq. (2.13) is shown in Fig. 2.15 for several ductility classes of steel. The failure mode depends on the hardening ratio of the rebar. For ductile reinforcement ($f_u/fy > 1.20$) concrete crushing is expected (Curve A) while rupture of tensile reinforcement restricts deformation capacity in case of both hardening ratios less than 1.05 and reinforcement ratios less or equal than 0.3.

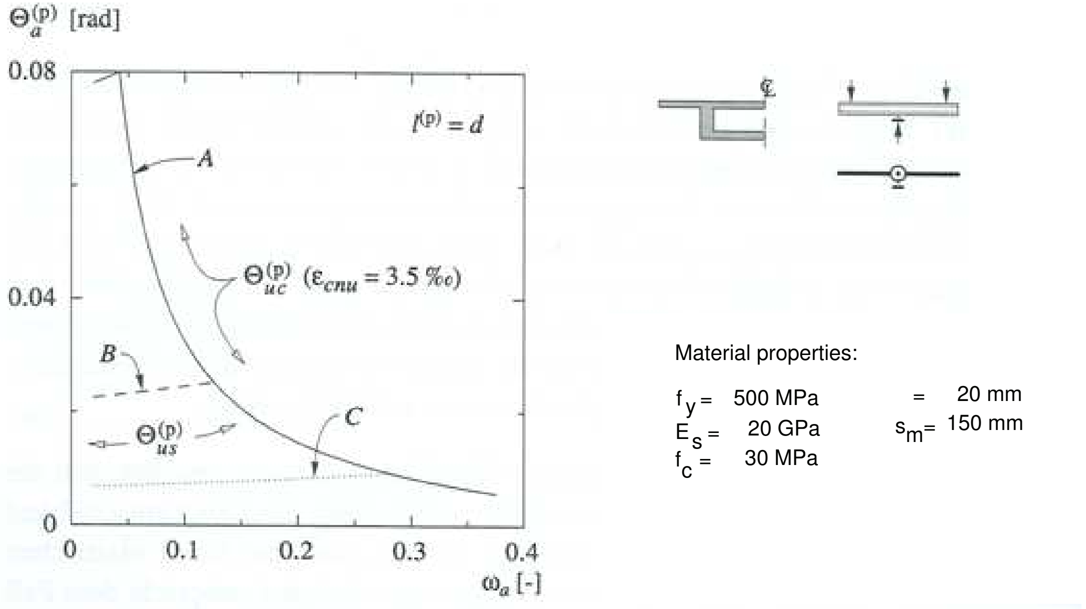

Fig. 2.15: Plastic rotation capacity of reinforced concrete beams according to Sigrist (1995), A-rebars of ductile behavior, C-cold formed steel.

Compression failure of beams

The rotation capacity of reinforced concrete beams behaving in flexure is restricted by concrete crushing and reinforcement rupture (Fig. 2.15). Cracking and discontinuities in the compressed part of beams are shown in Fig. 2.16.

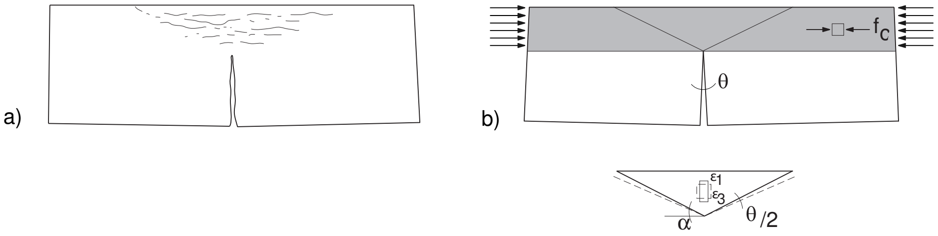

Fig. 2.16: Cracking (a) and discontinuites (b) in compression zone of beams according to Muttoni (1990) and Kanellopoulos (1986).

The principal strains ϵ_1 and ϵ_3 can be estimated as follows

$$\epsilon_3 = -\frac{\theta}{2}\tan(\alpha) \tag{2.15}$$

$$\epsilon_1 = \frac{\theta}{2}\cot(\alpha) \tag{2.16}$$

Muttoni (1990) proposed $\tan(\alpha) = 0.5$ for the longitudinal extension of discontinuity zone. This proposal was based on a flow rule for multiaxially loaded concrete.

Stress fields for beams failing in concrete crushing are shown in Fig. 2.17. Due to failure of the outermost fiber, the compressed part progressively shifts inside the beam in the post-peak branch of force-deflection relationship.

Compression failure of beams was also studied by Fantilli, Ferretti, Iori & Vallini (2002) who introduced sliding planes that are succesively removed to account for concrete failure. An angle of 17.5° is assumed for the extension of the crushing zone. Resulting extension of crushing zone: $2 \cdot x \cdot \cot(17.5°) \approx 6.4\,x$.

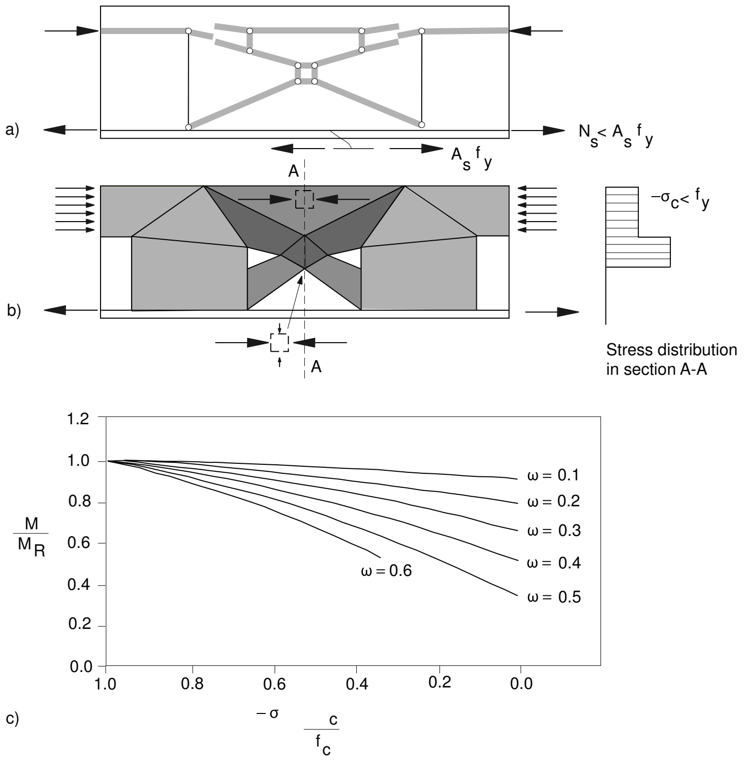

Fig. 2.17: Concrete crushing in beams. a) strut and tie model, b) stress field and stress distribution, c) softening in post-peak branch, according to Muttoni (1990).

2.5.3 Strut and Tie modeling

Strut and tie modeling of RC structures was motivated by

- Lower bound of plastic theory (Muttoni et al. 1996)
  - "Force distribution that fulfills equilibrium and material strength, kinematic compatibility not necessary."
  - Advantageous for calculation of ultimate loads
  - Additional checks are required for ensuring serviceability (e.g. crack widths) and deformation capacity (e.g. limitation of concrete strength, robustness reinforcement).

The shortcomings arising from lacking compatibility are partly removed when considering the suggestions made by Schlaich, Schaefer & Jennewein (1987) who proposed to develop strut and tie models based on the elastic force flow. However, ultimate load can be underestimated and the elastic force flow needs to be determined.

Strut and tie models are attracting because of economic solutions that provide generally smaller amounts of reinforcement than it is achieved with finite element models. Disadvantages include lacking compatibility and the limitation to ductile behavior.

2.5.4 Compression field models

To investigate the static-monotonic behavior of RC-panels, Kaufmann & Marti (1998) formulated the equilibrium at the crack. Steel stresses are derived by using the tension chord model (Marti et al. 1999). The constitutive relationships to compute steel stress included an amplification of steel stress due to strain concentration at the crack. A review of this model for possible application on lightly reinforced concrete shear walls has shown that this model predicts brittle behavior of lightly reinforced walls. Rebar rupture was predicted.

Other compression field models also have limited validity for lightly reinforced walls. The physical reason for this limited validity resides in the stress amplification at the crack that is included in such models in order to account for strain localization in the cracks. In addition, lower bound for the reinforcement ratio were given for some models (eg. Softened Membrane Model (Hsu & Zhu 2002), $\rho \geq 0.005$). Such difficulties restrict the field of application of compression field model to panels of which the reinforcement ratio is equal to or greater than 0.005.

2.6 Models for shear capacity

2.6.1 Fundamentals of shear design

For reinforced concrete structures, the nominal shear stress τ is usually defined as the ratio of shear to both width of cross section and internal lever arm:

$$\tau_{nom} = \frac{V}{b_w \cdot z} \tag{2.17}$$

Assuming the static height to be equal to 0.9 times the height of the gross section and assuming also that the internal lever arm equals 0.9 times the statical height, one can rewrite Eq. (2.17) to Eq. (2.18). The latter is usually used in the literature (e.g. (Paulay, Bachmann & Moser 1990), (Priestley, Verma & Xiao 1994)) :

$$\tau = \frac{V}{b_w \cdot 0.9^2 d} \approx \frac{V}{b_w \cdot 0.8d} \tag{2.18}$$

Shear reinforcement is activated with onset of diagonal cracking (Bachmann 1991). If diagonal cracks not produce the shear reinforcement thus can be omitted as it is the case for plates that are generally constructed without shear reinforcement. The concrete shear strength restricts the shear capacity for such elements. Concrete shear strengths are presented in Tab. 2.4. In addition, aggregate size and reinforcement diameter are also considered to derive shear capacity (Muttoni 2003).

While diagonal cracking controls the lower bound, the upper bound of shear capacity is attained when concrete crushing occurs. Concrete crushing is observed at compressive stresses less than the compressive strength of concrete, due to softening effects. The softening is considered by the following relationship (Bachmann 1991):

$$f_{c,red} = \xi \cdot \sin\beta \cdot f_{cw,min} \tag{2.19}$$

where

$f_{c,red}$: Effective compressive strength of concrete.
$f_{cw,min}$: Minimum cube compressive strength (2 % fractile value).
β : inclination of stirrups.
ξ : Coefficient ($\xi = 0.40..0.65$), depends on direction of principal stresses.

This relationships can be simplified for a truss model of 45° strut inclination and vertical stirrups to $f_{c,red} = 0.40 f_{cw,min}$.

2.6.2 Degradation of shear strength

Mechanisms of strength degradation

Biskinis, Roupakias & Fardis (2004) reported five mechanisms of shear strength degradation

1. Gradual reduction of aggregate interlock due to smoothing of interfaces because of cycling,
2. Degradation of dowel action, accumulation of inelastic strains,
3. Development of flexural cracks, reduction of contribution of compression zone due to cycling,
4. Reduction of aggregate interlock because of increasing crack widths due to bond slip,
5. Compression softening of concrete due to the accumulation of transverse tensile strains.

Limits of shear strength

Degradation in shear strength depends on the level of shear applied on the the structural element. Paulay & Bull (1979) reported classification of conventionally reinforced concrete beams in three broad groups:

- $\tau_u < 0.3\sqrt{f_c'}$: large number of cycles can be carried without deterioration in energy dissipation capacity
- $0.3\sqrt{f_c'} \leq \tau_u \leq 0.5\sqrt{f_c'}$: serious degradation of energy dissipation capacity must be expected
- $\tau_u > 0.5\sqrt{f_c'}$: premature failure of the plastic hinge due to sliding shear must be expected.

In this context, sliding shear means here complete destruction of concrete, thus horizontal forces only can resisted by dowel action and diagonal rebars.
Furthermore, a upper bound for members with horizontal reinforcement was proposed (Eq. (2.20). Diagonal reinforcement is required in case of greater shear stresses in order to avoid sliding shear.

$$\tau_u = 0.3(2 + r)\sqrt{f_c'} \text{ with } -1 < r < 0 \tag{2.20}$$

where r is the the ratio of maximum to minimum shear that develops in the section. In exceedance of τ_u (Eq. (2.20)), 75% of shear force should be resisted by diagonal reinforcement. The upper limit for members without diagonal reinforcement was proposed to yield $0.8\sqrt{f_c'}$ (Paulay & Bull 1979).

Conceptual model for shear strength degradation

The influence of the degradation of shear strength on the deformation capacity can be assessed by using both shear strength envelope and flexural response. Such assessment was reported by Priestley et al. (1994). It is shown in Fig. 2.18. Flexural response is assumed to be linear-elastic perfectly plastic. Failure is assumed at the intersection of the flexural response and the shear strength envelope.

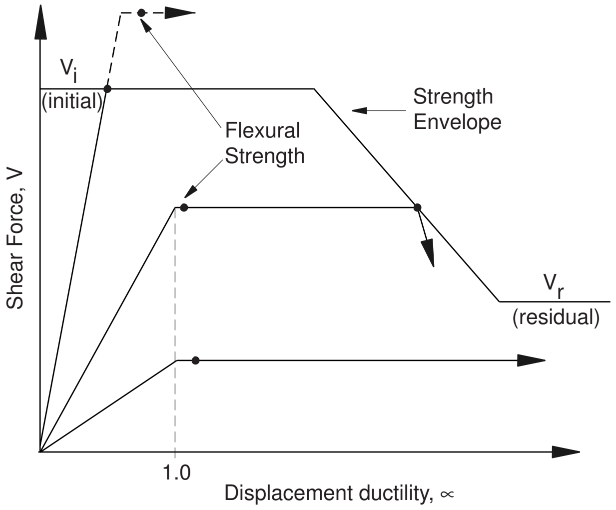

Fig. 2.18: Conceptual model for shear according to ATC-6 (Priestley et al. 1994).

2.6.3 General truss model

The truss model forms the fundamental approach of shear design of reinforced concrete. It was first published by Ritter (1899) who assumed 45° inclined struts and vertical stirrups.

The Swiss Standard SIA262 (2003) provides a more general approach that includes variable inclination of both struts and ties. The strut inclination α is arbitrary between 25° and 45°. So, the model is based on the ultimate limit state. It fairly predicts the behavior at serviceability since the arbitrary strut angle requires yielding of reinforcement that occurs only at large deformations (Bachmann 1991).

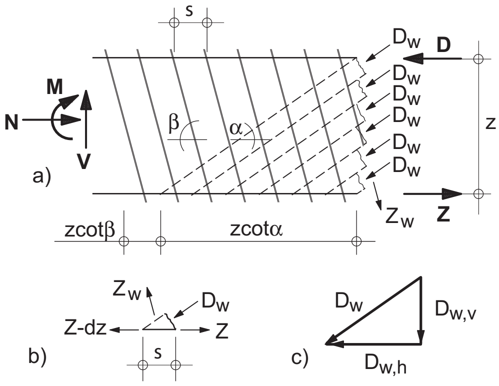

Fig. 2.19: General truss model. a) Global equilibrium, b) local equilibrium of lower chord, c) components of strut force.

The general truss model is shown in Fig. 2.19. Equilibrium in vertical direction can be written as follows:

$$V = \Sigma D_{w,v} + \Sigma Z_{w,v} \tag{2.21}$$

$$D_{w,v} = Z_{w,v} \tag{2.22}$$

where $\Sigma D_{w,v}$ and $\Sigma Z_{w,v}$ are the sums of vertical components of the strut forces and of the tie forces, respectively. The definition of both is given in the following equations:

$$\Sigma D_{w,v} = D_{w,v} \cdot \frac{z \cot \alpha}{s} \tag{2.23}$$

$$\Sigma Z_{w,v} = Z_{w,v} \cdot \frac{z \cot \beta}{s} \tag{2.24}$$

With the help of the relationship shown in Eq. (2.22), the vertical component of tie force $Z_{w,v}$ in Eq. (2.24) can be replaced by the respective strut force $D_{w,v}$ and Eq. (2.21) is rewritten to Eq. (2.25).

$$V = D_{w,v} \frac{z}{s} (\cot \alpha + \cot \beta) \tag{2.25}$$

The concrete stress in the strut $\sigma_{c,w}$ is supposed to be uniformly distributed over the strut width b_w. Equation (2.26) relates the concrete stress to the vertical component of the strut force.

$$\sigma_{c,w} = \frac{D_w}{b_w \cdot s \cdot sin\alpha} \text{ , } D_w = \frac{D_{w,v}}{sin\alpha} \rightarrow D_{w,v} = \sigma_{c,w} \cdot b_w \cdot s \cdot sin^2\alpha \tag{2.26}$$

Then, the shear force V and shear stress τ can be directly related to the concrete strut stress $\sigma_{c,w}$ by using Eq. (2.26) in Eq. (2.25):

$$V = \sigma_{c,w} \cdot b_w \cdot z \cdot (\cot \alpha + \cot \beta)\, sin^2\alpha \tag{2.27}$$

Equation (2.27) then simplifies to:

$$V = \sigma_{c,w} \cdot b_w \cdot z \cdot (\cot \beta \sin \alpha + \cos \alpha)\, sin\alpha \tag{2.28}$$

$$\tau = \sigma_{c,w} \cdot (\cot \beta \sin \alpha + \cos \alpha)\, sin\alpha \tag{2.29}$$

In addition, Equation (2.25) can also be written for the vertical component of the tie force:

$$V = Z_{w,v} \frac{z}{s} (\cot \alpha + \cot \beta) \tag{2.30}$$

Introducing the tie force

$$Z_{w,v} = Z_w \cdot \sin \beta \tag{2.31}$$

in Eq. (2.30), the shear force now relates directly to the force of the stirrups:

$$V = Z_w \frac{z}{s} (\cot \alpha \sin \beta + \cos \beta) \tag{2.32}$$

The maximum tie force depends on both the amount of transversal reinforcement and the yield stress of the reinforcement:

$$Z = A_s \cdot f_y \, , \; A_s = b_w \cdot s \rho_h \; \rightarrow \; Z = \rho_h \cdot f_y \cdot b_w \cdot s \tag{2.33}$$

Thus, one obtains both shear force and shear stress for members with uniformly distributed transversal reinforcement.

$$V = \rho_h \cdot f_y \cdot b_w \cdot z \cdot (\cot\alpha \sin\beta + \cos\beta) \tag{2.34}$$

$$\tau = \rho_h \cdot f_y \cdot (\cot\alpha \sin\beta + \cos\beta) \tag{2.35}$$

The variation of shear stress depending on the strut angle is shown in Fig. 2.20. The plots are based on Eq. (2.28) and (2.34). Cases of particular interest are shown in Tab. 2.3.

	α	β	τ_w	
			Reinf.	Concr.
(1)	45°	45°	$\sqrt{2}\,\rho_h\,f_y$	$\sigma_{c,w}$
(2)	45°	90°	$\rho_h\,f_y$	$0.50\,\sigma_{c,w}$
(3)	25°	90°	$2.14\,\rho_h\,f_y$	$0.38\,\sigma_{c,w}$

Tab. 2.3: General truss model - bounds of shear strength.

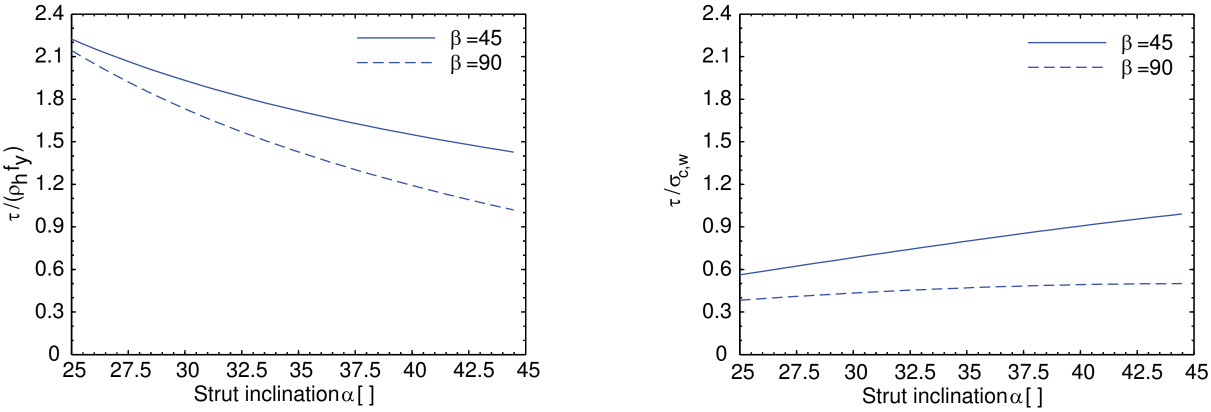

Fig. 2.20: Shear stress - strut angle relationships (Model SIA262).

For low reinforcement ratios, the shear capacity of stirrups is in most cases lower than the shear capacity of concrete struts, as it is shown in Fig. 2.21. This plot is based on the following assumptions:

- Reinforcement: $\rho_h = 0.3\%$, $f_y = 500\,MPa \rightarrow \rho_h\,f_y = 1.5$
- Concrete (Eq. (2.19)): $\sigma_{c,w} = 0.4\,f_c'$, $f_c' = 25\,MPa \rightarrow \sigma_{c,w} = 10\,MPa$

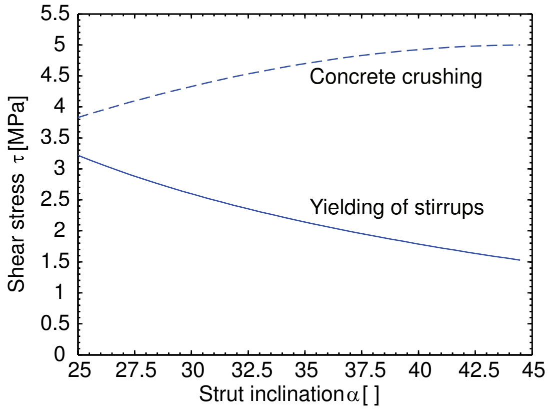

Fig. 2.21: Shear stress - low reinforced elements, ($\beta = 90°$).

2.6.4 Shear crack model

The shear crack model as it was included in SIA 162 (1968) considered contribution of concrete to the shear strength. Concrete contribution was also suggested by Leonhardt & Mönnig (1984) who investigated principal contributors to shear strength of T-girders (Fig. 2.22). It can be concluded from Fig. 2.22b that inclined concrete strut can provide utmost 60% of shear strength in case of rectangular cross-sections ($b/b_o = 1.0$).

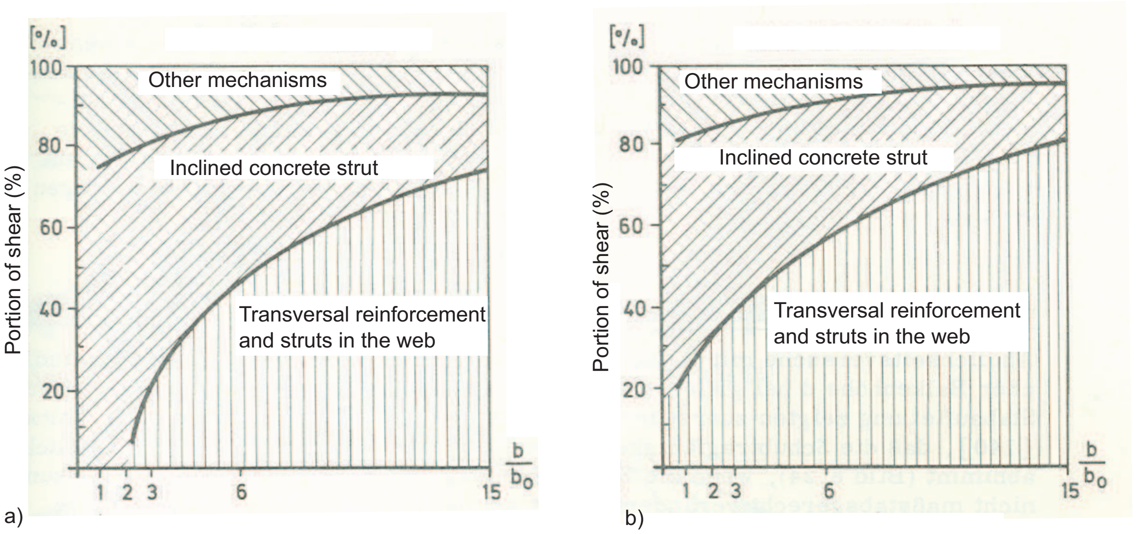

Fig. 2.22: Contributors to shear strength of T-girders, b - flange width, b_o-thickness of web, a) under service loads, b) at ultimate, according to (Leonhardt & Mönnig 1984).

Lefas & Kotsovos (1990) proposed shear design according to compressive force path for walls. They also identified the concrete compressive zone as principal contributor to shear strength. Other researches however suggested less contribution of concrete compression zone. According to Reineck (1991b) this part of cross-section transfers only 30% of shear.

The shear crack was reported in detail by Bachmann (1991). Fundamental idea was the division of shear strength into a **concrete** $V_{C,R}$ and **truss contribution** V_W. The concrete shear force $V_{C,R}$ was transmitted by the concrete compression zone while a truss formed by struts of 45°

inclination and ties developed the truss contribution. The range of tie inclination was limited to 45..90°.

Shear resistance of concrete compression zone

$$V_{C,R} = \tau_{c,R} \cdot b_w \cdot z \tag{2.36}$$

where:

$\tau_{c,R}$: Design concrete shear strength, equal to the lower bound of concrete shear strength τ_c (Tab. 2.4)

b_w : Width of concrete compression zone

z : Internal lever arm z (for beams: $z \simeq 0.9\,d \simeq 0.8h$)

Concrete	B25/15	B30/20	B35/25	B40/30	B45/35	B50/40
$f_c\,[N/mm^2]$	10	13	16	19.5	23	26
$\tau_c\,[N/mm^2]$	0.7	0.8	0.9	1.0	1.1	1.2

f_c : Design compression strength

τ_c : Lower bound of concrete shear strength

Tab. 2.4: Concrete shear strength and compressive strength according to SIA162 (1968).

Bachmann (1970) reported a relationship for the shear stress that was linked to the contribution of the concrete compression zone to the shear strength:

$$\tau_{c,R} = 0.4 + 0.025 f'_c \; [N/mm^2] \tag{2.37}$$

The evaluation of Eq. (2.37) is shown in Tab. 2.5.

f_c $[N/mm^2]$	$\tau_{c,R}$ $[N/mm^2]$	$\tau_{c,R}/\sqrt{f_c}$ $[-]$
25	1.03	0.21
35	1.28	0.22
50	1.65	0.23

Tab. 2.5: Concrete shear strength according to Bachmann (1970).

Shear strength of transversal reinforcement

$$V_{w,R} = A_{s,w} \cdot f_y \cdot \frac{z}{s} \cdot (\cot\beta + 1) \sin\beta \tag{2.38}$$

where:

$A_{s,w}$: Cross section of stirrups.
f_y : Yield strength of stirrups.
s : Spacing of stirrups.
z : Internal lever arm z (for beams: $z \simeq 0.9\, d \simeq 0.8h$).
β : Inclinaison of stirrups relative to the member axis.

2.6.5 Shear wall design

This section summarizes design specifications by Paulay et al. (1990) for both ductile shear walls and shear walls of restricted ductility. The review focuses on shear design. The design proposals include reduction factors in order to account for the following:

- Strength reduction due to possible variations of material strength
- Amplification of the earthquake action for both considering overstrength and the influence of higher modes

The strength reduction is shown in Eq. (2.39).

$$R = R_i \cdot \phi \tag{2.39}$$

where R is the shear strength or the flexural strength of the member and ϕ refers to a reduction coefficient:

- Shear $\phi = 0.85$
- Flexure $\phi = 0.90$

The nominal shear capacity is calculated by

$$V_i = \frac{V_u}{\phi} \tag{2.40}$$

The corresponding nominal shear stress can be determined by means of Eq. (2.18).

Ductile walls

Inclined compression A conservative value for ultimate shear stress is:

$$\tau_i = 0.9 \cdot \sqrt{f_c'} \quad [\frac{N}{mm^2}] \tag{2.41}$$

Another proposed formula allows to take overstrength and ductility demand into account:

$$\tau_i = (1.2 \cdot \frac{\phi_{o,w}}{\mu_\Delta} + 0.16)\sqrt{f_c'} \quad [\frac{N}{mm^2}] \tag{2.42}$$

When assuming restricted ductility ($\phi_{o,w} = 1.4$; $\mu_\Delta = 2.5$), this equation can be simplified as follows:

$$\tau_i = 0.83 \cdot \sqrt{f_c'} \quad [\frac{N}{mm^2}] \tag{2.43}$$

Inclined tension For this failure mode, the shear strength is supposed to consist of concrete and reinforcement contribution. The latter is based on a 45° truss model.

$$V_i = V_c + V_s \tag{2.44}$$

The concrete contribution is estimated as

$$\begin{aligned} V_c &= \tau_{c,i} \cdot 0.8 b_w l_w && (2.45)\\ \tau_{c,1} &= 0.27\sqrt{f_c'} + \frac{P_u}{4A_g} \text{ (outside of plastic hinges)} && (2.46)\\ \tau_{c,2} &= 0.6\sqrt{\frac{P_u}{A_g}} \text{ (plastic hinge region)} && (2.47)\\ A_g &= b_w \cdot l_w && (2.48) \end{aligned}$$

There is an upper bound for concrete contribution:

$$\tau_c = 0.2 \cdot f_c' \leq 6\ N/mm^2 \tag{2.49}$$

The steel contribution is calculated according to Eq. (2.50):

$$V_s = 0.8\, l_w \cdot f_y \cdot \frac{A_{sh}}{s} \tag{2.50}$$

Sliding shear The shear resistance mechanism in the sliding shear mode includes two contributors:

- Dowel action of vertical reinforcement V_{do}
- Contribution of concrete compression zone V_f

The parameters of friction mode are the following:

$$\begin{array}{lllllllllllll}
\text{Case 1: V=const.} & h_w \uparrow & \Rightarrow & M_R \uparrow & \Rightarrow & \rho_v \uparrow & \Rightarrow & x \uparrow & \Rightarrow & \frac{h_w}{l_w} \uparrow & \Rightarrow & V_f \uparrow \\
\text{Case 2: } h_w\text{,V=const.} & l_w \uparrow & \Rightarrow & x \downarrow & \Rightarrow & \frac{h_w}{l_w} \downarrow & \Rightarrow & V_f \downarrow
\end{array}$$

Hence, the aspect ratio $\frac{h_w}{l_w}$ has an impact on the sliding shear capacity. The friction mode theoretically becomes important for squat walls.
Mattock (1977) investigated the monotonic and cyclic shear behaviour of concrete joints. He concluded that the monotonic shear strength at concrete interfaces can be quantified as $0.35\, f'_c$. The degradation due to cyclic loading has been estimated as 20%. Therefore, the shear capacity of the concrete compression zone was conservatively suggested to $0.25\, f'_c$. The contribution of the compression zone to the sliding shear strength then was limited to V_f (Eq. (2.51)).

$$V_f = 0.25\, f'_c \cdot b_w \cdot x \tag{2.51}$$

Dowel action of vertical rebars is also accounted for. The yield force of the vertical rebars is reduced to 25 % for that. Finally, the shear strength in the friction failure mode equals:

$$V_i = 0.25\, b_w\, (\rho_v \cdot f_y \cdot l_w + f'_c \cdot x) \tag{2.52}$$

Walls of restricted ductility

Walls with restricted ductility are characterized by the following values for displacement ductility and overstrength:

$$\mu_\Delta = 2.0 \tag{2.53}$$
$$\phi_{o,w} = 1.4 \tag{2.54}$$

Elastic strength Shear walls will behave elastically if the shear stress is less than or equal to the limit provided by Eq. (2.55).

$$\tau_c = 0.27\sqrt{f'_c} + \frac{P_u}{4A_g} \tag{2.55}$$

Flexural behaviour Flexure dominates the response of walls if the shear load is less or equal to the shear load according to Eq. (2.56).

$$V_i = 0.48\sqrt{\frac{P_u}{A_g}} \cdot l_w \cdot b_w + 0.64 \cdot A_v \cdot f_y \cdot \frac{l_w}{s} \geq \phi_{o,w} V_E \tag{2.56}$$

In this case Paulay et al. (1990) recommend to reduce ductility according to Eq. (2.57) in order to account for sliding shear mode.

$$\mu_{\Delta,f} = 0.5\,(3 \cdot \frac{h_w}{l_w} + 1) \leq 5 \tag{2.57}$$

2.6.6 Seismic assessment of columns and walls

Priestley's model

Priestley et al. (1994) examined in detail both code provisions and available models in order to assess the seismic strength of reinforced concrete columns. As a consequence, the UCSD-model was formulated. It included the following relationship for shear strength was proposed:

$$V_n = V_c + V_p + V_s \tag{2.58}$$

where:

V_c : Concrete contribution, depending on ductility.
V_p : Axial load component.
V_s : Truss component.

Concrete contribution V_c

$$V_c = k\sqrt{f_c'}\,A_e \tag{2.59}$$

where:

k: Degradation factor, uniaxial ductility:
$\mu_\Delta \leq 2 \rightarrow k = 0.29$
$2 < \mu_\Delta < 4 \rightarrow k = 0.48 - 0.095\,\mu_\Delta$
$\mu_\Delta \geq 4 \rightarrow k = 0.1$
A_e: Effective shear area, $A_e = 0.8\,A_{gross}$

Axial load contribution V_p

$$V_p = P\tan\alpha = \frac{D - c}{2a}P \tag{2.60}$$

where:

D : Overall section depth or diameter.
P : Axial force.
a : Shear span.
c : Depth of compression zone.
α : Inclination of strut to the member axis.

The axial load contribution is independent of the achieved ductility. Important observations:

- If the aspect ratio decreases, the axial load contribution increases.
- If the axial load increases the axial load contribution can decrease because of steeper strut inclination.

Truss mechanism component V_s The truss mechanism component (Eq. (2.61)) accounts for the contribution of the horizontal transverse reinforcement by assuming a 30° angle between the compression diagonals and the vertical member axis or the corner-to-corner inclination whichever is larger.

$$V_s = \frac{A_\nu \, f_{yh} \, D'}{s} \cot 30^\circ \tag{2.61}$$

where:

A_ν : Total tranverse reinforcement area per layer.
D' : Core diameter, measured to centerline of transverse reinforcement.
f_{yh} : Yield strength of transverse reinforcement.
s : Spacing of transverse reinforcement along member axis.

In addition, Priestley et al. (1994) proposed a strength reduction factor that resulted from evaluation of the above relationships against experimental data. The USCD-model then provided a lower bound to the available data set. The strength reduction factor can be introduced directly in the model by the follows:

1. The upper and lower limits of k would be replaced by 0.25 and 0.085, respectively.
2. The axial load would contribute to shear capacity with $V_p = 0.85 \, P \tan \alpha$.
3. A 35° angle would be used for the truss mechanism.

Moehle's model

Sezen & Moehle (2004) reported a model for the seismic assessment of rectangular columns.

$$V_R = k \, (V_c + V_s) \tag{2.62}$$

The concrete contribution accounts for tensile stresses at diagonal cracking (Eq. (2.63)) and a contribution due to axial force.

$$V_c = 0.5\sqrt{f'_c}\left(1 + \frac{N}{0.5\sqrt{f'_c A_g}}\right)\left(A_g \frac{d}{L_s}\right) \tag{2.63}$$

$$V_s = \rho_w b_w z f_{yw} \cot\theta \tag{2.64}$$

$$k = 1.15 - 0.075\mu_\Delta, \; 0.7 \leq k \leq 1.0 \tag{2.65}$$

where:

d : Static height ("effective depth")
A : Concrete gross section
L_s : Shear span.
θ : Truss inclination ($\theta = 45^\circ$).

Revised UCSD - model

This proposal followed the concept shown in Fig. 2.18. The model which was published by Kowalsky & Priestley (2000) addressed the assessment of shear strength of circular columns. The UCSD-model was revised to account for the following:

- The effect of concrete compression zone on steel truss mechanism,
- The influence of aspect ratio on concrete shear resisting mechanism, and
- The impact of longitudinal steel ratio on the concrete shear resisting mechanism.

$$V_D = 0.85\,(\,V_c + V_p + V_s) \tag{2.66}$$

where:

V_c : Concrete contribution, depending on ductility.
V_p : Axial load component.
V_s : Truss component according to Eq. (2.60).

The factor 0.85 was introduced to correlate the model to experimental data in order to use it for design purpose.

Truss mechanism

The truss mechanism accounted only for transversal reinforcement that transfered shear across cracks. So, spiral reinforcement in the compressive zone was assumed to be not effective since there are no open cracks in this part of the cross-section. The inclination of crack plane was suggested to be equal to 30°. A simplified relationship for the truss component is shown in Eq. (2.67).

$$V_{sga} = \frac{\pi}{2} A_{sp} f_y \frac{D - c - cov}{s} \cot\theta \tag{2.67}$$

where:

A_{sp} : Spiral area.
D : Column depth.
c : Depth of compression zone.
cov : Concrete cover.
s : Spiral spacing.
θ : Inclination of crack plane.

Concrete mechanism

The following attempts were made:

- Shear strength increases as aspect ratio decreases - contribution of axial force to shear capacity.
- Smaller longitudinal ratios lead to decrease of shear strength because of:
  1. reduced dowel action
  2. more concentrated crack distribution, increased crack width, reduction of aggregate interlock
  3. smaller compression zone, smaller contribution of compression zone to shear strength

The effects of aspect ratio, longitudinal steel ratio, and ductility level are considered seperately by the factors α, β, and γ, respectively. The concrete contribution thus gives:

$$V_c = \alpha\beta\gamma\sqrt{f'_c}(0.8A_g) \tag{2.68}$$

where:

$$\begin{array}{lll}
\alpha & : & \frac{M}{VD} \leq 1.5 & \alpha = 1.5 \\
 & & 1.5 \leq \frac{M}{VD} \leq 2.0 & \alpha = 3 - \frac{M}{VD} \\
 & & \frac{M}{VD} \geq 2.0 & \alpha = 1.0 \\
\beta & : & \beta = 0.5 + 20\rho_l \leq 1.0 & \\
\gamma & : & \text{Curvature ductility (uniaxial)} & 0.05 \leq \gamma \leq 0.30,\ \gamma = 0.3625 - \frac{\mu_\chi}{48} \\
 & & \text{Displacement ductility (uniaxial)} & 0.05 \leq \gamma \leq 0.30,\ \gamma = 0.383 - \frac{\mu_\Delta}{24}
\end{array}$$

Kowalsky & Priestley (2000) suggested that in case of shear span ratios ($\frac{M}{VD}$) less than 1.5, the parameter α can be greater than 1.5. However, experimental evidence for this suggestion is lacking. The concrete contribution to shear strength is shown in Fig. 2.23 for shear span ratios equal to 1.5. Application of the concrete conctribution illustrated in Fig. 2.23 is shown in Sec. 5.4.5.

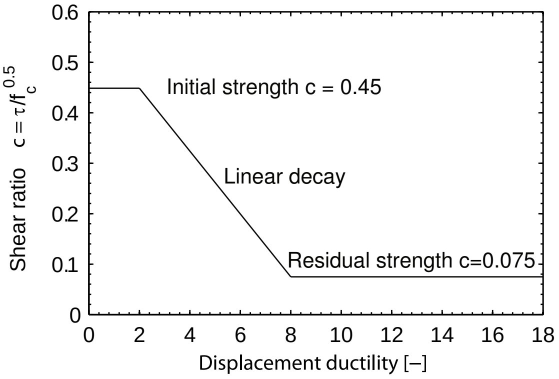

Fig. 2.23: Concrete contribution to shear strength according to Revised UCSD Model for shear span ratios equal to 1.5.

The model was used by Kowalsky & Priestley (2000) to predict shear strength of columns based on experimentally observed ductilities. The predictions were compared with experimental data and improvements due to the revision of the model were identified. Nevertheless, the shear capacity of columns failing in flexure was underestimated and the use of experimentally observed ductilities (yield displacements) was necessary to predict the achieved displacements. Recourse on computed flexural response was found to be not reliable.

Galal's model

Galal, Arafa & Ghobarah (2005) conducted experimental study on short RC columns to assess effectiveness of FRP jackets for retrofitting of columns that are vulnerable to brittle shear failure. The experimental data were compared with an analytical model that provides estimates for shear capacity depending on the ductility demand.

$$V_{\mu\leq 2} = V_c + V_p + V_s + V_f \tag{2.69}$$

$$V_{\mu=4} = 1/3(V_c + V_p) + V_s + V_f \tag{2.70}$$

$$V_{\mu\geq 6} = V_s + V_f \tag{2.71}$$

The contributions of concrete, axial force, transversal reinforcement, and of the FRP jacket to the shear capacity are calculated as follows:

$$V_c = 0.3\sqrt{f'_{cc}}A_e \tag{2.72}$$

$$V_p = k_p\frac{Pt}{2H} \tag{2.73}$$

$$V_s = \frac{A_v f_y v d}{d} \tag{2.74}$$

$$V_f = 0.95\,(2t_f)\,(\epsilon_{fe}E_f)\,d_f \tag{2.75}$$

where:

d	Distance compressed edge - tensile steel.
d_f	Depth of FRP in load direction.
f'_{cc}	Compressive strength of confined concrete.
f_{yv}	Yield strength of rebars.
k_p	Coefficient, = 1 for double curvature, = 0.5 for single curvature.
s	Spacing of rebars.
t	Height of the cross section.
t_f	Design thickness of FRP.
A_e	Area of effectively confined concrete core.
A_v	Cross sectional area.
P	Axial load on the column.
ϵ_{ef}	Design strain FRP.
E_f	Young's modulus FRP.

Thus, the model predicts that concrete and axial force contribution is reduced to zero when achieving ductilities greater than 6. Linear interpolation is required between the points of the cornerpoints of the model.

Mander's model

Mander, Kim & Dutta (2001) presented a model for shear strength degradation of columns that are subjected to single curvature and fixed-fixed ends. The proposed model considered the contributions of transversal steel, of normal force, and of concrete to shear capacity. The degradation of shear capacity was due to rupture of inclined concrete ties. It was estimated by removing successively the concrete ties in the region within which yielding of longitudinal reinforcement occurred. Thus, the concrete contribution decreased as yielding of longitudinal reinforcement spread in the column. The contributions of transversal steel and strut action due to normal force decayed not with increasing displacement.

Lopes' model

Lopes (2001b) studied the efficiency of horizontal reinforcement of shear walls. It was concluded that the concrete compression zone contributes significantely to the shear capacity. The concrete compressive force and the shear force are projected on an inclined crack plane which is subjected to shear stress τ_0. It was shown that this crack plane can not coincide with cracks that were formed in cycles prior to shear failure.

The shear capacity is independent of the inclination of the crack plane.

$$\begin{aligned} V_\theta &= \tau_0 \frac{\eta b_w l_w}{\cos\theta_0} && (2.76) \\ V_{cc} &= V_\theta \cos\theta_0 && (2.77) \\ V_{cc} &= \tau_0 \eta b_w l_w && (2.78) \end{aligned}$$

A Mohr-Coulomb failure envelope was proposed in order to determine the shear strength τ_0. Experimentally observed shear strength of walls (Lopes 2001a) correlated well with predictions that assume τ_0 equal to $0.2 f_c$. Lopes (2001b) then proposed the relationship shown in Eq. (2.79) for the contribution of concrete to shear capacity.

$$V_{cc} = 0.15 f_{cd} \eta b_w l_w \tag{2.79}$$

2.7 Code provisions for shear

2.7.1 Eurocode 2

EC2 (2002) provides a two level procedure for shear design by intergrading between

- Members without shear reinforcement $V_{Ed} < V_{Rd,c}$
- Members with shear reinforcement $V_{Ed} > V_{Rd,c}$

In general, the design for members with shear reinforcement does not account for concrete contribution. However, exceptions are made for direct struts (Eq. (2.87)).

Members without shear reinforcement

According to EC2 (2002), 6.2.2, the shear strength of of members without shear reinforcement is calculated as follows (Eq. (2.80)):

$$V_{Rd,c} = \left[C_{Rd,c}\, k\, (100\,\rho_l\, f_{ck})^{1/3} + 0.15\,\sigma_{cp}\right] b_w\, d \tag{2.80}$$

The minimum shear resistance $V_{Rd,c}$ is calculated as the follows:

$$V_{Rd,c} = (v_{min} + 0.15\,\sigma_{cp})\, b_w\, d \tag{2.81}$$

where:

f_{ck}	Characteristic cylinder strength [MPa].
k	$= 1 + \sqrt{\frac{200}{d}} \leq 2.0$.
ρ_l	$= \frac{A_{sl}}{b_w\, d} \leq 0.02$.
σ_{cp}	$= N_{Ed}/A_c \leq 0.2\, f_{cd}$.
γ_c	Partial factor for concrete for the ultimate limit state (EC2 (2002), 2.4.2.4, Table 2.1N): • Persistent and transient actions: $\gamma_c = 1.5$ • Accidental actions: $\gamma_c = 1.2$
b_w	Minimum width in the tensioned part of the cross-section.
d	Distance between compressed fiber and centroid of longitudinal reinforcement.
v_{min}	Depending on National Annex. Recommended value: $v_{min} = 0.035\, k^{3/2}\, f_{ck}^{1/2}$.
A_c	Concrete gross section [mm^2].
A_{sl}	Section of longitudinal reinforcement acting as tie for the 45° inclined concrete strut. It has to be fully anchored.
$C_{Rd,c}$	Depending on National Annex. Recommended value: $C_{Rd,c} = 0.18\, /\, \gamma_c$.
N_{Ed}	Axial force due to prestressing or loading. The influence of applied deformations on the axial force is neglected.
$V_{Rd,c}$	Design shear resistance of the member without shear reinforcement.

According to EC2 (2002), 6.2.2 (2), Eq. (2.80) applies to the shear resistance to regions that are cracked due to bending. If the tensile stress due to bending is less than the tensile strength of concrete, the section remains uncracked. The shear resistance then is calculated as the follows:

$$V_{Rd,c} = \frac{I \cdot b_w}{S} \sqrt{(f_{ctd})^2 + \alpha_l \, \sigma_{cp} \, f_{ctd}} \tag{2.82}$$

where:

b_w	Width of the cross at the centroidal axis.
α_l	$= l_x / l_{pt2} \leq 1.0$ (pretensioned tendons). $= 1.0$ (other types of prestressing).
f_{cdt}	Design tensile strength of concrete. $= f_{ctk,0.05} / \gamma_c$
$f_{ctk,0.05}$	Tensile strength of concrete - 5%-fractile. $= 0.7 \, f_{ctm}$
f_{ctm}	Tensile strength of concrete - mean. $= 0.30 \, f_{ck}^{2/3} \leq$ C50/60, sufficient for existing buildings (prEN 1992-1-1:2002, Tab. 3.1), this value is reduced to 2/3 for concrete ages greater than 28 days.
l_x	Distance between section to verify and begin of transmission length.
l_{pt2}	Upper bound of transmission length according to prEN 1992-1-1:2002, Eq. (8.17).
σ_{cp}	Compressive stress due to axial loading or prestressing ($\sigma_{cp} = N_{Ed}/A_c$ [MPa], $N_{Ed} < 0$ compression).
I	Second moment of inertia.
S	First moment of area about and above the centroidal axis.

Direct concrete struts are considered if the distance between the section to verify and the support fullfills the following: $0.5d \leq x \leq 2d$. In this case Eq.(2.80) is written as:

$$V_{Rd,c} = \left[C_{Rd,c} \, k \, (100 \, \rho_l \, f_{ck})^{1/3} \left(\frac{2d}{x} \right) + 0.15 \, \sigma_{cp} \right] b_w \, d \leq 0.5 \, b_w \, d \, \nu \, f_{cd} \tag{2.83}$$

where

$$\nu = 0.6 \left[1 - \frac{f_{ck}}{250} \right] \; [MPa]. \tag{2.84}$$

Members with shear reinforcement

The shear strength includes the contributions of shear reinforcement and of inclined chords (Eq. (2.85)).

$$V_{Rd} = V_{Rd,s} + V_{ccd} + V_{td} \tag{2.85}$$

where:

$V_{Rd,s}$	Shear strength due to shear reinforcement.
V_{ccd}	Shear component of inclined compression chord force.
V_{td}	Shear component of inclined tension chord force.

A concrete concribution to the shear strength is not accounted for.

$$\underbrace{\begin{aligned} V_{Rd,s} &= \tfrac{A_{sw}}{s}\, z\, f_{ywd}\, (\cot\theta + \cot\alpha)\, \sin\alpha \\ V_{Rd,max} &= \alpha_c\, b_w\, z\, \nu\, f_{cd}\, \tfrac{\cot\theta + \cot\alpha}{1+\cot^2\theta} \end{aligned}}_{V_{Rd}=min\left(V_{Rd,s}\,, V_{Rd,max}\right)} \tag{2.86}$$

where:

α	Angle between shear reinforcement and member axis.
θ	Inclination of struts relativ to member axis. Recommended range: $1 \leq \cot\theta \leq 2.5$.
b_w	Minimum width of web.
f_{ywd}	Yield strength of shear reinforcement.
ν	According to Eq. (2.84).
s	Stirrup spacing.
z	Internal lever arm, equal to 0.9d.
A_{sw}	Section of shear reinforcement.

In case of direct concrete struts ($0.5d < x < 2.0$), a concrete contribution is included in the design shear strength:

$$V_{Rd} = V_{Rd,ct} + A_{sw}\, f_{ywd}\, \sin\alpha \tag{2.87}$$

where:

$V_{Rd,ct}$	Eq. (2.83)
$A_{sw}\, f_{ywd}$	Yield force of reinforcement within the central 0.75x

The shear strength must not exceed the maximum shear strength $V_{Rd,max}$ (Eq. (2.86)).

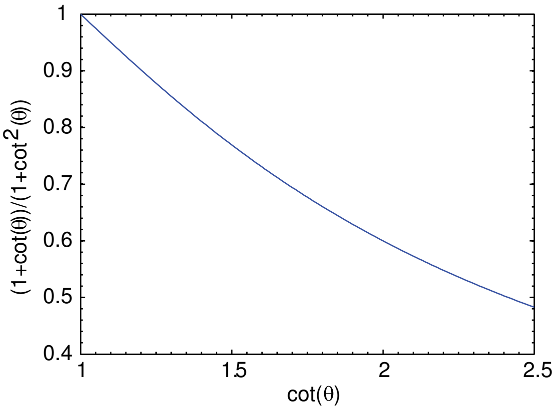

Fig. 2.24: Variation of maximum shear strength $V_{Rd,max}$ (Eq. (2.86)).

2.7.2 Eurocode 8

This section presents some provisions of EC8 (2003) related to shear walls.

Behavior factors

The behavior factors are calculated as follows:

$$q = q_0 \, k_w \geq 1.5 \tag{2.88}$$

where:

q_0 : Basic value, depending on ductility class, struct. system, and regularity in elevation.
k_w : Coefficient for failure mode of structural system $(0.5 \leq k \leq (1 + \alpha_0)/3 \leq 1)$.
α_0 : Aspect ratio of structural system. Similar wall dimensions: $\alpha_0 = \sum h_{wi} / \sum l_{wi}$.
h_{wi} : Wall height.
l_{wi} : Wall length.

For example, behavior factors near to 2.0 are attributed to structural wall systems including walls of aspect ratio 1.0. In addition, EC8 (2003) distinguishes three ductility classes:

- **L** Low ductility
  - application restricted to regions with low seismicity
  - design according to EC2 (2002)
  - $\mathbf{q = 1.5}$
- **DCM** Moderate ductility
  - Uncoupled walls: $q_0 = 3.0$
  - Core systems (elevator shafts etc.): $q_0 = 2.0$
- **DCH** High ductility

In case of irregularities in elevation, the basic value of behavior factor is reduced by 20 %. The ductility class DCM is assigned to low reinforced walls of great dimensions (“French walls”).

Low reinforced shear walls of great dimensions

Walls of moderate ductility require of concrete quality C16/20. The dimensions of ductile walls and low reinforced concrete walls have to satisfy the following condition:

- $b_{wo} = max\{0.15,\, h_s/20\}$

where h_s and b_{wo} are the storey height and the thickness of the wall, respectively.

Actions on design level

For low reinforced concrete shear walls of great dimensions, the following specifications for actions on design level are made:

1. The shear force V'_{ED} resulting from previous analysis has to be increased.
2. The increased shear force is calculated as shown in Eq. (2.89).

$$V_{ED} = V'_{ED}\,\frac{q+1}{2} \tag{2.89}$$

3. Axial forces due to rocking motion of long shear walls have to be taken into account for verifications at the ultimate limit state.
4. The increase or decrease in axial force due to rocking motion of long walls can be approximated to 50 % of the axial force if more precise calculations are omitted. For design purpose, the maximum or minimum value of the total axial force has to be considered, depending on which is the most unfavorable.
5. If the behavior factor q is less than or equal to 2.0, the variation of axial force due to rocking motion can be omitted.

Flexural strength

1. Verification of combined action of flexure and axial forces - horizontal cracks, plane sections.
2. Limit the normal stress in the concrete in order to prevent instabilities.
3. The precedent point can be verified by using EN 1992-1-1:2004 for second order effects, limitations of concrete compressive stress may additionally be required.
4. If the dynamic normal force is taken into account for verifications at ultimate limit state, the concrete ultimate strain can be increased up to $\epsilon_{cu2,c} = 0.005$. Further increase in strain is possible when considering only the core concrete in case of presence of confinement according to EN 1992-1-1:2004, 3.1.9.

Shear strength

1. Because of both increasing of design shear (Eq. (2.89)) and deformation dependent response of the structure, the minimum web shear reinforcement $\rho_{w,min}$ can be omitted if $V_{Ed} \leq V_{Rd,c}$ (p. 43). The concrete contribution to the shear strength $V_{Rd,c}$ is calculated according to EN 1992-1-1:2004, 6.2.2 by using Eq. (2.80).
2. If the condition $V_{Ed} \leq V_{Rd,c}$ is not satisfied, shear reinforcement has to be designed by using strut and tie models with or without variable strut inclination, whether is the most appropriated.
3. When using truss models, the strut width has to be smaller or equal to the minimum of both $0.25\, l_w$ and $4\, b_{wo}$.
4. Sliding in horizontal construction joints is prevented by dowel effect of vertical reinforcement of which the nominal anchorage length according to EN 1992-1-1:2004 needs to be increased by 50 %.

Detailing to ensure local ductility

1. Confinement is required for both vertical rebars that are needed to satisfy structural safety at ultimate limit state and vertical rebars resulting from minimum reinforcement exigencies.
    - Diameter: $d \geq 6mm$, $d \geq d_{bl}/3$, (d_{bl} - diameter of vertical rebars)
    - Spacing: $s = min\,\{100\, mm, 8\, d_{bl}\}$
2. The vertical rebars which are required to verify structural safety at ultimate limit state have to be concentrated in boundary elements at the edges of the cross-section.
    - Width of boundary element[1] $\geq$ min $\{b_w,\ 3\, b_w\, \sigma_{cm}/f_{cd}\}$
    - Diameter of rebars:
        - 12 mm in the first storey and in all storeys in which the wall length l_w decreases by more than $1/3\, h_s$.
        - 10 mm in all other storeys.
3. The real amount of vertical reinforcement in the wall has to be closed to what was required to verify the ultimate limit state, in order to prevent shear controlled behavior.
4. Continous vertical and horizontal ties have to be placed at
    - wall connections or connections between walls and stiffeners
    - the wall - slab connections
    - wall openings

    EN 1992-1-1:2004, 9.10, refers to the amount of reinforcement of such ties.

---

[1] σ_{cm}: average concrete compressive strength at ultimate limit state.

Squat walls of high ductility (class DCH)

1. If the aspect ratio of the wall is less or equal to 2.0 ($h_w/l_w \leq 2.0$), the flexural moment must not be modified. In addition, the increase of shear due to dynamic effects can be omitted.
2. The shear force resulting from previous analysis in augmented by using the follwing relationship:

$$V_{Ed} = \gamma_{Rd} \frac{M_{Rd}}{M_{Ed}} V'_{Ed} \leq q \cdot V'_{Ed} \tag{2.90}$$

3. The axial force ratio ν_d should be less or equal to 0.35.

Diagonal compression failure of squat walls

The shear strength $V_{Rd,max}$ is determined according to EC2 (2002) by assuming the following:

- Internal lever arm $z = 0.8 l_w$
- Strut inclination $\theta = 45°$, $\tan\theta = 1.0$

The shear strength $V_{Rd,max}$ according to EC2 (2002) is reduced to 40% in critical zones (plastic hinges).

For shear span ratios equal to or less than 2.0 a concrete contribution to the shear capacity is accounted for. (Eq. (2.91)).

$$V_{Ed} \leq V_{Rd,c} + 0.75 \rho_h f_{yd,h} b_{wo} \alpha_s l_w \tag{2.91}$$

where:

$V_{Rd,c}$: Shear strength according to Eq. (2.80).
ρ_h : Reinforcement ratio in horizontal direction.
$f_{yd,h}$: Yield strength of horizontal reinforcement.
α_s : Shear span.

Vertical web reinforcement should be also placed, according to Eq. (2.92):

$$\rho_h f_{yd,h} b_{wo} z \leq \rho_v f_{yd,v} b_{wo} z + minN_{Ed} \tag{2.92}$$

where:

ρ_v : Reinforcement ratio in vertical direction.
$f_{yd,v}$: Yield strength of vertical reinforcement.

2.8 Seismic evaluation of buildings

This section, provides an overview on current developments of the seismic evaluation of buildings. The evaluation of existing reinforced concrete buildings was the object of the research conducted by Peter (2000). The seismic vulnerability of existing was studied by Lang (2002), and Pellissier (2004) proposed an approach for the seismic evaluation based on risk management.

2.8.1 Stiffness of walls

Realistic elastic stiffness of walls is crucial according to Bachmann (2004) when evaluating or designing a building. The reduction of stiffness due to cracking can be estimated by the the following relationship which is based on the formula $\chi_y = M_n/(\alpha\, E_c\, I_g)$ for the yield curvature.

$$
\begin{aligned}
M_n &= \rho_v \cdot b_w \cdot \xi \cdot l_w \cdot \eta \cdot l_w \cdot f_y + n \cdot b_w \cdot l_w \cdot \eta' \cdot l_w \cdot f_c' && (2.93)\\
I_g &= \frac{b_w \cdot l_w^3}{12} && (2.94)\\
\alpha_K &= \frac{12}{\kappa_1} \cdot \frac{E_s}{E_c} \cdot \left[\rho_v \cdot \xi \cdot \eta + n \cdot \eta' \cdot (f_c'/f_y)\right] && (2.95)
\end{aligned}
$$

Assuming $\kappa_1 \approx 2.0$, $\eta \approx 0.55$, $\eta' \approx 0.40$, $\xi \approx 0.90$, $E_s/E_c \approx 6.0$, and $f_c'/f_y \approx 1/12$, Eq. (2.95) simplifies

$$\alpha_K \approx 0.18 \cdot \rho_v + 0.012 \cdot n \qquad (2.96)$$

where % is the unit of ρ_v and n. So, the stiffness of a wall of 0.3% vertical reinforcement ratio and of 3% axial force ratio reduces to 9% of the elastic stiffness.

2.8.2 Displacement based methods

Priestley (1997) proposed a displacement based approach for seismic assessment. Seismic action then is described by displacement response spectra rather than acceleration response spectra. The displacements directly can be related to strain-based limit states which are clearly more fundamental to damage than force-based methods. Priestley (1997) suggested that in regions of low to moderate seismicity displacement based methods may have increased significance in assessment. The finding that extreme events may have high peak spectral accelerations and low peak spectral displacements substantiated this suggestion.

Definition of limit states

The nonlinear behavior of reinforced concrete is modeled by using a bilinear moment curvature relationship that is defined by the following three points:

- the origin
- the nominal flexural moment and the curvature at yield (M_n, χ_y)
- the ultimate flexural moment and curvature (M_u, χ_u)

To estimate the corresponding flexural moments and curvatures one determines first yield, nominal strength and ultimate strength as follows (SIA2018 2004):

1. First yield: $M'_y = f(\chi'_y) \rightarrow \chi'_y = min(\chi(\epsilon_{cy}),\ \chi(\epsilon_{sy}))$
    - Concrete compressive strain $\epsilon_{cy} = \epsilon_{c1d} = 0.002$
    - Yield strain of rebars ϵ_{sy}, depends on steel properties.
2. Nominal strength: $M_n = f(\chi_n) \rightarrow \chi_n = min(\chi(\epsilon_{cu}),\ \chi(\epsilon_{sn}))$
    - Ultimate concrete compressive strain $\epsilon_{cu} = \epsilon_{c2d} = 0.004$
    - Strain of rebars $\epsilon_{sn} = 0.015$
3. Ultimate strength: $M_u = f(\chi_u) \rightarrow \chi_u = min(\chi(\epsilon_{cu}),\ \chi(\epsilon_{smax}))$
    - Ultimate concrete compressive strain $\epsilon_{cu} = \epsilon_{c2d} = 0.004$
    - Ultimate tensile strain ϵ_{smax}, depends on steel properties and reinforcement ratio:
        - If $M_n \geq 2M_{cr} \rightarrow \epsilon_{smax} = \epsilon_{su}$
        - If $M_n < 2M_{cr} \rightarrow \epsilon_{smax} = 0.5\epsilon_{su}$

The yield curvature in the bilinear model then is obtained by extrapolating the elastic branch up to the nominal strength ($\chi_y = \chi'_y \frac{M_n}{M'_y}$).

Material properties

According to (SIA2018 2004), the stress-strain relationship of concrete is as follows:

$$\sigma_c = f'_{ck} \frac{r \cdot \zeta}{r - 1 + \zeta^r} \tag{2.97}$$

where

$$\begin{aligned} r &= \frac{E_{cm}}{E_{cm} - \frac{f'_c k}{\epsilon_{c1d}}} \\ \zeta &= \frac{\epsilon_c}{\epsilon_{c1d}} \end{aligned}$$

The nonlinear response of reinforcing steel is modelled by a bilinear relationship that accounts for strain hardening.

2.8.3 Deflection calculations

Priestley & Park (1987) proposed a lumped plasticity model for deflection calculation of bridge bents which where modeled as cantilever columns (Fig. 2.25). According to this, the total tip deflection is supposed to consist of an elastic and a plastic contribution. The latter is due to the rotations inside a hinge of constant curvature. The length of this plastic hinge accounts for both the shear lag caused by inclined cracks and the yield penetration into the column base. Recently, the aforementioned lumped plasticity model was included in SIA2018 (2004) for displacement based evaluation of existing buildings.

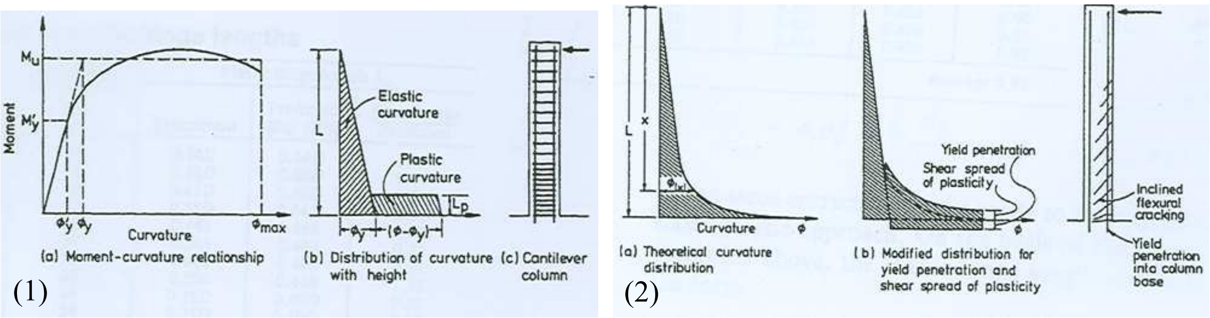

Fig. 2.25: Assumptions of lumped plasticity model, (1) Moment-curvature relationship, idealized curvature distribution, and reinforcement, (2) Theoretical curvature distribution, shear spread, and cracking (Priestley & Park 1987).

Using the concept of chord rotation and a bilinear moment-curvature relationship one can decompose the tip deflection as follows:

$$\Delta_u = \Delta_y + \Delta_p \tag{2.98}$$

where the ultimate tip deflection is splitted into an elastic and a plastic contribution. The elastic chord rotation due to a tip load can be written as:

$$\theta_y = \frac{\Delta_y}{L_v} = \frac{\frac{F_y {L_v}^3}{3EI}}{L_v} = \frac{M_y}{EI}\frac{L_v}{3} \tag{2.99}$$

Because of constant bending stiffness in the linear-elastic domain, Eq. (2.99) simplifies to:

$$\theta_y = \chi_y \frac{L_v}{3} \tag{2.100}$$

The plastic contribution to the tip deflection is equal to the product of plastic rotation and distance between center of the zone of lumped plasticity and the tip:

$$\Delta_p = \theta'_p \left(L_v - \frac{L_{pl}}{2} \right) \tag{2.101}$$

Then the plastic chord rotation is found by dividing Eq. (2.101) by the shear span:

$$\theta_p = \theta'_p \left(1 - \frac{L_{pl}}{2L_v} \right) \tag{2.102}$$

The ultimate chord rotation is the sum of both elastic and plastic contributions (Eq. (2.103)):

$$\theta_u = \theta_y + \theta_p \tag{2.103}$$

For real structures, the ultimate chord rotation is divided by a coefficient of partial safety of $\gamma_D = 1.3$ (SIA2018 2004). Assuming constant distribution of curvature in the zone of lumped plasticity, the plastic rotation equals the length of plastic zone multiplied by the difference between ultimate curvature and elastic curvature.

$$\theta_p = (\chi_u - \chi_y)\, L_{pl} \left(1 - \frac{L_{pl}}{2L_v}\right) \tag{2.104}$$

Hence, Eq. (2.98) can be rewritten (Priestley & Park 1987):

$$\Delta_{max} = \Delta_y + (\chi_u - \chi_y)\, L_{pl} \left(1 - \frac{L_{pl}}{2L_v}\right) L_v \tag{2.105}$$

A relationship between curvature ductility and displacement ductility is found by dividing Eq. (2.105) by the yield displacement Δ_y

$$\mu_\Delta = 1 + \frac{3}{C}\,(\mu_\chi - 1)\, \frac{L_{pl}}{L_v} \left(1 - \frac{L_{pl}}{2L_v}\right) \tag{2.106}$$

where the coefficient C includes increase in elastic flexibility due to the foundation while the length of the plastic hinge depends on the hardening ratio of reinforcing steel, the shear span, the yield strength, and the bar diameter (Eq. (2.107)):

$$L_{pl} = \alpha_{st}\,(0.08L_v + 0.022 f_y \phi) \tag{2.107}$$

Eq. (2.107) was essentially calibrated on test results of columns (Priestley, Seible & Calvi 1996). The reinforcement of these columns included steel grades currently used in New Zealand and in the US. The yield strength of such reinforcement is generally lower than that of reinforcement used in Europe but the hardening ratios are higher (Paulay et al. 1990). In SIA2018 (2004), the coefficient α_{st} accounts for lower hardening ratios of reinforcement due to the use of cold formed steel:

$$\begin{aligned} f_u/f_y < 1.15 \quad &\rightarrow \alpha_{st} = 0.8 \\ f_u/f_y \geq 1.15 \quad &\rightarrow \alpha_{st} = 1.0 \end{aligned}$$

Because of both the lower yield strength and the calibration on column tests, Eq. (2.107) possibly can not describe the plastic hinge length of shear walls of existing Swiss buildings. More research is necessary to investigate its validity.

2.9 Conclusions

This chapter intends to review the state of the art related to the scope of this research. Shear walls were reported to have well performed in past earthquakes while current methods for seismic evaluation still predict brittle shear failure of non-ductile walls. Reports from earthquake reconnaissance missions also highlight that there is only a limited number of total collapses of shear wall buildings. However, lightly reinforced walls are expected to have brittle behavior because of both possible strain localization at the base causing either rebar rupture or sliding and susceptibility to brittle shear failure caused by diagonal cracking.

The review of tests of slender walls provide evidence for seismic response dominated by flexure. Under dynamic loading, energy dissipation can be achieved by both plastic deformations and geometrically nonlinear response. Shear failure effectively is prevented by introducing hierarchical order of strength. Squat, lightly reinforced walls tend to fail either in diagonal tension or in sliding. The failure mode depend on the restraint of the top of the wall. In addition, the loading can influence the failure mode. Although sliding shear was not reported in dynamic tests, it is observed under static-cyclic loading.

A database of wall tests is established. However, the review of available experimental data shows that tests of appropriate wall configurations are missing. Such configurations should include the characteristics of shear walls prevalent in existing buildings. These walls have squat aspects ratios, uniformly distributed reinforcement and they are subjected to moderate levels of axial force.

Research on shear capacity of RC beams significantly advanced in the past 40 years and the results of this research form the base of both the standards and codes that are used today for shear design of RC members. Review of the literature provided evidence for concrete contribution to shear strength. However, such contribution is not considered in the general truss model.

Available models for members without transversal reinforcement show the potential to consider the decay of shear strength. Such decay is due to increase in deformation. The models consider shear failure by introducing both reference crack widths and relationships between shear transfer and these reference crack widths.

Several methods exist for the seismic assessment of columns that are susceptible to shear failure. Such models can predict shear failure due to increase in deformation and they show potential for the application on shear walls. Nevertheless, the displacement predictions of these models are generally a function of yield displacement. Since appropriate approaches for the yield displacement of squat walls not exist, further research on the deformation capacity of squat walls is required.

Chapter 3

Experimental investigations

3.1 Objective

The test series, which includes four specimens, focuses on shear dominated response of walls that are not designed for earthquake actions (Greifenhagen & Lestuzzi 2005). The test series investigates the deformation capacity of lightly reinforced concrete shear walls under reversed static-cyclic loading.

The goal of this experimental study is to contribute to a more realistic seismic evaluation of existing shear-wall buildings that were built prior to the introduction of earthquake-resistant design recommendations into building codes. Parameters of the test series are the axial force ratio, the horizontal reinforcement ratio, and the concrete compressive strength. The impact that different detailing of transversal reinforcement and lap splicing of vertical reinforcement can have on deformation capacity is not investigated in this study. Detailed description of the static-cyclic tests is provided elsewhere (Greifenhagen, Lestuzzi & Papas 2005).

3.2 Description of test series

3.2.1 Test program

The test program is illustrated in Fig. 3.1. It includes two test series, each consisting of two specimens.

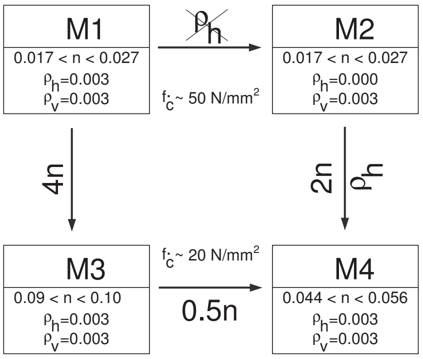

Fig. 3.1: Test program.

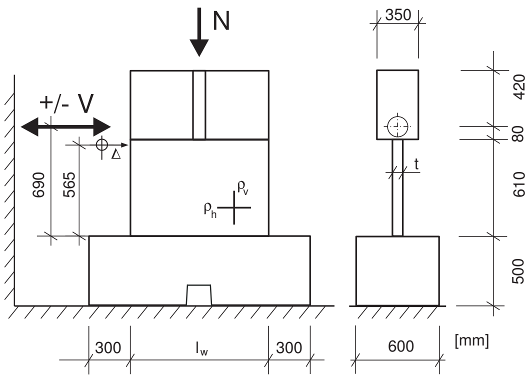

Fig. 3.2: Set-up of static-cyclic tests.

The objective of the first test series is to quantify the concrete contribution to shear capacity. For that, two identical specimens, M1 and M2, are tested but Specimen M2 has no horizontal reinforcement. Axial force ratio and concrete compressive strength are nearly the same for both specimens. The impact of axial force ratio on shear capacity is investigated in the second test series. Since the test set-up restricts the maximum axial force, both the concrete compressive strength and the gross section are reduced in the second test series in order to apply higher axial force ratio on the specimens at a given level of post-tensioning force.

3.2.2 Test set-up

The specimens represent at a 1:3 scale the lower part of a shear wall of an existing building. It is assumed that a simple cantilever subjected to both constant normal forces and static-cyclic lateral loads can model the behavior of a real shear wall under earthquake action in order to investigate its behavior in the laboratory. The modeling of the shear wall with a cantilever subjected to vertical and horizontal loading includes some assumptions on the seismic behavior of real buildings.

- First, the shear walls are assumed to be not coupled to each other because the stiffness of slabs is usually much smaller than that of the walls.
- Second, the dynamic behavior is governed by the fundamental mode of vibration, which generally dominates the response of 5- to 6-storey shear wall buildings.

The impact that the fundamental mode of vibration of the building on the test results is however small. In this context, the seismic behavior of a typical building is mentioned in order to emphasize that shear walls in existing buildings often behave as cantilevers.

The test set-up is shown in Fig. 3.2. The specimens consist of three parts:

1. The head beam through which the loads are transferred into the panel,
2. The panel which models a shear wall, and
3. The footing anchoring the specimen on the strong floor of the laboratory.

Table 3.1 includes dimensions of specimens, concrete compressive strengths, and axial force ratio. Concrete compressive strengths of specimens M1/M2 and M3/M4 are near to 50 and 25 MPa, respectively. These values refer to the cylinder strength at the tests.

Specimen	l_w^a [mm]	t^a [mm]	M/V [-]	ρ_v [%]	ρ_h [%]	f'_c [MPa]	n [%]
M1	1000	100	0.69	0.3	0.3	50.7	1.7 .. 2.7
M2	1000	100	0.69	0.3	0.0	51.0	1.7 .. 2.7
M3	900	80	0.69	0.3	0.3	20.1	4.4 .. 5.6
M4	900	80	0.69	0.3	0.3	24.4	9.0 .. 10.0

^{a}: Symbols l_w and t refer to Fig. 3.2

Tab. 3.1: Characteristics of specimens

The specimens are produced horizontally to facilitate the fabrication. Uplift of the footing is prevented by post-tensioned anchor rods. The head beam, panel and the footing are cast together as slab using simpler formwork than would be necessary to cast the specimen in upright position.

In real buildings, there are joints between slabs and walls. Such joints are neglected in the test set-up in order to maximize the shear transfer between panel and floor beam. Although this does not exclude sliding shear mechanisms, the number of cycles necessary to develop this mode is increased. Thus, the greater shear transfer permits the application of higher loads which can lead to other failure modes.

Reinforcement of specimens

The reinforcement of the specimens is illustrated in Fig. 3.3. Mild steel rebars of 6 mm diameter form the vertical reinforcement for all specimens and the horizontal reinforcement of specimen M1. Cold formed rebars of 4 mm diameter are used for the horizontal reinforcement of specimens M3 and M4.

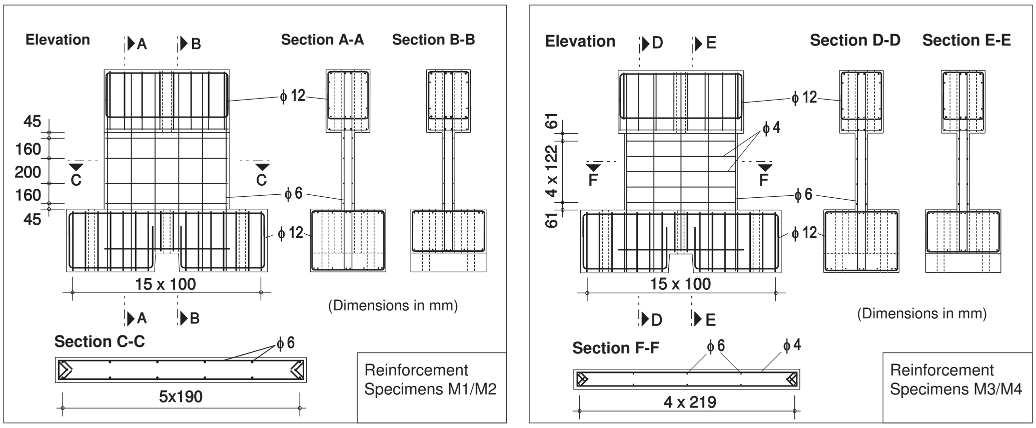

Fig. 3.3: Reinforcement of Specimens

Mean values of the mechanical properties of the rebars are shown in Tab. 3.2. The vertical reinforcement is enclosed by the horizontal reinforcement in the form of stirrups with end hooks of 135° that are anchored in the core concrete. The openings of the stirrups are staggered along the wall height. Rebars of 12 mm diameter were used for the reinforcement of the head beam and the footing.

Type	f_y	f_u	ϵ_y	ϵ_u	$\frac{f_u}{f_y}$
	[MPa]	[MPa]	[mm/m]	[cm/m]	[-]
4 mm cold formed bar	745	800	3.71	2.91	1.07
6 mm mild steel bar	504	634	2.85	11.05	1.26

Tab. 3.2: Properties of reinforcement

3.2.3 Testing procedure

The lateral cyclic load is applied by pushing the head beam with two actuators of 200 kN maximum force that are operated alternately. Two post-tensioning bars of 12 mm diameter are used to subject the specimens to axial loading (Fig. 3.4). The bars are placed at mid-length of the specimens at both sides of the panel. Circular ducts of 50 mm diameter in both the footing and the head beam prevent these bars from contributing to the lateral stiffness of the specimen. Anchoring is provided to the post-tensioning bars by screws and washers that are placed in a recess of the footing and above the head beam.

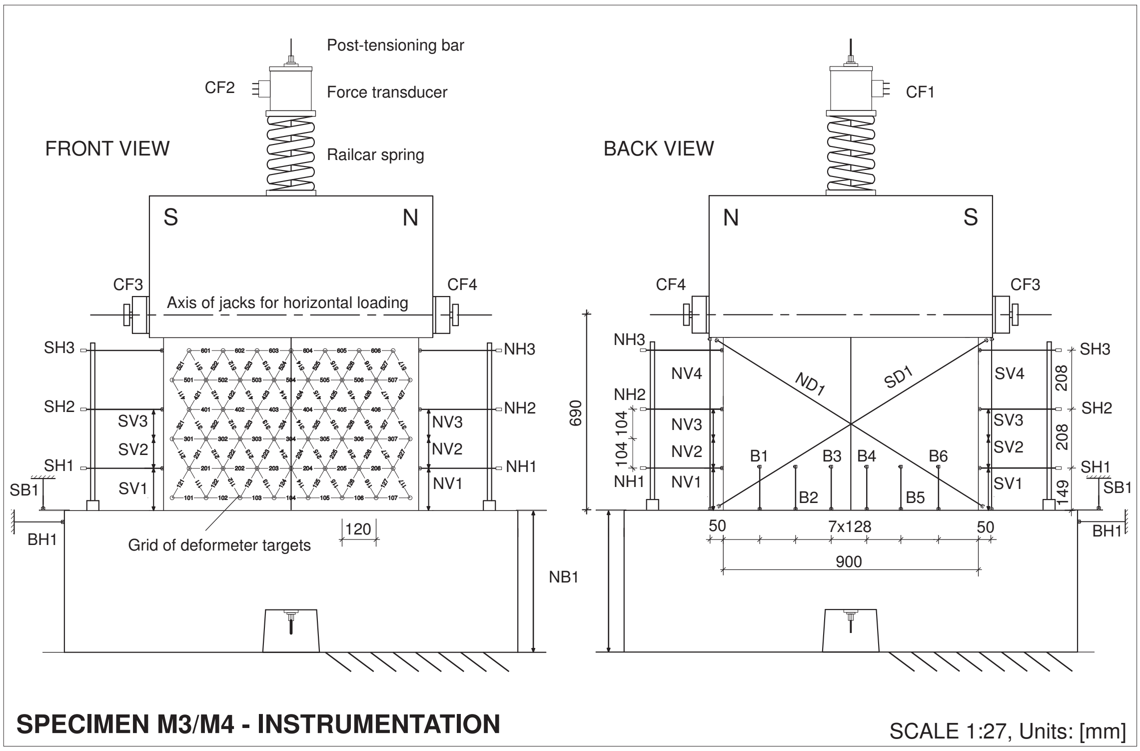

Fig. 3.4: Instrumentation of specimens M3 and M4.

Before the static-cyclic test, the vertical bars are alternately post-tensioned in small increments up to the target force by the help of a hydraulic jack. Because of the inability to maintain the vertical post-tensioning force constant level, railcar springs between the head beam and the anchor of the post-tensioning bars provide stiffness reduction to the post-tensioning system (Fig. 3.4). Thus, the uplift of the head beam due to rocking of the panel results in less increase of axial load.

Loads, in-plane displacements and strains on the concrete surface are monitored by instrumenting the specimens with force transducers, displacement transducers and deformeter targets, respectively. The load is quasi-statically applied in small increments up to a target displacement or a target force. At this point the displacement is kept constant in order to capture high-resolution images, measure crack widths and record strains on the surface. The force decreased during this time by 10% to 15 %. Finally, the specimen is gradually unloaded.

Loading histories

Force and displacement controlled loading histories are applied in order to simulate seismic actions by reversed static-cyclic loading. Specimens M1 and M2 are cycled at 25, 50, 100, 150 kN base shear and nominal axial force of 136 kN (Fig. 3.5). Two cycles are applied at each level of base shear. The specimens are then subjected to three cycles at 200 kN base shear which is near to the base shear at nominal flexural strength. Because of the limited load capacity of the actuators, further increase of base shear was not possible. The vertical post-tensioning force is then decreased to 106 kN and the specimen is subjected to two cycles of lateral loading. Subsequently, the vertical post-tensioning force is reduced to 86 kN and the specimen is cycled up to failure.

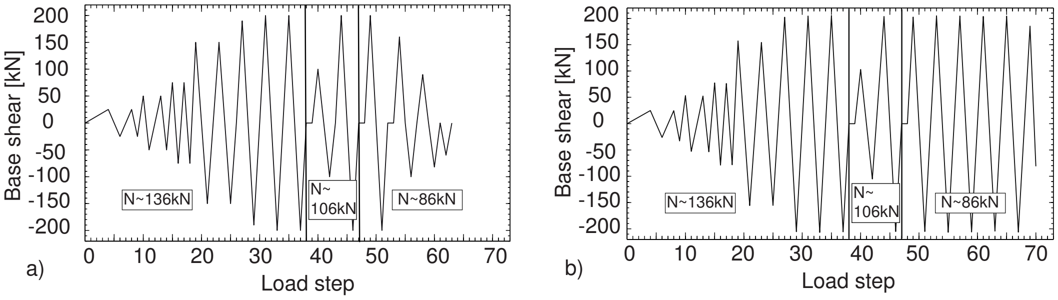

Fig. 3.5: Loading history of specimens, a) M1, b) M2.

Specimens M3 and M4 are subjected to constant nominal axial forces of 136 and 76 kN, respectively (Fig. 3.6). The cyclic loading regime of these specimen include load increments of 25 kN up to 75 % of the base shear at nominal flexural strength. It includes also displacement increments corresponding to the top lateral displacement at 75 % base shear at nominal flexural strength. The specimens are cycled two times at each magnitude of force or displacement.

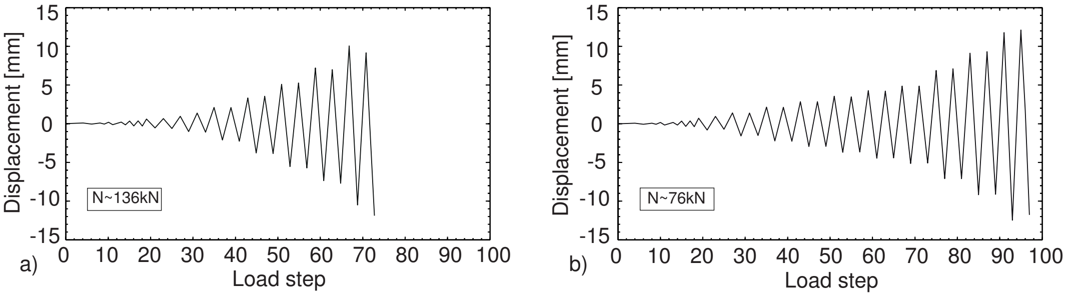

Fig. 3.6: Loading history of specimens, a) M3, b) M4.

3.3 Test results

3.3.1 Test observations

All specimens approximately develop the nominal flexural strength and hence, the observed maximum base shear is controlled by flexure, and not by premature shear failure. The observed maximum base shear of specimen M3 is even greater than the base shear at nominal flexural strength. The specimens fail due to increase in applied displacements. The ultimate displacement is restricted by shear failure or flexural failure, depending on the axial force ratio that is applied on the specimen.

Specimen M1

For specimen M1, cracking localizes at the base of the wall. Almost linear-elastic behavior is observed up to a magnitude of base shear of 150 kN which is closed to the predicted yielding of the outermost rebars. Then the slope of the response curve changes significantly. Displacements up to 3.5 mm and axial force of 136 kN results in a number of small inclined cracks that formed in a zone of 40 mm width between the footing and the first stirrup. The inclined crack (Fig. 3.7) occurs at 3.5 mm top lateral displacement. Reduction of axial force results in diminution of stiffness. The small cracks near to the base interconnect with increases of displacements and sliding movements in these cracks contributed substantially to the top lateral displacements. The rupture of the outermost rebars is observed at a top lateral displacement of 16.5 mm. Additionally, the vertical force is not constant during the test. It varies between 136 and 146 kN, 106 and 122 kN, 80 and 106 kN for nominal axial forces of 136 kN, 106 kN, and 86 kN, respectively.

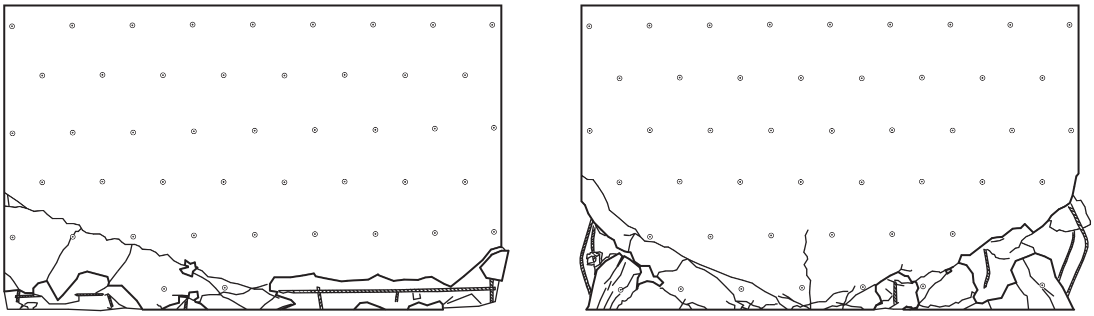

Specimen M1 ($n=0.02$, $\rho_v = \rho_h = 0.003$)   Specimen M2 ($n=0.02$, $\rho_v = 0.003$, $\rho_h = 0.0$)

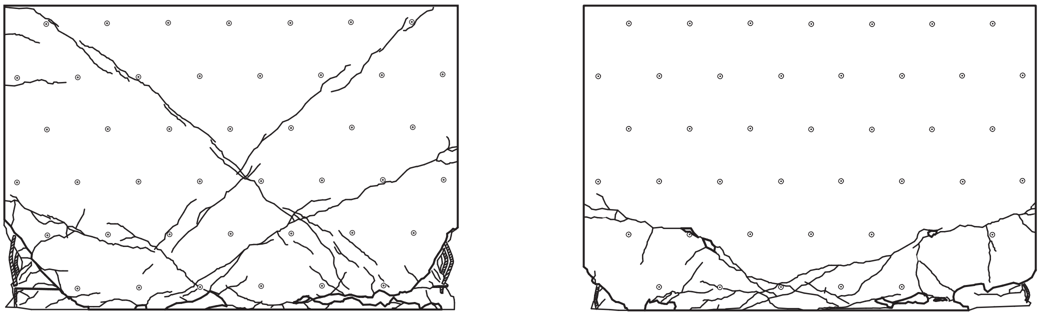

Specimen M3 ($n=0.10$, $\rho_v = \rho_h = 0.003$)   Specimen M4 ($n=0.05$, $\rho_v = \rho_h = 0.003$)

Fig. 3.7: Final crack patterns.

Specimen M2

During the test of specimen M2, residual displacements are already observed at a value of base shear equal to 150 kN. As for specimen M1, the slope of the response curve diminishes at the predicted yield of the outermost rebars. Reduce in stiffness due to both diminution of axial force and increasing number of cycles is also observed. However, at the toes of the wall the cracking extend up to one third of the wall height. A continuous base crack did not form. The concrete cover at the edges spalls at 5 mm displacement. The movement of the wall consists then of sliding at the load reversal and subsequent rocking. The test is halted at 15 mm top lateral displacement because the vertical displacements exceed the capacity of the test set-up. During the test of specimen M2, the vertical post-tensioning force varies between 136 and 144 kN, 106 and 112 kN, 75 and 108 kN for nominal axial forces of 136 kN, 106 kN, and 86 kN, respectively. The maximum axial force is observed at the peak of the half-cycles.

Specimen M3

Specimen M3 develops its maximum base shear of 176 kN at 3.2 mm top lateral displacement. At this time, cracking is limited to the lowest third of the wall. Small vertical cracks occur at the base of the wall near its edges (Fig. 3.8).

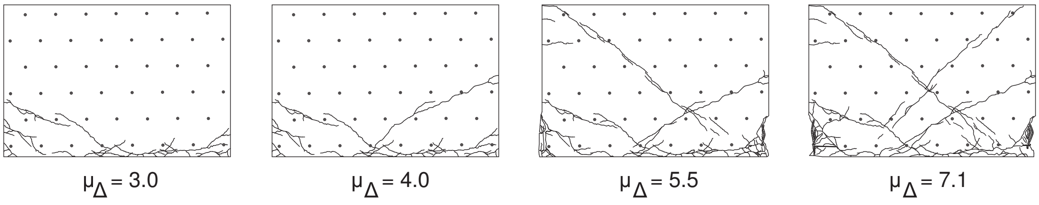

Fig. 3.8: Crack pattern of specimen M3 at selected displacement ductilities.

Increasing the displacement to 7 mm resulted in the formation of a diagonal corner to corner crack (Fig. 3.7). Due to the cracking, the restoring force decreased by nearly 15 %. Moreover, both spalling of concrete cover at the wall toe and buckling of the outermost rebars is observed at the begining of the cycle in which the diagonal crack formed. Despite the occurrence of the diagonal crack, the shear capacity of the specimen is yet greater than 80 % of the base shear at nominal flexural strength.

The second diagonal crack occurred at 8.7 mm top lateral displacement resulting in a drop of the restoring force by 30 %. In the lowest quarter of the wall, the vertical displacement at the edge increases significantly due to the formation of the second diagonal crack (Fig. 3.9). The crack pattern at this stage is shown in Fig. 3.7. Significant loss of shear capacity is observed in the subsequent cycles. Fig. 3.10 shows the edge of specimen M3 at 10 mm top lateral displacement, after the second diagonal crack occurred. Sudden concrete crushing along the base of the wall terminated the test of specimen M3.

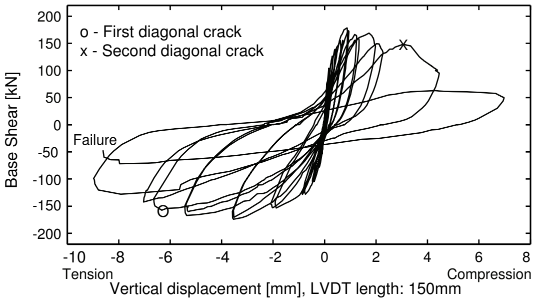

Fig. 3.9: Recorded vertical displacements near to bottom of specimen M3.

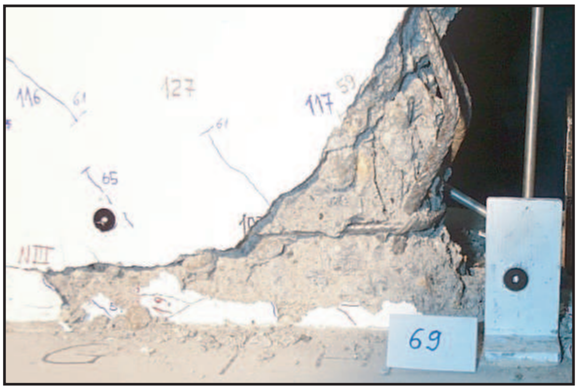

Fig. 3.10: Detail of specimen M3 at 10 mm top lateral displacement.

Specimen M4

The maximum shear capacity of specimen M4 is observed at 2.8 mm top lateral displacement. The crack pattern at maximum base shear ($\mu_\Delta = 2.6$) is very similar to that of specimen M3 (Fig. 3.8, Fig. 3.11). However, the hysteretic loops of specimen M4 are more pinched than those of the other specimens (Fig. 3.13). Spalling of the concrete cover at the wall toes is observed at 4.9 mm top lateral displacement.

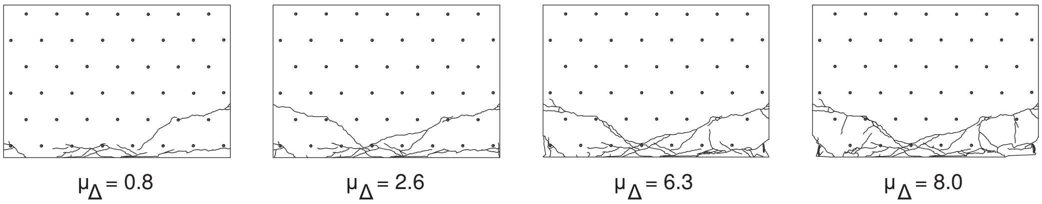

Fig. 3.11: Crack pattern of specimen M4 at selected displacement ductilities.

The outermost vertical rebars buckled at the displacement level of 7 mm. Nevertheless, the shear capacity at the subsequent displacement level of 9 mm is almost equal to the base shear at nominal flexural strength. The shear capacity decreases in the second cycle at this displacement level by 13 % while in previous cycles up to 7.5 % loss of shear capacity is observed due to repeated loading. Further increase in displacement lead to the failure of both the vertical rebars in tension and the concrete in compression at the wall edges. The maximum top lateral displacement yields 12.5 mm.

3.3.2 Force-deflection relationships

The force-displacement relationships are shown in Fig. 3.12 and Fig. 3.13. In addition to the observed responses, these plots include a bilinear approximation of the load-displacement envelope, the corresponding values of both ductility and drift, and the observed failure modes.
Shear modes are activated by increase in drift, not in base shear. Such activation leads to pinching of hysteretic loops (Specimen M4) and overall failure (Specimen M3). Sliding in cracks plays an important role as reloading curves of force vs. lateral displacement plots are generally linear (Fig. 3.13). Sliding deformation thus compensates other effects that produce nonlinearity, e.g. yielding of rebars.

Determination of yield displacement

The bilinear approximation is determined by extrapolating the observed top lateral displacement at first yield up to the nominal flexural strength ((Priestley & Kowalsky 1998),(Dazio et al. 1999)). Both first yield and nominal flexural strength are derived from moment-curvature relationships that are computed with the material properties shown in Tables 3.1 and 3.2. The assumptions for these calculations include elastic-perfectly plastic and parabolic-rectangular stress-strain relationships for reinforcing steel and concrete, respectively. Since perfectly elastic-plastic behavior of steel is assumed for the curvature analysis, the nominal flexural strength is equal to the maximum flexural strength. Equation (3.1) describes the extrapolation of yield yield displacement:

$$\Delta_y = \Delta_{y,1} \frac{F_y}{F_H} = \frac{\Delta_{y,1}}{\alpha_{y,1}} \tag{3.1}$$

The yield displacements of the specimens M1, M2, M3, and M4 are shown in Tab. 3.3.
Depending on the configuration of the test unit, yielding of the outermost rebars occurred between 76 % to 82 % of the nominal flexural strength. Paulay et al. (1990) suggested the base shear at first yield to be 75 % of the base shear at flexural strength. This suggestion agrees well with the results shown in Tab. 3.3.

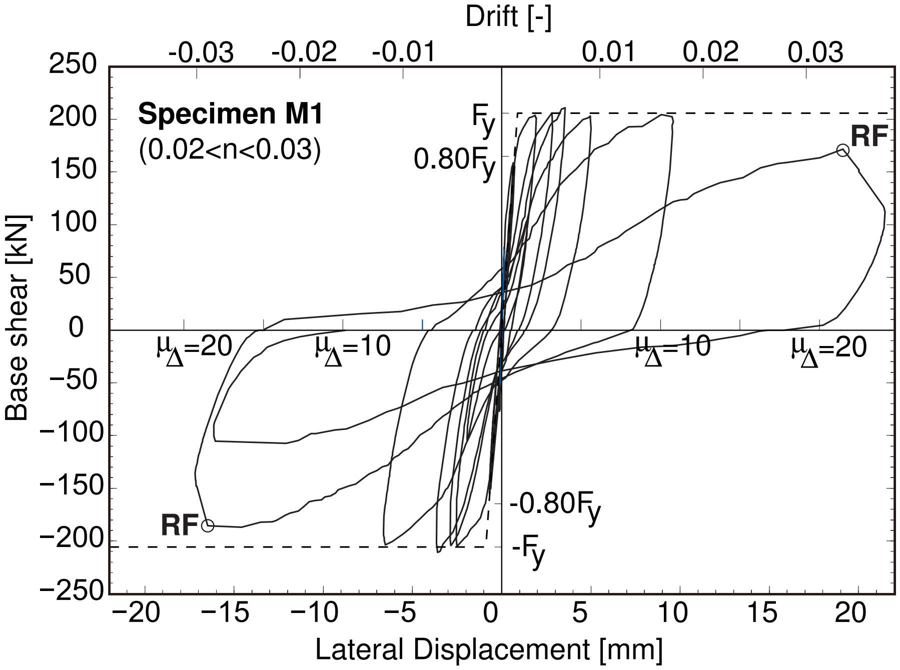

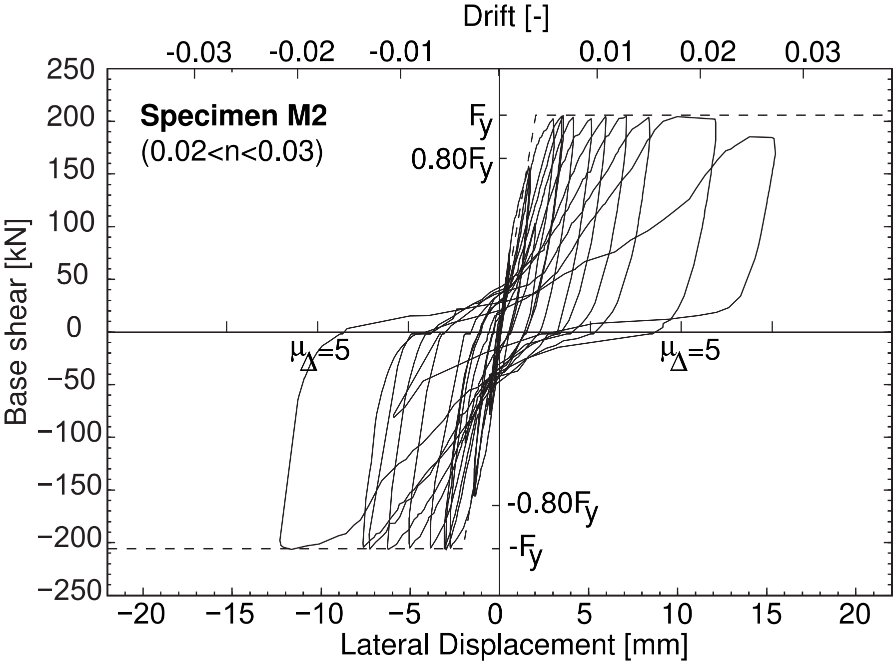

Fig. 3.12: Force-deflection relationships observed in static-cyclic tests (RF-Failure of vertical reinforcement, DC-Diagonal cracking, CF-Concrete crushing).

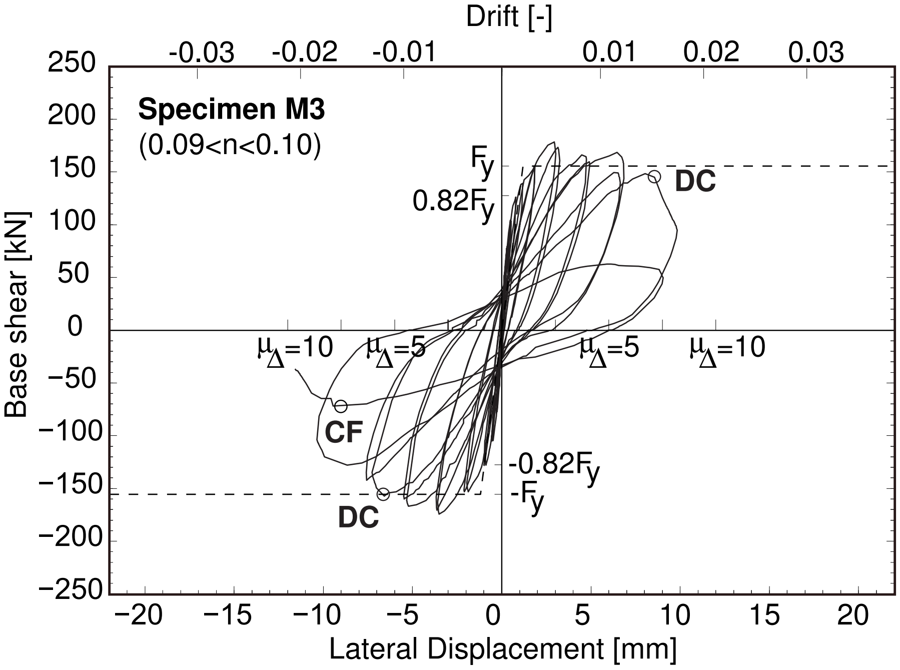

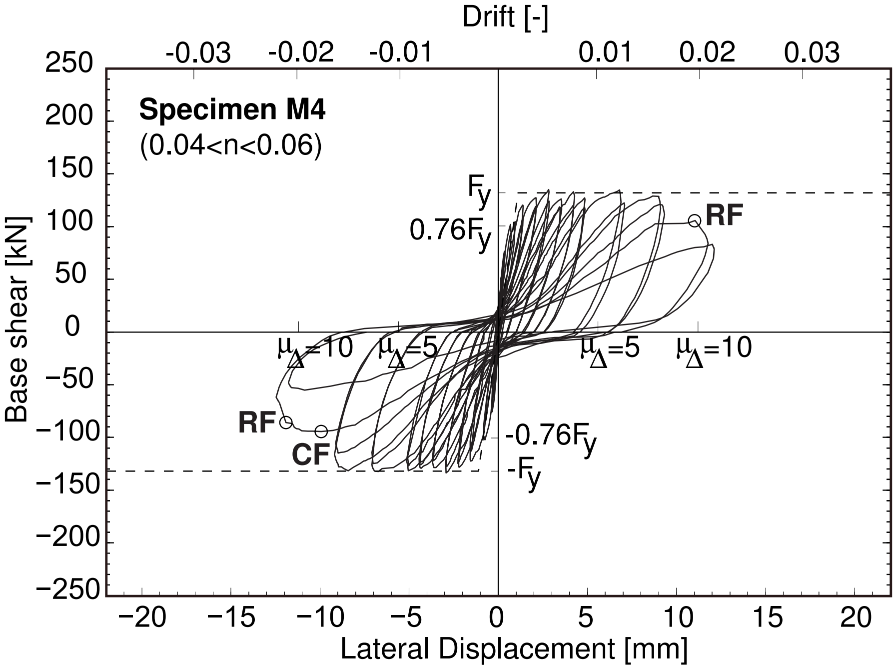

Fig. 3.13: Force-deflection relationships observed in static-cyclic tests (RF-Failure of vertical reinforcement, DC-Diagonal cracking, CF-Concrete crushing).

Specimen	M'_N [kNm]	M_N [kNm]	α_y	F_y [kN]	F'_y [kN]	$0.75F_y$ [kN]	F_H [kN]	$\alpha_{y,1}$	$\Delta_{y,1}$ [mm]	Δ_y [mm]	θ_y [mrad]
M1	115	144	0.80	206	165	154	155	0.75	0.67	0.89	0.91
M2	115	144	0.80	206	165	154	156	0.76	1.55	2.05	2.34
M3	89	109	0.82	155	127	116	127	0.82	1.00	1.22	1.33
M4	71	93	0.76	133	101	100	94	0.71	0.80	1.12	1.21

Tab. 3.3: Estimation of displacements and rotations at yield.

Pinching of hysteretic loops

Pinching of hysteretic loops begins at displacement ductilities near to 2.0 and amplifies as the number of cycles and the drift increase. Parameters that govern the pinching of hysteretic loops are the normal force ratio and the concrete compressive strength. Physical reason for the pinching in this context are sliding movements in the cracks. These movements lead to grinding of crack asperities and hence, progressive reduction of aggregate interlock. In addition, crack widths increase with greater lateral displacements and this reduces also the aggregate interlock effect.

Observed failure modes

The specimens M1, M3, and M4 fail in rupture of reinforcement, diagonal tension and concrete crushing. The axial force ratio determined the failure mode. Increase in axial force ratio leads to increase in shear stress that spreads cracking over the panel and augments susceptibility to diagonal tensile failure. Increase in normal force also increases stiffness and prevents sliding movements at the load reversal.

Due to the pinching of hysteretic loops for specimens M1, M2, and M4, the aggregate interlock in the base joint only transfers a small portion of shear. The concrete compressive zone is main contributor to shear transfer into the base. The corresponding stress field is shown in Fig. 3.14a.

As it is observed for specimen M3, the failure mode of diagonal tension is closely linked to concrete crushing. At maximum load, the concrete near the base is damaged by straining due to elongation of rebars. Vertical cracks form. In subsequent cycles these cracks result in weakening of concrete in compression. Thus, restoring force slips. The degradation of concrete continues until the concrete compression zone cannot transmit an appropriate part of shear which is redistributed to the aggregate interlock mechanism. This redistribution strains the panel, diagonal cracks occur and restoring force reduces again because of weakened flexural strength. Hence, diagonal tension is governed by the following mechanisms:

- Degradation of concrete tensile strength due to previous compressive loading,
- Shear lag of vertical tensile force,
- Shear transfer in the tensioned part of base joint provided by aggregate interlock,
- Decay of concrete contribution to shear strength due to weakening of concrete compressive zone.

The force flow in specimen M3 is illustrated in Fig. 3.14b.

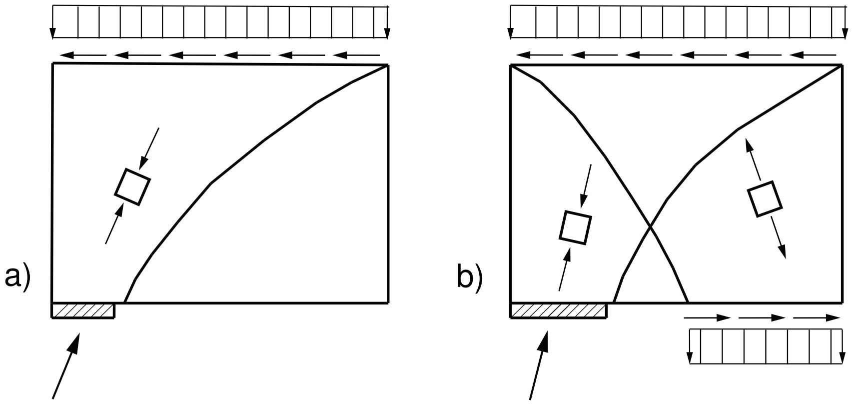

Fig. 3.14: Stress fields derived from observed specimen behavior: a) Specimens M1/M2/M4, b) Specimen M3.

However, continuous degradation of restoring force is observed before the aforementioned failure modes occur. Such degradation is due to both loss in bond strength and grinding of asperities on crack interfaces. Since it is common practice to define failure as a limit of decay in restoring force (EC8 2003), such mechanisms can govern the deformation capacity. The next section provides detailed analysis of decay in restoring force.

Degradation in restoring force

The degradation in restoring force is shown in Fig. 3.15 for both increase in ductility and drift. In these plots, the restoring force ratio denotes the base shear in second cycle divided by the base shear in first cycle. The base shears of both cycles correspond to the same displacement.

The decay of restoring force is partially caused by cyclic behavior of aggregate interlock, as reported by Walraven (1994): Sliding produces up to the previously achieved displacement level, then the asperities of crack lock in. So, both stiffness and transmitted shear increase up to maximum load of cycle. This is due to accumulation of damage at the contact surfaces. In the subsequent cycle, the crack slip necessary to lock in the crack asperities increases and consequently the restoring force decreases.

Assuming failure of specimens when restoring force ratio falls below 0.80, both ultimate displacement ductilities and drift can be estimated with the help of Fig. 3.15. They are shown in Tab. 3.4.

Specimen	M1	M2	M3	M4
Ductility μ_Δ	5.5	4.5	5.5	7.5
Drift φ	0.9	1.5	1.2	1.5

Tab. 3.4: Displacement ductilities and drifts at 20% decay of restoring force.

Strength and deformation capacity

The achieved drifts, shear stresses, and ductilities are shown in Tab. 3.5. The displacement ductility refers to the bilinear relationships shown in Fig. 3.12 and Fig. 3.13. The rotation ductility is computed from rotations of the head beam of which detailed analysis is provided in

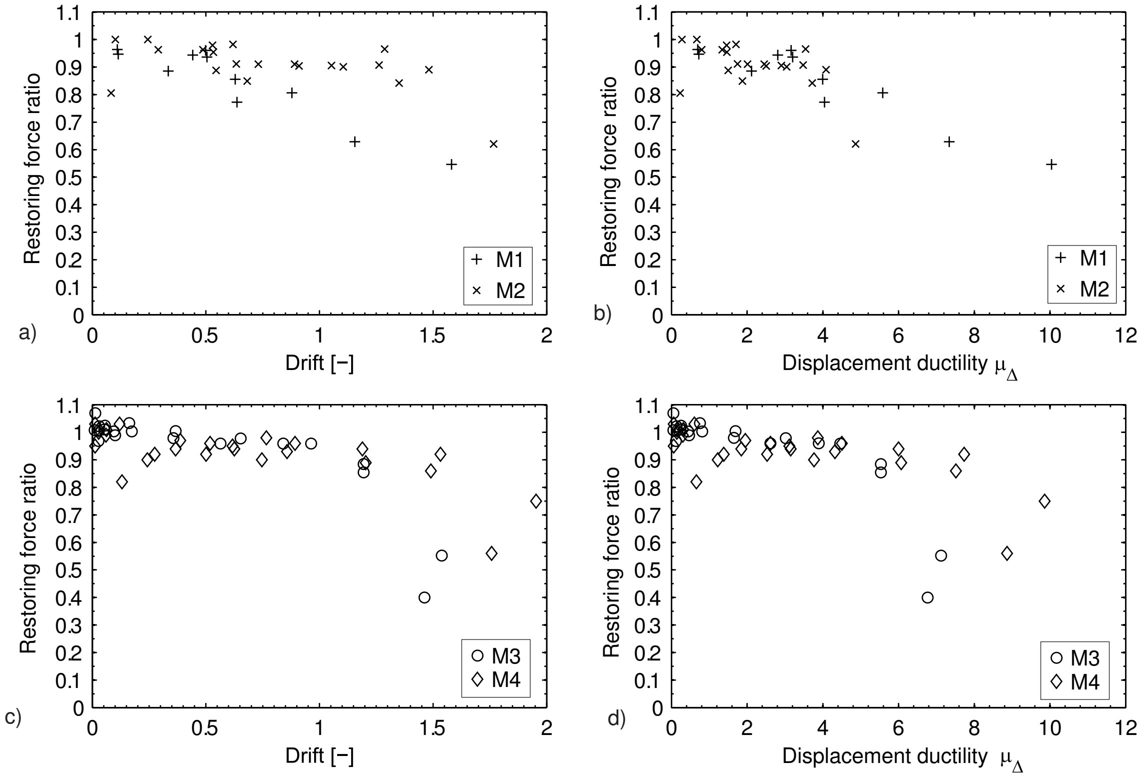

Fig. 3.15: Decay in restoring force, Specimens M1/M2 (a)(b), Specimens M3/M4 (c)(d).

Sec. 3.3.3. Failure is assumed when the base shear falls below the reference base shear. The latter is equal to the restoring force due to reloading of the test unit up to the displacement that is observed at maximum base shear of first cycles. This definition is different form that used in the previous section and it results in higher displacement ductility of specimen M2. However, for the other specimens the results are similar to each other.

The test results indicate that higher axial forces reduce displacement ductility and increase the shear capacity whereas concrete quality governs the drift at maximum base shear. For specimen M1, the localization of deformations in one crack results in reduction of drift capacity. Contrary to this, better performance is observed during test of specimen M4 because of spread of deformations that is induced by the increase in axial force ratio.

The observed displacement ductilities are greater than 5.6 and less than or equal to 8.0. Displacement ductilities between 2.1 and 2.6 were necessary to develop the maximum base shears. These displacement ductilities are based on experimentally observed displacements which correspond to yielding of outermost vertical rebars (p. 62). However, the static-cyclic envelopes curves include a significant descending branch. So, most of the aforementioned displacement ductility is achieved in the post-peak branch.

It is therefore not recommended to equate this ductilities with behavior factors as it is commonly achieved by applying the equal displacement rule. In a first step, the observed ductilities can be divided by the ductilities at maximum base shear in order to provide behavior factors. Nevertheless, detailed investigations how to determine behavior factors are behind the scope of this work and further research is necessary.

Maximum drift is observed for specimen M2 but the specimen M4 offered the maximum ductility. This originates from the yield displacement of specimen M2 which is greater than that

Test unit	Combin.	Axial force (N) [kN]	Axial force ratio (n) [-]	Base shear (F_H) [kN]	Shear stress (τ) [MPa]	Displ. (Δ) [mm]	Ductility (μ_Δ) [-]	(μ_θ) [-]	Drift (φ) [%]
M1	$F_{H,max,I}$	135	0.03	204	2.04	1.88	2.11	3.09	0.33
	$F_{H,max,II}$	137	0.03	189	1.89	1.88	2.11	4.08	0.33
	Δ_u	112	0.02	140	1.40	5.00	5.60	7.50	0.88
M2	$F_{H,max,I}$	140	0.03	203	2.03	2.88	1.40	1.54	0.51
	$F_{H,max,II}$	141	0.03	194	1.94	2.88	1.40	1.72	0.51
	Δ_u	112	0.02	156	1.56	12.13	5.92	6.53	2.15
M3	$F_{H,max,I}$	141	0.10	176	2.44	3.20	2.62	3.31	0.57
	$F_{H,max,II}$	141	0.10	168	2.33	3.20	2.62	3.39	0.57
	Δ_u	149	0.10	134	1.87	7.07	5.80	6.77	1.25
M4	$F_{H,max,I}$	82	0.05	135	1.88	2.80	2.50	3.23	0.50
	$F_{H,max,II}$	83	0.05	126	1.75	2.80	2.50	3.15	0.50
	Δ_u	87	0.05	101	1.40	9.00	8.04	9.69	1.59

Tab. 3.5: Strength and ultimate displacements.

of the other specimens (Tab. 3.3). Analyzing the force deflection relationship of specimen M2 (Fig. 3.12), small unloading stiffness and significant residual deflection are observed which indicate both sliding movements and open cracks after unloading. Hence, these effects are indirectly included in displacement ductility as long as they contribute to the decay in restoring force.

Envelopes for shear ratio are shown in Fig. 3.16. The envelope curves are computed by dividing the maximum base shear of half-cycle by both square root of concrete compressive strength and area of gross section. Base shears of first and second cycles are used for specimens M1/M2 and M3/M4, respectively. The plots reflect decreasing deformation capacity with increase in shear ratio. Both displacement ductility and drift thus are inversely proportional to the shear ratio.

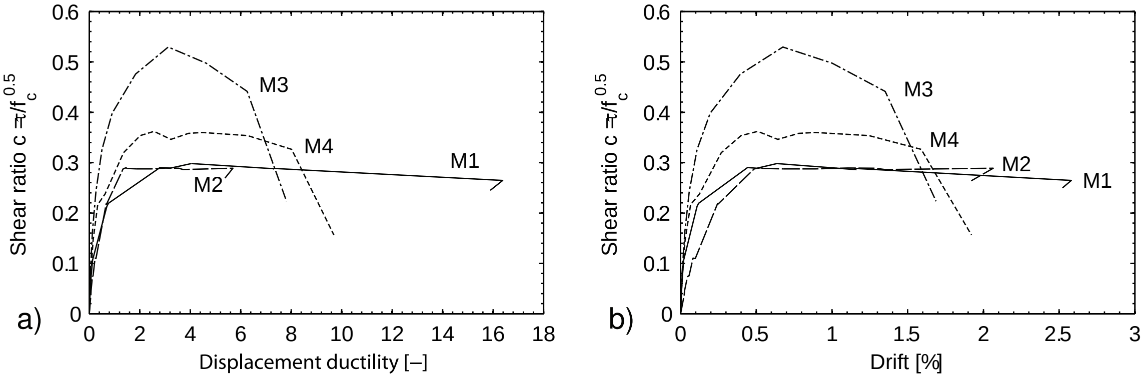

Fig. 3.16: Envelope curves for shear ratio, a) displacement ductility, b) drift.

3.3.3 Deflection quantities

Bending deflection

The instrumentation of the specimens enables the calculation of rotations at different wall heights. Selected results of this calculation are shown in Tab. 3.6 for half-cycles at 20% decay of base shear.

The data shown in Tab. 3.6 indicate that at ultimate base shear between 63% and 87% of the drift are due to the rotation of the head beam. The greatest ratio of rotations to drift is estimated for specimen M1 of which the response is dominated by rocking. In case of specimen M2, the observed sliding mechanism reduced the contribution of rotations to drift to 63%. The ratio of head beam rotations to drift is not sensitive to the axial force ratio because approximately 70% are estimated for both specimen M3 and specimen M4.

Fig. 3.18 plots the maxima per cycle of both the base shear and the lateral displacement to the rotation of head beam. The symbols NI/SI and NII/SII denote first and second cycles, respectively. The plots indicate a nearly linear relationship between the rotation of the head beam and the lateral displacements. The portion of deflection due to rotation of head beam decreases as the the lateral displacement increases. In particular, this portion reduces to nearly 50% of displacement for specimen M1 in case of loading in north. The decrease of flexural portion originates from increase of sliding portion. In addition, for specimens M3 and M4 the rotation contribution to deflection is similar in first and second cycles.

Spec.	LS	$\theta^a_{NV1-SV1}$ $[10^{-3}rad]$	θ_{B1-B6} $[10^{-3}rad]$	$\theta^b_{NV4-SV4}$ $[10^{-3}rad]$	φ $[10^{-3}]$	$\theta_{NV4-SV4}/\varphi^c$ $[-]$
M1	44	6.70	6.95	6.77	8.80	0.87
	46	-6.99	-5.86	-8.54	-	
M2	63	-	10.3	-11.9	21.50	0.63
	65	-	15.2	-	-	
M3	59	8.59	10.4	9.11	12.50	0.72
	61	-6.77	-10.5	-8.85	-	
M4	87	9.45	6.89	11.0	16.00	0.73
	89	-11.9	-10.6	-12.3	-	

[a] $\theta_{NV1-SV1}$ - rotation bottom part (base length of 150 mm)

[b] $\theta_{NV4-SV4}$ - rotation of head beam (base length of 610 mm)

[c] $\theta_{NV4-SV4}/\varphi$ - rotation of head beam divided by drift, average of both half-cycles.

[d] Note: indexes refer to the displacement transducers shown in Fig. 3.4

Tab. 3.6: Ultimate rotations.

Deflection due to sliding and distortion

Shear and flexure quantities are shown in Fig. 3.19. Description of symbols is provided in the glossary (p. 158). The contributions of flexure, distortion, and sliding to the lateral displacement are computed from the peak values per cycle. The displacement components plotted in this figure are normalized to the observed lateral displacement.

The deflection quantities are calculated in three steps:

1. Flexural components originate from rotations (Fig. 3.17b) that are derived from vertical displacements on two different heights (Fig. 3.17a) according to Pilakoutas & Elnashai (1993)

2. The deflections due to distortion (Fig. 3.17c) are estimated by applying Eq. (3.2).

$$\Delta_{\gamma} = \frac{(\Delta_2 - \Delta_{F2}) - (\Delta_1 - \Delta_{F1})}{h_2 - h_1} h_2 \qquad (3.2)$$

3. The sliding components are determined by the help of Eq. (3.3).

$$\Delta_{sl} = \Delta_2 - \Delta_{F2} - \Delta_{\gamma} \qquad (3.3)$$

The averaged displacement components are shown in Fig. 3.19 for the available data. Note that not all displacements are recorded up to failure because of removal of displacement transducers due to concrete spalling. For all specimens, 70% of the deflection are due to flexure and 30% are due to sliding and distortion. The contribution of sliding component increases with both ductility and drift.

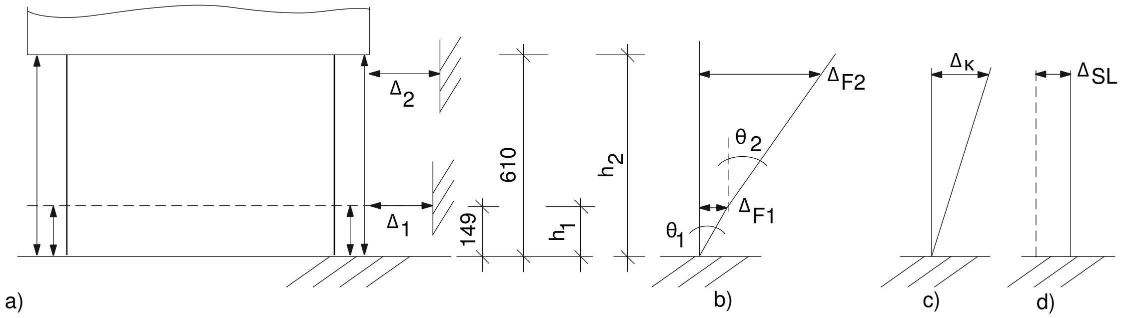

Fig. 3.17: Estimation of deflection quantities. a)Position of displacement transducers, b) flexural displacement, c) distortion, d) sliding.

For specimen M3, the portion due to flexure increases up to 80% until displacement ductility equal to 2.0 is attained and then it decreases. For specimen M4, flexural portion decreases to 70% at displacement ducility 5.0. Sliding portions generally increase as ductility and drift increases. However, the results of this analysis agree fairly with data shown in Fig. 3.18 because the data recording of horizontal and vertical transducers along the boundary of the panel is more sensitive to the crack pattern than the data recorded on the head beam.

In case of slender, ductile walls, deflection due to both distortion and sliding can represent up to 30% of the deformation inside the plastic hinge (Dazio 2000). Nevertheless, these diplacement components constitued only 10 to 14 % of the top lateral displacement because of rigid body motions of the upper part of the walls. Hence, deformation of cantilever squat walls is similar to the deformation inside the plastic hinge of slender walls.

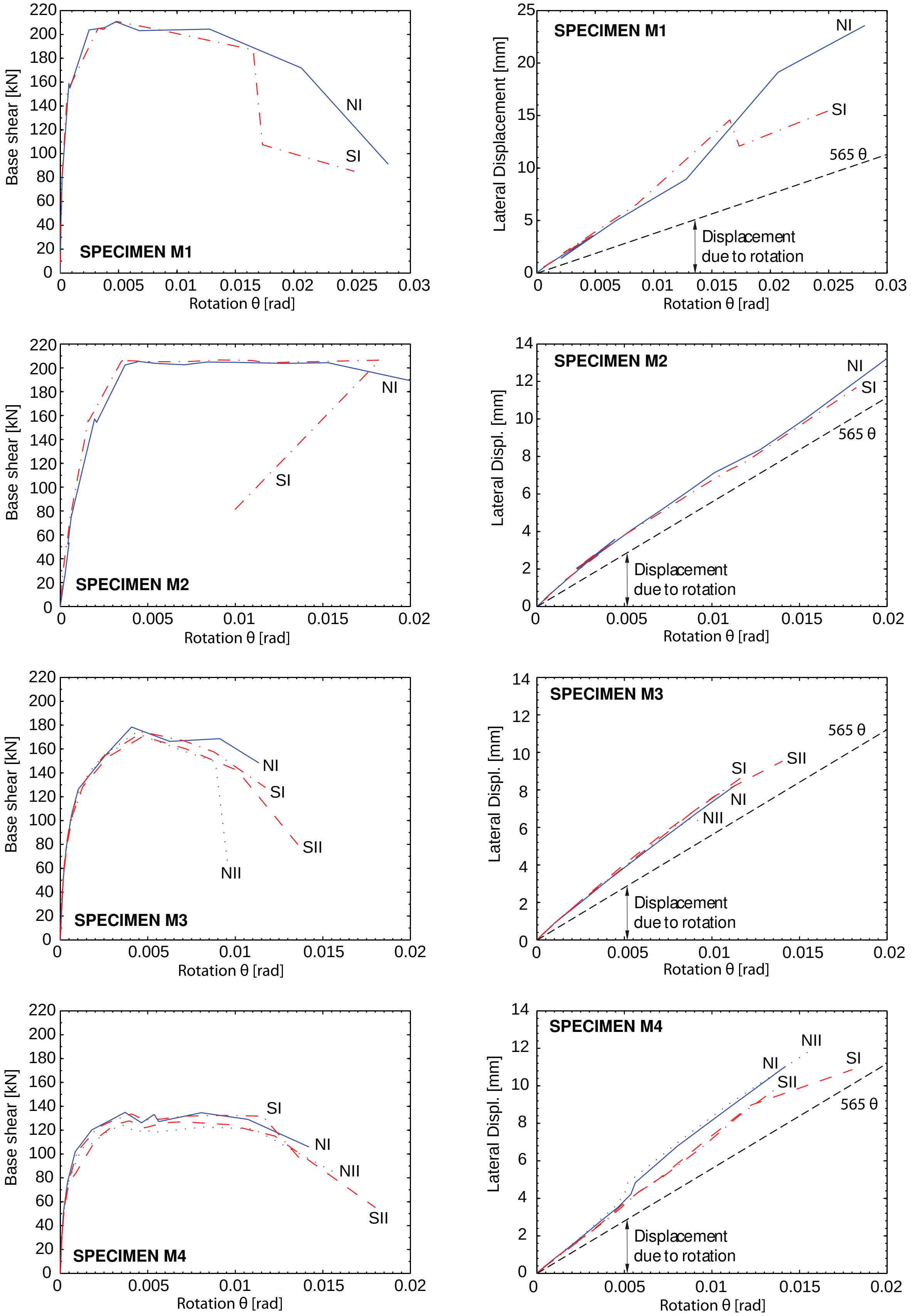

Fig. 3.18: Rotations of head beam.

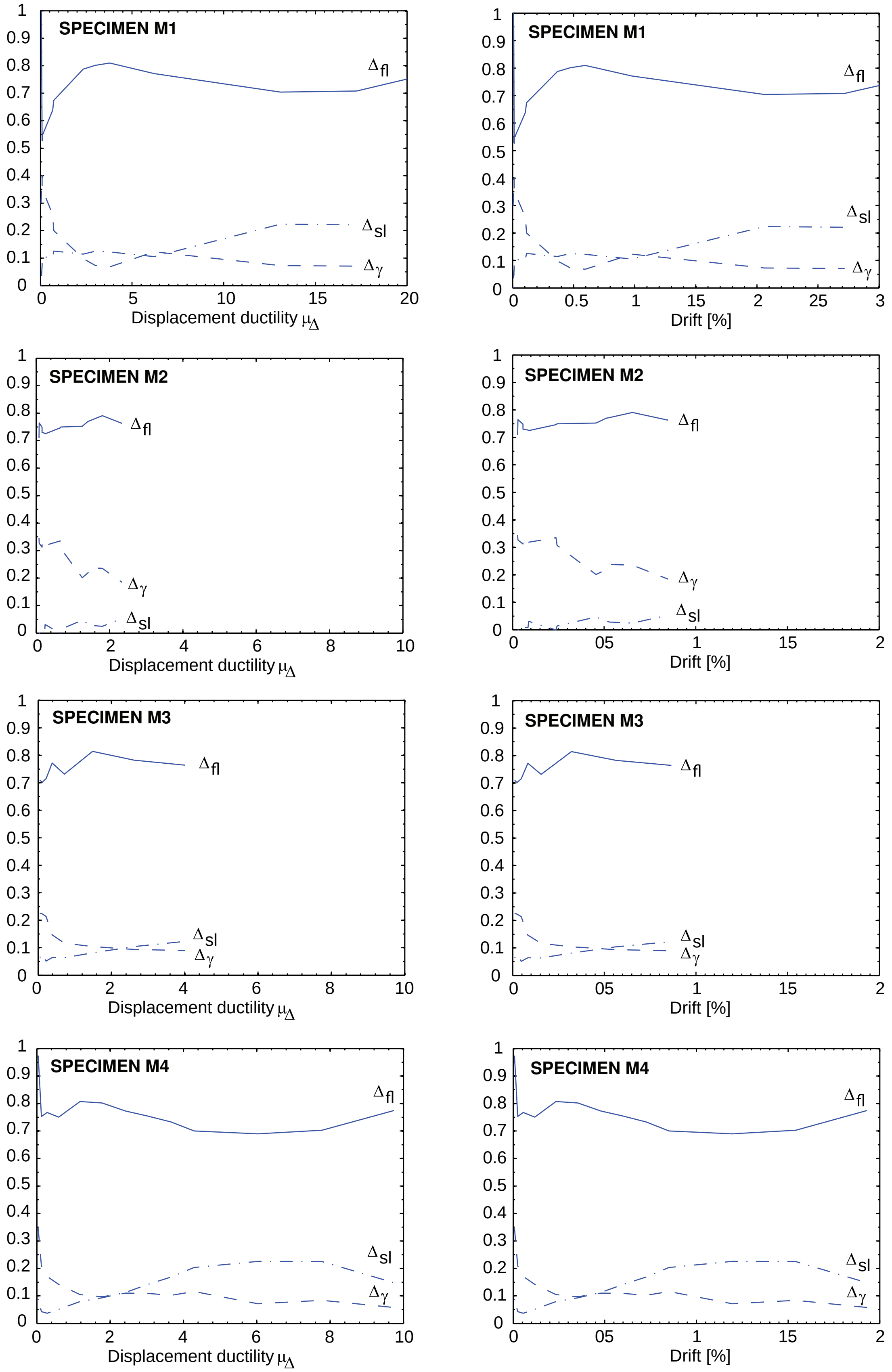

Fig. 3.19: Deflection quantities normalized to lateral displacement.

3.3.4 Principal strains

Strains are measured on the concrete surface by means of deformeter and targets. The principal strain patterns derived from these data only partly allowed to identify deformation fields that are commonly used for compression field approaches. This is due to small straining of the concrete which remained uncracked during some tests.

3.4 Analysis of test results

3.4.1 Effective stiffness

The decay of stiffness with increasing displacement is an important concern in the seismic assessment of RC structures. Since stiffness and mass repartition influence the level of base shear, more realistic approaches for stiffness can result in reduction of the base shear for which the structure has to be verified. In this section, the decay in secant stiffness is investigated at several levels of ductility and drift.

The model shown in Fig. 3.20a provides estimates for linear-elastic stiffness of the specimens. It includes both the head beam and the panel. Plane stress state is assumed. The difference in thickness of head beam and panel is considered in the elastic modulus.

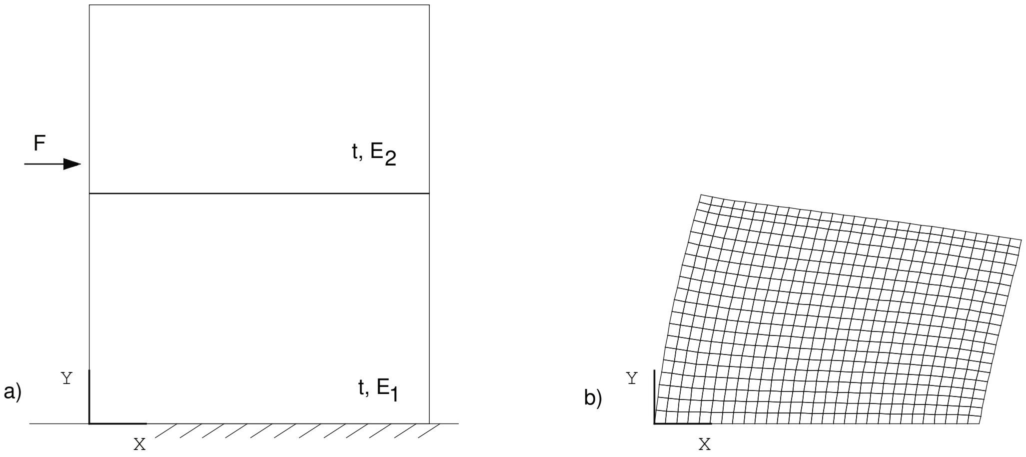

Fig. 3.20: Calculation of elastic stiffness. a) Model, b) Deformed shape of panel.

The deformed shape of the panel indicates the restraining that is provided to the panel by the head beam (Fig. 3.20b). Accounting for both, the restraining of the panel by the head beam and the shear distortion due to the low aspect ratio of the panel, finite element analysis provides realistic estimates of elastic stiffness. By contrast, Eq. (3.4) describes the stiffness of a cantilever undergoing flexural deformation.

$$K_{flex} = \frac{3EI}{l^3} \tag{3.4}$$

The results of the finite element analysis and stiffness estimation according to Eq. (3.4) are shown in Tab. 3.7. The symbol K_{FEM} refers to the elastic stiffness that is computed by means of the finite element model. It is found that shear deformation reduces elastic stiffness by more than

60 %. Compared to specimens M1/M2, less stiffness reduction is found for specimens M3/M4 because of the higher aspect ratio. The results indicate that elastic deflection is theoretically composed of nearly 60 % distortion and 40 % deflection due to flexure. Elastic analysis thus predicts a displacement response governed by shear distortion, which is not confirmed by the test results. The analysis of test data (Fig. 3.18, Fig. 3.19) has shown that flexure is the major contributor to the lateral displacement.

Specimen	K_{FEM}	I	E	l	K_{flex}	K_{FEM}/K_{flex}
	$[kN/mm]$	$[10^{-3}m^4]$	$[MN/m^2]$	$[m]$	$[kN/mm]$	$[-]$
M1/M2	1242	8.33	34000	0.61	3743	0.33
M3/M4	844	4.86	34000	0.61	2184	0.39

Tab. 3.7: Reduction of elastic stiffness due to elastic shear deformation.

The aforementioned elastic stiffness K_{FEM} is now compared with secant stiffness computed from the test data. The secant stiffness is defined as the maximum force divided by the maximum displacement. The stiffness ratio refers to the ratio of secant stiffness to the elastic stiffness.

The decay of stiffness ratio with increase in displacement ductility is shown for elastic and plastic response in Fig. 3.21a and Fig. 3.21b, respectively.

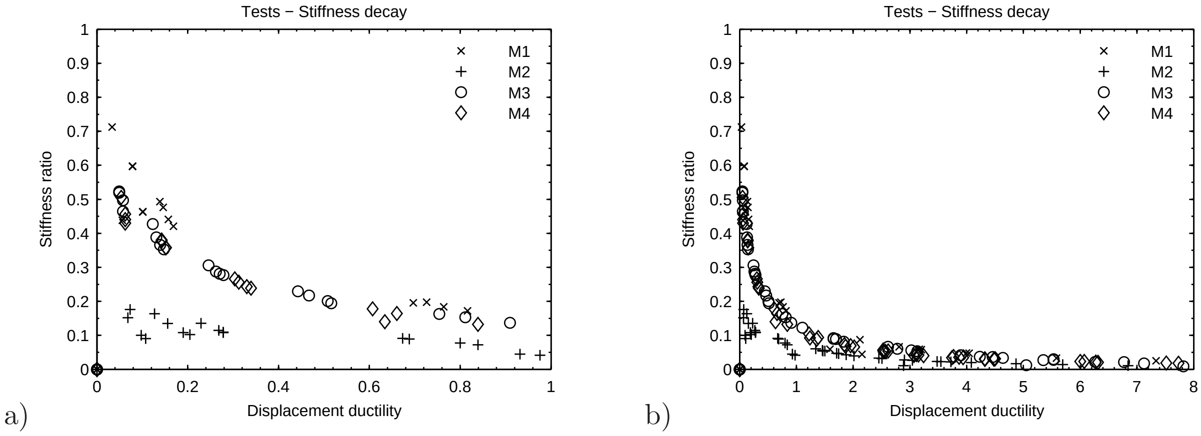

Fig. 3.21: Stiffness ratio vs. displacement ductility, a) elastic response, b) plastic response.

Elastic response is supposed if the displacement ductility is less than 1.0. In this range of ductilities the stiffness ratio decreases to 0.15. The data for specimen M1, M3, and M4 follow the same graph. So, the relationships between displacement ductility and stiffness ratio for these specimens are similar. The stiffness ratios of specimen M2 are generally smaller than that of the other specimens because of residual deformations that are observed at begin of the test (Sec. 3.3.1, p. 60). Such residual deformations indicate degradation of aggregate interlock causing reduction of stiffness.

The maximum stiffness ratio of 0.70 is observed for specimen M1 at the begin of the test. The stiffness ratio of specimens M3 and M4 is equal to 0.50 at the begin of the test. That means small lateral displacements corresponding to fractions of yield displacement result in significant reduction of elastic stiffness. Further reduction of stiffness is observed with increasing ductility (Fig. 3.21b). So, stiffness ratios of 0.1 and 0.05 are computed at displacement ductilities of

2.0 and 5.0, respectively. Similar drops in stiffness are reported by Lestuzzi (2000) for slender ductile walls and Ile (2000) for squat walls.

Bachmann (2004) proposed a formula for evaluation of stiffness at first yield (Sec. 2.8.1, p. 50). Assuming that:

1. Internal lever arm of reinforcement is equal to 0.60,
2. The portion wall length within which the rebars yield is equal to 0.70,
3. The internal lever arm of concrete compressive force yields 0.40 (M3) and 0.45 (M1), and
4. The ratio of yield strength to concrete compressive strength is equal to 12 (M1) and 25 (M3),

Then, Eq. (2.96) simplifies to the following:

$$\begin{aligned} Specimen\,M1:\ \alpha_K &= 15\rho_v + 1.35n = 0.09 && (3.5) \\ Specimen\,M3:\ \alpha_K &= 15\rho_v + 0.56n = 0.10 && (3.6) \end{aligned}$$

Note that the stiffness ratios estimated by Eq. (3.5) and Eq. (3.6) correspond to the reduction of flexural stiffness while the results shown in Fig. 3.21a refer to the elastic stiffness, which includes shear deformation.

Comparison with experimental results thus requires normalization to the elastic stiffness. Dividing the stiffness ratios according to Eq. (3.5) and Eq. (3.6) by the ratio K_{FEM}/K_{flex} (Tab. 3.7) provides this normalization. Reduction of elastic stiffness to 0.27 and 0.26 times the elastic stiffness is calculated for specimens M1 and M3, respectively. These values well agree with the test data for displacement ductilities of 0.75 that are plotted in Fig. 3.21a. As it is shown in Tab. 3.3 first yield occurs at displacement ductility of approximately 0.75.

The decay of stiffness ratio with increase in drift is shown in Fig. 3.22. Again, the data points for specimens M1, M3, and M4 follow the same graph. The stiffness ratios for specimen M2 are initially less than that for the other specimens but similar stiffness ratios are observed for drifts greater than 0.4 %. Drift limits of 0.5 % are usually admitted in seismic evaluation in order to limit damage of the non-structural elements. As it is shown in Fig. 3.22a, the stiffness ratio is less than 0.10 in this range of drifts.

Conclusions

To conclude, it is shown that the stiffness of reinforced concrete shear walls drops significantly even in case of displacement ductilities less than 1.0. This reduction is found to be insensitive to axial force ratio and concrete compression strength. Predictions based on the curvature at first yield provide an upper limit to the effective stiffness. In addition, the analysis indicates that stiffness reduction is an inherent property of reinforced concrete walls that depends not on reinforcement detailing.

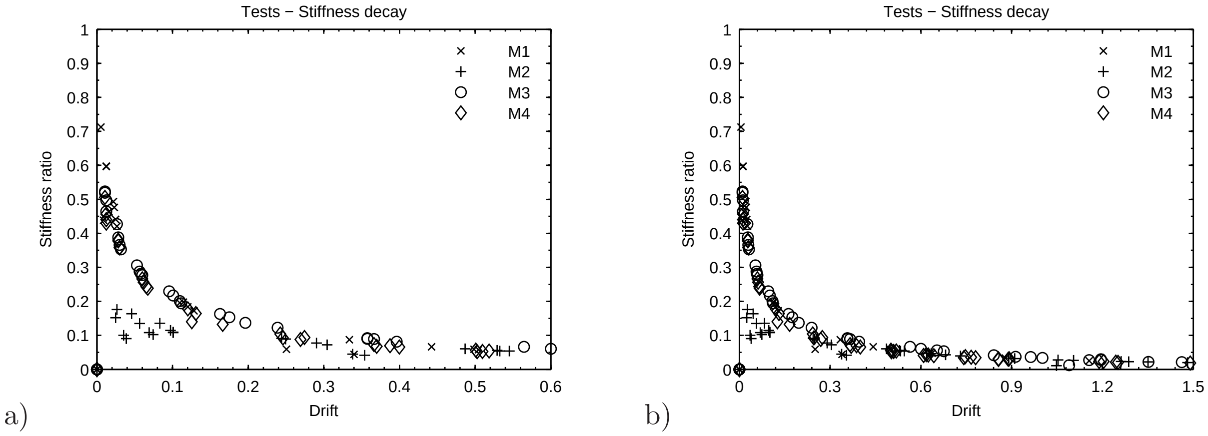

Fig. 3.22: Secant stiffness ratio vs. drift, a) drifts less than 0.6%, b) drifts up to 1.5%.

3.4.2 Energy dissipation and equivalent damping

Energy dissipation

Structural elements of non-ductile design are commonly thought to provide less capacity to dissipate energy than structural elements of ductile design. In this section, the energy dissipation of the test units is compared with that observed by Dazio (2000) during tests of ductile shear walls. The dissipated energy is equal to the area that is enclosed by the hysteretic loops. It is shown for each load step in Fig. 3.23a. The dissipated energy per load steps increases monotonically for both specimens M1 and M2 of which the loading is force controlled. For specimens M3 and M4, the energy dissipation in second cycles is smaller than that in first cycles. Note that the loading of these specimens is displacement controlled.

The cumulative energy dissipation is shown in Fig. 3.23b. Maximum energy dissipation is observed for specimen M1, while the plot for specimen M3 displays the minimum energy dissipation. Nevertheless, energy dissipation is closely linked to the applied loading. Since loading histories of the specimens are different from each other, relationships between test parameters and the dissipated energy are difficult to identify. A more suitable mean to compare energy dissipation is the energy ratio that denotes the ratio of the dissipated energy to the introduced energy. The latter corresponds to the area below the graph of force-deflection relationship. So, the introduced energy is calculated for each half-cycle.

The energy ratio is plotted against displacement ductility and drift in Fig. 3.24a and 3.24b, respectively. For all specimens, the energy ratio monotonically increases beginning from ductility of 1.0 up to the failure of the specimen. In addition, the curves for specimen M3 and M4 are nearly identical. Thus, the energy ratio is insensitive to the axial force ratio. Energy ratios at maximum ductilities are shown in Tab. 3.8. Maximum ductilities are determined in Sec. 3.3.2 (p. 66). All specimens dissipated approximately 70 % of the introduced energy.

Specimen	M1	M2	M3	M4
μ_Δ	5.6	5.9	5.7	8.0
α_E	0.70	0.78	0.67	0.70

Tab. 3.8: Energy ratios at selected displacement ductilities.

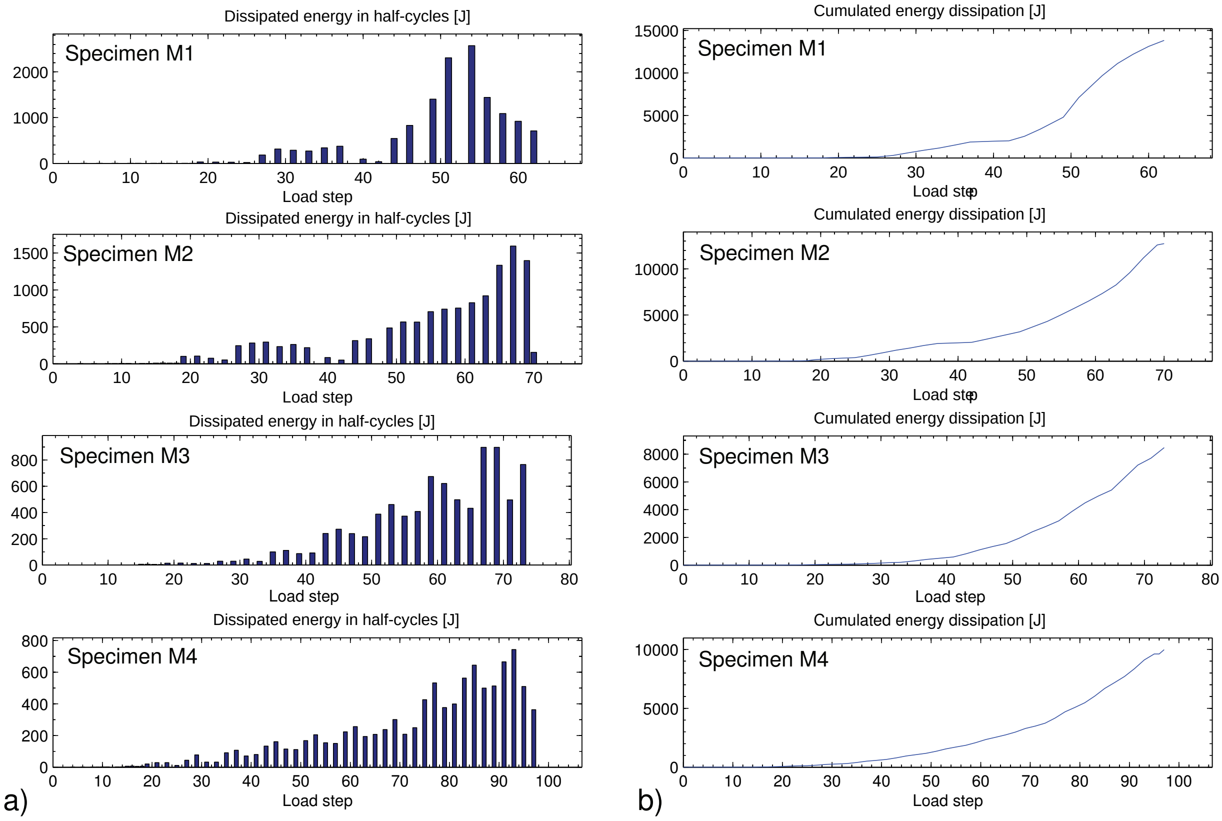

Fig. 3.23: Energy dissipation of specimens, a) dissipated energy in half-cycles, b) cumulated energy dissipation.

Similar findings on energy ratio were made by other researchers. Dazio (2000) found energy ratios of approximately 0.60 for slender, ductile walls subjected to static-cyclic loading and displacement ductilities up to 6.0. Numerical simulations investigating the influence of axial force on the behavior of such walls provided energy ratios between 0.45 and 0.80 for axial force ratios between 0.13 and 0.035, respectively. The decrease in energy dissipation with increase in axial force is assumed to originate from both pinching of hysteretic loops and reduction of residual displacements. Lestuzzi (2000) examined records of dynamic tests of slender, ductile walls for energy dissipation. It is observed that the energy ratio is insensitive to the flexural strength of the walls. Energy ratios were between 0.60 and 0.70.

The aforementioned analysis of test data indicate that shear walls of low to moderate axial force ratio can dissipate between 60 and 70% of the introduced energy regardless of detailing of reinforcement. However, the mechanisms providing this energy dissipation are substantially different. Energy dissipation in squat walls is due to sliding and degradation of concrete while the plastic straining of rebars adds dissipation capacity to slender walls of ductile detailing. In addition, the pinching due to increase of axial force leads to flag-shape hysteresis loops and consequently to decrease in energy dissipation. Pinching of hysteretic loops can also originate from sliding movement at load reversal. In this case, pinching increases energy dissipation because of increase of residual displacements. Energy dissipation is not an appropriate mean to identify non-ductile configurations since the energy ratio determined from data of static cyclic tests is insensitive to it. Nevertheless, the calculations presented before have shown that sliding can provide energy dissipation. But it is not ensured that the sliding mechanism will occur in

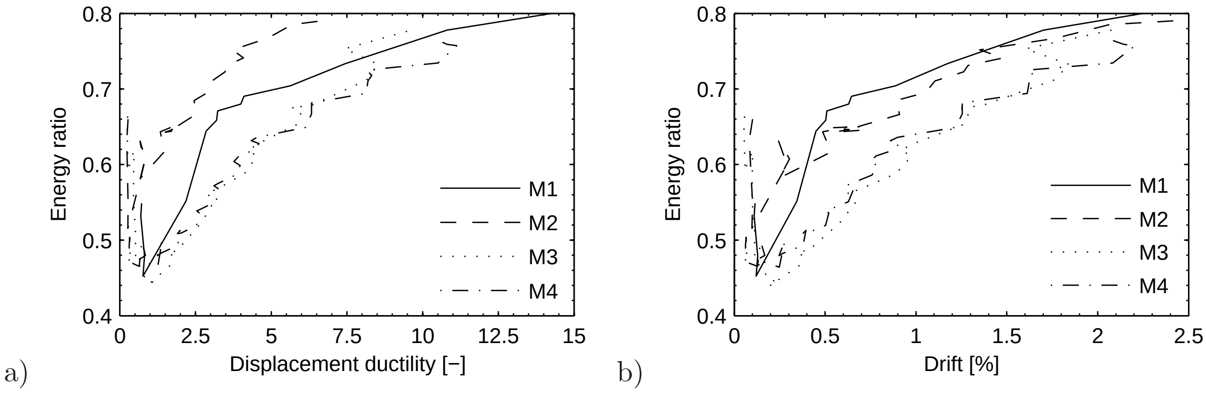

Fig. 3.24: Energy ratios, a) energy ratio vs. displacement ductility, b) energy ratio vs. drift.

case of dynamic loading. It is also shown, that this mechanism can compensate the reduce in energy dissipation due to non-ductile design.

Energy dissipation due to geometrically nonlinear behavior was observed in dynamic tests (Coin et al. 2002). Such energy dissipation can be neglected for the tested specimens because the lateral displacements are too small and there are no inertia forces in a static-cyclic test. In addition, the post-tensioning system applying the axial force on the specimens was designed to have a linear-elastic behavior throughout the test series.

Equivalent damping

Equivalent damping is a mean to introduce the energy dissipation in a dynamic calculation. The equivalent damping ratio is defined as follows (Eq. (3.7)):

$$\xi_{eq} = \frac{A_d}{4\pi A_i} \tag{3.7}$$

Figure 3.25a illustrates the definition of the symbols A_d and A_i that are used in Eq. (3.7). The symbol A_d denotes the dissipated energy per cycle and the symbol A_i the elastic energy. Application of Eq. (3.7) on the aforementioned tests is shown in Fig. 3.25b. For displacement ductilities greater than 2.0 the test data follow the graph that was proposed by Priestley (2000). Hence, this proposal can be also applied on dynamic calculations of lightly reinforced shear walls.

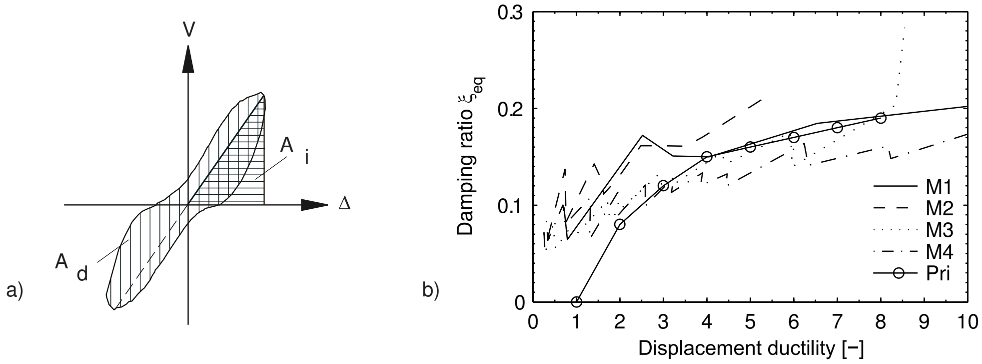

Fig. 3.25: Equivalent damping ratio. a) Definition of A_d and A_i, b) Equivalent damping ratio vs. displacement ductility (Pri - Priestley (2000)).

3.4.3 Recalculation of shear strength

The portion of shear strength exceeding the contribution of horizontal reinforcement can originate from both inherent shear capacity of concrete and direct concrete strut (Sec. 2.6). In this section, the observed shear strength is compared with both the shear capacity provided by direct concrete strut plus horizontal reinforcement and the shear capacity due to inherent concrete shear strength plus horizontal reinforcement.

Direct concrete strut

The shear strength due to contribution of both direct concrete strut and horizontal reinforcement is calculated according to Eq. (3.8).

$$V_R = Ntan(\alpha) + V_s \tag{3.8}$$

The calculation of shear strength uses the maximum observed normal force (Tab. 3.9). The direct concrete strut is assumed to coincide with the line of trust. For simplicity, the latter is modeled by a straight line of inclination α that links the centers of compression at the upper and lower boundary of the panel. While the eccentricity of the resultant at the upper boundary refers to the ratio of bending moment to normal force, curvature analysis provides the position of the concrete compression force at the base of the wall. The direct strut is illustrated in Fig. 3.9a. The portion of effective reinforcement depends on the shear lag, which is determined by both the internal lever arm and the inclination of the strut. The definition of the internal lever arm z is shown in Fig. 3.9a whereas the force flow due to transverse reinforcement contribution is illustrated in Fig. 3.9b.

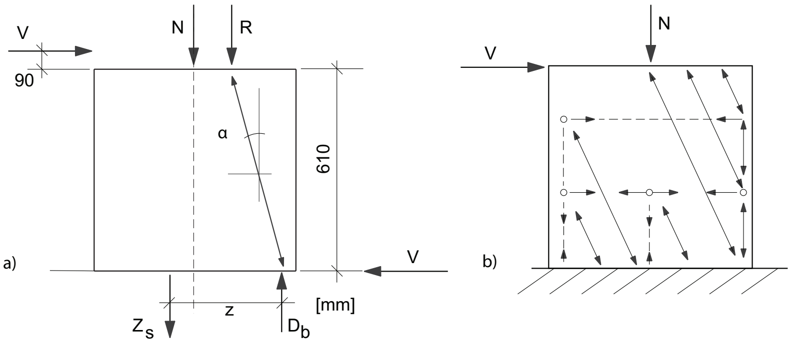

Fig. 3.26: Shear strength of specimens M1-M4: a) geometry of direct concrete strut, b) Strut and tie model.

Since the calculated shear lag of all specimens is greater than the height of the panel, the total horizontal reinforcement is accounted for the shear strength. Yield strength of horizontal reinforcement is as follows:

- M1/M2: $V_s = 8 \cdot 14.3 = 112kN$
- M3/M4: $V_s = 10 \cdot 9.37 = 93.7kN$

The ratios of calculated to observed shear strength are shown in Tab. 3.9. Note that the observed shear strength represents a lower bound because brittle shear failure is not observed in the tests. This lower bound agrees well with the calculated shear strength in case of specimens

M1, M3 and M4. The calculation underestimates shear strength by 4 to 9%. Nevertheless, only 37% of shear strength of specimen M2 can be explained by assuming direct strut plus transverse reinforcement. Hence, other mechanisms that are not included in this calculation also contribute to shear strength.

Specimen	N $[m]$	α $[°]$	$\tan\alpha$ $[-]$	z $[m]$	$z\ \cot\alpha$ $[m]$	$N\ \tan\alpha$ $[kN]$	V_s $[kN]$	V_R $[kN]$	V_{exp} $[kN]$	V_R/V_{exp} $[-]$
M1	137	28	0.53	0.56	1.06	73	112	185	203	0.91
M2	141	28	0.53	0.56	1.06	75	0	75	204	0.37
M3	141	25	0.47	0.55	1.17	66	94	160	176	0.91
M4	83	23	0.42	0.52	1.22	35	94	129	135	0.96

Tab. 3.9: Shear strength due to direct strut and horizontal reinforcement.

Efficiency of horizontal reinforcement

Another method to assess the shear strength is to account for inherent shear strength of concrete. Equation (3.9) describes the shear strength in this case.

$$V_R = V_c + V_s \tag{3.9}$$

Minor cracking of the panel is observed for both specimen M1 and M2 (Fig. 3.7). That means the concrete shear strength is not exceeded during the tests of these specimens and shear ratio corresponding to the maximum base shear represents a lower bound of the concrete shear strength. This lower bound is now used to assess efficiency of transverse reinforcement of the specimens M3 and M4. The stiffness of the concrete contribution is supposed to be significantly greater than the stiffness of the reinforcement contribution. So, reinforcement is activated if the shear demand exceeds the strength provided by the concrete contribution. Results of the calculation are shown in Tab. 3.10.

Assuming inherent shear strength of concrete as contributor to shear strength, the observed shear strength can be explained for all specimens. In addition to the concrete contribution 40% and 90% of horizontal reinforcement are necessary to meet the observed shear strength of specimens M4 and M3, respectively. These results correlate well with the observed crack pattern of the specimens. The upper half of specimen M4 remained uncracked while cracking extended over the whole panel of specimen M3.

Specimen	n $[-]$	V $[kN]$	f'c $[MPa]$	$0.28\sqrt{f_c}$ $[MPa]$	V_c $[kN]$	$V_{s,R}$ $[kN]$	$V_{s,exp}$ $[kN]$	$V_{s,exp}/V_{s,R}$ $[-]$
M1	0.03	204	51	2.00	200	112	0.00	0.00
M2	0.03	203	51	2.00	200	112	0.00	0.00
M3	0.10	176	20	1.25	90.2	94	85.8	0.91
M4	0.05	135	24	1.37	98.8	94	36.2	0.39

Tab. 3.10: Efficiency of horizontal reinforcement.

3.5 Conclusions

The chapter presents a series of static cyclic tests of lightly reinforced shear walls that are not designed for earthquake actions. The four specimens model the bottom part of a real shear wall in 1:3 scale. They are tested as cantilevers subjected to both constant axial force and static cyclic lateral loading. The reinforcement consists of uniformly distributed rebars that lead to reinforcement ratios of 0.003. The objective of the test series is to investigate the shear dominated behavior of lightly reinforced concrete shear walls.

It is shown that non-ductile, lightly reinforced walls can attain drifts between 0.8 and 2.1% by developing shear capacities of 1.4 up to 2.0 MPa. This depends on both concrete compressive strength and axial force ratio. Preliminary brittle shear failure is not observed. The strength is governed by flexural strength while the deformation capacity is restricted by sliding and concrete crushing. Low to moderate ductile behavior ($5.6 < \mu_\Delta < 8.0$) is observed for all specimens (Tab. 3.11). It is not recommended to equate these ductilities directly to behavior factors.

The test results fail to confirm the beneficial effect that horizontal reinforcement is widely believed to have on deformation capacity. The horizontal reinforcement caused concentrated deformation and hence, it resulted in increase of damage. In addition, small vertical reinforcement ratios and moderate axial force ratios restrict the flexural capacity. The restricted flexural capacity can prevent shear modes of failure. In addition, the observed shear strength originates partly from inherent shear strength of concrete. Since this contributor to shear strength is not included in truss models, such models underestimate significantly the shear strength.

The shear ratio governs the failure modes of the test units. Shear ratio is defined as the shear stress divided by the square root of compressive concrete strength. Increase in shear stress ratio causes both widespread crack pattern and weakening of concrete. The latter results in reduction of deformation capacity whereas a more widespread crack pattern is beneficial for static-cyclic behavior. These opposite tendencies are well reflected by the test series.

The plastic deflection of the specimens is composed of flexure (70%) and shear portions (30%). However, it was predicted that the elastic deflection is governed by shear. In addition, curvature-based reduction of stiffness can well predict the effective stiffness at first yield.

Depending on the configuration of the test unit, up to 70% of the introduced energy are dissipated. Thus, it is found that lightly reinforced walls can have similar energy dissipation capacity as walls of ductile design. Principal contributor to energy dissipation is sliding in cracks.

Dowel action of rebars contributing to sliding shear strength is not observed. For lightly reinforced walls, the stiffness of the mechanism providing dowel action is significantly less than the stiffness of other contributors to shear capacity.

Specimen	n	τ^a_{max}	$\tau_{max}/\sqrt{f'_c}$	τ_u	φ^b_{max}	φ_u	Δ_y	μ_Δ
	[%]	$[MPa]$	[−]	$[MPa]$	[%]	[%]	$[mm]$	[−]
M1	2.2	2.04	0.28	1.40	0.33	0.88	0.89	5.6
M2	2.2	2.03	0.28	1.56	0.51	2.15	2.05	5.9
M3	9.5	2.44	0.52	1.86	0.57	1.25	1.22	5.8
M4	5.0	1.88	0.38	1.40	0.50	1.59	1.12	8.0

[a] Stresses refer to concrete gross-section., [b] Drifts refer to LVDT-position: $\varphi = 0.565/\Delta$ $[mm]$

Tab. 3.11: Summary of specimen performance.

Chapter 4

Analytical model for deformation capacity

4.1 Overview

In this section the formulation of the rotation-based model is presented. The modeling aims at deriving a rationale for the shear strength envelope of squat walls subjected to static-cyclic loading. Therefore, relationships between base shear and rotation are established. The chapter thus addresses the following:

- Formulation of the model
- Proposal for shear strength envelope

As it is observed in static-cyclic tests, deformation due to flexure represents a portion of 70% of lateral deflection and only 10% of lateral deflection originate from distortion (Sec. 3.3.3). Another contributor to deflection is sliding. The dynamic response of sliding mechanism is thought to be substantially different from static-cyclic response. Sliding probably not produces under dynamic loading (Sec. 2.3.5, p. 11). Hence, sliding mechanisms and distortion mechanisms are not included in the analytical model in order to propose a lower bound for deformation capacity under seismic loading.

4.1.1 Use of shear crack model

The squat shear wall is modeled as a plastic hinge consisting of discrete cracks and rigid bodies (Fig. 4.1a). The cracks are inclined relative to the member axis. Opening of the cracks results in rotation which is assumed to be constant over the length of the plastic hinge.

This concept, denominated shear crack hinge, was originally proposed by Bachmann (1967) for modeling plastic hinges in support zones of continuous RC beams. Contrary to flexural hinges in spans, inclined cracks form in such zones because of both bending and shear. A short review of this model is provided in Sec. 2.5 (p. 22). To use this model for shear walls, it is re-formulated herein to account for the following:

- Axial force,
- Uniformly distributed vertical reinforcement,

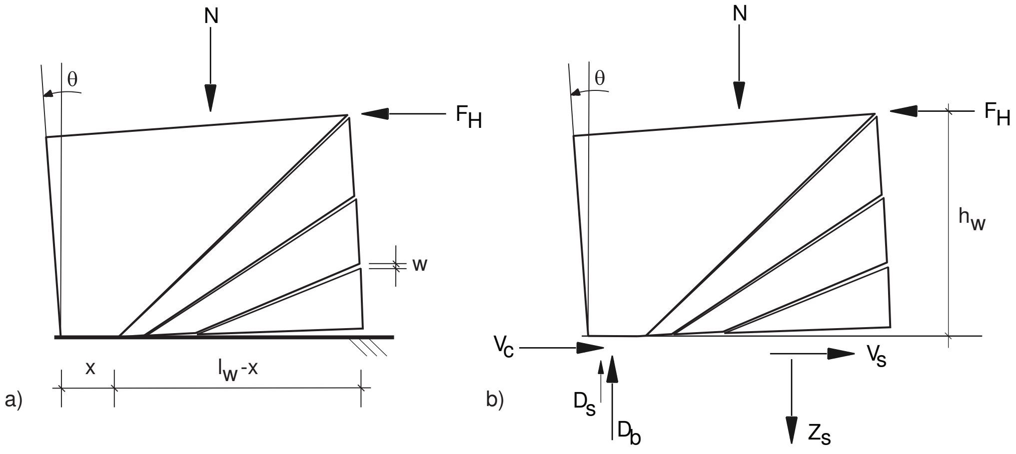

Fig. 4.1: Wall with discrete crack modeling, a) model geometry, b) reaction forces in the base joint.

- Crack pattern observed in static cyclic tests (Fig. 3.7).
- Localization of concrete compressive strains near the base.

The formulation of the discrete crack model for walls is based on assumptions for crack pattern, strain localization of concrete and failure mode. The assumptions are:

1. Concrete compressive strains localize near the base of wall.
2. The crack pattern that forms is similar to the discrete crack pattern shown in Fig. 4.1 .
3. Failure originates either from the rupture of rebars, either from the crushing of concrete or from sliding shear mode.

The validity of these assumptions is checked during the modeling process. The loads and reactions included in the model are illustrated in Fig. 4.1b. Flexure applied by the base shear (F_H) and lever arm (h_w) is equilibrated by the compression forces, of both concrete (D_b) and rebars (D_s), and the tensile force of rebars (Z_s). It is also equilibrated by the axial force (N). The base shear is transmitted by concrete contribution (V_c) and aggregate interlock action in the tensioned part of base joint (V_s).
The utilization of a model which was originally proposed for beams (Sec. 2.5, p. 22) for lightly reinforced shear walls necessitates some modifications. The model is modified by introducing the following characteristics:

- Pivot point for non-parallel struts in distance of x below the base joint (Sec. 4.2.2, p. 87).
- Aggregate interlock forces acting on the base joint (Sec. 4.3.1, p. 90).
- Relationship between crack width of base joint and sum of crack widths (Sec. 4.4.1) .
- Plastic localization of compressive strains near to the base (Sec. 4.4.2).
- Direct concrete strut excluding inclined cracks in concrete compression zone (Sec. 4.5.4, p. 110).

The aforementioned modifications enable the utilization of shear crack hinge for computation of static-cyclic envelope curve. Further information is provided in the related sections.

4.1.2 Section deformation

In the proposed model, the concrete deformation in compression localizes near the base while the rebar deformation in tension is distributed over the entire wall height. So, strictly speaking, the assumption of plane sections is not valid inside the plastic hinge. The inclined cracks stagger the tensile forces relative to the compressive forces. This phenomenon is commonly denoted as shear lag and is investigated in Sec. 4.3.2. The rebar strains also tend to localize near the base. This depends on both crack pattern and bond properties.

However, it is observed from the analysis of test results (Sec. 3) that the gradient of the observed static-cyclic envelopes decreases at the predicted yield base shear (Fig. 3.12 and Fig. 3.13). The yield base shear was computed by using Bernoulli's assumption of plane sections. It indicates that this assumption is valid in the pre-yield response. So, it is assumed that section deformation occurs after the onset of yielding of the vertical rebars. Thus, the static-cyclic envelope is subdivided into two stages:

1. Pre-yield, and

2. Post-yield.

This subdivision is illustrated in Fig. 4.2. The assumption of plane sections is supposed to be valid in the pre-yield response while non-planar sections are allowed after the first yield of rebars. Since the relationship between the curvatures in the compressed and tensioned part of the cross-section are too difficult to estimate, they are not analyzed in detail. Strains and deformations at the outermost fibers are used to identify limit states.

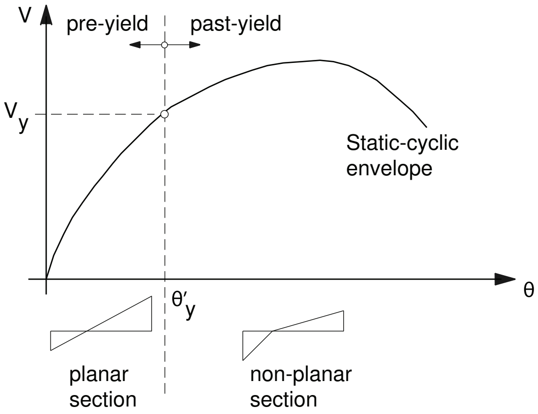

Fig. 4.2: Subdivision of response into pre-yield and post-yield stage.

Linear strain distribution is assumed in both the compressed and the tensioned part of the cross section (Fig. 4.3). Physical reasons for the different curvatures in this two parts are:

- Redistribution of tensile forces due to yielding of outermost rebars.
- Formation of inclined cracks during loading process due to shear-flexure interaction.
- Softening of concrete because of bond effects and subsequent load reversal (Sec. 4.4.2, p. 102).

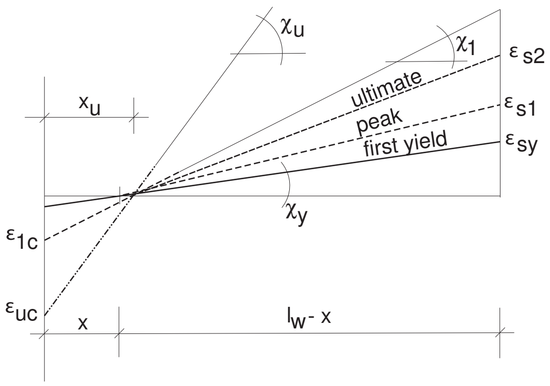

Fig. 4.3: Evolution of strains with increasing displacement.

Tests have shown that the neutral axis depth slightly increases from x up to x_u during the loading process (Fig. 4.3). However, the neutral axis depth is assumed to be constant during the loading process.

To conclude, the aforementioned phenomena make the evaluation of curvature nearly impossible. The introduction of section deformation offers the advantage of explicit calculation of overall rotation. Such calculation can be based either on the deformation of the tensioned fiber or on the deformation of compressed fiber. This is valid according to plastic theory, when equilibrium condition is fulfilled.

4.1.3 Failure modes included in the model

The model provides insight into the following failure modes:

- Concrete crushing,
- Reinforcement rupture,
- Sliding.

In this context, concrete crushing includes the failure mode of diagonal tension. Consider contribution of the concrete compression zone to shear strength. This contribution provokes transversal straining in the concrete that decreases the compressive strength. Hence, concrete crushing and diagonal tension are only different in the level of softening. Detailed information about concrete crushing is provided in Sec. 4.3.3 and Sec. 4.5.4.

Reinforcement rupture refers to tensile failure of vertical rebars near the base. Estimates of the crack width corresponding to this failure are made with the help of the bond model described by Maekawa et al. (2003). This model is shortly reviewed in Sec. 2.4.4 (p. 20). Reinforcement rupture is investigated in Sec. 4.4.1 and Sec. 5.4.1. Rupture of horizontal rebars is not investigated because of its irrelevance to the examined walls.

Degradation of aggregate interlock is analyzed in the context of shear strength decay restricting the deformation capacity. It is assumed that the efficiency of aggregate interlock decreases as the crack width near the base increases. For further details refer to Sec. 4.5.5.

4.2 Formulation

4.2.1 Motivation

The motivation to develop a rotation-based model arise from the following:

- 70% of plastic deformation capacity in static cyclic tests due to rotation of head beam (Fig. 3.18).
- Sliding was not observed in dynamic tests (Sec. 2.3.5) and hence, it is not included in the model.
- Importance of accumulated local damage for global behavior (Fig. 3.10).
- Underestimation of deformation capacity by lumped plasticity model.

The lumped plasticity model (Sec. 2.8.3) is an efficient method to estimate the deflection of columns and ductile slender walls. However, it is found that this model significantly underestimates the performance of specimens described in Sec. 3.3.

Curvature is a local quantity that describes the strain state of a plane section. Curvature analysis provides relationships between flexural moment and strains. Advantages include easy to use kinematics allowing computation of flexural strength without restrictions of material law. Disadvantages and difficulties reside in the local characteristics of curvature. Appropriate integration limits have to be considered in order to determine both rotations and displacements.

For lightly reinforced walls, experimental evidence proves that flexural response is accurately predicted by a curvature analysis including the following:

- First yield
- Maximum base shear
- Failure mode (Concrete crushing, rebar failure)

The results of curvature analysis of specimens M1, M2, M3, and M4 are shown in Fig. 4.4. These results provide the input for the calculation of chord rotations, which are later used to bilinear relationships between base shear and tip displacement (p. 51). Both ultimate rotations and displacements are shown in Tab. 4.1. Although the test results indicate a flexural dominated response (p. 69) the method according Priestley & Park (1987) underestimates deformation capacity by 52 to 75 %.

Possible reasons for the underestimation of deformation capacity are the following:

- Localized deformation near the base.
- Underestimation of length of plastic hinge in the model.
- Degradation of bond between reinforcement and concrete with increased deflection.

Thus, further investigation into the deformation capacity of walls is necessary in order to enhance the prediction of deflection.

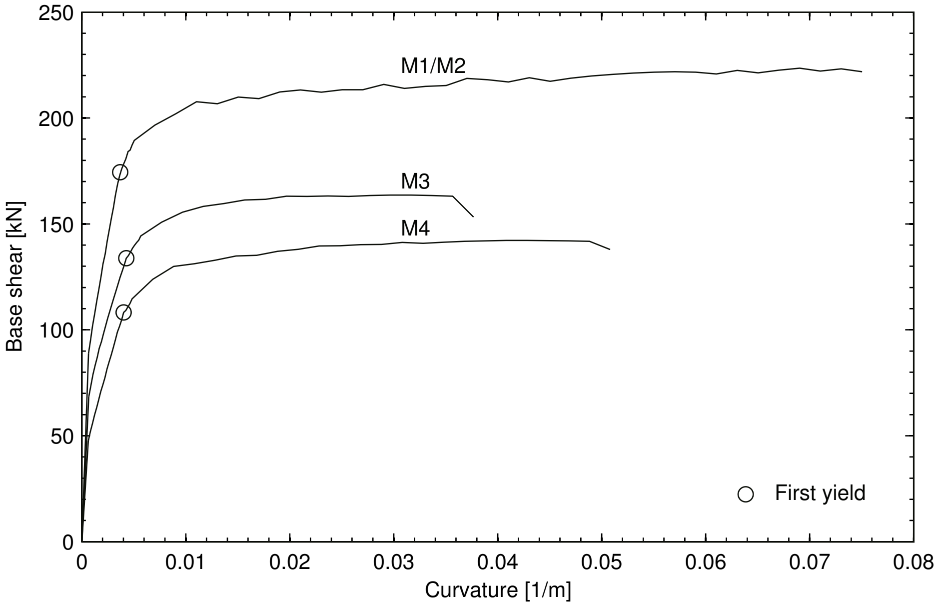

Fig. 4.4: Relationships between base shear and curvature of specimens M1, M2, M3, and M4.

		M1	M2	M3	M4
LP[a]	Δ_u [mm]	4.0	4.0	1.5	2.6
	Θ_u [10^{-3}]	7.2	7.2	2.7	4.6
Tests	Δ_u [mm]	17	12	7.1	10
	Θ_u [10^{-3}]	17	18	9.0	12
$\frac{LP}{Tests}$	Δ_u [mm]	0.24	0.33	0.21	0.26
	Θ_u [10^{-3}]	0.42	0.40	0.30	0.38

[a] Lumped plasticity model (Priestley & Park 1987)

Tab. 4.1: Rotations and displacements according to (Priestley & Park 1987), Sec. 2.8.3

4.2.2 Model geometry

The determination of crack pattern is shown in Fig. 4.5. The crack pattern depends on

- Neutral axis depth,
- Crack spacing, and
- Shear ratio.

The crack spacing s is explained in Section 4.2.2. Consider a fan-centered shape of crack pattern. So, it is assumed that the inclined cracks meet at a common point. These cracks define struts of variable width. The pivot point is assumed to be located in distance x below the base of the wall. The variable x refers to an average depth of neutral axis which is determined by preliminary curvature analysis.

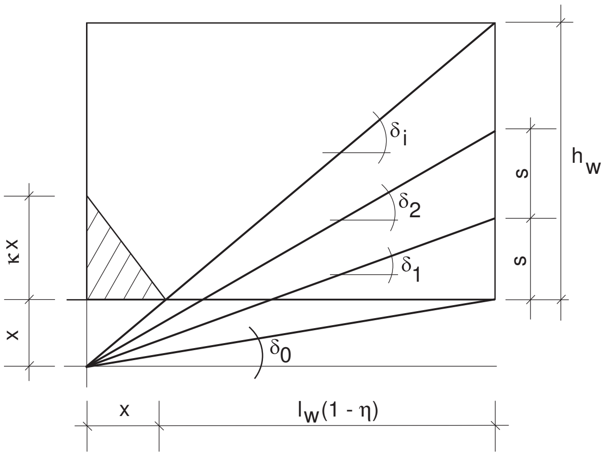

Fig. 4.5: Geometry of discrete crack model.

Neutral axis depth

Preliminary curvature analysis provides the position of neutral axis. The assumption of plane sections for this calculation is valid due to the following reasons of:

- Correct prediction of first yield by curvature analysis (Fig. 3.12 and Fig. 3.13).
- Depth of neutral axis is not sensitive to increase in curvature up to peak response.

The assumption of constant neutral axis depth underestimates deformation capacity in the post-peak branch of force-rotation relationship. In real structures, the depth of neutral axis is expected to slightly increase in post-peak branch due to concrete crushing at the outermost fiber. This would extenuate the decay in base shear in the post-peak branch. Nevertheless, the test data give evidence for a constant depth of the neutral axis during the loading process.

Crack spacing

Discrete crack modeling necessitates estimations of the crack pattern. The average crack spacing for cyclic loading can be determined based on the relationships described in Sec. 2.4.4. It is assumed that the amount of vertical boundary reinforcement governs the crack spacing. Nevertheless, linking the maximum bond stress to the effective tensile strength of concrete seems to be inappropriate for cyclic loading because cracks form in cycles with relatively small loading intensity. In such cycles, only minor damage to bond is expected as rebars are subjected to low strain level.

However, the shear ratio also influences the crack pattern. This is substantiated by the test series reported in Sec. 3. The test series included four specimens with similar reinforcement ratios but the crack patterns are substantially different (Fig. 3.7). Since base shears corresponding to flexural strength are observed in all tests, the tensile forces per unit of length are also of same magnitude in all tests. Nevertheless, the panel of specimen M1 remains uncracked while cracking extended over the whole height of specimen M3.

It is proposed to relate the shear ratio to the vertical extension of the zone within which cracking is expected by a linear relationship (Fig. 4.6a). In case of shear ratios less than or equal to 0.3, cracking is limited to the base joint while fully developed crack patterns are expected for shear

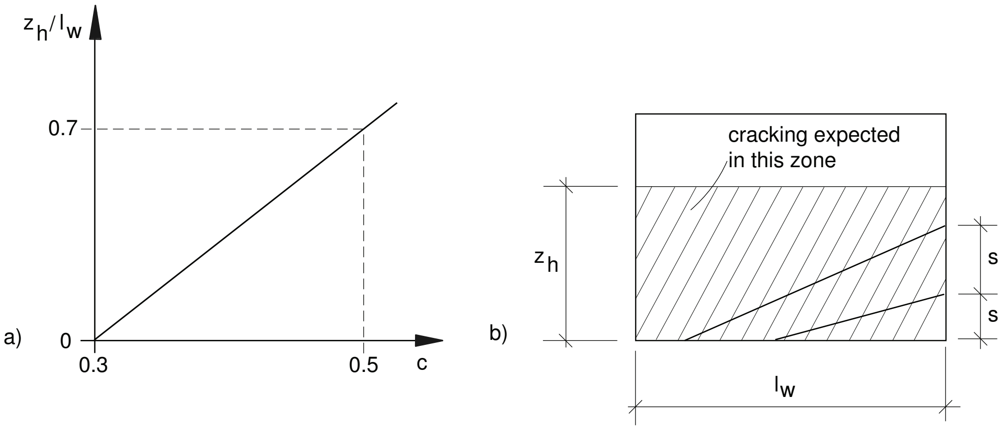

Fig. 4.6: Determination of crack pattern, a) relationship between vertical extension of cracking and shear ratio, b) crack pattern.

ratios greater than or equal to 0.5. In the zone determined by z_h, the crack spacing is governed by the effective tensile strength of concrete (Fig. 4.6b).

Effective tensile strength of concrete refers to the reduced tensile strength. The reduction of tensile strength originates from previous tensile-compressive loading causing micro-cracks in the concrete. Detailed information on this process is given in Section 2.4.2.

Herein, maximum bond stress is assumed to be equal to $\tau_{b0} = 2f_{ct}$ and effective tensile strength is assumed to be in the range between 20 and 40% of nominal tensile strength $(0.2 < f_{ct} < 0.4)$. Then, the average crack spacing for cyclic loading is found to be between 20 to 40% of the values expected for monotonic loading (Eq. (4.1)). Thus, the average crack spacing is insensitive to the concrete compressive strength.

$$0.05d\frac{1-\rho}{\rho} < s_{cycl} < 0.1d\frac{1-\rho}{\rho} \tag{4.1}$$

In Eq. (4.1), the lower and upper bound of crack spacing corresponds to effective concrete tensile strength of 20 and 40 % of the nominal tensile strength, respectively.

In addition, only the maximum crack spacing is of interest for the model geometry. If the upper bound of crack spacing is assumed, the calculated crack widths are overestimated. Since crack width governs rebar failure and degradation of aggregate interlock, the deformation capacity of the wall is underestimated. Hence, the model will provide conservative predictions of deformation capacity.

Example

Discrete crack pattern is developed for unit wall length in accordance with test results for specimens M3 and M4. This development includes the following assumptions:

- Maximum crack spacing: d=6mm, $\rho_h = \rho_v = 0.3\%$, $\rightarrow$ $\bar{s} \approx 200\,\text{mm}$
- Arbitrary value of neutral axis depth: $\eta = 0.15$

Both the observed crack pattern of specimen M3 and the assumed crack pattern are shown in Fig. 4.7. Note that the crack pattern of the model agrees well with the observed one.

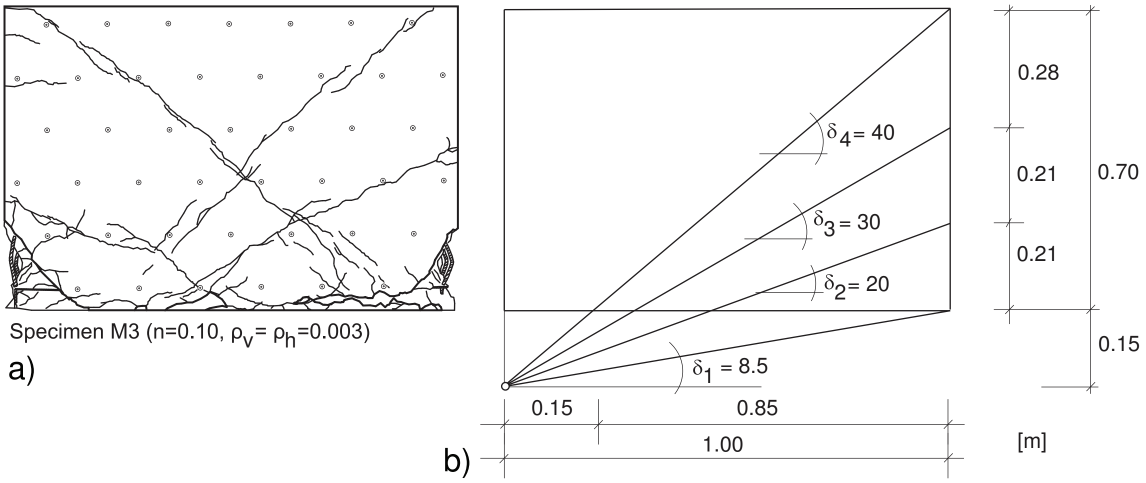

Fig. 4.7: Development of crack pattern: a) test (Specimen M3), b) crack pattern for wall length of 1 m and wall height of 0.70 m.

4.3 Internal and external forces

4.3.1 Equilibrium at cracks

This section investigates the force flow inside the plastic hinge. The internal and external forces are shown in the free-body diagram in Fig. 4.8a. External vertical and horizontal forces are the axial force N and the base shear F_H, respectively. The concrete compression zone is assumed to contribute to both shear and flexural strength. Hence, the internal force in the concrete compression zone is decomposed into the horizontal component V_c and vertical component D_b. Forces on the crack interface are modeled by B_i and Z_i.

The free-body diagram of a strut is shown in Fig. 4.8b. It is assumed that the point of application of the vertical tensile force Z_i is located in the center of the strut element. The strut force D_i models aggregate interlock in the tensioned part of the base joint. It does not correspond to an additional compressive force beside the concrete compression force. The aggregate interlock force is equilibrated locally by both friction and contact.

Shear walls are subjected to vertical and horizontal forces. Assuming discrete cracks (Fig. 4.8) one can write the equilibrium of momentum on point O:

$$\sum M_{(O)} \overset{!}{=} 0: \; F_H\,(h_w + m_i) + D_b\, z_b' - N\,(0.5\, l_w) - Z_i\,(z_b' + \xi_i l_w) - B_i\, e_i - V_c\, m_i = 0 \quad (4.2)$$

where V_c is the concrete contribution to the shear capacity. The resulting forces at the crack interface, B_i and Z_i, include the forces of horizontal and vertical rebars, respectively. They also include the effect of aggregate interlock at the crack interface.

Equilibrium in vertical and horizontal direction is written in Eq. (4.3) and Eq. (4.4), respectively.

$$\sum V \overset{!}{=} 0: \quad D_b - N - Z_i \quad = 0 \quad (4.3)$$

$$\sum H \overset{!}{=} 0: \quad F_H - V_c - B_i \quad = 0 \quad (4.4)$$

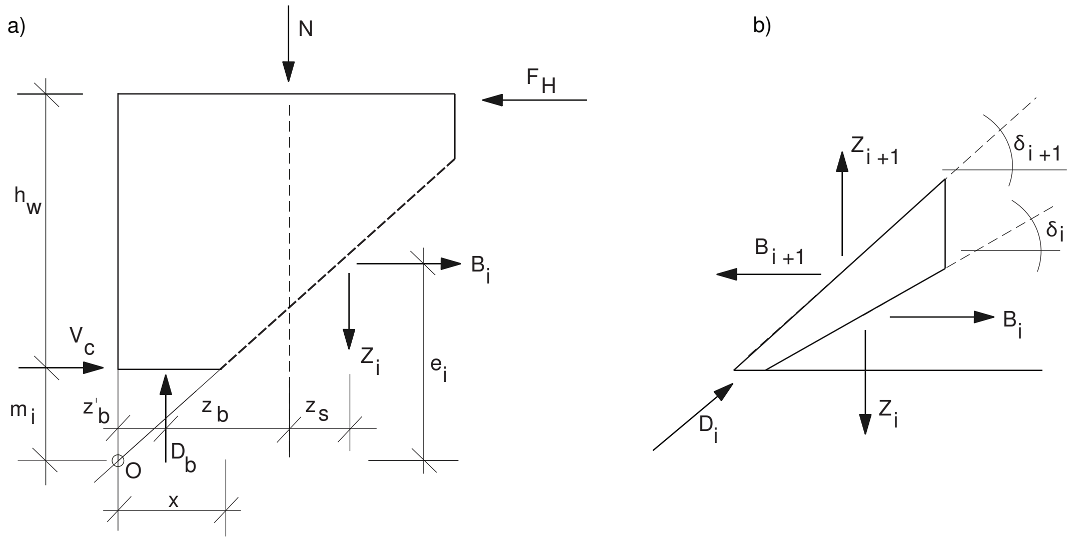

Fig. 4.8: Free body diagrams, a) panel, b) strut .

Inserting both Eq. (4.3) and Eq. (4.4) in Eq. (4.2) one can eliminate the concrete compression force D_b and the concrete contribution to shear strength V_c. The resulting relationship is solved for the vertical tensile force Z_i (Eq. (4.5)).

$$Z_i = \frac{1}{\xi_i l_w} \left[F_H h_w + N \left(z_b' - 0.5 l_w \right) - B_i \left(e_i - m_i \right) \right] \tag{4.5}$$

Assuming that the horizontal crack force is entirely due to horizontal reinforcement, B_i is equal to the yield force of the horizontal reinforcement crossing the crack (Eq. (4.6)). This relationship simplifies for a 45° inclined crack to Eq. (4.7).

$$B_i = f_y \rho_h b_w \left(l_w \tan \delta_i - m_i \right) \tag{4.6}$$

$$B_{45} = f_y \rho_h b_w l_w \left(1 - \eta \right) \tag{4.7}$$

For further investigation of the internal forces, it is useful to write the horizontal force in the crack (B_i) as a function of the force in a 45° inclined crack (B_{45}). This is shown in Eq. (4.8).

$$B_i = B_{45} \frac{\tan \delta_i - m_i / l_w}{1 - \eta} \tag{4.8}$$

The distribution of stresses along the crack interface is difficult to estimate because it depends on both the crack width and the degradation state of aggregate interlock. It is assumed that the resultant horizontal force is evenly distributed over the crack plane. Hence, the lever arm of the horizontal force is equal to the following:

$$e_i = \frac{l_w \tan \delta_i - m_i}{2} + m_i \tag{4.9}$$

The increments of both vertical and horizontal forces on crack interface (Fig. 4.8) are defined as follows:

$$\Delta B_i = B_i - B_{i+1} \tag{4.10}$$

$$\Delta Z_i = Z_i - Z_{i+1} \tag{4.11}$$

The lever arm of vertical rebars is supposed to yield a constant value over the height of the plastic hinge. The lever arm of concrete contribution to shear strength m_i is also supposed to be of constant value. Inserting Eqs. (4.5), (4.7), and (4.8) into Eqs. (4.10) and (4.11) one obtains

$$\Delta B_i = \frac{B_{45}}{1-\eta}\left[\tan\delta_i - \tan\delta_{i+1}\right] \tag{4.12}$$

$$\Delta Z_i = \frac{B_{45}}{2\xi(1-\eta)}\left[(\tan\delta_{i+1} - \eta)^2 - (\tan\delta_i - \eta)^2\right] \tag{4.13}$$

The increments in the horizontal and vertical forces on the crack interface originate from the presence of aggregate interlock force D_i (Fig. 4.8). Equation (4.13) provides a mean to study the decay of tensile force along wall height. The decay is investigated in the next section.

4.3.2 Investigation of shear lag

The previously developed equations describes the variation of tensile force along wall height. This variation is calculated for a wall of length equal to unity and a aspect ratio equal to 1.0. The result then is compared with the variation of tensile forces according to elastic theory.

For specimens M1, M2, M3, and M4, the relationship between tensile force ratio and curvature is shown in Fig. 4.9a. The tensile force ratio refers to the ratio of tensile force to maximum tensile force. First yield occurres at curvatures near to 0.005 corresponding to tensile force ratio of 0.6. The variation of the internal lever arm of the cross-section is shown in Fig. 4.9b. For plastic response, the internal lever arm converges to 0.55 times the wall length. Hence, a lower bound of 0.5 times the wall length is assumed for the lever arm in the subsequent calculations.

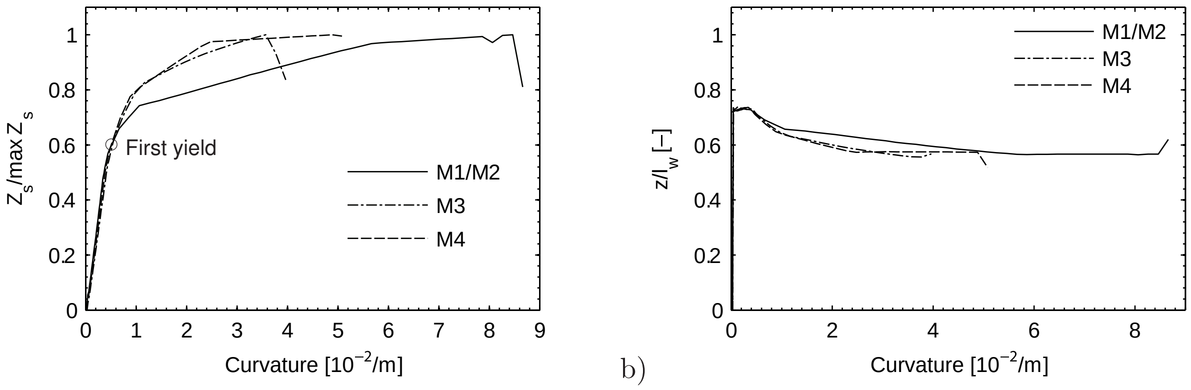

Fig. 4.9: Curvature analysis for Specimens M1, M2, M3, and M4: a) Increase in tensile forces, b) Decrease of lever arm.

The ratio of maximum tensile force to the yield force of horizontal reinforcement crossing a 45° inclined crack is written in Eq. (4.14) where λ refers to the ratio of vertical to horizontal reinforcement. The factor $\left(0.5+\frac{f_u}{2f_y}\right)$ accounts for strain hardening. The maximum tensile force denotes the tensile force developed in vertical reinforcement at tensile failure of rebars.

$$\frac{Z_{max}}{B_{45}} = \frac{(1-2\eta)\, l_w \rho_v b_w f_y}{\rho_h b_w l_w f_y\,(1-\eta)} \cdot \left(0.5+\frac{f_u}{2f_y}\right) = \frac{\lambda\lambda'\,(1-2\eta)}{(1-\eta)} \tag{4.14}$$

where:

$$\begin{aligned} \lambda &= \frac{\rho_v}{\rho_h} \\ \lambda' &= 0.5+\frac{f_u}{2f_y} \end{aligned}$$

Inserting Eq. (4.14) in Eq. (4.13) and cumulating the variation of tensile force results in a relationship for the decay of tensile force along wall height:

$$Z_i = Z_{max} - \sum_{j=1}^{i} \Delta Z_j \;\rightarrow\; \frac{Z_i}{Z_{max}} = 1 - \frac{1-\eta}{\lambda\lambda'\,(1-2\eta)} \sum_{j=1}^{i} \frac{\Delta Z_j}{B_{45}} \tag{4.15}$$

Hence, variation of tensile force ratio along wall height depends on the following parameters:

- Neutral axis position (η, Eq. (4.15)).
- Internal lever arm between concrete and rebar forces (ξ, Eq. (4.13)).
- Ratio of vertical to horizontal reinforcement (λ, Eq. (4.15)).
- Hardening ratio of reinforcement (λ', Eq. (4.15)).
- Shear span ratio.

On the other hand, the variation of tensile force along height is independent of

- Wall length,
- Reinforcement ratios (ρ_h, ρ_v), and
- Yield strength of reinforcement.

Equation (4.15) is now used to calculate the variation of tensile force along wall height. The latter is calculated for infinitely small crack spacing in order to derive envelope curves for tensile force. Results of this calculation are shown in Fig. 4.10b. The symbol z_h refers to the coordinate along tensioned boundary (Fig. 4.10a).

It is observed that both an increase in the depth of neutral axis and an increase in the vertical reinforcement augment the shear lag (Fig. 4.10b). For horizontal reinforcement equal to vertical reinforcement and normalized neutral axis depth of 0.3, the shear lag can attain up to 0.30 times

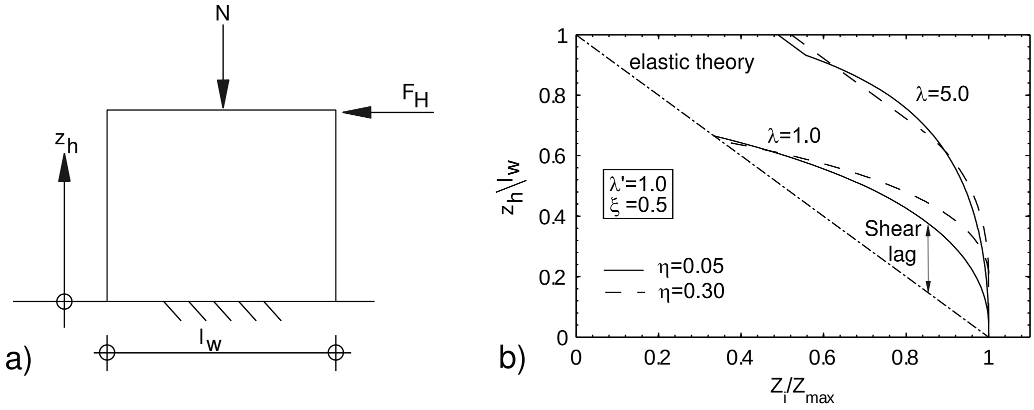

Fig. 4.10: Shear lag in squat walls of aspect ratio equal to 1.0, a) definitions, b) shear lag for $\lambda = 1.0$ and $\lambda = 5.0$.

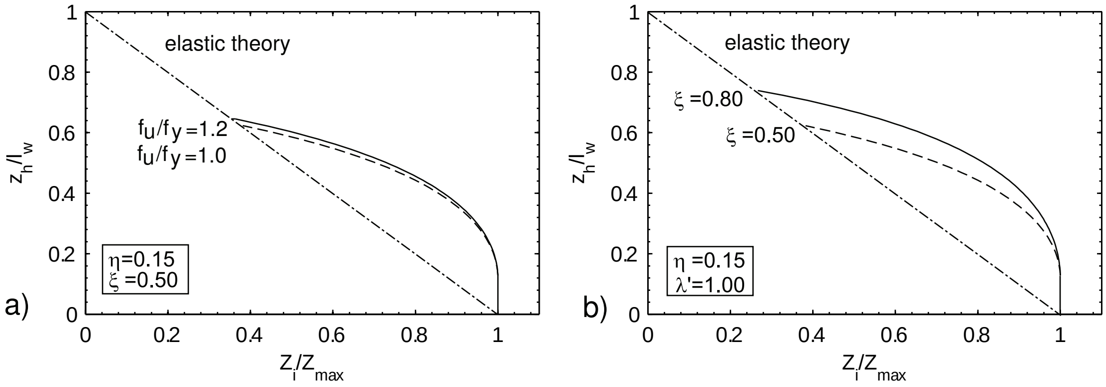

Fig. 4.11: Variation of tensile force along wall height (aspect ratio equal to 1.0), a) influence of hardening ratio, b) influence of lever arm.

the shear span. Note that the lumped plasticity model proposed by Priestley & Park (1987) includes the assumption of shear lag equal to 0.08 times the shear span (Sec. 2.8.3).

The influence of hardening ratio and internal lever arm on shear lag is shown in Figs. 4.11a and 4.11b, respectively. According to these results, the shear lag is not sensitive to the hardening ratio while it is sensitive to the internal lever arm. Increasing the lever arm from 0.5 up to 0.8 times the wall length results in increase of shear lag by 0.05 times the wall height. This corresponds to 20% of the shear lag at the smaller lever arm.

Since shear lag is not sensitive to the hardening ratio, the latter is assumed to be equal to the following calculations. Further investigations on shear lag are made in Sec. 5.4.3 (p. 132).

4.3.3 Concrete compression force

The compression force developed in the concrete due to shortening of the outermost fiber is calculated by integrating an appropriate stress-strain relationship. In the numerical model, this is achieved by subdividing the concrete compression zone into a finite number of fibers of constant strain, calculating strain, stress, and axial force of each fiber, and cumulating fiber forces. The integration of concrete stresses is summarized by Eq. (4.16).

$$D_b = \int_x \sigma_c\left(\epsilon_c\right) d\epsilon \tag{4.16}$$

The stress-strain relationship is modeled by an envelope curve similar to that proposed by Karsan & Jirsa (1969). It is shown in Sec. 2.4.1 that such envelope curve encloses the cyclic response of concrete in compression. The stress-strain relationship is shown in Fig. 4.12a. It consists of two branches:

- Parabolic branch modeling pre-peak behavior
- Linear branch modeling post-peak behavior

The relationship proposed in SIA2018 (2004) is used for the pre-peak branch. It is described in Eq. (4.17). Pre-peak behavior is assumed for strains less than or equal to 0.002.

$$\sigma_c = f_c' \frac{r \cdot \varsigma}{r - 1 + \varsigma^r} \tag{4.17}$$

where

$$\begin{aligned} r &= \frac{E_{cm}}{E_{cm} - \frac{f_c'}{\epsilon_{c1d}}} \\ \varsigma &= \frac{\epsilon_c}{\epsilon_{c1d}} \end{aligned}$$

Strain softening of concrete is modeled by linear decay of stress in the post-peak branch. Maximum stress decay is equal to 0.8 times the peak strength. Failure occurs when the strain exceeds ultimate strain which is assumed to yield three times the peak strain. Equation 4.18 describes the post-peak reponse.

$$\sigma_c = f_c' \left(1.4 - 0.4 \frac{\epsilon}{\epsilon_{1c}}\right) \tag{4.18}$$

The sensitivity of normalized concrete compression force to ultimate strain is shown in Fig. 4.12. In this figure, the normalized compression force is plotted against the strain of outermost fiber. Since the concrete compression force was normalized to the maximum concrete compression force, the curves are independent of the depth of neutral axis. In case of ultimate strain equal to three times the peak strain, maximum compression force occurs at strain of 0.003. Increase in ultimate strain slightly increases the strain corresponding to maximum compressive force, and it extenuates decay of this force in the post-peak branch.

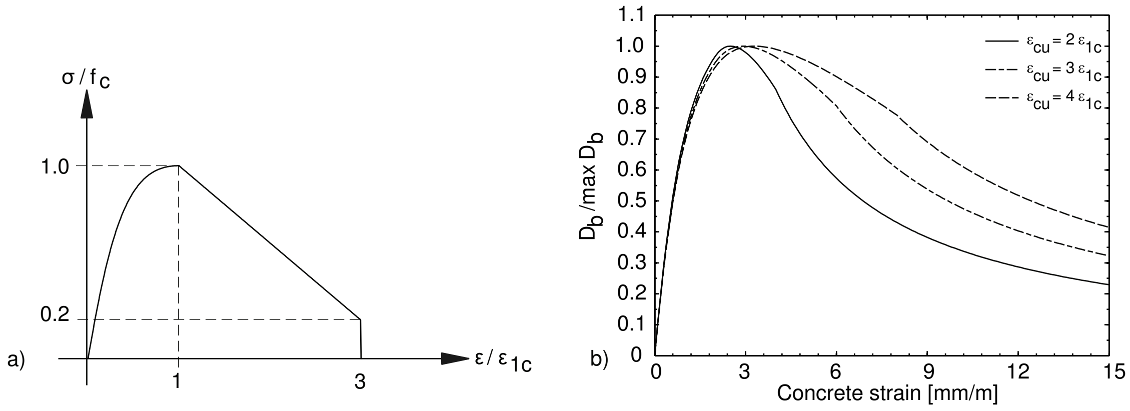

Fig. 4.12: Calculation of concrete compression force, a) stress-strain relationship, b) influence of ultimate strain on decay of concrete compression force.

4.3.4 Base shear - rotation relationship

The base shear due to rotation is equal to the flexural moment at the base divided by the shear span. The internal forces in the base joint are used for the calculation of the bending moment. The equilibrium of axial forces provides the internal forces.

While the points of application of internal forces are defined for planar sections by both strain state and material law, it is not the case for non-planar sections. Both cases are shown in Fig. 4.13. When section deformation occurs the curvature χ' in the compressed part of the cross-section is not equal to that in the tensioned part (χ). Since the relationship of these curvatures depends on bond characteristics and crack formation it varies during loading process.

The rotation based formulation of the model provides an explicit relationship between the rotations, strains, and the concrete compressive force (Sec. 4.4.2). Then, the internal force of longitudinal rebars can be calculated by supposing equilibrium in axial direction (Eq. (4.19)).

$$Z_s = D_b - N \ \leq \ Z_{max} \tag{4.19}$$

The tensile force Z_s normally does not exceed Z_{max} because of preliminary curvature analysis (p. 88). Since the curvature in the tensioned part of cross section is too difficult to estimate, the point of application of tensile rebar force is unknown. Two limit cases, first yielding and rupture of outermost rebar, are investigated and it is assumed that the lever arm of tensile forces varies linearly with increase in tensile force (Fig. 4.14).

The point of application of tensile force Z_s depends on straining of the longitudinal rebars. At yielding, the distribution of tensile forces is triangular (Fig. 4.14a). With increase in straining, yielding of rebars propagates into the cross-section and the force distribution changes to trapezoidal (Fig. 4.14a). The lever arm of tensile reinforcement is determined for these two limit cases. Between these cases, the lever arm is linearly interpolated. The corresponding relationship is illustrated in Fig. 4.14b. The base shear then is calculated as follows:

$$F_H(\theta) \ = f(\theta) = \ D_b\, z_b + D_s\, z_s' + Z_s\, z_s \tag{4.20}$$

Note that in Eq. (4.20) both the internal forces and lever arms explicitly depend on the rotation inside the plastic hinge.

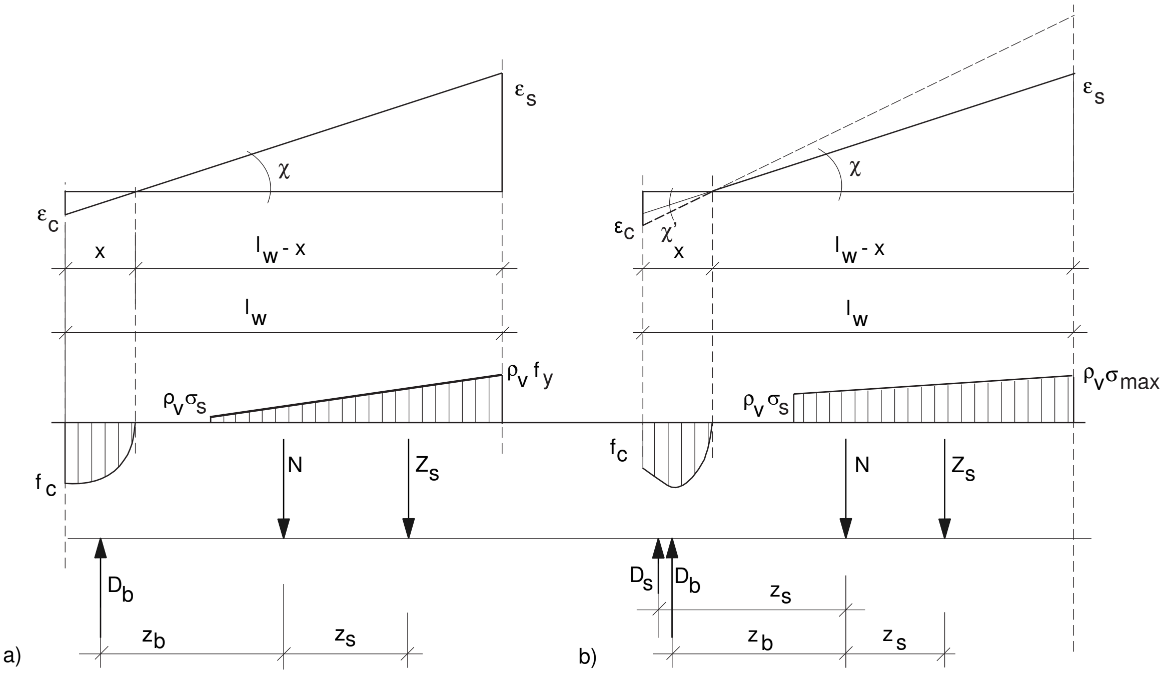

Fig. 4.13: Equilibrium of axial forces.

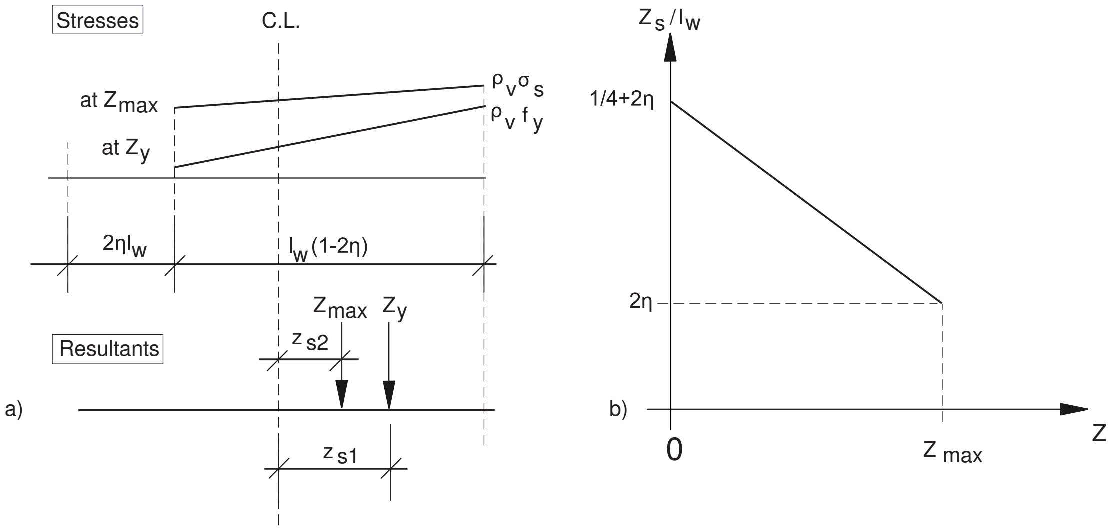

Fig. 4.14: Tensile forces of longitudinal rebars, a) stress distributions and point of application, b) relationship between lever arm and tensile force.

4.4 Kinematic relationships

The deformed shape and the strains at the compressed edge are shown in Fig. 4.20. Rotations basically can be determined from both the shortening of compressed fibre (Eq. (4.22)) and the sum of crack widths (Eq. (4.21)).

$$\theta_s = \frac{\sum_{j=1}^{i} w_j}{l_w(1-\eta)} \tag{4.21}$$

$$\theta_c = \frac{w'}{\eta l_w} \tag{4.22}$$

The rotations due to opening of cracks and the rotations due to shortening of compressed fiber are separately investigated in the next section.

4.4.1 Tensioned boundary

In this section, a kinematic relationship between crack widths is derived. Such kinematic relationships enable explicit calculation of rotation from the crack width of the base joint. The kinematic relationship is derived in three steps:

1. Calculation of vertical tensile forces in cracks
2. Estimation of strain localization in cracks
3. Determination of kinematic relationship

The kinematic relationship is established for the discrete crack pattern shown in Fig. 4.7.

Vertical tensile forces in cracks

The model and the variation of tensile force along wall height are shown in Fig. 4.15.

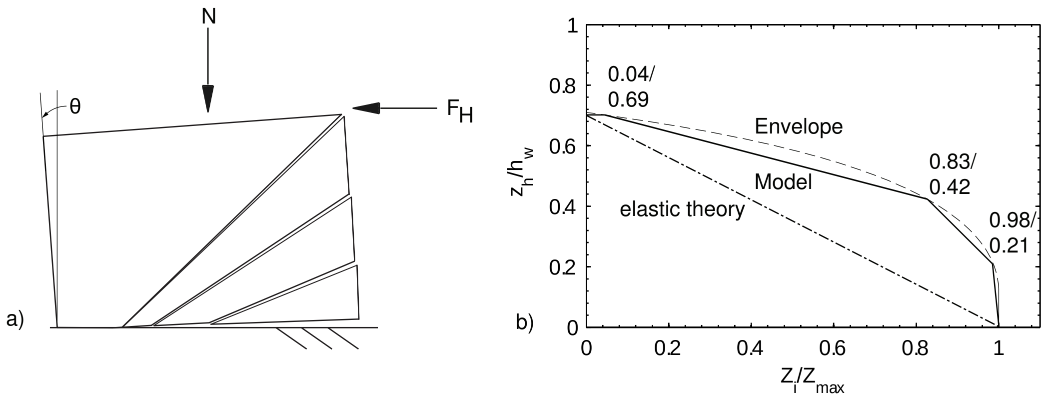

Fig. 4.15: Vertical tensile forces at crack interfaces, a) model geometry, b) tensile force ratios.

In Fig. 4.15, the magnitudes of the tensile forces are plotted at the normalized coordinate z_h/h_w. The variable z_h denotes the vertical distance from the base and h_w refers to the shear span. Note that the tensile force in the second crack is equal to 83% of the tensile force in the base joint.

Localization of strains

The localization of strains after yielding of reinforcement in the base crack is illustrated in Fig. 4.16b. Rebar forces, strains and slips of outermost rebar are plotted along the tensioned boundary. They are calculated for the tensile force variation shown in Fig. 4.15 by using the bond model proposed by Maekawa et al. (2003). Note that yield strain of rebars is equal to 2.9 mm/m. Further information of this bond model is provided in Sec. 2.4.4 (p. 20).

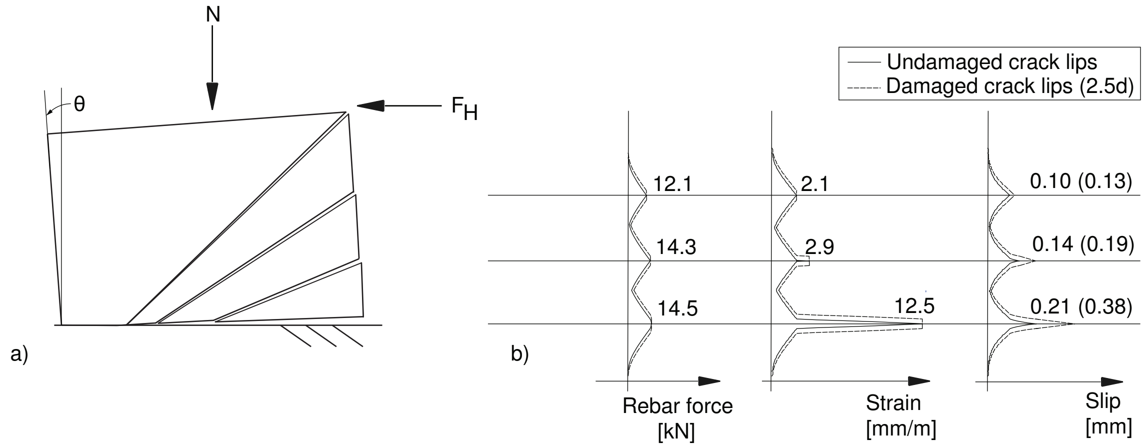

Fig. 4.16: Localization of strains in base joint, a) model with crack pattern, b) rebar force, strain, and slip at tensioned boundary.

Figure 4.16b includes the rebar forces, strains, and slips for both the assumption of undamaged crack lips (solid line) and damaged crack lips (dashed line). The latter refers to the proposal made by Maekawa & Qureshi (1997) that includes bond degradation near the crack interface. The length of bond degradation is equal to 2.5 times the diameter of rebar. It is observed that such bond degradation increases the slip in base crack, and hence, the crack width, by 70%.

Crack width ratio

The crack width ratio denotes the sum of crack widths on the tensioned outermost fiber divided by the crack width of the first crack near the base. It is described in Eq. (4.23).

$$\alpha_w = \frac{\sum w}{w_1} \tag{4.23}$$

To determine the crack width ratio, the aforementioned analysis of tension chord is carried out for selected levels of straining of the the outermost rebar. These strain levels are:

1. Yielding of rebar in the base crack.
2. Yielding of rebar in second crack ($z_h/h_w = 0.21$, Fig. 4.15).
3. Crack width of base joint equal to 1.0 mm.
4. Rupture of rebar.

Rupture of rebar is assumed to occur at strains less than the ultimate strain observed in tensile tests (Tab. 3.2). Due to both spalling of cover concrete and weakening of the core concrete, rebars buckle in compression cycles and they are subsequently exposed to large plastic straining in tension. This process results in reduction of deformation capacity of rebars that is difficult to quantify. It is assumed that the ultimate strain decreases by one third due to low cycle fatigue. Hence, ultimate strain of 7.4% is used in the analysis while ultimate strain equal to 11% is observed in monotonic tensile tests.

Both the bond behavior of rebar and the crack width ratios are shown in Fig. 4.17. Bond stress, tensile force, strain, and slip are plotted along the rebar in Fig. 4.17a. Note that a 250 mm length is required to transfer the tensile force at rebar rupture to the surrounding concrete.

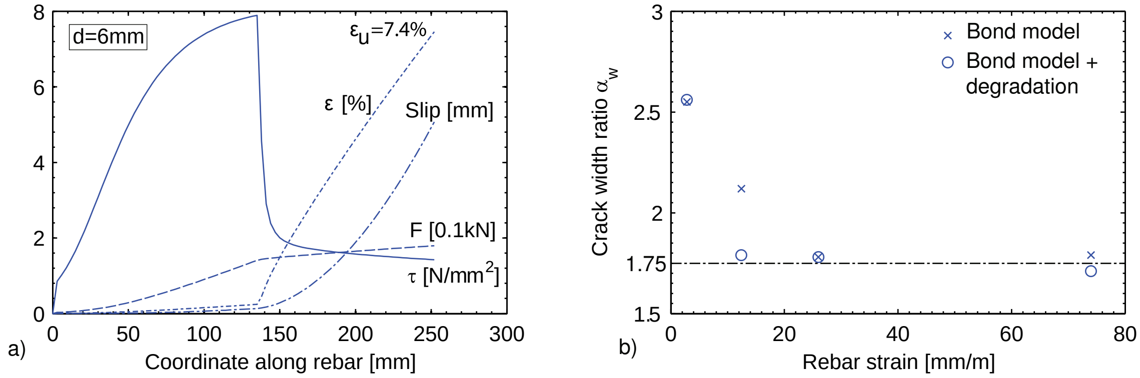

Fig. 4.17: Determination of crack width ratio, a) bond behavior of rebar, b) Variation of crack width ratio with straining of rebar.

Due to localization of strains in the base joint, the crack width ratio decreases with increasing strain (Fig. 4.17b) and it converges to approximately 1.75 for strains greater than 20 mm/m. This convergence is found to be insensitive to the degradation of bond near the crack lips.

The crack width ratio depends on vertical extension of cracking which is a function of the shear ratio. It is determined as follows:

$$\begin{array}{rcrcl} & & c \leq 0.3 & : & \alpha_w = 1.0 \\ 0.3 & < & c \leq 0.5 & : & \alpha_w = 3.8\,c - 0.13 \\ & & c > 0.5 & : & \alpha_w = 1.75 \end{array} \tag{4.24}$$

Equation (4.24) accounts for the influence of shear ratio on the crack pattern (Fig. 4.6). For shear ratios less than or equal to 0.3, cracking is limited to the base joint. Hence, the sum of crack widths is equal to the width of the crack near the base and crack width ratio yields 1.0. Contrary to this, zone of cracking extends over the entire height of the panel in case of shear ratios equal to or greater than 0.5. Crack width ratio thus is equal to 1.75.

Comparison of the proposal for the crack width ratio (Eq. (4.24)) with test results is shown in Figs. 4.18 and 4.19. In Fig. 4.18, the observed crack width ratio is plotted for selected displacement ductilities. For specimen M3, Equation (4.24) provides an upper bound of the observed crack width ratios while for specimen M4 the observed values generally are greater than the proposal according Eq. (4.24).

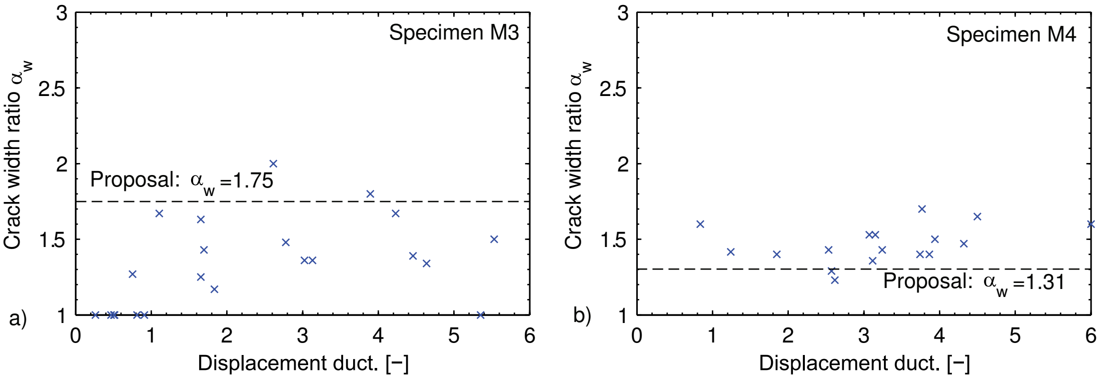

Fig. 4.18: Comparison of the proposal for the crack width ratio (Eq. (4.24)) with test results, relationship between crack width ratio and ductility, a) Specimen M3, b) Specimen M4.

The relationship between crack width ratio and shear ratio (Eq. (4.24) is shown in Fig. 4.19. Test results are also shown in this figure. The proposed linear relationship provides lower and upper bounds to the test results of specimens M4 and M3, respectively.

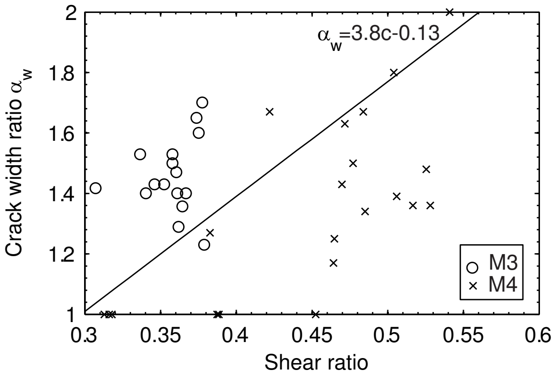

Fig. 4.19: Comparison of the proposal for the crack width ratio (Eq. (4.24)) with test results, relationship between crack width ratio and shear ratio.

The crack width ratio is used in Sec. 5.4.1 to calculate ultimate rotations for variation of the shear ratio. It is also used in Sec. 4.5.5 to establish a relationship between mean crack width and and rotation (p. 117).

4.4.2 Compressed boundary

This section aims to establish relationships between concrete compressive strains and rotations of the plastic hinge. An assumption of plastic distribution of strains is made to account for the damage due to tensile straining and subsequent compressive loading of concrete. The anchorage length of rebars is found to govern the plastic strain distribution.

Plastic strain distribution

The rotation due to deformation of the compressed fiber is illustrated in Fig. 4.20a. Assuming the pivot point to be coincident with the neutral axis in the base joint, the rotation of plastic hinge is equal to the shortening of the compressed fiber divided by the depth of neutral axis:

$$\theta_c = \frac{w'}{x} \tag{4.25}$$

The shortening of the compressed fiber w' is calculated by integration of the strains along the height of the wall (Eq. (4.26)).

$$w' = \int_{h_w} \epsilon_b(z)dz = f(k) \cdot h_w \cdot \epsilon_c \tag{4.26}$$

where $f(k)$ includes the localization characteristics of the strain distribution in vertical direction and $\epsilon_{b,max}$ is the maximum compressive strain. The strain variation along the compressed fiber is shown in Fig. 4.20b.

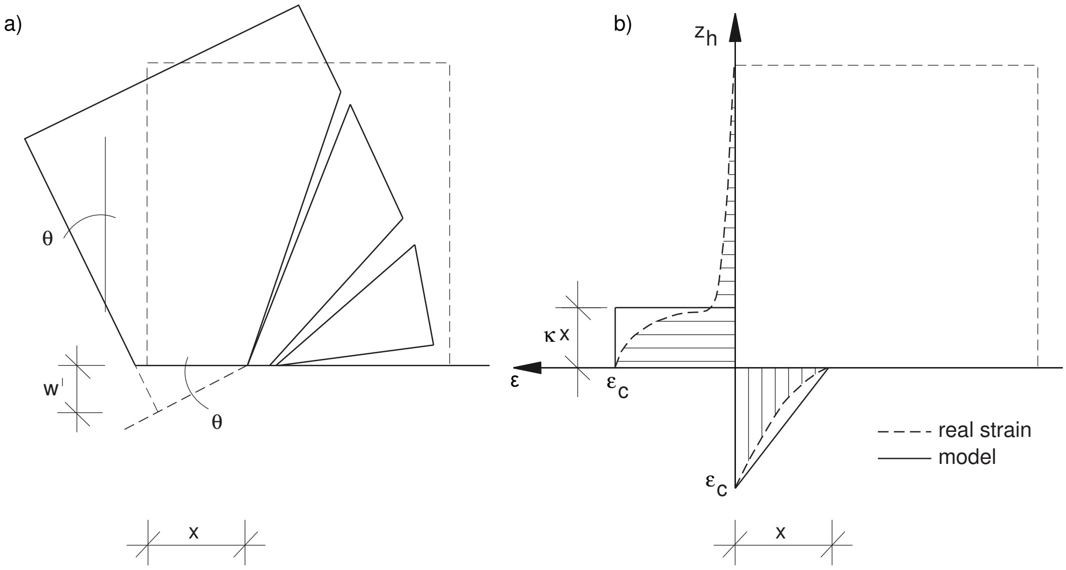

Fig. 4.20: Kinematic relationships, a) deformed shape , b) strain distribution.

Since the real strain distribution is too complex to estimate, simplifications are suggested in order to facilitate integration of strains. These simplifications are:

1. Strains localize in the zone near the base.
2. The localized strains are significantly greater than the strains outside the localization zone.
3. The vertical extension of localization zone is linked to the depth of neutral axis.
4. The strain distribution between the outermost compressed fiber and the neutral axis is linear.

Consider the localization of strains as it is described in Eq. (4.27).

$$f(k) = \left(\frac{\kappa x}{h_w}\right)^{k'} \tag{4.27}$$

Using Eqs. (4.27) and (4.26) in Eq. (4.25) establishes a relationship between rotations and strains that is shown in Eq. (4.28).

$$\theta_c = \kappa^{k'} \left(\frac{x}{h_w}\right)^{k'-1} \epsilon_c \tag{4.28}$$

The parameter k' permits to investigate two limit cases for the strain distribution along height. They are shown in Fig. 4.21a. First, uniform strain distribution is obtained when the parameter k' is equal to zero. Second, the other limit case, $k' = 1$, models a zone of constant strain $\epsilon_{b,max}$ near the base of the wall. The parameter κ is the ratio of the vertical extension of the localization zone to the neutral axis depth.

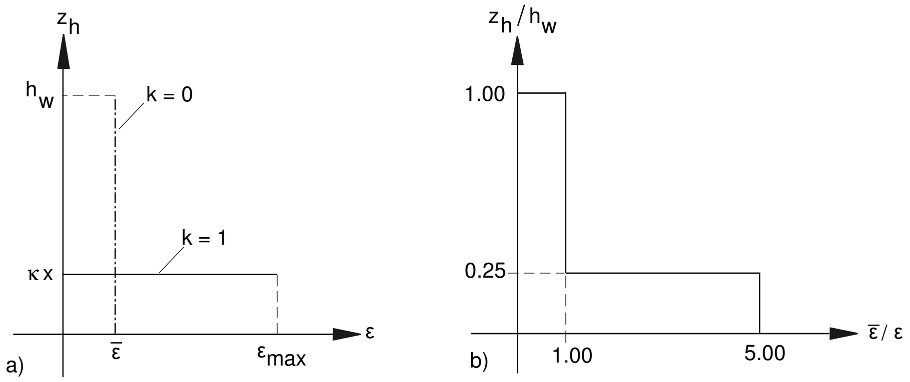

Fig. 4.21: Strain distribution at compressed boundary, a) limit cases for parameter k', b) experimentally observed (Specimen M3).

Significant damage near the base of shear wall is observed in static-cyclic tests (Fig. 3.10). The upper part of the wall showed minor damage. Moreover, the analysis of the records from the vertical displacement transducers has shown that the strains in the bottom quarter are significantly greater than the strains in the upper par of the wall.

An example for the results of this analysis is shown in Fig. 4.21b. In the plot, the strains near the base yield five times the strains in the upper part of the wall. Hence, the assumption of uniform strain distribution along the height is not valid. For simplicity, a value of 1.0 is assumed for the parameter k'. Equation (4.28) then simplifies as follows:

$$\theta_c = \kappa \cdot \epsilon_c \tag{4.29}$$

The parameter κ describes the vertical extension of the localization zone. It is investigated in the next section.

Extension of plastic zone

Damage near the base of the wall originates from straining in tensile cycles and subsequent compressive loading. In addition, the concrete is subjected to transverse straining in compression cycles. The impact of transverse straining on concrete compressive strength is investigated in Sec. 4.5.4.

Bond mechanics provides an answer to the observed damage. Anchoring of rebars is helped by lugs. If the rebar is pulled out, struts form between the lugs and the surrounding concrete. For further transfer of the strut forces into the concrete, the struts need to be supported by tensile rings. The stress field corresponding to this mechanism are illustrated in Fig. 4.22a.

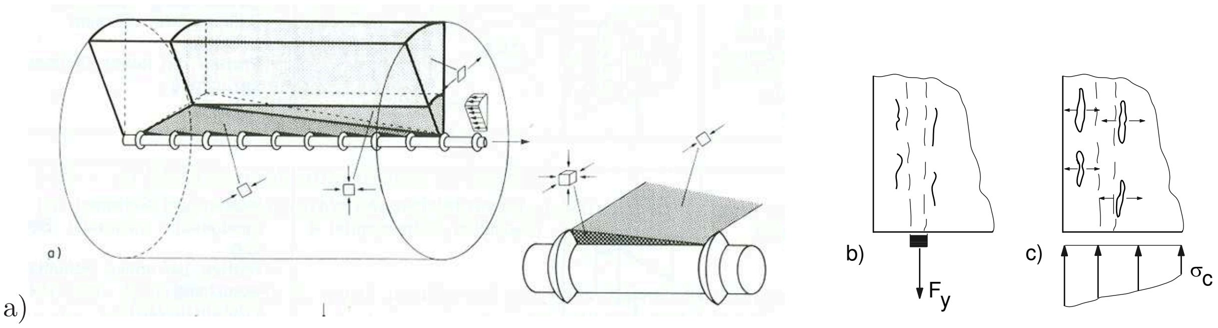

Fig. 4.22: Splitting cracks due to anchoring of rebars, a) stress fields explaining bond mechanism (Muttoni et al. 1996), b) behaviour of splitting cracks in tension, c) in compression cyles.

In case of cyclic loading, the concrete surrounding the rebars is subjected to tension due to anchoring of rebars and to compression when loading direction is reversed. Note that the forces caused by the tensile rings are perpendicular to the compression forces in subsequent cycle. Failure of the tensile rings results in formation of cracks parallel to the rebar that later widen in compression. Such vertical cracks are observed at plastic strains of rebars (Sec. 3.3.1, p. 61). The formation of cracks and their widening under compression is shown in Fig. 4.22b.

For static-monotonic loading, many researchers proposed relationships between the position of neutral axis and the extension of the plastic zone (Sec. 2.5.2, p. 24). It is widely accepted that the extension of the plastic zone is equal to two or three times the depth of neutral axis. The investigation on bond mechanism shows that concrete damage is sensitive to this mechanism. Therefore, the following definition is proposed for the parameter κ:

$$\kappa \;= \max \begin{pmatrix} \frac{l_{anc}}{x} \\ 1.0 \end{pmatrix} \tag{4.30}$$

Hence, the parameter κ, due to dependency on the depth of neutral axis, implicitly includes the influence of both axial force and vertical reinforcement on the strain localization. It includes also the damage due to bond mechanism because of the anchoring length (l_{anc}). The latter can be calculated by using an appropriate bond model. However, it is assumed that damage due to cyclic loading is substantially different from that due to monotonic loading. So, the minimum extension of plastic zone is greater than or equal to the depth of neutral axis. This is 50% of the extension for monotonic loading.

The parameter κ now accounts for constant damage of concrete. It does not depend on the applied level of straining. By contrast, tests show that damage accumulates with increase in straining. Since the physical phenomenon is complex and detailed experimental studies are not available, the parameter κ is assumed to increase linearly from zero to the upper bound (Eq. (4.30)) in the pre-peak branch of concrete stress-strain relationship. The post-peak behavior is modeled by a constant parameter κ. The relationship between parameter κ and the concrete strain is shown in Fig. 4.23. In this figure, the symbol κ' denotes the effective portion of strain localization factor κ.

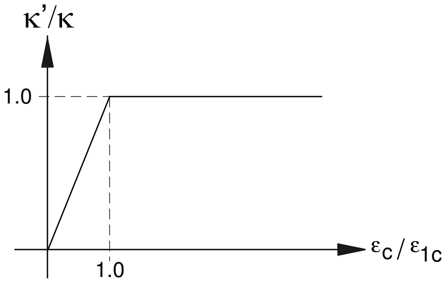

Fig. 4.23: Variation of strain localization parameter κ with increase in concrete strain.

Considering the linear increase of parameter κ in the pre-peak branch of stress-strain relationship, Eq.(4.29) modifies to Eqs. (4.31) and (4.32) in pre-peak and post-peak branch, respectively.

$$\epsilon_c \leq \epsilon_{1c} \;\rightarrow\; \theta_c = \kappa\,\frac{\epsilon_c^2}{\epsilon_{1c}} \tag{4.31}$$

$$\epsilon_c > \epsilon_{1c} \;\rightarrow\; \theta_c = \kappa\,\epsilon_c \tag{4.32}$$

Formulation of equilibrium, constitutive relationships and kinematic relationships provides all elements necessary to calculate the force-rotation envelope. Tab. 4.5 summarizes the parameters of the model. The performance of model is assessed by using it for recalculation of test data in Sec. 5.4.2, p. 130.

4.5 Proposal for shear strength envelope

4.5.1 Bounds of shear strength

Shear strength interacts with deformation. The more the deformation increases the less is the shear capacity of a structural element. The interaction between shear and deformation forms the cornerstone of a variety of models for seismic assessment of columns (Sec. 2.6.6, p. 37). Analysis of experimental data for walls (Secs. 2.3.3 and 3.3) enables the identification of the following bounds of deformation capacity:

1. Bound of strength
2. Bound of shear restricted by deformation capacity
3. Bound of flexural failure

These bounds define the feasible domain of deformation capacity that is shown in Fig. 4.24. According to the assumptions of the previously formulated analytical model, the domain of feasibility is plotted in a plane defined by both shear ratio and rotations.

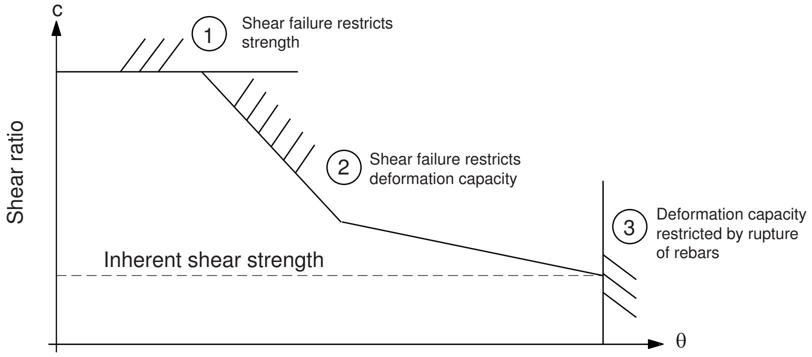

Fig. 4.24: Bounds of shear strength envelope.

In addition to the aforementioned bounds, Fig. 4.24 also includes the inherent shear strength. Elastic shear response is expected for walls of shear ratios less than the inherent shear strength. Test data clearly substantiate the assumption of inherent shear strength of concrete while current design (Secs. 2.6.3 and 2.7) does not explicitly account for such inherent strength.

Consider the shear strength envelope shown in Fig. 4.24. The bound of strength controls the response in force that is independent of the applied deformation. The strength then decreases with increase in rotation. Hence, the formulation of bounds should enable the following predictions:

- Prediction of initial strength
- Prediction of strength decay

This section is dedicated to the formulation of bounds of shear strength envelope that is based on cumulative shear model. The contributions of concrete and reinforcement are separately investigated and the shear capacity as a function of rotations is calculated by cumulating these two principal contributors.

4.5.2 Characteristics of shear response

The static-cyclic behavior of shear walls is characterized by strength, drift, and ductility. Deformation capacity is linked to the crack pattern which depends on the amount of reinforcement and the level of axial force. A few concentrated cracks result in strain localizations which can induce susceptibility to brittle shear failure. This subsection summarizes failure modes, aggregate interlock action, and parameters governing shear response.

Failure modes

Experimental and theoretical investigations have shown that strength and deformation of squat walls is restricted by the following failure modes (Secs. 3.3.2 and 4.1.3):

- Concrete crushing
- Diagonal tension
- Sliding
- Rupture of reinforcement

Shear strength of walls can be restricted by both diagonal tension and concrete crushing. Deformation can be restricted by sliding, concrete crushing, and rupture of reinforcement. However, there is little experimental evidence for strength restriction by concrete crushing in case of lightly reinforced walls. The shear strength of such walls is generally restricted by diagonal tension. Nevertheless, significant deterioration of concrete and subsequent concrete crushing is expected for shear ratios greater than 0.8 (Eq. (2.43)).

Aggregate interlock and cyclic loading

Shear response is closely linked to aggregate interlock action in cracks (Sec. 2.4.3). Aggregate interlock depends on roughness, crack width, and the normal force acting on the asperities inside the crack. The shear capacity of the crack interface decreases with widening of cracks because of reduction of contact surfaces between the crack lips.

Cyclic loading causes degradation of aggregate interlock. Consider a cycle of loading. If cracks open in tension half-cycle, there is relative displacement between crack lips that leads to residual crack width after unloading. Closure of cracks requires both normal force relative to the crack interface and sliding to lock in the asperities. If normal force and slip is provided, the crack closes in the compression cycle and grinding of asperities occurs due to normal force and slip. Increase in number of cycles then results in smoothing of the crack interface. The roughness of the interface degrades and the capacity to transfer shear in the crack will also degrade. Moreover, widening of cracks due to deterioration of bond introduces further reduction of shear capacity.

Degradation of shear capacity in cracks leads to decay of base shear. In case of lightly reinforced walls, deformation localizes in a few cracks. Hence, aggregate interlock in these cracks significantly degrades with increase in both deflection and number of cycles. A proposal for decay of aggregate interlock is made in Sec. 4.5.5.

Principal parameters of shear response

Experimental and theoretical investigations show that the axial force ratio, the amount of both vertical and horizontal reinforcement, and the reinforcement detailing govern the response of shear walls. The following list summarizes the influence of increase in both amount of reinforcement and axial force ratio on the wall response.

- Horizontal reinforcement ↑
  - Reduces crack width of inclined cracks
  - Less crack slip
  - Better transmission of shear in cracks
  - Increases susceptibility to concrete crushing
- Vertical reinforcement ↑
  - Increase of shear strength demand
  - Decrease of crack spacing
- Axial force ↑
  - Enhances shear transfer across cracks
  - Reduces crack width
  - Decreases residual drift
  - Diminishes drift capacity
  - Augments shear demand

The list indicates that the formulation of shear strength envelope should include all three parameters because they can have positive or negative impact on deformation capacity.

4.5.3 Elements of shear strength envelope

The elements of the shear strength envelope are presented in this subsection. These elements are subsequently used to establish relationships for the bounds of the shear strength envelope and they are shown in Fig. 4.25. The formulation of the shear strength envelope consists of four principal elements:

- Inherent shear strength (Sec. 4.5.6)
- Concrete contribution (Sec. 4.5.4)
- Reinforcement contribution (Sec. 4.5.5)
- Upper limit of shear strength (Sec. 4.5.6)

Inherent shear strength and the upper limit of shear strength form the lower and upper bounds for the shear strength envelope. Elastic response in shear is expected for shear ratios less than or equal to the inherent shear strength. The contributions of concrete and reinforcement include considerations on both initial strength and strength decay. Hence, shear capacity is equal to initial strength times the decay factor (Eq. (4.33)).

$$V = \lambda_c V_c + \lambda_s V_s \tag{4.33}$$

In function of the failure mode, the decay factors λ_c and λ_s either depend on the applied rotation or are equal to 1.0.

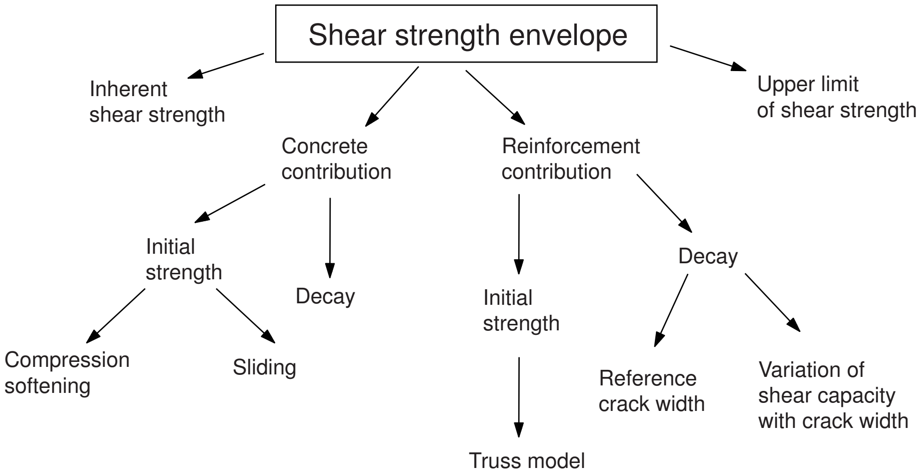

Fig. 4.25: Elements of shear strength envelope.

Application of shear crack model

The previously developed analytical model (Secs. 4.2, 4.3, and 4.4) provides a rational base to formulate separate contributions of

- Concrete compression zone, and
- Horizontal reinforcement

to shear capacity. The concept of this formulation is illustrated in Fig. 4.26. Shear transfer to the base is achieved by both an inclined concrete strut and a truss. The concrete strut allows to account for both the axial force and the amount of vertical reinforcement by one parameter which is the concrete compressive force in the base joint. Contributions of concrete and reinforcement are separately investigated in order to bound the shear strength envelope by the following criteria:

1. Initial shear strength
2. Concrete crushing
3. Sliding

All formulations are explicitly based on rotations.

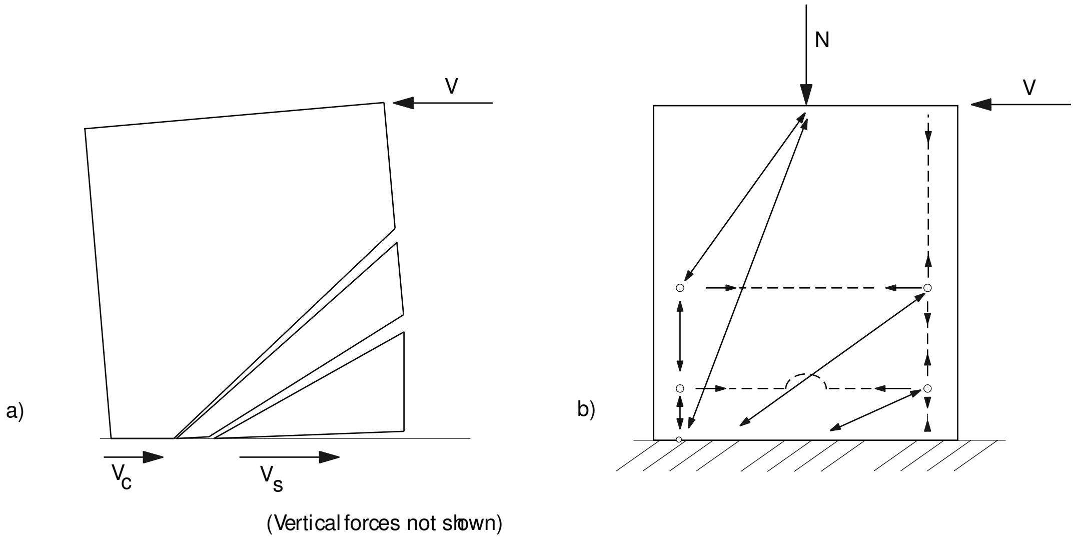

Fig. 4.26: Formulation of shear envelope a) forces, b) mechanisms.

4.5.4 Concrete contribution

Both initial strength and strength decay are investigated in order to assess the contribution of concrete to shear capacity. The assessment of concrete contribution is based on plastic theory for reinforced concrete (Sec. 2.5). The decay of concrete contribution is investigated for concrete crushing. It is assumed that, in sliding shear mode, the decayed strength is equal to the initial strength.

Initial concrete contribution

The initial concrete contribution denotes the portion of shear strength that is carried by the compressed part of cross section before strength decay occurs. The latter is due to increase of deformation. The concrete compression zone can fail in two modes:

- Concrete crushing due to both axial compression and transversal straining.
- Sliding due to degradation of aggregate interlock.

The stress resultants in the concrete compression zone near the base are shown in Fig. 4.27a. Due to load reversals, the concrete compression zone is weakened by crossing cracks. Vertical cracks originate from bond mechanism of vertical rebars (Fig. 4.22). Inclined cracks are caused by transversal straining. Both cracks and the assumed directions of principal stresses are shown in Fig. 4.27b.

Compression softening Consider the compressed toe of a wall. The symbol R denotes the resultant of both horizontal and vertical stresses (Fig. 4.27b). At failure, the stress field shown in this figure yields the following capacity (Eq. (4.34)):

$$R = \zeta\, f_c\, b_w\, \frac{x}{\cos\alpha} \tag{4.34}$$

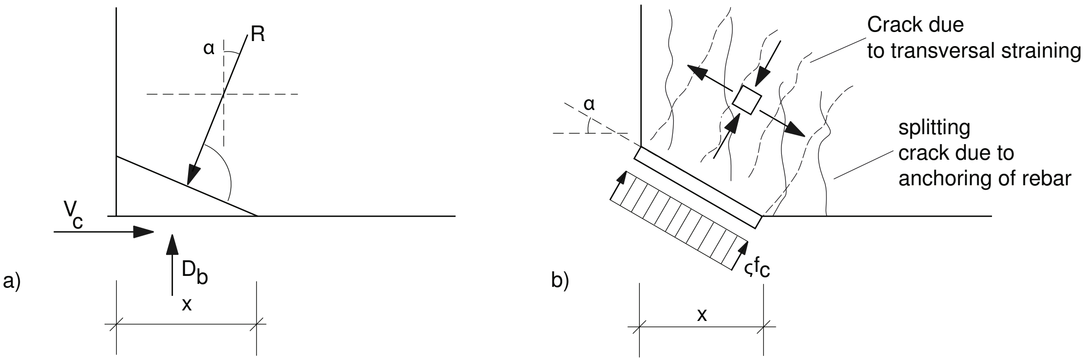

Fig. 4.27: Model for concrete contribution, a) stress resultants, b) stress field.

where the parameter ζ includes compression softening due to transversal straining. The concrete contribution to shear strength is related to this capacity according to Eq. (4.35):

$$V_c = R \sin\alpha \tag{4.35}$$

The maximum concrete compression force D_b is now determined by integrating an appropriate stress-strain relationship, e.g. that shown in Fig. 4.12. It yields:

$$D_b \approx 0.85 f_c x b_w \tag{4.36}$$

Inserting Eqs. (4.35) and (4.36) in Eq. (4.34) results in:

$$V_c = \zeta\, D_b \frac{\tan\alpha}{0.85} \tag{4.37}$$

Based on the proposals made by Vecchio & Collins (1986) compression softening is considered by $\zeta = 0.4$. Limits for lower and upper bound of strut inclination are assumed to 25° and 45°, respectively. Thus, lower and upper bounds for concrete contribution are as follows:

$$0.22 \leq \frac{V_c}{D_b} \leq 0.47 \tag{4.38}$$

Sliding strength Consider sliding in the base joint. The relationship between concrete compression force and concrete contribution to shear strength yields

$$V_c = \mu\, D_b \tag{4.39}$$

The contribution of the concrete compression zone to the shear strength thus results from a normal force on the interface and a corresponding friction constant μ (Eq.4.39). According to Walraven (1994), the friction constant is assumed equal to 0.4 (Sec. 2.4.3, p. 16).

Determination of V_c The friction constant is inside the interval between the lower and the upper bound established in Eq. (4.38). The assumption that the concrete contribution is equal to the concrete compression force times the friction constant would be conservative for both compression softening and sliding. Hence, the concrete contribution is chosen equal to 40% of the concrete compression force. This is shown in Eq. (4.40).

$$D_b = 0.85 x b_w f'_c \rightarrow V_c = 0.40 D_b = \; 0.34\,\eta\; b_w\, l_w\, f_c \tag{4.40}$$

Validation of proposal for initial strength

The concrete compression zone is supposed to supply the initial contribution to shear capacity at least until the peak of base shear is achieved. The proposal for this contribution (Eq. (4.40)) thus can be validated on test data describing preliminary shear failure. Static-cyclic tests investigating concrete contribution to shear strength were reported by Lopes (2001b).

Observed and calculated shear strengths are shown in Tab. 4.2. Note that for specimens SW16 and SW17 the supply/demand ratio of shear was equal to 0.75. The shear supply refers to the shear strength while the shear demand denotes the base shear corresponding to nominal flexural strength. The predictions of concrete contribution accurately agree with the test data. The model slightly overestimates the shear strength of specimen SW17. To conclude, the formulation of initial concrete contribution enables the prediction of shear strength in case of both diagonal tension failure and concrete crushing.

Specimen	Test V_{exp} $[kN]$	Failure mode	Concrete contrib. $0.4\,D_b$ $[kN]$	Reinf. contrib. V_s $[kN]$	Prediction $0.4\;D_b + V_s$ $[kN]$	Ratio Pred./Test $[-]$
SW13	108	Concrete crushing	40	73	113	1.05
SW16	80	Diagonal tension	40	42	82	1.03
SW17	84	Diagonal tension	40	52	92	1.10

Tab. 4.2: Validation of proposed initial concrete contribution (Tests: Lopes (2001b)).

Decay of concrete contribution

The concrete contribution decays with increase in rotation because of the following processes:

- Softening due to transversal straining when subjected to compression,
- Splitting caused by yielding of vertical rebars in tension cycles,
- Grinding of asperities at load reversals reducing sliding strength.

Herein, the object of this section is to derive criteria for shear strength envelope. It is not the objective to focus on the force-displacement relationship. Therefore, only the failure point is of particular interest. Failure is assumed when the decay of base shear is equal to 20%. The application of this assumption on the concrete compression force is shown in Fig. 4.28.

Fig. 4.28 plots the ratio $D_b/max\,D_b$ to the strain of the outermost compressed fiber. The ratio $D_b/max\,D_b$ refers to compression force divided by maximum compression force. The latter is described by Eq. (4.36). The compression force denotes the result of integration of stresses at the strain of outermost fiber.

The ratio $D_b/max\,D_b$ is independent of the position of neutral axis. However, the decay depends on the stress-strain relationship used for the concrete. Assuming both the stress-strain relationship shown in Fig. 4.12a and decay of the ratio $D_b/max\,D_b$ of 0.2, the ultimate strain is equal to 0.006. Note that this strain corresponds to the ultimate strain in Fig. 4.12a.

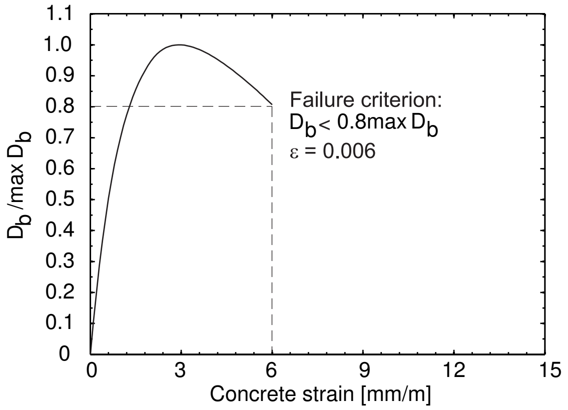

Fig. 4.28: Failure criterion for concrete crushing.

Kinematic relationships between strain at the outermost fiber and the rotation inside the plastic hinge are derived in Sec. 4.4.2. Using these relationships, the proposal for initial strength, and the assumptions on decay of concrete compression force, one can establish the following four equations:

$$\theta_c = l_{anc}\,\frac{\epsilon_c}{x} \tag{4.41}$$

$$D_{b,max} = 0.85\,x\,b_w\,f_c \tag{4.42}$$

$$D_{b,u} = 0.8\,D_{b,max} \tag{4.43}$$

$$V_c = 0.4\,D_b \tag{4.44}$$

Inserting Eqs. (4.41), (4.42), (4.43) in Eq. (4.44), the degraded concrete contribution to shear strength then is equal to

$$V_c\left(\theta_{uc}\right) = 0.27\,b_w\,f_c\,\frac{l_{anc}\,\epsilon_{cu}}{\theta_{uc}} \tag{4.45}$$

The concrete contribution according to Eq. (4.45) describes the failure mode of concrete crushing. The decay factor of concrete contribution can be determined by comparing Eqs. (4.40) and (4.45). Hence, decay factor of concrete contribution yields:

$$\lambda_c = 0.8\,\frac{\kappa\,\epsilon_{cu}}{\theta_c} \tag{4.46}$$

It is of particular interest to compare the concrete contribution with proposals from the literature. Therefore, Eq. (4.45) is rewritten as follows:

$$V_c = 0.27\,\eta\; b_w\, l_w\, f_c\, \frac{\kappa\,\epsilon_{cu}}{\theta} \tag{4.47}$$

Note that Paulay et al. (1990) proposed the equation $V_c = 0.25\eta\; b_w\, l_w\, f_c$ for the contribution of concrete compression zone to sliding strength. Assuming sliding shear mode, this proposal would include decay of concrete compression force. However, tests have shown that sliding shear strength is significantly underestimated by applying this proposal.

Division of Eq. (4.47) by the area of gross-section gives the the shear ratio corresponding to the degraded concrete contribution (Eq. (4.48)).

$$\frac{\tau}{\sqrt{f_c}} = 0.27\,\sqrt{f_c}\,\eta\,\frac{\kappa\,\epsilon}{\theta} \tag{4.48}$$

Eq. (4.48) includes the factor $0.27\,\sqrt{f_c}$ which is near to the concrete shear strength of $0.3\,\sqrt{f_c}$.

Conclusions

To conclude, proposals for both the initial strength and the strength decay of concrete contributions are made. These proposals apply on lightly reinforced concrete shear walls failing in sliding shear or concrete crushing.

- Sliding shear mode (Eq. (4.40))

  $$V_c = 0.34\,\eta\; b_w\, l_w\, f_c$$

- Concrete crushing (Eq. (4.47))

  $$V_c = 0.27\,\eta\; b_w\, l_w\, f_c\, \frac{\kappa\,\epsilon_{cu}}{\theta}$$

Decay of concrete contribution is derived for concrete crushing. For sliding shear strength, it is assumed that degraded shear strength is equal to the initial shear strength.

4.5.5 Reinforcement contribution

The reinforcement contribution to shear strength refers to the portion of base shear that is transfered in the tensioned part of the wall. Due to the degradation of aggregate interlock, the reinforcement contribution decays in sliding shear mode. Reference crack width and decay of shear capacity are investigated for this failure mode. For concrete crushing, the degraded reinforcement contribution is equal to the initial strength.

Initial shear strength

The initial reinforcement contribution in case of concrete crushing is based on the general truss model (Sec. 2.6.3). Consider a truss angle of 45° and an internal lever arm of half the wall length. The latter originates from distributed vertical reinforcement as it is shown in Fig. 4.9. The reinforcement contribution to shear capacity then can be written as follows:

$$V_s = 0.5 f_y \, \rho_h \, b_w \, l_w \tag{4.49}$$

The shear crack model is used for determination of the reinforcement contribution for sliding shear mode. The reinforcement contribution models the portion of shear that is transfered in the tensioned part of the base joint. According to Eq. (4.7), the reinforcement contribution is equal to the yield force of horizontal reinforcement crossing a 45° inclined crack. Equation (4.7) is rewritten:

$$V_s = (1 - \eta) \, f_y \rho_h \, b_w \, l_w \tag{4.50}$$

For shear walls of moderate axial force and vertical reinforcement ratio, the upper bound for the dimensionless depth of neutral axis yields 0.2. Hence, Eq. (4.50) modifies to $V_s = 0.8 \, f_y \rho_h \, b_w \, l_w$ which is common practice for the calculation of the shear strength of beams (Sec 2.6.1).

Reference crack width

Shear in the tensioned part is transferred to the base joint by aggregate interlock. Consider that uniform shear transfer per strut element depends on average crack width along the element. In this section, the relationship between crack width at tensioned boundary and reference crack width is established. The reference crack width is used in the next section to estimate shear decay due to degradation of aggregate interlock.

The kinematics of the strut elements are shown in Fig. 4.29. The elements are assumed to rotate. The pivot point for this rotation is located at the outermost compressed fiber at a distance x below the base. The parameter l_i denotes the horizontal distance between the pivot point and the center of the baseline of the i-th element. Calculation of this distance is shown in Eq. (4.51).

$$l_i = \frac{x}{2} \left(\frac{1}{\tan\, \delta_i} + \frac{1}{\tan\, \delta_{i+1}} \right) = \frac{x}{2} T \tag{4.51}$$

The angle Θ' refers to the rotation of the i-th element. Note that this angle is not equal to the overall rotation of plastic hinge because of contribution of all cracks to this rotation. The ratio

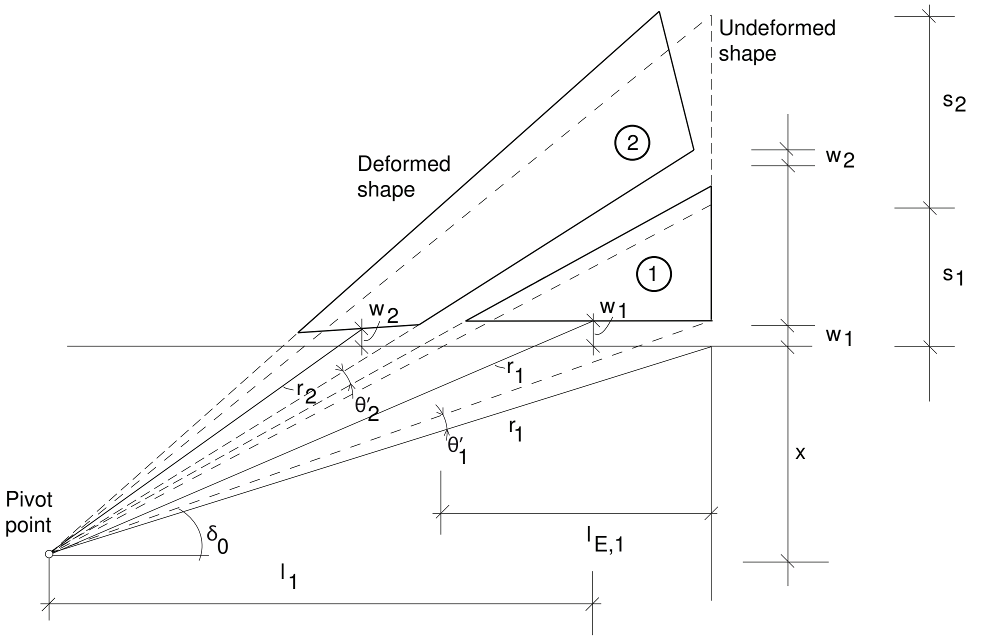

Fig. 4.29: Kinematics for average crack widths

of crack width at outermost fiber (w_i) to the crack width at the center of the element ($\bar{w}_i$) is equal to the ratio of radii r'_i and r_i.

$$\begin{aligned} \bar{w}_i &= \Theta'_i \, r_i \\ \Theta'_i &= \tfrac{1}{r'_i} \sum_{j=1}^{i} w_j \end{aligned} \implies \bar{w}_i = \frac{r_i}{r'_i} \sum_{j=1}^{i} w_j \tag{4.52}$$

The ratio of radii r'_i and r_i is determined by using Eq. (4.51). This is shown in Eq. (4.53).

$$\begin{aligned} r'_i &= \tfrac{l_w}{\cos\,\delta_i} \\ r_i &= \tfrac{x}{2\,\cos\,\delta_i} T \end{aligned} \implies \frac{r_i}{r'_i} = \frac{\eta}{2}\, T \tag{4.53}$$

Inserting Eq. (4.53) in Eq. (4.52) the crack width in the center of strut element is found (Eq. (4.54)). This equation now is evaluated for neutral axis depths of 0.10 and 0.15, and the crack pattern is shown in Fig. 4.7. Mean crack width of first element for neutral axis depths of 0.10 and of 0.15 are equal to 0.64 and 0.7 times the crack width at outermost fiber, respectively.

$$\bar{w}_i = \frac{\eta}{2} (\cot\,\delta_i + \cot\,\delta_{i+1}) \sum_{j=1}^{i} w_j \tag{4.54}$$

Consider that the capacity to transfer shear in the base joint is the same for all elements and consider also that the cracks are closed. The portion of shear transferred per element is proportional to the element length which can be calculated with the help of Eq. (4.55).

$$l_{E,i} = x \left(\frac{\tan\,\delta_{i+1} - \tan\delta_i}{\tan\,\delta_{i+1}\,\tan\delta_i} \right) \tag{4.55}$$

An example of element lengths is shown in Tab. 4.3. The element lengths are calculated for unit wall length and the crack pattern shown in Fig. 4.7.

Element (i)	Length of element and length portion $\eta = 0.10$ $l_{E,i}$	$l_{E,i}/\sum l_{E,i}$	$\eta = 0.15$ $l_{E,i}$	$l_{E,i}/\sum l_{E,i}$
1	0.72	0.82	0.59	0.72
2	0.10	0.12	0.15	0.18
3	0.05	0.06	0.08	0.10

Tab. 4.3: Element lengths for shear transfer in the base joint.

Examination of Tab. 4.3 shows that the length portion of the first element is equal to 82% and 72% for neutral axis depths of 0.10 and 0.15, respectively. Hence, this element would transfer to the bigger part of shear. Since the real distribution of shear between the elements is to difficult to determine, it is assumed that the behavior of the first element governs the shear transfer in the base joint. According to aforementioned calculation of mean crack widths (p. 116), the reference crack width for degradation of aggregate interlock is chosen equal to 0.65 times the crack width at outermost fiber (Eq. (4.56)).

$$\bar{w} \overset{!}{=} 0.65\, w_1 \tag{4.56}$$

Other researchers proposed similar relationships for the reference crack width. For example, Muttoni (2003) made a proposal that includes reference strain for aggregate interlock yielding 0.4 times the strain of the outermost fiber (Sec. 2.4.3, p. 16).

Decay of reinforcement contribution

The reference crack width is derived in the previous subsection while this section focuses on a relationship between reference crack width and shear decay. Aggregate interlock degrades due to widening of cracks (Sec. 4.5.2). It is assumed that the decay of shear capacity is closely linked to the total surface of contact areas that are perpendicular to the crack.

Walraven (1994) proposed a method for the estimation of contact areas in rough cracks (Sec. 2.4.3). This method is used herein. The sum of contact areas perpendicular to the crack is calculated for unit length in function of the dimensionless crack width and it is normalized to its maximum value. A third order polynomial approximates the resulting relationship between decay of shear capacity and and dimensionless crack width (Eq. (4.57)).

$$\lambda_s = -12\left(\frac{\bar{w}}{d_g}\right)^3 + 15\left(\frac{\bar{w}}{d_g}\right)^2 - 6.9\frac{\bar{w}}{d_g} + 1.1 \tag{4.57}$$

The dimensionless crack width denotes the crack width divided by the maximum size of aggregates. Numerical evaluation of Eq. (4.57) is shown in Fig. 4.30. Note that the curve shown in Fig. 4.30 well agrees with that of Fig. 2.11 which was used by Skrikerud & Bachmann (1986) for the modeling of the shear transfer across cracks in unreinforced concrete dams.

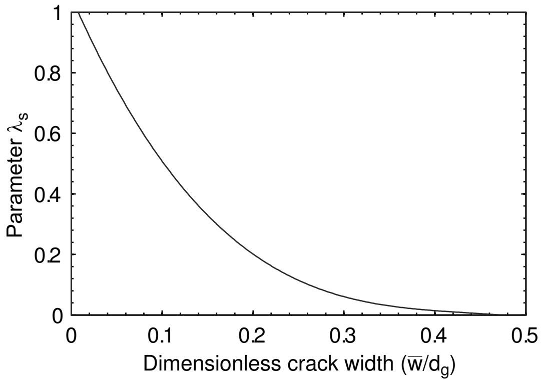

Fig. 4.30: Degradation of aggregate interlock with increase in crack width.

4.5.6 Lower and upper bounds of shear strength

Inherent shear strength

Elastic shear response is expected if the shear ratio is less than or equal to the inherent shear strength. The latter basically originates from concrete tensile strength. However, it is too difficult to study in detail the effect of tensile strength on shear strength. So, available data are used in order to provide a lower bound of inherent shear strength.

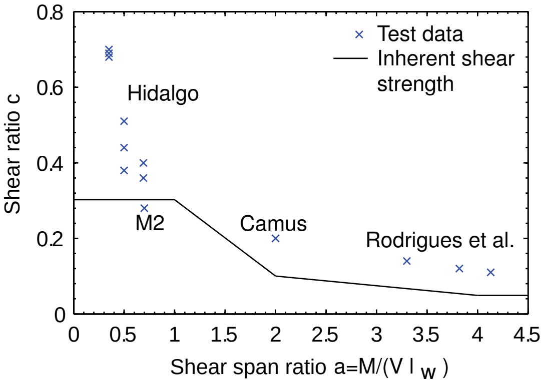

Fig. 4.31: Proposal for inherent shear strength of concrete and validation by test data.

The selected tests include both unreinforced specimen failing in diagonal tension and unreinforced specimen behaving elastically in shear. The experimental data are shown in Fig. 4.31. In this context, the term unreinforced refers to lacking transverse reinforcement. Hidalgo et al. (1998) investigated the static-cyclic behavior of squat shear walls failing in diagonal tension (Sec. 2.3.4). Rodrigues et al. (2005) investigated shear-flexure interaction in beams which also failed in diagonal tension (Sec. 2.4.3). Both test series thus form an upper bound of inherent shear strength. Elastic shear response was observed by Coin et al. (2002) and Greifenhagen et al. (2005).

The analysis of the aforementioned experimental data has shown that inherent shear strength is related to the shear span ratio a. The latter refers to the shear span divided by the height of the gross-section. The proposal for inherent shear strength is presented in Eq. (4.58). It is also included in Fig. 4.31.

$$\begin{array}{rcccccl} & & a & \leq & 1.0 & : & c_i = 0.3 \\ 1.0 & \leq & a & \leq & 2.0 & : & c_i = 0.5 - 0.2\ a \\ 2.0 & \leq & a & \leq & 4.0 & : & c_i = 0.15 - 0.025\ a \\ & & a & \geq & 4.0 & : & c_i = 0.05 \end{array} \tag{4.58}$$

The inherent shear strength is assumed to be equal to $0.3\sqrt{f_c}$ for shear span ratios less than or equal to 1.0. It linearly decreases to $0.1\sqrt{f_c}$ up to shear span ratio of 2.0. Further linear decrease to $0.05\sqrt{f_c}$ is assumed up to shear span ratio equal to 4.0 and then it is constant.

Upper limit of shear strength

Limitation of the shear stress is required in order to account for concrete deterioration due to high levels of shear. Upper bounds of shear strength are shown in Tab. 4.4 for selected values of concrete compressive strength. The bounds of shear strength according to the general truss model (Tab. 2.3) are used for this calculation. Maximum and minimum values correspond to strut inclinations of 25° and 45°, respectively. The shear strength is computed as follows

- minimum: $\alpha = 25°$, $\tau_{c,u} = 0.38\zeta f'_c$
- maximum: $\alpha = 45°$, $\tau_{c,u} = 0.50\zeta f'_c$

where ζ accounts for compression softening due to transversal straining. A value of 0.4 is used for this parameter. The shear strength normalized to the square root of concrete compressive strength is also shown in Tab. 4.4. Paulay et al. (1990) proposed ultimate shear stress for walls of 0.83 to 0.9 $\sqrt{f'_c}$ (Eq. (2.41) and (2.43)). For commonly used concrete strengths of 25 to 30 MPa, this proposal well agrees with predictions according to the general truss model.

f'_c	$\zeta f'_c$	$\alpha = 25°$		$\alpha = 45°$	
		$\tau_{c,u}$	$\tau_{c,u}/\sqrt{f'_c}$	$\tau_{c,u}$	$\tau_{c,u}/\sqrt{f'_c}$
16.0	6.4	2.43	0.61	3.20	0.80
25.0	10.0	3.80	0.76	5.00	1.00
30.0	12.0	4.56	0.83	6.00	1.10
35.0	14.0	5.32	0.90	7.00	1.18
40.0	16.0	6.08	0.96	8.00	1.26

Units: [MPa]

Tab. 4.4: Upper limit of shear strength vs. concrete failure according to General Truss Model (Sec. 2.6.3).

4.5.7 Summary of the shear strength envelope

Investigations on initial strength and strength decay were conducted in the previous sections for both concrete and reinforcement contribution. These investigations form the framework of assessement of deformation capacity that is shown in Fig. 4.30. The established criteria for initial shear strength, concrete crushing, and sliding are summarized in the following. In addition, inherent shear strength of walls is suggested according to Eq. (4.58). The application of the shear strength envelope is shown in Sec. 4.5, p. 106.

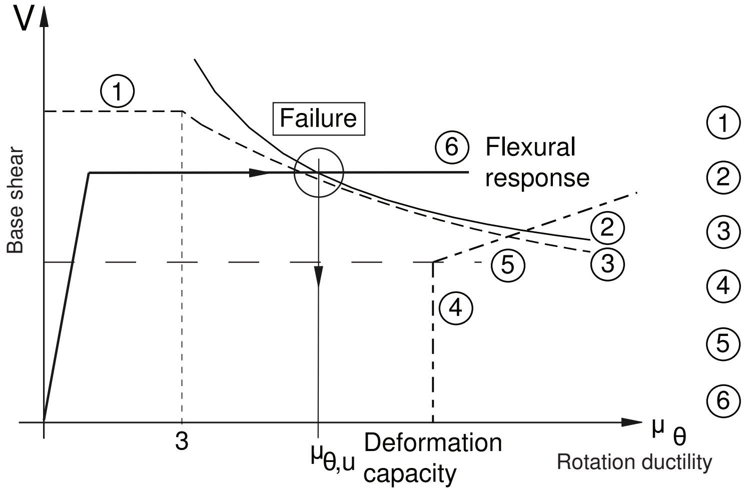

Fig. 4.32: Assessment of deformation capacity.

Initial shear strength

The initial shear strength is composed of contributions of both concrete compression force and reinforcement. The latter is calculated by assuming a 45° inclined crack. Equation (4.59) describes the initial shear strength:

$$V = 0.4\,D_b + V_s = (0.34\,\eta\,f_c + (1-\eta) f_y\,\rho_h)\,b_w\,l_w \leq 0.8\,\sqrt{f_c}\,b_w\,l_w \tag{4.59}$$

Concrete crushing

A truss model embracing an inclined concrete strut is used to assess deformation capacity restricted by concrete crushing (Eq. (4.60)). The assumptions of this model include localization of concrete strains near the base and an internal lever arm of half of the wall length.

$$V = 0.4\,D_b\,(\theta) + V_s = \left(0.27\eta\,f_c\,\frac{\kappa\,\epsilon_{cu}}{\theta} + 0.5 f_y\,\rho_h\right)\,b_w\,l_w \tag{4.60}$$

Sliding

Degradation of shear capacity due to sliding in the base joint is modeled by Eq. (4.61). It is assumed that the reinforcement contribution degrades and concrete supplies constant shear capacity which is equal to the concrete compression force times a friction constant.

$$V = 0.4\,D_b + V_s\,(\theta) = (0.34\,\eta\,f_c + \lambda_s\,(1-\eta)\,f_y\,\rho_h)\,b_w\,l_w \tag{4.61}$$

4.6 Conclusions

An analytical model is proposed for the assessment of deformation capacity of squat shear walls subjected to static-cyclic loading. The model includes assumptions on crack pattern, strain localization, bond, and strength decay.

Possible applications of the model are the predictions of both the static-cyclic envelope and the shear strength envelope. The model is valid within lower and upper limits of application which are shear stresses equal to $0.3\sqrt{f_c}$ and $0.8\sqrt{f_c}$, respectively.

The development of the model is motivated by the underestimation of deformation capacity when using lumped plasticity approaches from the literature. The shear wall is modeled as a plastic hinge over the entire wall height. Hence, the rotation of this plastic hinge is equal to the lateral drift. Deflection due to sliding is not included in the model.

Kinematic relationships are established that relate both strains and crack widths to the rotation. Therefore, the base shear can be explicitly computed from rotations by using constitutive relationships and bond models from the literature. In addition, section deformation is assumed to occur in plastic response.

The contributions of concrete and transversal reinforcement to shear capacity are formulated in terms of initial strength and strength decay due to increase in rotation. Four bounds define the shear strength envelope. These bounds are the upper limit of shear strength, concrete crushing, sliding mode, and elastic shear response.

The parameters of the model are shown in Tab. 4.5.

Symbol	Designation	Value
α_w	Crack width ratio	Eq. (4.24)
c	Shear ratio, $c = \frac{\tau}{\sqrt{f_c}}$	$0.3 \leq c \leq 0.8$
s	Average crack width on tensioned boundary	$0.05d\frac{1-\rho}{\rho} \leq s \leq 0.1d\frac{1-\rho}{\rho}$
$\bar{w}$	Reference crack width	$0.65\, w_1$
x	Neutral axis depth	
α_w	Crack width ratio	$1.0 \leq \alpha_w = 3.5c \leq 1.75$
ϵ_{1c}	Peak strain (concrete)	0.003
ϵ_{cu}	Ultimate strain (concrete)	0.006
λ_s	Decay of shear strength due to widening of cracks	Eq. (4.57)
κ	Coefficient of strain localization	$1.0 \leq \kappa \leq \frac{l_{anc}}{x}$
μ	Friction constant of rough concrete	$0.4 \leq \mu \leq 0.47$
ξ	Ratio of internal lever arm to wall length	0.5

Tab. 4.5: Parameters of analytical model.

Chapter 5

Validation

5.1 Contents

In this chapter, predictions achieved with the previously developed analytical model are made for the follows:

- Static-cyclic envelope curve
- Domain of feasibility of rotations
- Deformation capacity assessed with the static-cyclic envelope

This chapter also includes the application of the analytical model for the static-monotonic response. The prediction is compared with both test data and another prediction achieved with a strut and tie model. Conclusions are presented at the end of each section.

In addition, attempts are made for the application of the shear strength envelope for the identification of full-size walls susceptible to shear.

5.2 Comparison with strut and tie model

5.2.1 Strut and tie model

The specimens tested by Maier & Thürlimann (1985) are used to compare predictions of the analytical model with those made by strut and tie model. The reinforcement ratio of these specimens are:

- Specimen S4: $\rho_v = \rho_h = 1.03\%$
- Specimen S9: $\rho_v = 1.03$, $\rho_h = 0.00\%$

The observed failure modes of specimen S4 and S9 are concrete crushing and diagonal tension, respectively. The strut and tie model is shown in Fig. 5.1a and the calculation of the non-linear response is illustrated in Fig. 5.1b. The force distribution between the subsystems is based on actual stiffness of subsystems which are assumed to have equal lateral displacements.

The strut and tie model consists of superimposed subsystems (Fig. 5.2a). Each subsystem is composed of a strut and a tie. Linear-elastic and linear-elastic- perfectly plastic behavior

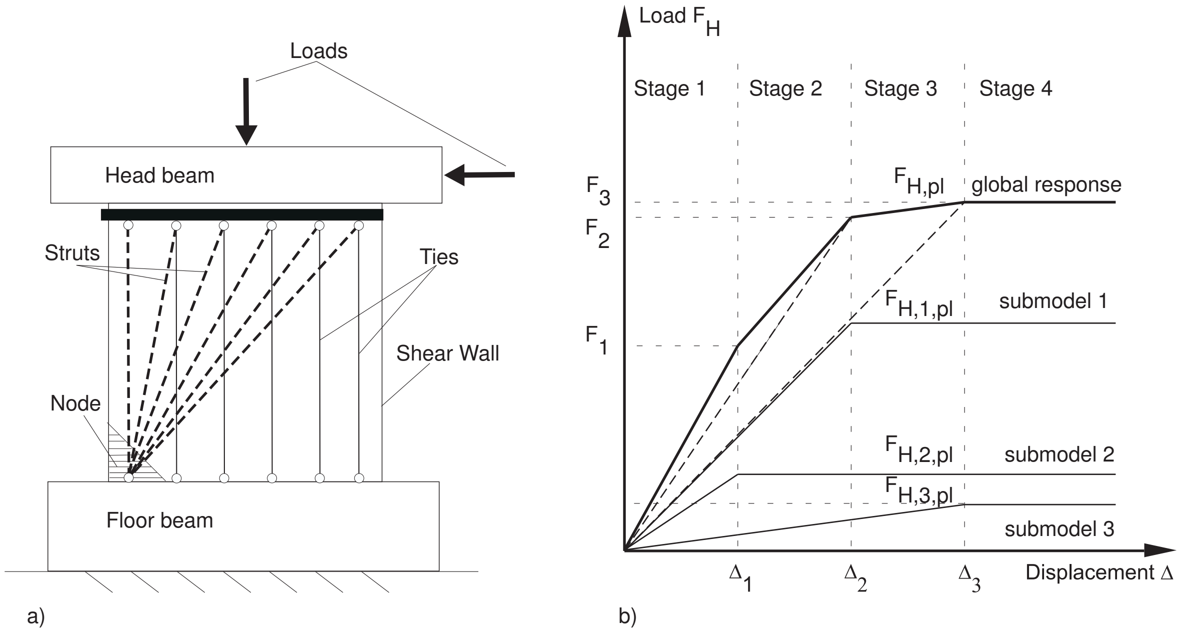

Fig. 5.1: Strut and tie modeling of Specimen S4: a) model, b) solution strategy.

is assumed for struts and ties, respectively (Fig. 5.2b). In addition, the stiffness of the ties considers the stiffness of rebars. Tension-stiffening due to concrete surrounding the rebars is not included in the model. It is assumed that the tension-stiffening has only minor influence on stiffness because of reinforcement ratios equal to 1%.

The resultants of horizontal and vertical forces are calculated in the node (Fig. 5.1a) and assumptions are made on compression softening ($\zeta = 0.5$).

Analytical model

The stress-strain relationships are shown in Fig. 5.3a. They are based on the models available in the literature (Sec. 2.4.1). Since specimen S9 has no transversal reinforcement, softening is considered according to the model shown in Fig. 2.9.

The localization parameter of compressive strains is partly based on the results of literature review presented in Sec. 2.5.2. The parameter κ is assumed to increase linearly from 0 to 2.0 up to peak strain, it decreases then until the maximum compressive force of concrete is attained (Fig. 5.3b). The parameter κ is constant in the post peak range. So, the variation of the parameter κ is completely different as what is proposed in Fig. 4.23.

Results

Results of modeling are shown in Figs. 5.4a and 5.4b for the strut and tie model and the analytical model, respectively. Both model accurately predict strength and ascending branch of force-displacement relationship. Note that the curves shown in Fig. 5.4b only include the displacements due to rotations. However, the advantage of the analytical model is to clearly predict when concrete crushing occurs.

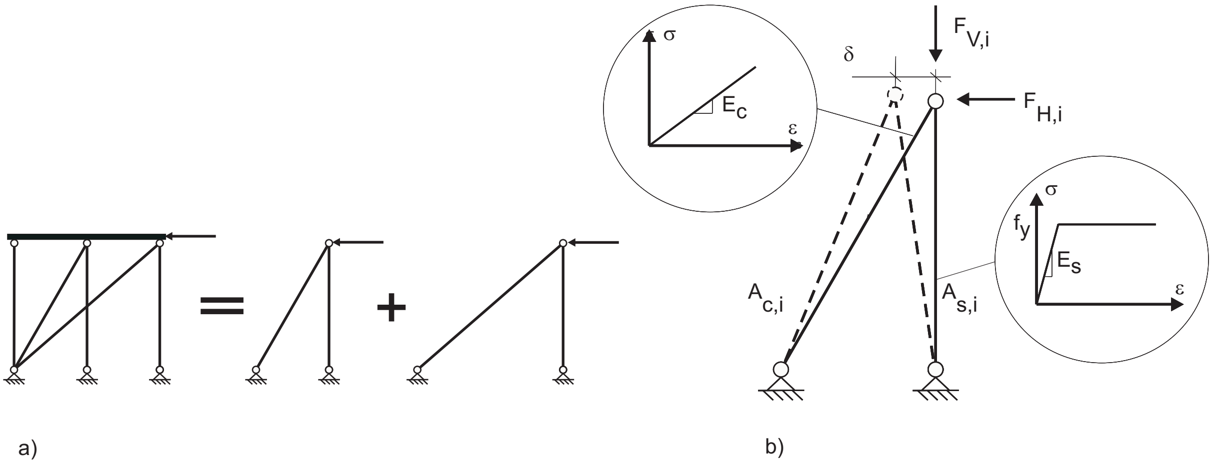

Fig. 5.2: Strut and tie modeling, a) submodels, b) loads and stress-strain relationships of submodel.

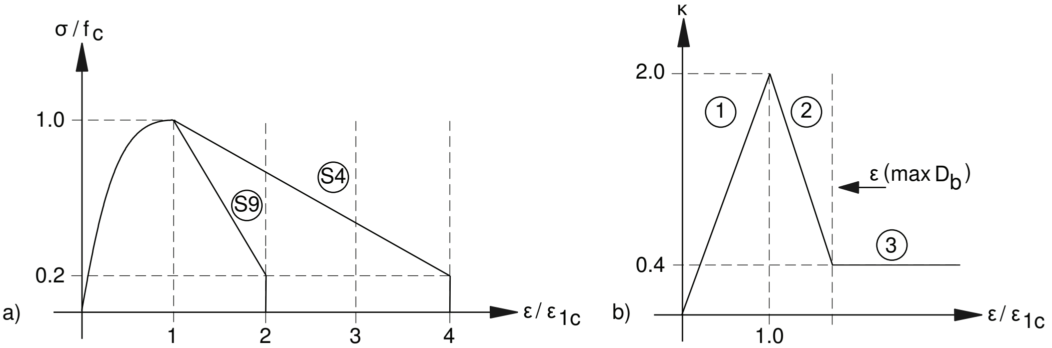

Fig. 5.3: Application of analytical model on specimens S4 and S9, a) stress-strain relationships, b) Variation of strain localization coefficient.

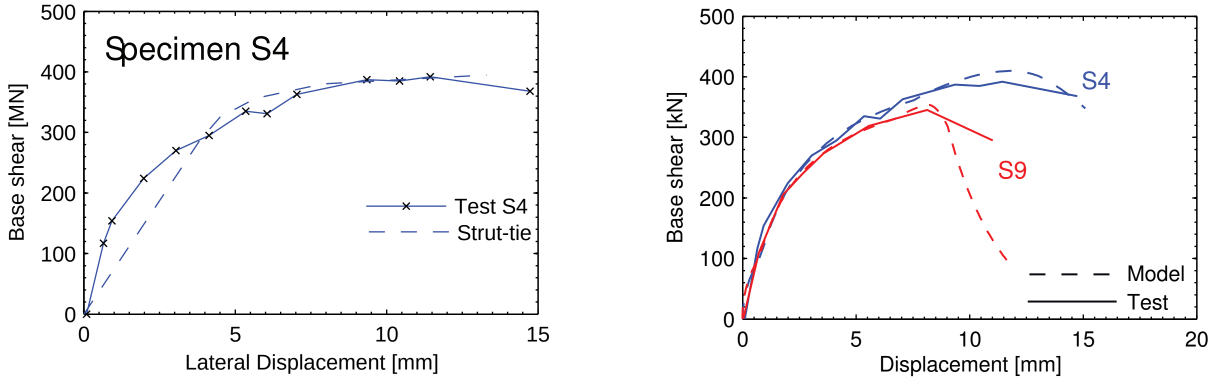

Fig. 5.4: Force displacement relationship (S4, S9), a) Strut and tie model, b) analytical model (RM).

5.3 Application of cracked membrane model

5.3.1 Description

This section presents the application of the cracked membrane model (Kaufmann & Marti 1998) for the calculation of the static-cyclic envelope curve of specimen M3 (Sec. 3.3.1, p. 61). As it was concluded in (Sec. 2.5.4, p. 26), the application of compression field models on members with low reinforcement is not possible. However, there is experimental evidence that the tensile strength of concrete under cyclic loading is significantly less than that under static-monotonic loading (Sec. 4.2.2, p. 88). Therefore, the effective tensile strength is used in the relationships of the cracked membrane model.

The cracked membrane model is slightly modified to consider displacement controlled loading. So the distortion γ_{xz} is introduced as independent parameter. Strains and stresses then are iteratively computed by using the following scheme that provides basically a set of two equations (Eq. (5.6),(5.7)) to determine two unknowns (ϵ_z, θ). Although the algorithm includes only two variable, it revealed the that use of an probabilistic search algorithm is appropriate. The algorithm PGSL proposed by (Raphael & Smith 2003) is used to enhance convergence.

5.3.2 Algorithm

1. Set distortion γ_{xz}.

2. Suppose vertical strain ϵ_z and strut inclination θ.

3. Calculate horizontal strain

$$\epsilon_x = \epsilon_z + \frac{\gamma_{xz}}{\tan(2\theta)} \tag{5.1}$$

4. Principal strains

$$\epsilon_3 = \frac{\epsilon_x + \epsilon_z}{2} - \frac{1}{2}\sqrt{(\epsilon_x - \epsilon_z)^2 + \gamma_{xz}^2} \tag{5.2}$$

$$\epsilon_1 = \frac{\epsilon_x + \epsilon_z}{2} + \frac{1}{2}\sqrt{(\epsilon_x - \epsilon_z)^2 + \gamma_{xz}^2} \tag{5.3}$$

5. Calculate steel stresses, including tension stiffening

6. Compute concrete stresses, including softening

$$f_{c2} = \frac{f_c^{2/3}}{0.4 + 30\,\epsilon_1} \tag{5.4}$$

$$\sigma_c = f_{c2}\,(\epsilon_3^2 + 2\,\epsilon_3\,\epsilon_{Co})/\epsilon_{Co}^2 \tag{5.5}$$

7. Compute equilibrium

$$eqX = \rho_X\, \sigma_{Xsr} + \sigma_C (\sin(\theta))^2 \tag{5.6}$$
$$eqZ = -\sigma_Z + \rho_Z \sigma_{Zsr} + \sigma_C (\cos(\theta))^2 \tag{5.7}$$

8. Check convergence

$$f = abs(eqX) + abs(eqZ) + abs(eqTh); \tag{5.8}$$

9. Adapt (ϵ_z, θ) if convergence not achieved, and re-run steps 1 to 6
10. Calculate shear stress

$$\tau_{XZ} = -\sigma_C\ \sin(\theta)\ \cos(\theta) \tag{5.9}$$

11. Repeat calculation for next γ_{xz}

The variable eqTh introduces a penalty function for tensile concrete stresses:

$$\epsilon_3 > 0 \quad \rightarrow \quad eqTh = \left|10^3 \epsilon_3\right| \tag{5.10}$$
$$\epsilon_3 < 0 \quad \rightarrow \quad eqTh = 0 \tag{5.11}$$

A value of 0.1 is given to the threshold for the objective function f.

5.3.3 Results

Both the results of the calculations and experimental data are shown in Fig. 5.5. The envelope of second cycles of specimen M3 is compared with the predicted response. The model accurately predicts strength. However, the post-peak branch is not predicted.

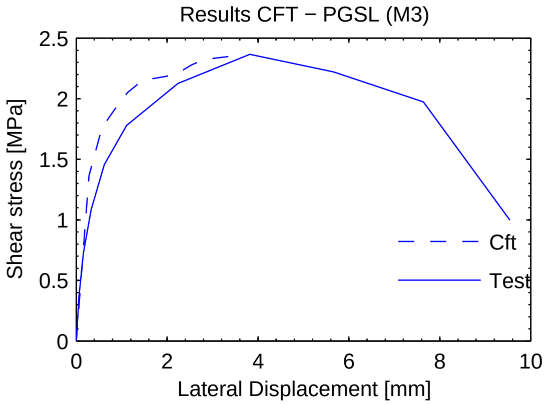

Fig. 5.5: Modeling of specimen M3 using compression field approach.

5.4 Application of analytical model

In this section, the analytical model developed in Chapter 4 is validated using the test data presented in Chapter 3. Validation is provided for

- The domain of feasibility for rotations.
- The envelope of static-cyclic response.
- The shear strength envelope.

The estimated deformation capacity is compared with the predictions according to the lumped plasticity model (Priestley & Park 1987). In addition, the ductility supply evaluated according to both the analytical model and the Revised UCSD-model (Kowalsky & Priestley 2000) are analyzed. It is found, that the proposed analytical model accurately predicts both drifts and ductility. The analytical model shows the potential to enhance significantly the prediction of the deformation capacity of squat walls.

5.4.1 Domain of feasibility for rotations

The rotation capacity of a wall is supposed to be restricted by both

- Tensile failure of vetical reinforcement
- Crushing of concrete.

The previously formulated analytical model (Secs. 4.1, 4.2, 4.3, 4.4) provides relationships that describe the domain of feasibility bounded by these failure modes. Such relationships are subsequently derived and validated.

Tensile failure of reinforcement

The rotation at tensile failure of vertical reinforcement depends on the crack pattern, the ratio of crack widths, and the bond properties of rebars. For rebars of 6 mm diameter and concrete compressive strength of 25 MPa, the crack width at tensile failure of vertical rebars approximately equals

$$w_{max} = 8.6\,mm$$

This crack width is calculated according to Sec. 4.4.1, (p. 99). The calculation of this crack width includes two assumptions:

1. an unbonded length of 2.5 times the diameter of rebar on both sides of the crack, and
2. the rebar is fully anchored.

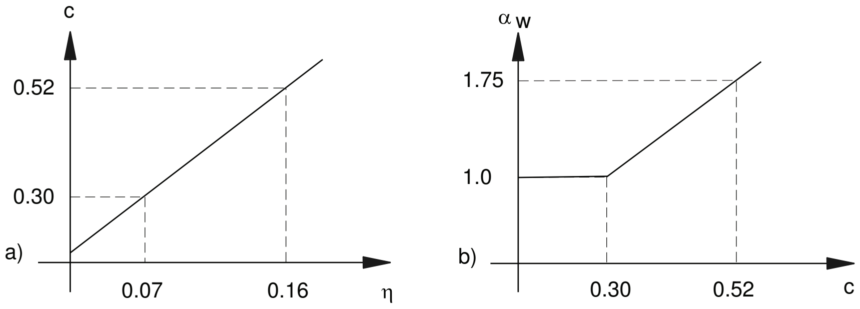

Fig. 5.6: Relationships between shear ratio and neutral axis (a), and between sum of crack widths and shear ratio (b).

A linear relationship is supposed between shear ratio (c) and normalized neutral axis depth because the depth of neutral axis (η) is proportional to the flexural strength. According to Sec. 4.2.2 (p. 88), proportionality is supposed between shear ratio c and the vertical extension of cracking. Since the vertical extension of cracking influences the crack width ratio, proportionality is also supposed between crack width ratio (α_w) and shear ratio. The relationships $c - \eta$ and $\alpha_w - c$ are shown in Figs. 5.6a and 5.6b, respectively. Both relationships are calibrated on the test results by assuming shear ratios of 0.30 and 0.52 for uncracked panel and fully developed crack pattern, respectively.

To link rotation and crack width of base crack, the crack width ratio (Eq. (4.23)) is used in Eq. (4.21). Hence, the latter equation modifies to Eq. (5.12).

$$\theta_s = \frac{\sum w}{l_w(1-\eta)} \rightarrow \theta_s = \frac{\alpha_w w_1}{l_w(1-\eta)} \tag{5.12}$$

Inserting the relationships shown in Fig. 5.6 into Eq. (5.12), one obtains a criterion for rotation capacity at failure of vertical reinforcement:

$$\theta_{us} = \frac{w_{max}\,(3.8\,c - 0.13)}{1000\,l_w(1.1 - 0.4\,c)} \tag{5.13}$$

where units of the maximum crack width and the wall length are millimeters and meters, respectively.

Concrete crushing

Concrete crushing is assumed to occur at the concrete compressive strain equal to 0.006 (Sec. 4.3.3, p. 94). It is also assumed that the anchoring length of rebars is equal to 250 mm.

Equation (4.29) provides a kinematic relationship between concrete strains and rotations. Using both, Eq. (4.30) and the relationship plotted in Fig. 5.6a, in Eq. (4.29), a criterion for rotation capacity restricted by concrete crushing is obtained. This criterion is shown in Eq. (5.14). It is evaluated for the aforementioned concrete strain and anchoring length.

$$\theta_{uc} = \frac{\epsilon_{cu}\,l_{anc}}{l_w(0.42\,c - 0.047)} \rightarrow \theta_{uc} = \frac{1.5}{1000\,l_w(0.4\,c - 0.05)} \tag{5.14}$$

Note that in Eq. (5.14) the unit of wall length is Meter.

Results

The criteria for rotation capacity at concrete crushing and rebar rupture are plotted in Fig. 5.7 for a selected range of both shear ratios and wall length. The test results are also shown in this figure. The curves accurately predict the observed failure modes of specimens (Sec.3.3).

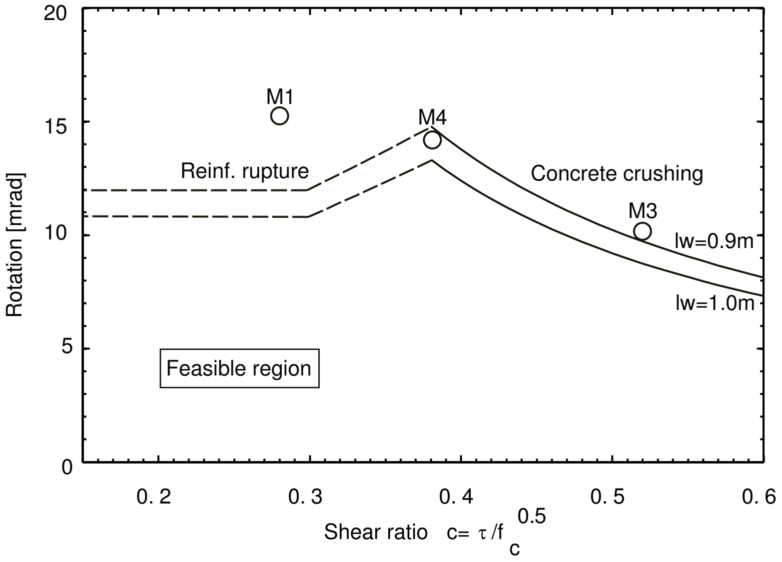

Fig. 5.7: Feasible region of rotation capacity.

The feasible region consists of three zones:

- Constant rotation capacity ($c < 0.3$)
- Increasing rotation capacity ($0.3 \leq c \leq 0.38$)
- Decay of rotation capacitiy ($0.38 < c$)

The rotation capacity is constant for shear stresses less than $0.3\sqrt{f_c}$ because of the elastic shear response caused by the inherent shear strength of concrete. When the shear ratio increases from $0.3\sqrt{f_c}$ to $0.38\sqrt{f_c}$, cracks form in the panel. The rotation capacity increases up to the bound of concrete crushing is attained. For shear stresses greater than $0.38\sqrt{f_c}$, the rotation capacity decreases due to concrete crushing.

Increase in wall length induces reduction of deformation capacity. Since the criteria for rotation capacity are based on the strains of the outermost fibers of the gross section, increasing the distance between the fibers results in decrease of rotation.

5.4.2 Static-cyclic envelope

Calculation steps

The formulation of analytical model that is presented in Secs. 4.2, 4.3, and 4.4 enables the calculation of the envelope curve of static-cyclic response. The algorithm for this calculation is divided into 12 steps:

1. Compute moment-curvature relationship
2. Determine discrete crack pattern (Sec. 4.2.2)
3. Set rotation.
4. Calculate maximum compressive strain. (Eqs. (4.31), (4.32)).
5. Calculate concrete compressive force by integration of stresses (Eq. (4.16)).
6. Determine reinforcement force from axial equilibrium condition (Eq. (4.19)).
7. Calculate lever arm of tensile force (Fig. 4.14).
8. Compute base shear and bending moment (Eq. (4.20)).
9. Adapt neutral axis position (in post peak-range only, Fig. 5.9).
10. Increase the rotation and repeat the steps 3 to 9 up to failure.
11. Check for preliminary failure of vertical reinforcement Eq. (5.12), Fig. 5.6.
12. Check shear capacity (Sec. 4.5).

Both the calculated and the observed static-cyclic envelopes are shown in Fig. 5.8. The criterion for rebar failure is derived from Eq. (5.12),the relationship between crack width ratio (a_w) and shear ratio (c, Fig. 5.6), and the relation $V = c\sqrt{f_c}\,A_g$. The analytical model accurately predicts failure mode, pre-peak and post-peak branch of static cyclic envelope. Note that the envelope of second cycles is used for the validation of the model.

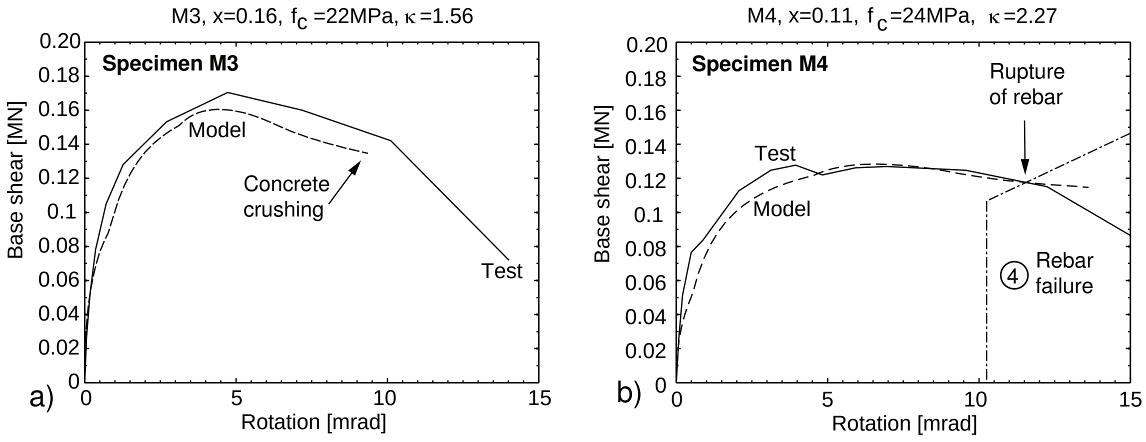

Fig. 5.8: Predicted and measured rotations, a) Specimen M3, b) Specimen M4.

Neutral axis position in postpeak branch

The post-peak response shown in Fig. 5.8 is calculated by assuming increase in position of neutral axis. The neutral axis position x increases in post-peak branch due to:

- Spalling of concrete cover
- Softening and crushing of concrete
- Tensile capacity of vertical reinforcement

Increasing the depth of neutral axis enhances correlation with the test data for both specimens M3 and M4 and enables calibration of the model. Fig. 5.9 shows the scheme used for the increase of neutral axis position (x). The validity of the relationship for parameter s_0 is limited to increments in rotation of 10^{-4}.

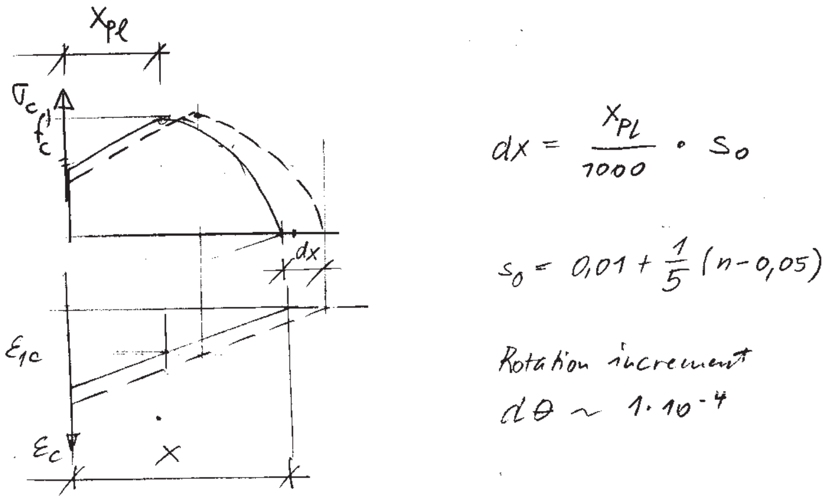

Fig. 5.9: Increase of neutral axis in post-peak branch.

Result summary

The results are summarized in Tab. 5.1. The rotation response of specimen M4 is overestimated by 6% while the response of specimen M3 is correctly predicted. However, the calculated drift is equal to approximately 75% of the observed drift, since deflection due to both sliding and distortion is not included in the model.

Specimen	Pred. θ_{pr} $[mrad]$	Test θ_{te} $[mrad]$	Pred./Test θ_{pr}/θ_{te} $[-]$	Drift pred. $\varphi_{pr}/\varphi_{te}$ $[-]$
M3	9.5	9.0	1.06	0.76
M4	11.5	11.5	1.00	0.73

Tab. 5.1: Result summary for validation of static cyclic envelope (Tests: Tab. 3.6).

5.4.3 Plastic hinge length

Since deformation capacity is underestimated for the specimens M1, M2, M3 and M4, better results can be achieved by increasing the plastic hinge length for shear spans less than 2.0. Analysis of variation of tensile force along wall height indicates shear lag of 0.2 for shear span ratio of 1.0 (Fig. 4.10). A proposal for plastic hinge length is shown in Eq. (5.15):

$$l_p = \alpha_l \, L_v + 0.022 \, d_s \, f_y \quad \begin{array}{rcl} l_v \leq 1.0 & : & \alpha_l = 0.2 \\ 1.0 < l_v < 2.0 & : & \alpha_l = 0.32 - 0.12 \, l_v \\ l_v \geq 2.0 & : & \alpha_l = 0.08 \end{array} \tag{5.15}$$

In addition, analysis of the yield penetration part in Eq. (2.107) shows that the yield penetration is underestimated by 33% for bars of 6 mm diameter. According to the results shown in Fig. 4.17 the yield penetration of such bars is equal to 100 mm. The yield strength of these rebars is equal to 504 MPa. Dividing yield penetration by both yield strength of rebars and rebar diameter gives 0.033. Equation (5.15) thus modifies to Eq. (5.16).

$$l_p = \alpha_l \, L_v + 0.033 \, d_s \, f_y \tag{5.16}$$

However, the aforementioned yield penetration is calculated for concrete compressive strength equal to 25 MPa. Yield penetrations smaller than the aforementioned value are expected for concrete compressive strengths greater than 25 MPa. Hence, the proposal given by Eq. (5.16) should be used for only compressive strengths equal to or less than 25 MPa.

5.4.4 Shear strength envelope

The shear strength envelope enables rapid, explicit estimation of deformation capacity. The failure point is defined as the intersection of the shear strength envelope and the bilinear model approximating flexural response of the structural element.

Calculation steps

The calculation starts with curvature analysis that provides base shear at first yield, nominal flexural strength, and neutral axis position. Then, the next steps are performed according to the following list:

1. Curvature analysis for determination of flexural strength and neutral axis position.
2. Calculation of yield rotations (Eq. (5.17)).
3. Bilinear model.
4. Estimation of initial shear strength (Eq. (4.59)).
5. Determination of relation of reference crack width to rotation (Eq. (5.18)).
6. Calculation of shear strength decay (Eqs. (4.60), (4.61)).
7. Determination of the shear strength envelope (Eqs. (4.60), (4.61))
8. Assessment of deformation capacity (Fig. 4.32).

Step 1: Curvature analysis

The base shear - curvature relationships of the specimens M1, M3, and M4 are shown in Fig. 4.4. The dimensionless neutral axis positions are equal to 0.07, 0.12, and 0.18 for specimen M1, M2, and M3, respectively.

Step 2: Yield rotations

The calculation of yield rotations requires the sum of crack widths at first yield ($\sum w$), the ratio of base shear at first yield to the base shear at nominal flexural strength (α_y, Tab. 3.3), the wall length (l_w), and dimensionless neutral axis position (η).

$$\theta_y = \frac{\sum w}{\alpha_y \, lw(1-\eta)} \tag{5.17}$$

Replacing the variables in Eq. (5.17) by the appropriate values for Specimen M3, results in Eq. (5.18).

$$\theta_{y\,M3} = \frac{0.70}{0.82 \, \cdot \, 0.9(1-0.18)} = 1.16 \approx 1.2 \tag{5.18}$$

The yield rotation of specimen M4 is assumed to be equal to the yield rotation of specimen M3. Both, the yield rotation for specimen M3 and the yield rotation for specimen M4 compare favorably with the yield rotations determined from the test data (Tab. 3.3).

Step 3: Bilinear model

The bilinear model approximates the flexural response. It consists of linear-elastic - perfectly plastic relationship. Linear-elastic response is assumed up to yield rotation and base shear at nominal flexural strength.

Step 4: Estimation of initial shear strength

The initial shear strength is calculated by using Eq. (4.59). The initial strengths of specimens M1, M3, and M4 are indicated in Figs. 5.11, 5.12, and 5.13, respectively.

Step 5: Reference crack widths

Next, the relationship between the reference crack width and the rotation is established by inserting Eq. (4.56) in Eq. (5.12):

$$\theta = \frac{\alpha_w \bar{w}}{0.65\, l_w (1-\eta)} \;\rightarrow\; \bar{w} \;=\; \frac{0.65\;\theta}{\alpha_w}\, l_w\,(1-\eta) \tag{5.19}$$

Consider the relations between the shear ratio and the crack width ratio (Eq. (4.24)), the wall lengths, and the depths of neutral axis position. The reference crack width then can be related to the rotation of the plastic hinge. This is shown in Eqs. (5.20) and (5.21).

$$\bar{w}_{M3} \;=\; \frac{0.65}{1.75}\, 0.9\,(1-0.18)\,\theta \;=0.27\,\theta \tag{5.20}$$

$$\bar{w}_{M4} \;=\; \frac{0.65}{1.30}\, 0.9\,(1-0.12)\,\theta \;=0.40\,\theta \tag{5.21}$$

Step 6: Decay of shear capacity

The results obtained in Eqs. (5.20) and (5.21) are used in Eq. (4.57) to establish a relation between rotation in the plastic hinge and the shear decay due to opening of the base crack. Since shear decay is assumed to occur only in the post-peak branch, three times the yield rotation is added to the rotation due to opening of the reference crack. Thus, the decay curves are shifted along the axis of rotations. The decay of shear capacity is shown in Fig. 5.10 for both specimen M3 and specimen M4.

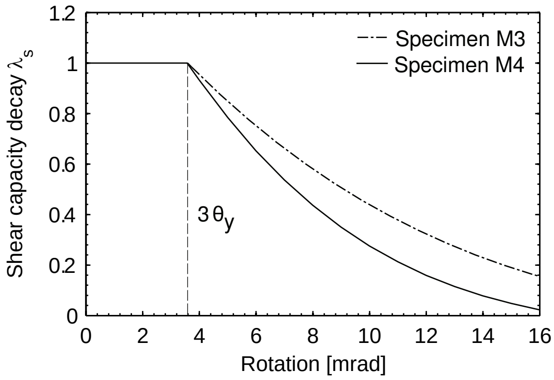

Fig. 5.10: Decay of shear capacity due to widening of base crack (Specimens M3 and M4).

The curves shown in Fig. 5.10 predict greater decay of shear capacity for specimen M4 than for specimen M3. Since the shear ratio of specimen M4 is less than the shear ratio of specimen M3, smaller vertical extension of cracking is expected for specimen M4. Thus, cracking localizes near the base and specimen M4 needs greater crack width of the base joint to achieve the same rotation as specimen M3.

Step 7: Determination of the shear strength envelope

According to Step 4, and Eqs. (4.60), and (4.61), the shear strength envelope is enclosed by the criteria for initial strength, concrete crushing and sliding shear. Note that in sliding shear mode the concrete contribution is equal to the initial shear strength while in concrete crushing constant reinforcement contribution is assumed (Sec. 4.5.7). The shear strength envelopes of specimens M1, M3, and M4 are shown in Figs. 5.11, 5.12, and 5.13, respectively.

Step 8: Determination of deformation capacity

The deformation capacity is determined by extrapolation of the bilinear model to the shear envelope. This is shown in Figs. 5.11, 5.12, and 5.13, respectively. The results are summarized in Tab. 5.2.

Assessment of specimen M1

The assessment of deformation capacity of specimen M1 is shown in Fig. 5.11. The shear ratio corresponding to the flexural strength is less than the inherent shear strength. Thus, the deformation capacity is governed by rupture of rebars. Both yield rotation and ultimate rotation are underestimated. The calculated rotation is equal to 10.3 mrad while rupture of vertical reinforcement was observed in test at 16.5 mrad.

Possible reason for underestimation of ultimate rotation is the spalling of concrete at the wall edges that is not considered in the analytical model. Such spalling leads to increase of the the crack width at the strain corresponding to rebar failure and hence, it also increases rotations.

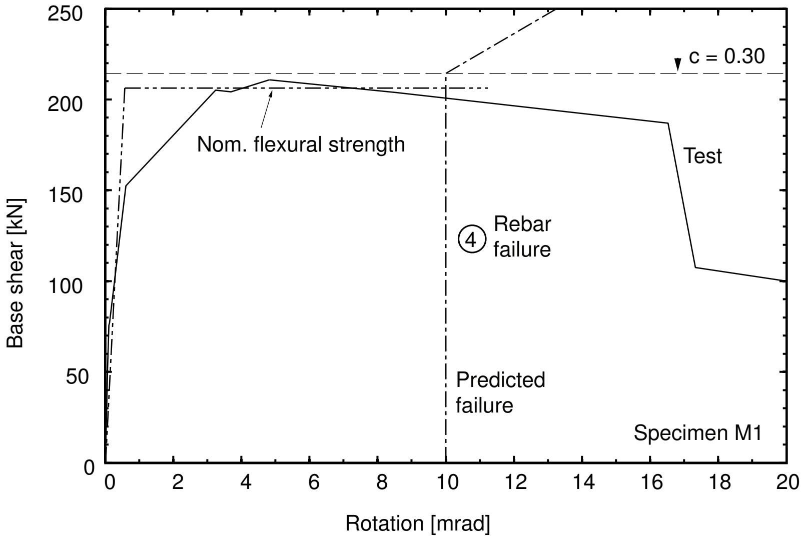

Fig. 5.11: Validation of shear strength envelope (Specimen M1).

Assessment of specimen M3

The assessment of specimen M3 is shown in Fig. 5.12. The bilinear model realistically approximates the observed static-cyclic envelope. Predicted failure is sliding shear whereas concrete crushing is observed in the test. The estimated ultimate rotation is equal to 7.2 mrad. The analysis of experimental data concludes at ultimate rotation of 9.0 mrad. Tab. 5.2 provides a summary of results.

However, the criteria for sliding shear and concrete crushing are very close to each other near the failure point. The correct failure mode thus can be obtained by further calibration of the model on a wider range of test data.

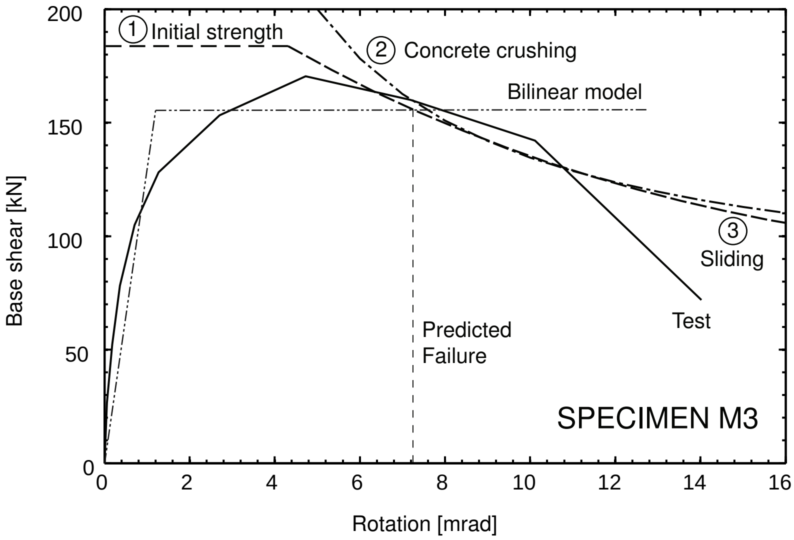

Fig. 5.12: Validation of shear strength envelope (Specimen M3).

Assessment of specimen M4

Fig. 5.13 illustrates the assessment of specimen M4. Sliding shear is predicted for rotation equal to 6.7 mrad (criterion 2, Fig. 5.13). However, this result significantly underestimates the rotation capacity and further calibration of the criterion for sliding shear is required.

The criterion for sliding shear is calibrated by both the reduction of the portion of reinforcement contribution which is expected to decay and the increase of friction constant. For the formulation of reinforcement contribution, it is assumed that this contribution decreases as the reference crack width of the lowermost element increases (Sec. 4.5.5, p. 117). This assumption includes the simplification that the entire reinforcement contribution is transfered by the lowermost element. Nevertheless, it is shown in Tab. 4.3 that the contribution of this element yields only 80%.

Consider constant shear capacity for the part of base joint outside the lowermost element and decay of shear capacity for the rest of the base joint. The reinforcement contribution thus is subdivided into a constant portion (20%) and a decaying portion (80%), and Eq. (4.61) modifies to Eq. (5.22).

$$V = 0.47\, D_b + V_s\,(\theta) = (0.40\,\eta\, f_c + (0.2 + 0.8\,\lambda_s)\,(1-\eta)\, f_y\, \rho_h)\, b_w\, l_w \tag{5.22}$$

In addition, Eq. (5.22) includes the modified friction constant of 0.47. According to Eq. (4.38), the upper bound of concrete contribution is equal to 0.47 times the concrete compression force ($0.47\,D_b$). Preliminary failure of the concrete contribution is excluded as this contribution is less than or equal to the aforementioned upper bound.

The assessment of deformation capacity by using Eq. (5.22) is also shown in Fig. 5.13. Eq. (5.22) corresponds to the criterion 2a. Better prediction of deformation capacity is now achieved, and the ultimate rotation is equal to 8.8 mrad.

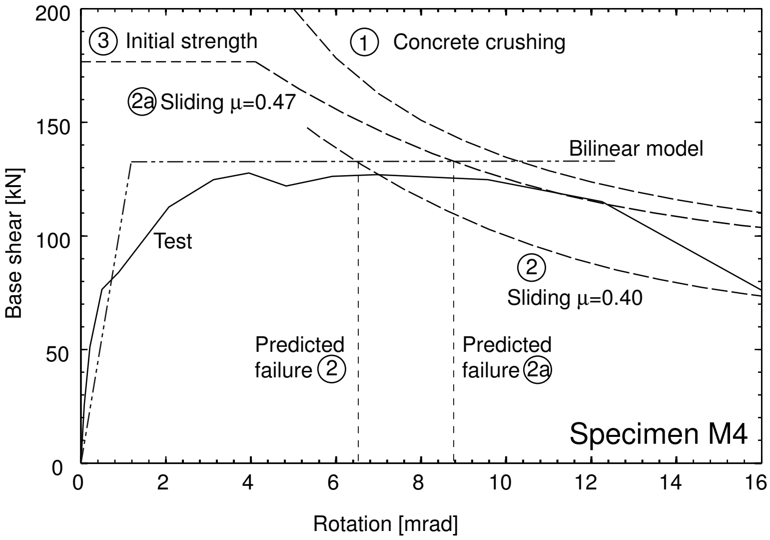

Fig. 5.13: Validation of shear strength envelope (Specimen M4).

Result summary

Table 5.2 summarizes the results from the assessment of deformation capacity. Note that the test results refer to the rotation at 20% decay (Tab. 3.6). So, the model overestimates the drift for specimen M1 because the decay of shear capacity in elastic shear mode is not included in the model.

For specimens M3 and M4, the proposed model predicts approximately 80% of the rotation capacity. Moreover, drift predictions of 58% and 56% are achieved for specimen M3 and M4, respectively. Hence, the proposed model performs significantly better than the lumped plasticity model which only predicts utmost 26% of the drift capacity of the specimens.

Specimen	Pred. θ_{pr} $[mrad]$	Test θ_{te} $[mrad]$	Pred./Test θ_{pr}/θ_{te} $[-]$	Drift pred. $\varphi_{pr}/\varphi_{te}$ $[-]$
M1	10.3	7.7	1.34	1.17
M3	7.2	9.0	0.80	0.58
M4	8.8	11.5	0.77	0.56

Tab. 5.2: Results summary for validation of shear strength envelope (Tests: Tab. 3.6).

5.4.5 Comparison with Revised UCSD model

The revised UCSD model (Kowalsky & Priestley 2000) represents a rational tool to assess the deformation capacity of columns that are susceptible to shear failure (Sec. 2.6.6). In this section the ductility supply according to the revised UCSD model is compared with the ductility supply predicted by the proposed analytical model. The latter enables prediction of the rotation ductility. According to the assumptions of this model, the rotation ductility is equal to the ductility supply in drift. Since the drift is equal to the lateral displacement divided by the wall height, the rotation ductility then is equal to the displacement ductility. In addition, the calculated ductilities are validated by experimental data.

The shear capacity according to the revised UCSD model includes contributions of axial force, concrete, and transversal reinforcement (Eq. (2.66)). Herein, both the contribution of axial force and the reduction factor 0.85 are omitted. Hence, Eq. (2.66) modifies to Eq. (5.23).

$$V_R = V_c\left(\mu_\Delta\right) + V_s \tag{5.23}$$

The concrete contribution is calculated according to Fig. 2.23. The initial concrete contribution is equal to $0.45\sqrt{f_c}$. This contribution linearly decays to $0.075\sqrt{f_c}$ for increase of displacement ductility from 2.0 to 8.0. Reinforcement contribution, shear ratio at nominal flexural strength, and initial shear strength are shown in dimensionless form in Tab. 5.3.

Specimen	f_c	$A_g\sqrt{f_c}$	V_s	$\frac{F_y}{A_g\sqrt{f_c}}$	$\frac{V_s}{A_g\sqrt{f_c}}$	$\frac{V_R}{A_g\sqrt{f_c}}$ [a]
	$[MPa]$	$[-]$	$[kN]$	$[-]$	$[-]$	$[-]$
M1/M2	50	0.71	112	0.30	0.16	0.61
M3	21	0.33	94	0.47	0.28	0.73
M4	25	0.36	94	0.37	0.26	0.71

[a]: Initial shear strength

Tab. 5.3: Application of revised UCSD model, dimensionless strength of specimens M1, M2, M3 and M4.

Both experimental data of specimens M1, M2, M3, and M4 and the shear strength envelopes of specimens M1 and M3 are shown in Fig. 5.14a in dimensionless form. The latter refers to the presentation of base shear and deflection by shear ratio and displacement ductility, respectively. Yield displacements derived from experimental data are used to determine the ductilities of the specimens. The strength envelopes are calculated according to Eq. (5.23). It is observed that the strength envelope of specimen M3 encloses the experimentally observed static-cyclic envelopes of specimens M1, M2, M3, and M4.

The assessment of ductility supply of specimens M1 and M2 is shown in Fig. 5.14b. Failure is assumed at the intersection of the bilinear model and the shear strength envelope. The predicted ductility supply is equal to 6.7. However, the shear strength envelope underestimates the shear strength of specimen M1 and M2. Note that the envelopes of the first cycles are plotted in Fig. 5.14b. Consider failure at 20% decay of base shear. In this case, the observed ductility of specimen M1 is equal to 8.5. The revised UCSD model thus predicts 76% of the observed ductility.

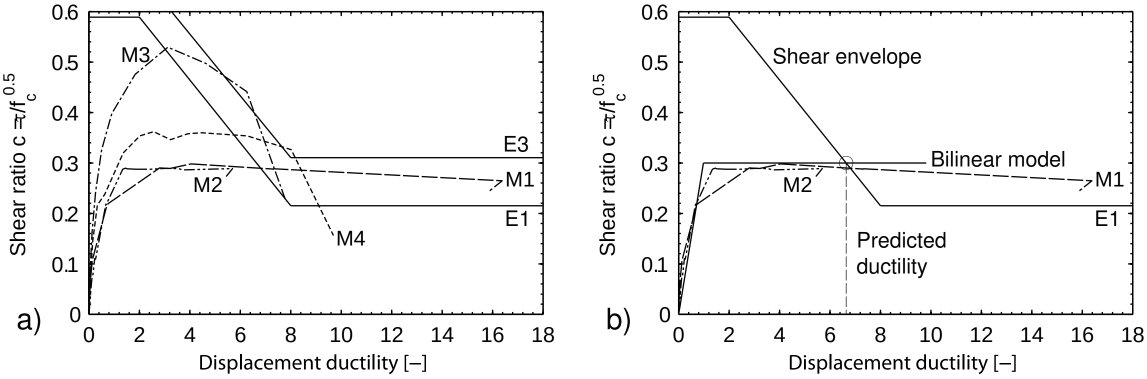

Fig. 5.14: Assessment of specimens using revised UCSD model (Eq. 2.59), a) Overview experimental data and shear envelopes (E1- shear envelope M1, E3 - shear envelope M3), b) assessment of specimen M1.

The evaluation of ductility supply of specimen M3 according to Eq. (5.23) and the proposed model is shown in Fig. 5.15a and Fig. 5.15b. The criteria 1, 2, and 3 in Fig. 5.15b refer to concrete crushing, sliding mode, and initial strength, respectively. Test data are also shown in these figures. Note that the displacement and rotation ductilities observed in the tests are different from each other. However, the predicted ductilities of both models are similar. Both models predict ductilities between 5.0 and 6.0.

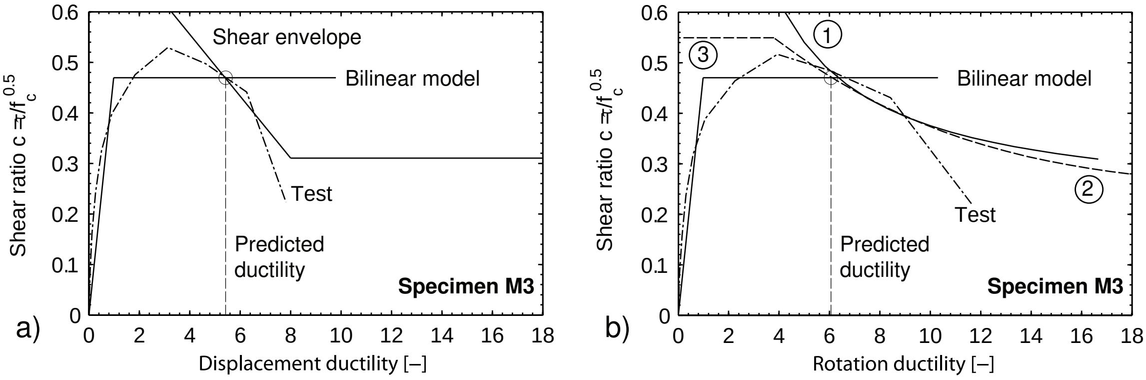

Fig. 5.15: Assessment of ductility supply of Specimen M3, a) revised UCSD model, b) proposed model (Sec. 4.5.7).

For the assessment of ductility of specimen M4, the proposed model includes the calibration introduced by Eq. (5.22). The assessment of ductility is shown in Fig. 5.16. As it was observed for specimen M3, prediction of both models are similar.

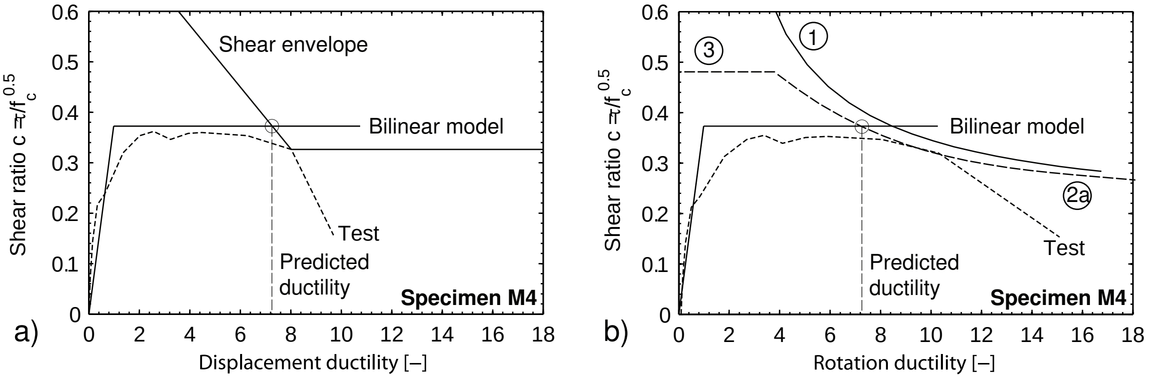

Fig. 5.16: Assessment of ductility supply of Specimen M4, a) revised UCSD model, b) proposed model (Sec. 4.5.7).

Result summary

The ductility supply according to the revised UCSD-model is compared with the ductility supply estimated with the proposed model. The yield displacements shown in Tab. 3.3 are used as input parameter of the revised UCSD-model. According to Priestley & Kowalsky (1998), the ductility is based on the level of straining of vertical rebars. Such approach can also be applied on lightly reinforced shear walls since it is applied on reinforced columns too (Kowalsky & Priestley 2000), (Sezen & Moehle 2004). However, the reinforcement layout of columns and walls are different and walls are susceptible to sliding shear which results in some bias in ductility.

A summary of results is provided by Tab. 5.4. Both models, the revised UCSD model and the proposed model predict 80% and 74% of ductility supply of specimens M3 and M4, respectively. Slighly better prediction is achieved the proposed model for specimen M3 (88%). However, the proposed model fails to predict the ductility supply of specimen M1 while the revised UCSD model overestimates the ductility supply of this specimen by 20%.

Specimen	Test[a]	UCSD		RM[b]	
	μ_Δ	μ_Δ	$\frac{UCSD}{Test}$	μ_θ	$\frac{RM}{Test}$
M1	5.6	6.7	1.20	20	3.57
M3	6.8	5.4	0.80	6.0	0.88
M4	9.7	7.2	0.74	7.2	0.74

[a] Tab. 3.5, [b] Revised UCSD (Eq. (5.23)),

[c] Proposed model (Sec. 4.5).

Tab. 5.4: Ductility supply according to revised UCSD and proposed model.

If contribution of axial force to shear capacity is neglected the revised UCSD model is a robust tool to predict the ductility supply of walls susceptible to shear failure. Nevertheless, the yield displacements from test data are required to achieve this prediction. Since the proposed model provides both estimate for drifts at yield and ductility it shows better potential for seismic evaluation.

5.5 Assessment of shear strength of full-size walls

In this section, attempts are made for the seismic assessment of full-size walls. These attempts include the definition of response types of walls in order to enhance identification of walls susceptible to shear. Furthermore, curvature analysis of shear walls prevalent in existing buildings enables the determination of shear demands which are subsequently compared with both the shear supply according to the general truss model and the shear supply according to the proposed model. The investigations are limited to possible enhancements in the assessment of shear strength.

5.5.1 Definitions

The static-cyclic behavior of lightly reinforced shear walls is governed by both the shear demand τ_M and the shear capacity ratio. The shear demand is equal to the shear stress at maximum flexural strength (Eq. (5.24)).

$$\tau_M = f(n,\, \rho_v,\, A,\, f'_c) = \frac{\phi M_N}{h_w\, l_w\, b_w} \tag{5.24}$$

In Eq. (5.24), the symbol ϕ denotes the overstrength factor, which accounts for the difference between maximum flexural strength and nominal flexural strength. Such a difference is due to hardening of reinforcing steel. Curvature analysis of selected wall configurations has shown that lightly reinforced walls have overstrength less than or equal to 1.1 (p. 146). The overstrength thus is given a value of 1.1. Note that the overstrength of ductile structures is usually greater than 1.1 due to higher strain levels.

The advantages of the definition of the shear demand (Eq. (5.24)) are in the reduction of the number of parameters. Further reduction of parameters is achieved by introducing the the definition of shear ratio. In this section, the shear ratio refers to the demand in shear stress normalized to the square root of compressive strength (Eq. (5.25)).

$$c = \frac{\tau_M}{\sqrt{f'_c}} \tag{5.25}$$

Thus, the shear ratio implicitly includes the following parameters:

- Axial force,
- Concrete compressive strength, and
- Vertical reinforcement ratio.

The shear demand/supply ratio is defined as the ratio of the shear capacity to the maximum expected base shear. The latter is equal to the base shear at nominal flexural strength times 1.1 in order to include overstrength (Eq. (5.26)).

$$\alpha_V = \frac{1.1\, V_N}{V_R} \tag{5.26}$$

5.5.2 Classification of walls

Failure types as defined by Yoshikawa & Miyagi (2001) for columns (p. 7) can also be identified for shear walls. Herein, the term response type is used instead of failure type in order to distinguish clearly between failure mode and response. The advantage of introducing response types in addition to failure modes facilitates identification of the global behavior. Response types thus include one or more failure modes.

The seismic response of a given structure depends on the mechanism forming under reversed lateral loading. Therefore, it is also appropriate for non-ductile structures to focus on hierarchical order of strength of possible mechanisms rather than on the verification of ultimate load. Classification of walls can enhance the identification of structures that are vulnerable to seismic action. The following types of response are defined:

- Elastic shear
- Low-ductile to moderate-ductile response
- Brittle shear

The classification of walls into response types is shown in Fig. 5.17. Note that this figure refers to shear walls of shear span ratios less than or equal to 1.0. The inherent shear strength is less than $0.3\sqrt{f_c}$ (Fig. 4.31) in case of shear span ratios greater than 1.0.

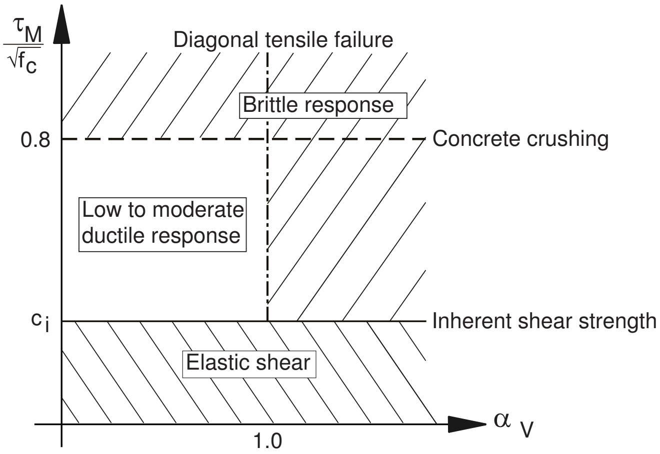

Fig. 5.17: Failure modes and expected response of low-rise shear walls.

Elastic shear

Elastic shear response is expected if the shear demand (Eq. (5.24)) is less than the inherent shear strength (Eq. (4.58)). Response in rocking or sliding occurs if walls behaving in elastic shear are subjected to cyclic loads. Rupture of vertical reinforcement is expected for elastic shear. However, as long as the structural safety under wind and gravity loads is not affected by rupture of vertical reinforcement, the latter is beneficial for seismic behavior. The rupture of vertical reinforcement leads to reduction of the shear demand and hence, it provides in-built base isolation against preliminary shear failure. The criterion for elastic shear is:

$$\tau_M \leq c_i \sqrt{f'_c} \tag{5.27}$$

Experimental evidence for such behavior is provided by the tests of specimens M1 and M2 (Sec. 3) and the specimen Camus 2000-1 (Coin et al. 2002).

Low to moderate-ductile response

Low to moderate ductile response is expected if the shear ratio is between the upper and lower bound of the shear strength envelope proposed in Sec. 4.5. This is shown in Eq. (5.28).

$$0.3\sqrt{f_c} \leq \tau_M \leq 0.8\sqrt{f_c} \tag{5.28}$$

Walls behaving in low to moderate ductile response can fail in concrete crushing, sliding, or rupture of reinforcement. The shear demand ratio needs to be greater or equal to 1.0 to achieve such response ($\alpha_V \leq 1.0$).

Brittle shear

Brittle shear response includes both preliminary shear failure ($1.0 > \alpha_V$) and failure of concrete due to shear stresses greater than the upper bound of shear strength envelope ($\tau_M \geq 0.8\sqrt{f'_c}$).

5.5.3 Curvature capacity of full-size shear walls

The study focuses on cantilever walls of a range of wall length, normal force, vertical and horizontal reinforcement ratios. Both uniformly distributed reinforcement and shear span ratio equal to 1.0 are assumed. Objective of this parametric study is to determine the flexural capacity of walls prevalent in existing buildings. The flexural capacity is subsequently used to calculate the shear demand of such walls. The study includes the following parameters:

- Horizontal reinforcement ($0.2\% \leq \rho_h \leq 1.0\%$)
- Vertical reinforcement ($0.2\% \leq \rho_v \leq 1.0\%$)
- Normal force ($0.02 \leq n \leq 0.10$)
- Wall length ($2.00\,\mathrm{m} \leq l_w \leq 10.0\,\mathrm{m}$)

Nominal flexural strength and ultimate flexural strength are calculated by assuming limit states of strain according to SIA2018 (2004). Limit strains are shown in Tab. 5.5. Moment-curvature relationships are computed by using an iterative procedure. This procedure provides the neutral axis positions for monotonically increasing values of curvature based on the equilibrium of internal axial forces.

Concrete			Reinforcement		
ϵ_{c1d} $[mm/m]$	ϵ_{c2d} $[mm/m]$	ϵ_{cu} $[mm/m]$	ϵ_{y} $[mm/m]$	ϵ_{mn} $[cm/m]$	ϵ_{su} $[cm/m]$
2.0	4.0	4.0	2.0	1.5	5.0

Tab. 5.5: Limits of strain assumed in the curvature analysis of full-size walls.

The results of curvature analysis are shown in Fig. 5.18. The flexural strength increases as the wall length increases (Fig. 5.18a). Relationships between shear demand and axial force ratio are shown in Fig. 5.18b for several ratios of vertical reinforcement. The lower and upper bound of shear demands correspond to shear ratios(c) of 0.13 and 0.55, respectively. Note that the test series presented in Chapter 3 included four specimens of shear demands between 0.28 and 0.52 (Tab. 3.11).

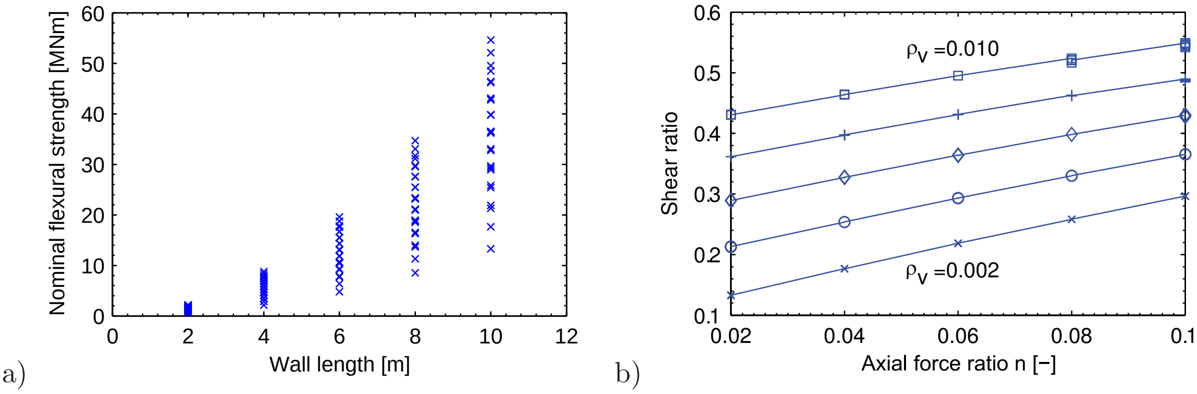

Fig. 5.18: Results overview, a) Nominal flexural strength as a function of wall length, b) Shear ratio as a function of axial force ratio.

Neutral axis position

The positions of neutral axis are shown in Fig. 5.19. Linear relationships relate the neutral position to the axial force ratio. The results plotted in Fig. 5.19 are summarized using the linear relationship given in Eq. (5.29).

$$\eta = 0.01\,(1 + n) + 0.14\rho_v \tag{5.29}$$

Eq. (5.29) is particularly useful for rapid estimation of flexural strength. It helps to reduce the number of iterations that is necessary to determine the neutral axis position at axial equilibrium. Upper and lower bounds of dimensionless position of neutral axis are equal to 0.24 and 0.06, respectively. However, the position of neutral axis can depend on the strain limit assumed for the analysis. Since the assumptions of limit strains are conservative, the calculated upper bounds are also conservative.

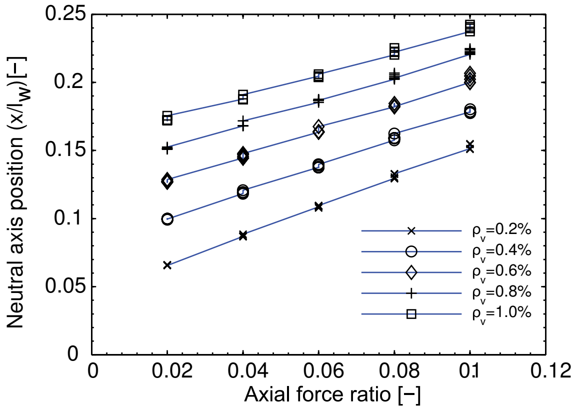

Fig. 5.19: Dimensionless position of neutral axis (η) as a function of axial force ratio (n).

Yield curvatures and curvature ductility

The yield curvatures are not sensitive to both vertical reinforcement axial force ratio (Fig. 5.20a) while the ultimate curvature are sensitive to these parameters (Fig. 5.20b). Increase in both, vertical reinforcement and normal force reduces the curvature capacity.

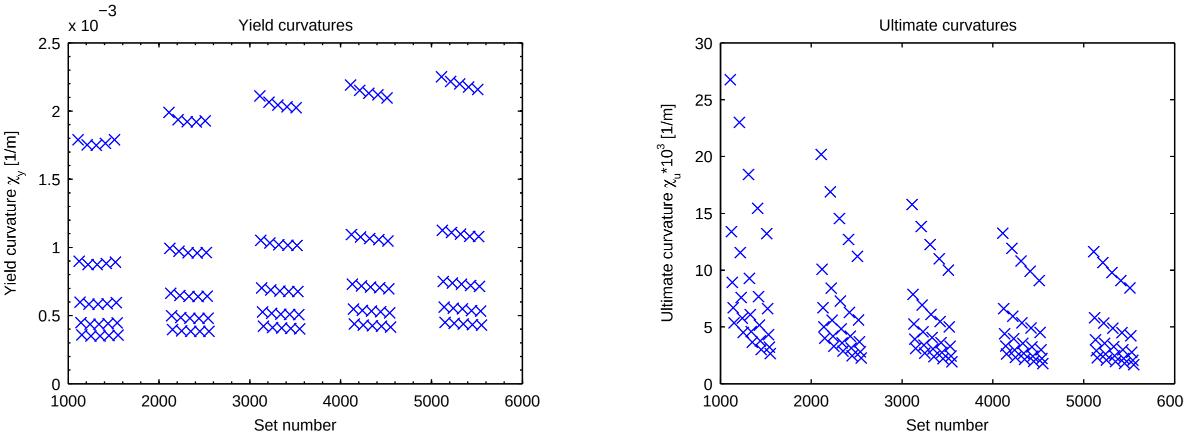

Fig. 5.20: Yield and ultimate curvatures.

In Fig. 5.20, the set number refers to an identifier of 4-digits. The first, second, and third digit denotes vertical reinforcement ratio, axial force ratio, and wall length, respectively. The parameter are arranged of ascending order in the sets. The variation of yield curvature however correlates with the variation of wall length. Equation (5.30), originally proposed by Priestley & Kowalsky (1998), is commonly used to predict the yield curvature of rectangular walls (SIA2018 2004).

$$\chi_y = 2.0\,\frac{\epsilon_y}{l_w} \tag{5.30}$$

The prediction quality of this expression is shown in Fig. 5.21. Predictions achieved with Eq. (5.30) slightly underestimates the yield curvature. The scatter increases as the wall length decreases.

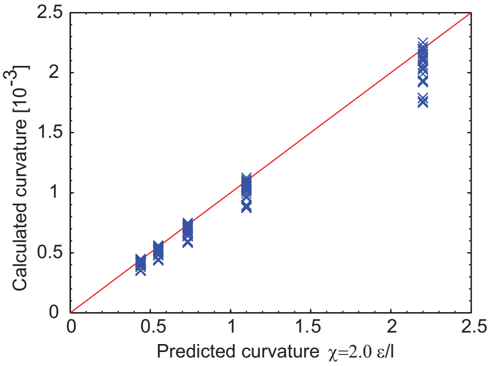

Fig. 5.21: Prediction quality of yield curvature according to Eq. (5.30).

Curvature ductilities

Curvature ductilities are sensitive to both vertical reinforcement and axial force (Fig. 5.22). Increase in vertical reinforcement or axial force results in decrease of curvature ductility. In addition, it is revealed that the curvature ductility is insensitive to the wall length.

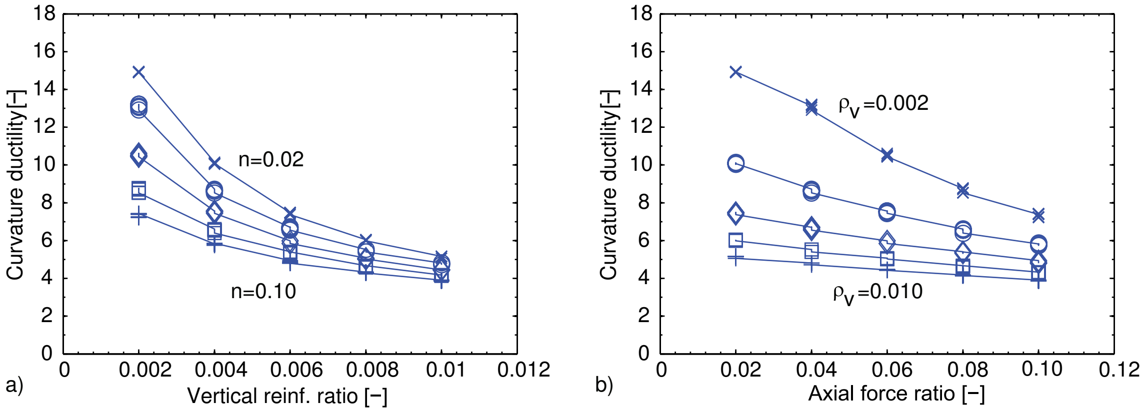

Fig. 5.22: Curvature ductilities vs. ρ_v (a) and Curvature ductilities vs. n (b).

Ratio of maximum to nominal flexural strength

In the context of capacity design, the ratio of maximum to nominal flexural strength denotes the overstrength that can develop in case of high levels of straining. Appropriate estimates of overstrength are required to avoid preliminary shear failure. The calculated ratios of maximum flexural strength to nominal flexural strength are shown in Fig. 5.23. Increase in vertical reinforcement or axial force results in decrease of both curvature capacity and rebar strain at maximum flexural strength. So, the overstrength also decreases as both vertical reinforcement ratio and axial force ratio increase.

Overstrength is due to strain hardening of reinforcement. Consequently, a overstrength of a wall failing in concrete crushing is less than the overstrength developing in wall for which tensile failure is expected. Walls without adequate confinement of the concrete compression zone are more susceptible to concrete crushing than walls with confined boundaries because deformation capacity of concrete increases with the level of confinement. Hence, the overstrength of walls that are not designed for seismic loads is less than that of capacity designed walls. So, the overstrength of the analyzed configurations is less than 1.1, while in seismic design generally the ratio of M_R to M_N is admitted greater than or equal to 1.2.

Conclusions of curvature analysis

The moment-curvature relationships are investigated for a set of full-size shear walls prevalent in existing buildings. It is found that the shear demand due to nominal flexural strength is in the range between $0.13\sqrt{f_c}$ and $0.55\sqrt{f_c}$. In addition, the ratio of nominal flexural strength to ultimate flexural strength is less than 1.1.

The lever arm to wall-length ratio is revealed to be insensitive to the variation of the parameters ($z/l_w = 0.53..0.55$). For rapid evaluation, the lever arm should be taken equal to the half of the wall length.

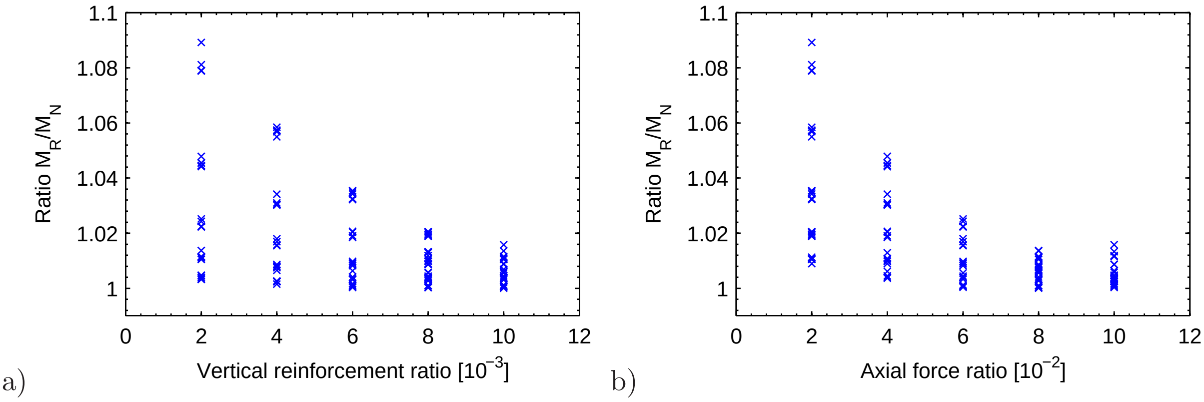

Fig. 5.23: Overstrength of walls with distributed reinforcement, a) as a function of vertical reinforcement ratio, b) depending on axial force ratio.

Calculation of the lever arm by using the ratio of flexural strength to tensile force of rebars is not valid for the investigated configurations because normal force significantly contributes to the flexural strength.

The vertical reinforcement ratio governs the predicted failure mode in the curvature analysis. Concrete failure is predicted for vertical reinforcement ratios equal to or greater than 0.004 regardless of normal force ratio.

The upper bound of dimensionless neutral axis depth is equal to 0.25. According to Eq. (4.50), the lower bound of shear strength in sliding mode is equal to $V_s = 0.75 f_y \rho_h \, b_w \, l_w$.

5.5.4 Susceptibility of full-size walls to shear

In this section, enhancements introduced by the proposal for shear strength envelope are examined for real structures. Selected wall configurations from the database presented in the previous section are used to identify such enhancements. The parameters of this study include:

- Axial force ratio.
- Ratios of both horizontal and vertical reinforcement.

The aspect ratio of all configurations studied herein is assumed to be equal to 1.0. The analysis is limited to cantilever walls. The shear supply is calculated according to the general truss model (Sec. 2.6.3) and the proposed shear strength envelope (Sec. 4.5.7). The calculation includes variation of strut angles in order to determine the maximum shear strength according to the general truss model.

The feasible region for wall configurations with the same amount of vertical and horizontal reinforcement is shown in Fig. 5.24a. The shear demand/supply ratios are based on the previously conducted curvature analysis and the general truss model. It is found that the bigger part of walls of reinforcement ratios less than 0.004 is susceptible to shear failure. The response types for such walls are shown in Fig. 5.24b. It is worth to note that elastic shear response is expected for a significant portion of walls that would fail in brittle shear when evaluated according to the general truss model.

Feasible regions for other ratios of vertical to horizontal reinforcement are shown in Figs. 5.25, 5.26, and 5.27. It is found that the proposed shear envelope predicts brittle shear failure ($\alpha_V > 1.0$) only for some configurations of 0.002 horizontal reinforcement. For other configurations, low to moderate ductile behavior is predicted while according to the general truss model brittle behavior is still expected up to 0.008 horizontal reinforcement.

To conclude, brittle shear failure can be excluded for the bigger part of the examined walls. The proposed shear strength envelope thus shows the potential to evaluate full size shear walls more realistically than it is achieved by using the general truss model.

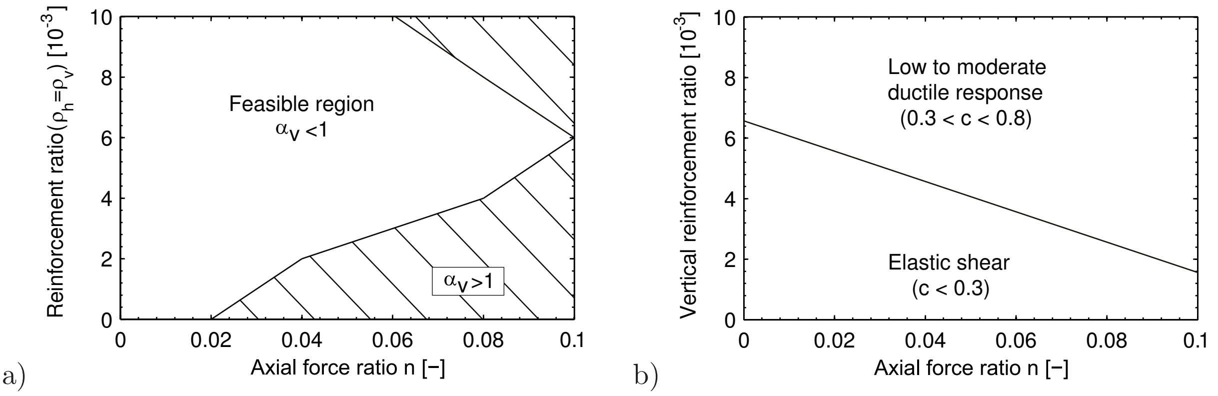

Fig. 5.24: Demand/supply ratios and response modes for $\rho_h = \rho_v$, a) demand/supply ratios (Eq. (5.26), shear strength according to the General truss model, $z = 0.5\,l_w$), b) regions of elastic shear response ($c \leq 0.3$) and of moderate ductile behavior ($c > 0.3$).

Domain of application of analytical model

This section (Sec. 5.5) shows possible application of the previously developed analytical model on the assessment of full-size walls. The shear strength envelope is used to calculate demand/supply ratios for shear and the results of this calculation are compared with predictions according to the general truss model. It is shown that the proposed shear strength envelope can lead to more realistic results than they are achieved with the general truss model.

The analytical model allows for the assessment of deformation capacity of squat cantilever shear walls under static-loading. While application on the assessment of shear strength of full-size walls is possible, there are some limitations for the assessment of deformation capacity. Such limits of application reside for example in the shape of cross-sections, the analytical model is formulated for rectangular cross-sections. In addition, rotation restraints and lap splicing were precluded. Nevertheless, the model shows good potential for extension in order to be applied on such situations too. For this, further research is needed that is beyond the scope of the present work.

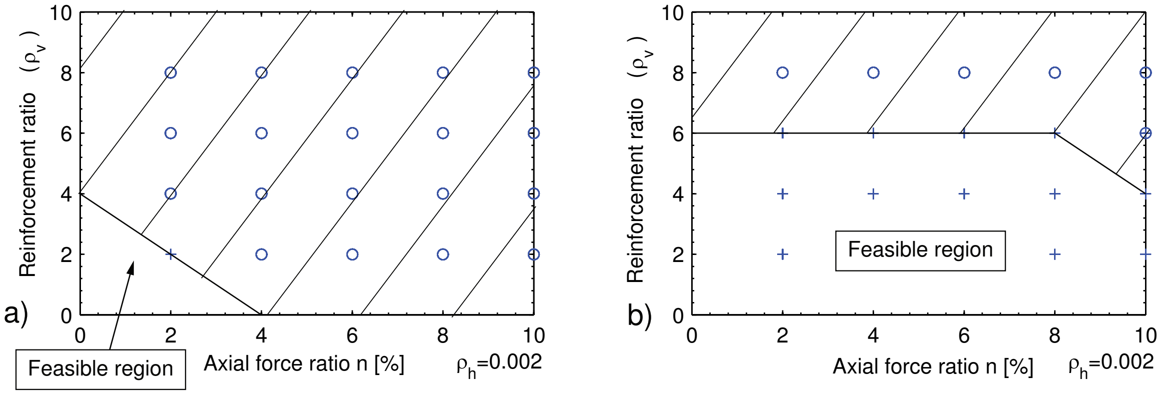

Fig. 5.25: Regions of feasibility, a) General Truss model ($z = 0.5\,l_w$, $\rho_h = 0.002$), b) proposed method ($\rho_h = 0.002$).

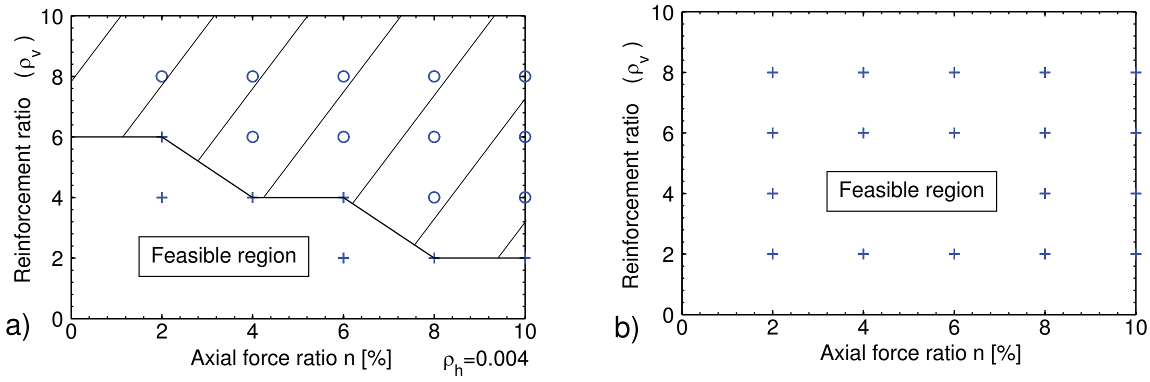

Fig. 5.26: Regions of feasibility, a) General Truss model ($z = 0.5\,l_w$, $\rho_h = 0.004$), b) proposed method ($0.004 \leq \rho_h \leq 0.008$).

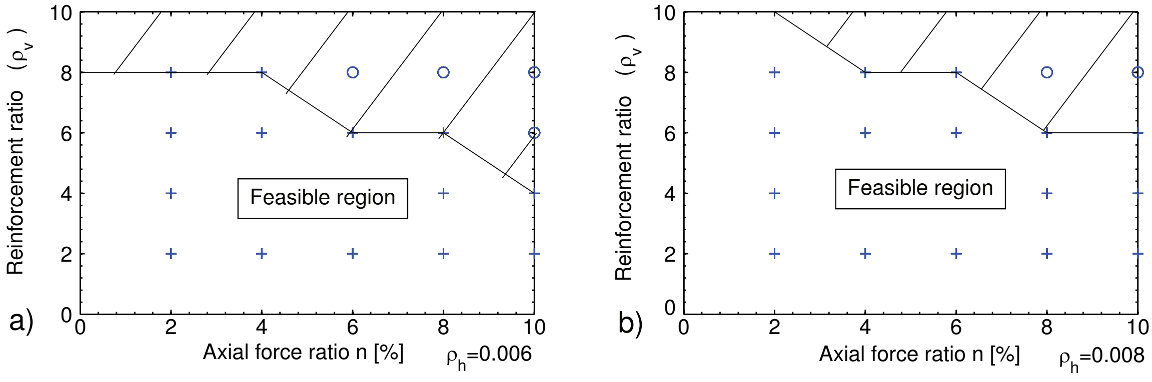

Fig. 5.27: Regions of feasibility (General Truss model, $z = 0.5\,l_w$), a) $\rho_h = 0.006$, b) $\rho_h = 0.008$.

Chapter 6

Summary

6.1 Review of thesis

Increased knowledge of the seismic hazard in countries with moderate exposure necessitates both the adequate design of new structures and the assessment of existing structures. The research presented herein focuses on the latter task which includes the seismic evaluation of structures that are not designed to withstand earthquake actions. Such structures represent the majority of the building stock. In this context, the static-cyclic behavior of lightly reinforced shear walls is investigated. The term lightly reinforced refers to insufficiencies in the amount of reinforcement as well as lacking seismic detailing compared to what is required by code specifications for new buildings. The following keywords thus apply on this research:

- Seismic evaluation of existing buildings
- Non-ductile response
- Reinforced concrete shear walls
- Displacement-based assessment.

Literature review on the observed shear wall performance has shown that despite of the lack of reinforcement and detailing only a limited number of total collapses of shear wall buildings were reported by earthquake reconnaissance missions. The study of available experimental data on low rise shear walls revealed that low to moderate ductility can be expected for such walls. Nevertheless, the study also revealed that experimental data for wall configurations prevalent in existing shear wall buildings are missing. Displacement-based approaches allow seismic assessment that is closer to what happens in case of an earthquake than it is possible with force-based methods. The application of such approaches however requires well-grounded knowledge on the actual deformation capacity of the structure. Since the seismic behavior of non-ductile shear walls can be governed by brittle shear, insufficient deformation capacity is widely expected. Principal objectives of the present research were:

- Provide additional experimental data on behavior of lightly reinforced R.C. shear walls under cyclic lateral loading,
- More realistic modeling for the seismic evaluation of potentially vulnerable structures.

In this context, the thesis aimed at substantiating the displacement-based assessment of existing buildings.

6.2 Conclusions

6.2.1 Experimental investigations

Static-cyclic tests of four non-ductile, lightly reinforced walls showed drifts between 0.8 and 2.1 % by developing shear capacities of 1.4 up to 2.0 MPa. Parameters were concrete compressive strength, amount of horizontal reinforcement, and axial force ratio. Expected preliminary shear failure was not observed, the response of all specimens was characterized by moderate ductility supply. Moreover, the plastic deformation of specimens was governed by flexure while strength degradation with increase in displacement was due to shear mechanisms.

Small reinforcement ratios and low axial force levels limit the maximum base shear. Such limitation provides base isolation to rectangular walls that effectively can prevent brittle shear failure.

Squat, lightly reinforced shear walls can provide similar ratios of dissipated to introduced energy as ductile slender walls. The capacity to dissipate energy essentially originates from sliding shear mechanisms.

It has been shown that the shear intensity governs both the crack pattern and the failure modes of lightly reinforced reinforced shear walls. The shear intensity refers to the shear stress at nominal flexural strength normalized to the square root of concrete compressive strength. Hence, this parameter implicitly includes concrete compressive strength, level of axial force, and the vertical reinforcement ratio. Horizontal reinforcement was not activated up to shear stresses of $0.3\sqrt{f'_c}$.

6.2.2 Modeling

It is interesting to note in this summary concerning modeling that attempts to model the behavior of walls using plasticity theory did not lead to usable results. It came out, that this theory even tough potentially very interesting is not an appropriate tool. Shortcomings reside in lacking deformation compatibility of plasticity based approaches which allow efficient modeling of force flow in reinforced concrete structures. While the objective of design for static-monotonic loading is to precisely describe ultimate load the seismic assessment aims at evaluating deformation capacity. Since the static-cyclic response is governed by locally accumulating damage the compatibility becomes crucial.

An analytical model for the evaluation of the deformation capacity was proposed (Fig. 6.1). The model includes assumptions on both discrete cracks and strain localization at the compressed boundaries. The model is used to estimate length of plastic hinge, to predict the static-cyclic envelope curve, and to derive the envelope of shear strength. Predictions of the static-cyclic envelope achieved with this model agree particularly well with the aforementioned test results. The model has shown ability to predict peak base shear as well as ultimate displacement and failure mode (Sec. 5.4.2).

Shear strength envelopes are proposed for shear walls of which the strength is determined by flexural strength and of which the deformation capacity is restricted by shear (Sec. 4.5). Failure criteria are concrete crushing and degradation of aggregate interlock in the base joint. In addition, a criterion for rupture of vertical reinforcement is also proposed (Fig. 6.1). In combination with idealized bilinear response due to flexure, the proposed shear strength envelope represent an easy-to-use mean for the assessment of deformation capacity. This assessment method allows to predict both the deformation capacity and the failure modes of the test units (Sec. 4.5).

The shear strength of lightly reinforced shear walls includes significant contribution of concrete that is due to the portion of base shear transmitted in the compressed part of the cross section.

Other contributor to shear strength is aggregate interlock in the web. This mechanism depends on transverse web reinforcement. Hence, It is proposed to add concrete contribution to the shear strength computed by the general truss model (Sec. 4.5.4).

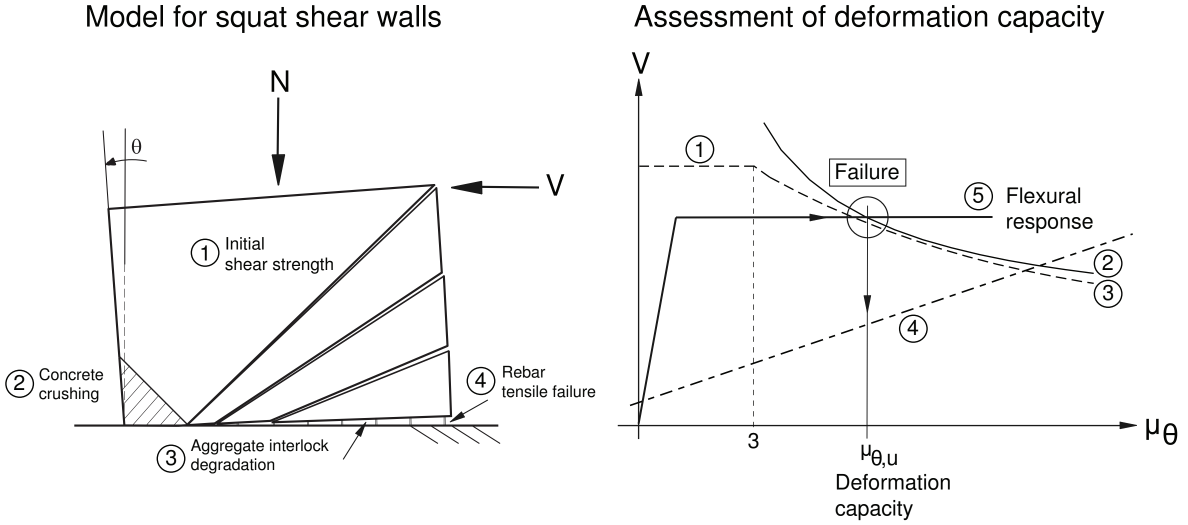

Fig. 6.1: Model for squat shear walls and assessment of deformation capacity.

6.2.3 Application on full-size walls

The chapter on application shows good potential to be used in practical application assuming that the appropriate knowledge transfer can be done. Potentially the model highlights actual seismic capacity which current models fail to account for. In particular, buildings with low reinforcement ratios which would be found to require expensive retrofit with traditional evaluation methods might be shown to have sufficient seismic capacity in areas of moderate seismicity. This of course applies only on selected situations where horizontal bracing is provided by lightly reinforced shear walls. However, in existing buildings such walls are prevalent.

For the seismic evaluation of existing buildings, it was proposed to classify non-ductile shear walls according to the expected failure type. Both the shear ratio and shear demand/supply ratios are used to achieve this classification.

A parameter study has shown that shear ratios of common shear wall configurations are greater or equal to $0.1\sqrt{f_c'}$ and less than $0.6\sqrt{f_c'}$. According to test series on small scale units, brittle shear failure can be excluded for cantilever walls of these shear ratios.

The domain of shear susceptible walls significantly reduces if inherent shear strength of $0.3\sqrt{f_c'}$ is introduced. Elastic shear response is expected for walls of shear demand less than or equal to the inherent shear strength. Such walls would fail in rupture of vertical reinforcement. However, walls would continue to bear vertical loads and overall stability of the structure would not be affected.

6.3 Recommendations for further research

Since the proposed model is only based on limited experimental data, there is an obvious need for further experimental investigations.

The present research focuses on the static-cyclic behavior of lightly reinforced concrete shear walls. Experimental investigations were made on small-scale test units that modeled cantilever walls. Although the test series was carefully conceived in order to maximize congruence with full-size structures, it necessitated a number of limitations. Further experimental research in the field should include the following:

- Validate suggestions on inherent concrete contribution by tests of framed walls.
- Study role of reinforcement detailing, particularly the effect of lap splicing near to the base.
- Provide evidence for dynamic sliding shear.

This can be achieved by a test series in possibly real scale that also would provide answers to the size effect which is included in the tested configurations.

Another important aspect of further research in the field is to study the behavior of wall as a structural element. In the present research, the walls were modeled as cantilevers. This assumption merits further investigations whether in existing building configurations there is, or there is not, sufficient restraining of the wall to provoke brittle shear failure.

While the degree of restraining generally refers to the repartition of stiffness in vertical direction, torsional effects are induced by locally concentrated stiffness in the horizontal direction. Deeper knowledge of plastic distribution of forces in the horizontal direction is required which can result in more realistic seismic assessment. Nowadays, the latter commonly includes the elastic distribution of seismic forces. To conclude, the behavior of wall as structural element can be studied numerically, and in a first step, the outcome of the present research is particularly useful to calibrate the tools for such studies.

The ductility of the tested specimens is analyzed by applying procedures that are commonly used for structural elements of ductile design. For such elements the behavior factors are equated to the ductility. However, further research is necessary how to derive behavior factors for structures of non-ductile design.

In addition, limitations of the proposed model can arise from scale effects. The detailed study of scale effects is beyond the scope of this thesis. Such scale effects should be carefully studied before model is applied in practice.

Bibliography

Aoyama, H.; Noguchi, H.: Mechanical properties of concrete under load cycles idealizing seismic actions, in: Structural concrete under seismic actions, Bulletin d'information 131, pp. 31–63, Comité Euro-International du Beton (CEB), Rome 1979.

Bachmann, H.: Zur plastizitätstheoretischen Berechnung statisch unbestimmter Stahlbetonbalken, PhD-Thesis, ETH Zürich (1967).

Bachmann, H.: Influence of Shear and Bond on Rotational Capacity of Reinforced Concrete Beams, Publications of the International Association for Bridge and Structural Engineeering 30(2) (1970) pp. 12–27.

Bachmann, H.: Stahlbeton I. Vorlesungsautographie, ETH Zürich, Institut für Baustatik und Konstruktion (IBK), Zürich 1991.

Bachmann, H.: Neue Tendenzen im Erdbebeningenieurwesen, Beton- und Stahlbetonbau 99(5) (2004) pp. 356–371.

Bazant, Z. P.; Gambarova, P.: Rough cracks in reinforced concrete, Journal of the Structural Division 106(4) (1980) pp. 819–841.

Biskinis, D.; Roupakias, G.; Fardis, M. N.: Degradation of shear strength of reinforced concrete members with inelastic cyclic displacements, ACI Structural Journal 101(6) (2004) pp. 773–783.

Coin, A.; Mazars, J.; Bisch, P.: Projet Camus 2000 - Rapport final, Centre d'Expertise du Bâtiment et des Travaux Publics (CEBTP), St. Rémy lès Chevreuse 2002.

Collins, M.; Kutchma, D.: How safe are our large, lightly reinforced concrete beams, slabs, and footings?, ACI Structural Journal 96(4) (1999) pp. 482–490.

Darwin, D.; Pecknold, D. A.: Analysis of cyclic loading of plane R/C structures, Computers & Structures 7(1) (1977) pp. 137–147.

Dazio, A.: Entwurf und Bemessung von Tragwandgebäuden unter Erdbebeneinwirkung, PhD-Thesis, ETH Zürich (2000).

Dazio, A.; Wenk, T.; Bachmann, H.: Versuche an Stahlbetonwänden unter zyklisch-statischer Einwirkung, IBK Bericht No. 239, ETH Zürich, Institut für Baustatik und Konstruktion (IBK), Zürich 1999.

EC2: Eurocode 2. Design of concrete structures - Part 1: General rules and rules for buildings, European Committee for Standardization (CEN), Bruxelles 2002.

EC8: Eurocode 8. Design of structures for earthquake resistance, Part 1: General rules, seismic actions and rules for buildings, European Committee for Standardization (CEN), Bruxelles 2003.

Fantilli, A. P.; Ferretti, D.; Iori, I.; Vallini, P.: Mechanical Model for Failure of Compressed Concrete in Reinforced Concrete Beams, Journal of Structural Engineering 128(5) (2002) pp. 637–645.

Fehling, E.: Zur Energiedissipation und Steifigkeit von Stahlbetonbauteilen unter besonderer Berücksichtigung von Rissbildung und verschieblichem Verbund, PhD-Thesis, Technische Hochschule Darmstadt (1990).

Fintel, M.: Performance of buildings with Shear Walls in Earthquakes of the Last Thirty Years, PCI Journal 40(3) (1995) pp. 62–80.

Fouré, B.: Un programme d'essais des murs de contreventement, in: Colloquium AFPS-SECED Experimental Methods in Earthquake Engineering and Structural Dynamics, Association Francaise du Genie Parasismique (AFPS), Saint-Rémy-lès-Chevreuse 1993.

Galal, K.; Arafa, A.; Ghobarah, A.: Retrofit of RC square short columns, Engineering Structures 27(5) (2005) p. 801.

Ghee, A. B.; Priestley, M. J. N.; Paulay, T.: Seismic shear strength of circular reinforced concrete columns, ACI Structural Journal 86(1) (1989) pp. 45–59.

Greifenhagen, C.; Lestuzzi, P.: Static-cyclic tests on lightly reinforced concrete shear walls, Engineering Structures 27(11) (2005) pp. 1703–1712.

Greifenhagen, C.; Lestuzzi, P.; Papas, D.: Static-cyclic tests on reinforced concrete shear walls with low reinforcement ratios, Rapport IMAC No. 4, Ecole polytechnique fédérale de Lausanne, Lausanne 2005.

Hidalgo, P. A.; Jordan, R. M.; Ledezma, C.: Experimental study of reinforced concrete walls under shear failure, in: 6th U.S. National conference on earthquake engineering, Seattle 1998.

Hidalgo, P. A.; Ledezma, C.; Jordan, R. M.: Seismic behavior of squat reinforced concrete shear walls, Earthquake Spectra 18(2) (2002) pp. 287–308.

Hsu, T. T. C.; Zhu, R. R. H.: Softened Membrane Model for Reinforced Concrete Elements in Shear, ACI Structural Journal 99(4) (2002) pp. 460 – 469.

Ile, N.: Contribution à la compréhension du fonctionnement des voiles en béton armé sous sollicitation sismique: apport de l'experimentation et de la modélisation à la conception, PhD-Thesis, INSA Lyon (2000).

Kanellopoulos, A.: Zum unelastischen Verhalten und Bruch von Stahlbeton, IBK Bericht No. 153, ETH Zürich, Institut für Baustatik und Konstruktion (IBK), Birkhaeuser, Basel 1986.

Karsan, I. D.; Jirsa, J. O.: Behavior of concrete under compressive loading, Journal of the Structural Division 95(ST12) (1969) pp. 2543–2563.

Kaufmann, W.; Marti, P.: Structural concrete: cracked membrane model, Journal of Structural Engineering 124(12) (1998) pp. 1467–1475.

König, G.; Fehling, E.: Zur Rissbreitenbeschränkung im Stahlbetonbau, Beton- und Stahlbetonbau 83(6) (1988) pp. 161–167.

Kowalsky, M.; Priestley, M. J. N.: Improved Analytical Model for Shear Strength of Circular Reinforced Concrete Columns in Seismic Regions, ACI Structural Journal 97(3) (2000) pp. 388–396.

Lang, K.: Seismic vulnerability of existing buildings, PhD-Thesis, ETH Zürich (2002).

Lefas, I.; Kotsovos, M.: Strength and Deformation Characteristics of Reinforced Concrete Walls under Load Reversals, ACI Structural Journal 87(6) (1990) pp. 716–726.

Lefas, I.; Kotsovos, M.; Ambraseys, N.: Behavior of Reinforced Concrete Structural Walls: Strength, Deformation Characteristics, and Failure Mechanism, ACI Structural Journal 87(1) (1990) pp. 23–31.

Leonhardt, F.; Mönnig, F.: Vorlesungen über Massivbau - Teil 1: Grundlagen zur Bemessung im Stahlbetonbau, Springer, Berlin 1984.

Lestuzzi, P.: Dynamisches plastisches Verhalten von Stahlbetonwänden unter Erdbebeneinwirkung, PhD-Thesis, ETH Zürich (2000).

Lestuzzi, P.; Wenk, T.; Bachmann, H.: Dynamische Versuche an Stahlbetontragwänden auf dem ETH-Erdbebensimulator, IBK Bericht No. 240, ETH Zürich, Institut für Baustatik und Konstruktion (IBK), Zürich 1999.

Lopes, M. S.: Experimental shear-dominated response of RC walls: Part I: Objectives, methodology and results, Engineering Structures 23(3) (2001a) pp. 229–239.

Lopes, M. S.: Experimental shear-dominated response of RC walls. Part II: Discussion of results and design implications, Engineering Structures 23(5) (2001b) pp. 564–574.

Maekawa, K.; Pimanmas, A.; Okamura, H.: Nonlinear mechanics of reinforced concrete, Spon Press, New York 2003.

Maekawa, K.; Qureshi, J.: Computational model for reinforcing bar embedded in concrete under combined axial pullout and transverse displacement, Concrete Library of JSCE 29(June) (1997) pp. 217–233.

Maier, J.; Thürlimann, B.: Bruchversuche an Stahlbetonscheiben, IBK Bericht 8003-1, ETH Zürich, Institut für Baustatik und Konstruktion (IBK), Zürich 1985.

Mander, J.; Kim, J.; Dutta, A.: Shear Flexure Interaction Seismic Analysis and Design, in: Modeling of inelastic behavior of RC Structures, pp. 369–382, ASCE, Reston 2001.

Marti, P.; Alvarez, M.; Kaufmann, W.; Sigrist, V.: Tragverhalten von Stahlbeton, IBK Publikation SP-008, ETH Zürich, Institut für Baustatik und Konstruktion (IBK), Zürich 1999.

Mattock, A.: Shear transfer under cyclically reversing loading, across an interface between concretes cast at different times, Report SM 77-1, University of Washington (1977).

Monti, G.; Nuti, C.: Nonlinear cyclic behavior of reinforcing bars including buckling, Journal of Structural Engineering 118(12) (1992) pp. 3268–3284.

Muttoni, A.: Die Anwendbarkeit der Plastizitätstheorie in der Bemessung von Stahlbeton, IBK Bericht No. 176, ETH Zürich, Institut für Baustatik und Konstruktion (IBK), Birkhäuser, Basel 1990.

Muttoni, A.: Schubfestigkeit und Durchstanzen von Platten ohne Querkraftbewehrung, Beton- und Stahlbetonbau 98(2) (2003) pp. 74–84.

Muttoni, A.; Schwartz, J.; Thürlimann, B.: Bemessung von Betontragwerken mit Spannungsfeldern, Birkhaeuser, Basel 1996.

Paulay, T.; Bachmann, H.; Moser, K.: Erdbebenbemessung von Stahlbetonhochbauten, Birkhaeuser, Basel 1990.

Paulay, T.; Bull, I.: Shear effects on plastic hinges of earthquake resisting reinforced concrete frames, in: Structural concrete under seismic actions, Bulletin d'information 132, Comité Euro-International du béton (CEB), Rome 1979.

Paulay, T.; Priestley, M. J. N.; Singe, A. J.: Ductility in Earthquake Resisting Squat Shearwalls, ACI Journal 79(4) (1982) pp. 257– 269.

Pellissier, V.: Evaluation de stratégies pour la gestion du risque sismique du bâtiment, PhD-Thesis, Ecole polytechnique fédérale de Lausanne (2004).

Peter, K.: Erdbebenüberprüfung bestehender Stahlbetongebäude, Ph.D. thesis, Ecole polytechnique fédérale de Lausanne (2000).

Pilakoutas, K.; Elnashai, A. S.: Interpretation of testing results for reinforced concrete panels, ACI Structural Journal 90(6) (1993) pp. 642–645.

Popov, E.: Bond and Anchorage of Reinforcing Bars Under Cyclic Loading, ACI Journal 81(4) (1984) pp. 340–348.

Priestley, M. J. N.: Displacement-based seismic assessment of reinforced concrete buildings, Journal of Earthquake Engineering 1(1) (1997) pp. 157–192.

Priestley, M. J. N.: Performance Based Seismic Design, in: XII World Conference on Earthquake Engineering, Auckland 2000.

Priestley, M. J. N.; Kowalsky, M.: Aspects of Drift and Ductility Capacity of rectangular cantilever structural Walls, Bulletin of the New Zealand National Society forEarthquake Engineering 31(2) (1998) pp. 73–85.

Priestley, M. J. N.; Park, R.: Strength and ductility of concrete bridge columns under seismic loading, ACI Structural Journal 84(1) (1987) pp. 61–76.

Priestley, M. J. N.; Seible, F.; Calvi, G.: Seismic Design and Retrofit of Bridges, Wiley, New York 1996.

Priestley, M. J. N.; Verma, R.; Xiao, Y.: Seismic Shear Strength of Reinforced Concrete Columns, Journal of Structural Engineering 120(8) (1994) pp. 2310–2328.

Raphael, B.; Smith, I. F. C.: A direct stochastic algorithm for global search, Applied Mathematics and Computation 146(2-3) (2003) pp. 729–758.

Reineck, K.: Ein mechanisches Modell für das Tragverhalten von Stahlbetonbauteilen ohne Stegbewehrung, Bauingenieur 66 (1991a) pp. 323–332.

Reineck, K.: Ultimate Shear Force of Structural Concrete Members without Transverse Reinforcement Derived from a Mechanical Model, ACI Structural Journal 88(5) (1991b) pp. 592–602.

Ritter, W.: Die Bauweise Hennebique, Schweizerische Bauzeitung 17 (1899) pp. 1–9.

Rodrigues, R. V.; Burdet, O.; Muttoni, A.: Experimental investigations of the shear capacity of plastic hinges, in: fib Symposium "Keep Concrete Attractive", vol. 2, pp. 651–656, FIB, Budapest 2005.

Rothe, D.: Untersuchungen zum nichtlinearen Verhalten von Stahlbetonwandscheiben unter Erdbebenbeanspruchung, of VDI-Fortschrittsberichte, Reihe 4, Nr. 117, VDI-Verlag, Düsseldorf 1992.

Salonikos, T.; Kappos, A.; Tegos, A.; Penelis, G.: Cyclic load behaviour of low slenderness reinforced concrete walls: design basis and test results, ACI Structural Journal 96(4) (1999) pp. 649–660.

Schlaich, J.; Schaefer, K.; Jennewein, M.: Toward a consistent design of structural concrete, PCI Journal 32(3) (1987) pp. 74–150.

Sezen, H.; Moehle, J.: Shear Strength Model for Lightly Reinforced Concrete Columns, Journal of Structural Engineering 130(11) (2004) pp. 1692–1703.

SIA2018: Vérification de la sécurité parasismique des bâtiments existants, Cahier technique, Société suisse des ingénieurs et des architectes (SIA), Zürich 2004.

SIA262: Structures en béton, Norme suisse, Société suisse des ingénieurs et des architectes (SIA), Zürich 2003.

Sigrist, V.: Zum Verformungsvermögen von Stahlbetonträgern, PhD-Thesis, ETH Zürich (1995).

Skrikerud, P.; Bachmann, H.: Discrete crack modeling for dynamically loaded, unreinforced concrete structures, Eartquake Engng Struct. Dyn. 14 (1986) pp. 297–315.

Thiele, K.; Wenk, T.; Bachmann, H.: Versuche an Stahlbetontragwänden unter pseudodynamischer Einwirkung, IBK Bericht No. 257, ETH Zürich, Institut für Baustatik und Konstruktion (IBK), Zürich 2000.

Vecchio, F.; Collins, M.: The modified compression-field theory for reinforced concrete elements subjected to shear, ACI Journal 83(2) (1986) pp. 219–231.

Walraven, J.: Rough Cracks subjected to Earthquake Loading, Journal of Structural Engineering 120(5) (1994) pp. 1510–1524.

Wyllie, L. A.; Abrahamson, N.; Bolt, B.; Castro, G.; Durkin, M. E.: The Chile Earthquake of March 3, 1985 - Performance of Structures, Earthquake Spectra 2(2) (1986) pp. 293–371.

Yoshikawa, H.; Miyagi, T.: Ductility and Failure Modes of Single Reinforced Concrete Columns, in: Modeling of inelastic behavior of RC structures, (Edited by P. Benson Shing; T. Tanabe), pp. 351–368, ASCE, Reston, VA 2001.

Glossary

Latin letters

A_d : Dissipated energy per cycle.
A_i : Elastic strain energy.
A_g : Concrete gross-section.
A_{sh} : Cross-sectional area of horizontal rebars.
a : Shear span ratio (Lever arm of base shear divided by wall length).
c : Shear ratio (Eq. (5.25)).
c_i : Shear ratio at inherent shear strength (Eq. (4.58)).
D_b : concrete compressive force.
d : Displacement measured by using LVDT.
d_g : Maximum aggregate size [mm].
E : Young's modulus.
f_c' : Mean concrete compressive strength on cylinder.
f_y : Mean yield strength of rebars.
f_u : Mean tensile strength of rebars.
F_y : Base shear at nominal flexural strength.
F_y' : Base shear at first yield.
F_H : Applied base shear.
$F_{H,max,I}$: Maximum base shear developed in first cycle.
$F_{H,max,II}$: Maximum base shear developed in second cycle.
h_w : Wall height.
h/l : Geometric slenderness ratio.
I : Moment of inertia.
k_{dg} : Coefficient aggregate size, $k_{dg} = \frac{48}{d_g+16}$.
K : Stiffness.
LP : Lumped plasticity model (Sec 2.8.3).
l_w : Wall length.
l_{anc} : anchorage length of rebars.
M_N : Nominal flexural strength.
M_N' : Bending moment at first yield.
M_R : Maximum flexural strength.
P_u : Normal force (compression with positive sign).
RM : Rotation based model (Sec 4).
s : Crack spacing.
t : Panel thickness.
V_{max} : Maximum base shear.
V_M : Base shear at maximum flexural strength.
V_R : Shear capacity.
V_u : Ultimate base shear.
V_c : Nominal shear force - concrete contribution.
V_{do} : shear force due to dowel action of vertical reinforcement.
V_i : Nominal shear force.
V_s : Nominal shear force - reinforcement contribution.
V_u : Ultimate design shear force.
V_y' : Base shear at onset of yielding.
v : Nominal shear stress ratio.
w : Crack width.
$\bar{w}$: Reference crack width.
w' : Shortening of compressed fiber.
x : Position of neutral axis.

Greek letters

α : Strut inclination relative to member axis.
α_y : Ratio of nominal flexural strength to bending moment at first yield.
$\alpha_{y,1}$: Ratio of base shear near to first yield to base shear at nominal flexural strength.
α_V : Demand/supply ratio of shear strength.
α_K : Stiffness ratio.
α_{st} : Reduction factor for plastic hinge length.
α_w : Ratio of sum of crack widths to the crack width in the base joint.
ϵ_c : Concrete strain.
ϵ_{1c} : Peak strain of concrete.
ϵ_{cu} : Ultimate concrete strain.
ϵ_{mn} : Strain of rebars at nominal flexural strength.
ϵ_y : Yield strain of rebars.
ϵ_u : Uniform Strain. Maximum uniformly distributed strain before necking occurs.
γ_V : Shear capacity ratio (Eq. (5.26)).
ϕ : strength reduction factor; 0.85 for Shear and 0.9 for Bending.
$\phi_{o,w}$: Ideal overstrength factor.
Δ_{max} : Top lateral displacement at maximum base shear.
Δ_u : Top lateral displacement at failure.
$\Delta_{u,exp}$: Top lateral displacement at failure (Test).
Δ'_y : Displacement at onset of yielding.
Δ_{fl} : Displacement due to flexure.
Δ_γ : Displacement due to distortion (panel deformation).
Δ_{sl} : Displacement due to sliding shear.
φ : Drift.
η : Ratio of neutral axis position to wall length.
κ : Localisation parameter of concrete strains (Eq. (4.30)).
λ : Ratio of vertical to horizontal reinforcement.
λ_c : Decay factor of concrete contribution to shear strength due to increase in deformation.
λ_s : Decay factor of reinforcement contribution to shear strength due to increase in deformation.
μ : Friction constant.
μ_Δ : Displacement ductility.
$\mu_{\Delta,fl}$: Displacement ductility at tensile failure of longitudinal reinforcement.
θ : Rotation.
θ'_y : Rotation at onset of yielding.
ρ_h : Geometric reinforcement ratio in horizontal direction.
ρ_v : Geometric reinforcement ratio in vertical direction.
ρ_e : Geometric reinforcement ratio of vertical boundary reinforcement.
σ_c : Concrete compressive stress.
ς : Ratio of concrete strain to peak concrete strain (Eq. (4.17)).
τ_b : Bond stress.
τ_c : Concrete shear strength, $\tau_c = 0.3\sqrt{f'c}$.
$\tau_{c,lim}$: Maximum concrete contribution to shear strength.
$\tau_{c,u}$: Upper bound of shear stress.
τ_{max} : Maximum shear stress, maximum base shear divided by concrete gross-section.
τ_M : Shear stress at maximum flexural strength (Eq. (5.24)).
τ_{nom} : Nominal shear stress.
τ_u : Ultimate shear stress, ultimate base shear divided by concrete gross-section.
ξ : Ratio of internal lever arm to wall length.
ξ_{eq} : Equivalent damping ratio.
ζ : Softening coefficient, reduction of compressive strength due to transversal straining.

List of Figures

List of Tables

Christian Greifenhagen
(Dipl-Ing., Civil Engineering)

Chemin du Reposoir 2
1007 Lausanne
christian.greifenhagen@a3.epfl.ch

Nationality: German
Date of birth: 15.08.1973

Education

2002 – 2006.	PhD-Student at Applied Computing and Mechanics Lab (IMAC), Structural Engineering Institute, EPF Lausanne, Switzerland.
1996 – 2001	Studies in Civil Engineering at Technische Universität Dresden. Focus on Structural Engineering, Grade: Dipl-Ing.
1998 – 1999	Exchange student at ESTP Paris, France. Branch: Structures.
10/95-03/96	Studies in Architecture, Technische Universität Dresden.

Professional Experience

2004	Lecturer, Introduction of Swisscodes SIA261/262, Seismic safety.
2001 – 2002	Design Engineer, Ingenieurbüro Prof. Jäger, Radebeul, Germany.
1993 - 1995	Carpenter, Apprenticeship with specialization in concrete works.

Recognitions

2001	Gustav-Grüning Prize for excellence in Diploma thesis in Statics.

Publications

ISI journals:

Greifenhagen, C. & Lestuzzi, P. (2005), Static-cyclic tests on lightly reinforced concrete shear walls, Engineering Structures, 11(27):1703-1712.

Conference proceedings:

Greifenhagen, C. & Lestuzzi, P. (2006), Failure modes and deformation capacity of lightly reinforced concrete shear walls*.* The Second fib Congress, Naples (*Paper accepted)*.

Greifenhagen, C. & Lestuzzi, P. (2005), Versuche zum Verformungsvermögen schwach bewehrter Stahlbetontragwände unter statisch-zyklischen Einwirkungen. In: Aktuelle Themen des Erdbebeningenieurwesens und der Baudynamik, D-A-CH Tagung 2005 in Köln, DGEB Publikation Nr.13.

Other publications:

Greifenhagen, C., Lestuzzi, P. & Papas, D. (2005), Static-cyclic tests on reinforced concrete shear walls with low reinforcement ratios, Rapport IMAC No 4, EPF Lausanne.

Fäh, D., Christen A., Gülerce, U. & Greifenhagen, C. (2003), Single station ambient vibration measurements and interpretation for the cities of Adapazari and Gölcük, Turkey. Report to the DRM-MERM Project, Schweizerischer Erdbebendienst, ETH Zürich.

Jäger, W. & Greifenhagen, C. (2002), Rechenprogramme für den Mauerwerksbau. In: Mauerwerkskalender 2002, Ernst & Sohn, Berlin.

Greifenhagen, C. (2001), Analyse des Tragverhaltens der Kathedrale von Noto (Sizilien) unter aussergewöhnlichen Belastungen mit Hilfe der FE-Methode. Diplomarbeit, Lehrstuhl für Statik, TU Dresden.